VNIVERSITAT DE VALÈNCIA

Study of the Yukawa coupling to leptons using *pp* collisions at $\sqrt{s} = 13$ TeV with the ATLAS detector

Tesi Doctoral
Programa de Doctorat en Física

Sergi Rodríguez Boscà

Departament de Física Atòmica, Molecular i Nuclear
IFIC (Universitat de València - CSIC)

Sota la supervisió de

Prof. Luca Fiorini

June 18, 2020

EL Prof. **Luca Fiorini**, Contractat Doctor mitjançant la Universitat de València

Certifica:

Que la present memòria "**Study of the Yukawa coupling to leptons using *pp* collisions at $\sqrt{s} = 13$ TeV with the ATLAS detector**" ha sigut realitzada sota la seua direcció en l'Institut de Física Corpúscular, centre mixt de la Universitat de València i del CSIC, per **Sergi Rodríguez Boscà** i constitueix la seva tesi per optar al títol de Doctor en Física per la Universitat de València.

I per a que així conste, en compliment de la legislació vigent, presenta en el departament de Física Atòmica, Molecular i Nuclear de la Universitat de València la referida Tesi Doctoral, i firma el present certificat.

València, a 06 de Març de 2020

Prof. Luca Fiorini

Contents

List of Acronyms

ADC Analog-to-Digital Converter.
ALFA Absolute Luminosity For ATLAS.
ALICE A Large Ion Collider Experiment.
ATLAS A Toroidal LHC ApparatuS.

BDT Boosted Decision Tree.
BR Branching Ratio.

CB Combined muons.
CBA Cut-Based Analysis.
CERN Conseil Européen pour la Recherche Nucléaire.
CKKW Matrix element matching scale.
CKM Cabibbo-Kobayashi-Maskawa.
CL Confidence Level.
CM Calorimeter-tagged muons.
CMS Compact Muon Solenoid.
CR Control Region.
CSC Cathode Strip Chamber.

df Different Flavour.

EB Extended Barrel.
EM Electromagnetic.
EMB Electromagnetic Barrel.
EMEC Electromagnetic end-cap.

FCAL Forward calorimeter.

ggF Gluon-Gluon Fusion.

HEC Hadronic End-cap Calorimeters.
HPTO High p_{T} objects.

IBL Insertable B-layer.
ID Identification.
ID Inner Detector.
IP Interaction Point.
ISO Isolation.

JVF Jet Vertex Fraction.
JVT Jet Vertex Tagger.

LAr Lead-liquid Argon Detector.
LB Long Barrel.
LEP Large Electron Positron.
LFV Lepton Flavour Violating.
LHC Large Hadron Collider.
LHCb LHC-beauty experiment.
LHCXSWG LHC Higgs Cross-Section Working Group.
LINAC Linear Accelerator.
LS1 Long Shutdown 1.
LS2 Long Shutdown 2.
LUCID LUminosity measurement using Cherenkov Integrating Detector.

MC Monte Carlo.
MDT Monitored Drift Tube.
ME Extrapolated muons.

MMC Missing Mass Calculator.
MVA MultiVariate Analysis.

NN Neural Network.

OS Opposite sign.

PDF Parton Distribution Function.
PMNS Pontecorvo-Maki-Nakagawa-Sakata.
PMT PhotoMultiplier Tube.
PS Proton Synchrotron.
PV Primary Vertex.

QCD Quantum Chromodynamics.
QFT Quantum Field Theory.
QSF Resummation scale.

ROD Read-Out Driver system.
RPC Resistive Plate Chamber.

SA Stand-Alone muons.
SCT Semi-Conductor Tracker.
sf Same Flavour.
SM Standard Model.
SPS Super Proton-Synchrotron.
SR Signal Region.
SS Same sign.
SSB Spontaneous Symmetry Breaking.
ST Segment-tagged muons.

TGC Thin Gap Chamber.
TileCal Tile Calorimeter.
TRT Transition Radiation Tracker.

VBF Vector Boson Fusion.
VEV Vacuum Expectation Value.
VH Vector Boson production.
VL Validation region.
VR Validation Region.

Preface

The work reported in this thesis was carried out during the Run 2 operation years of the Large Hadron Collider. It describes two physics analyses where the Yukawa couplings of the Higgs boson have an important role for the understanding of the Higgs boson particle, discovered in July 2012.

The motivation to study the Yukawa couplings lies in the Standard Model of particle physics, which is the best theoretical framework developed so far to describe the behaviour of sub-atomic particles and their interactions. However it has still unsolved problems. For instance the modification of the theory to account for massive neutrinos or why the charged lepton mixing is highly suppressed. Therefore a good understanding and precise measurements of the Standard Model predictions are necessary, in particular in the Yukawa sector of the theory.

At the Large Hadron Collider one possible way to measure the lepton Yukawa coupling of the Higgs boson is through its decay into a pair of tau leptons. The procedure to obtain the cross-section measurement of the Higgs boson is explained in Chapter 4. Additionally, the cross-section is measured independently for the two main production modes of the Higgs boson, gluon-gluon fusion and vector boson fusion.

Several physics results have demonstrated the existence of neutrino oscillations which can only happen if neutrinos are massive. Many non-SM theories assume that the charged lepton mixing could appear in nature allowing lepton flavour violating decays. Two independent searches for decays of the Higgs boson into leptons of different flavours are performed in Chapter 5.

The first part of the thesis sets up the context, both theoretical and experimental, in which the work of this thesis was done. The description of the theoretical framework

of the Standard Model, including the Higgs mechanism and the Yukawa interactions is presented in Chapter 1. Chapter 2 describes the experimental setup, the CERN organization, the LHC, the ATLAS experiment and the object reconstruction used in the analyses. Additionally, the Monte Carlo simulations and data-driven techniques used to describe the signal and background processes are described in Chapters 3 and A.1.

Finally, Chapter 6 summarizes the main findings of the thesis and compares them with previous results as well as predictions of the Standard Model of particle physics.

1.- Theory

The theoretical concepts necessary to understand and motivate the contents of this thesis are presented in this chapter. It provides the description of the Standard Model of particle physics (SM). The SM is an effective theory valid up to a certain energy scale. It lacks explanation for fine-tuning issues such as the hierarchy problem, the strong CP problem and for experimental observations such as neutrino oscillations, matter-antimatter asymmetry, dark matter and dark energy. Consequently, the field is still actively searching for new physics phenomena beyond the Standard Model.

1.1 The Standard Model Lagrangian

The SM constitutes one of the most powerful theoretical framework to describe the modern physics phenomena, being able to describe several experimental facts with very high precision. This mathematical construction considers the particles as perturbations of fundamental quantum fields. The interactions included in the SM framework are three of the four fundamental forces of nature: electromagnetic (EM), weak and strong force. The theory fails explaining the remaining force, gravity, within the probabilistic world of the quantum physics and therefore gravity will not be considered. In any case gravity effects are totally negligible for the analyses described in the thesis.

The SM is a gauge Quantum Field Theory (QFT) based on the Lie's symmetry group, $SU(3)_C \times SU(2)_L \times U(1)_Y$, whose electroweak subgroup $SU(2)_L \times U(1)_Y$ is spontaneously broken at low energies.

The SM is described by a Lagrangian formalism and the particles are expressed in terms of fields. These fields can be distinguished by its intrinsic angular momentum,

called *spin*. According to this property, two different kind of particles can be defined: *fermions* with a semi-integer value of spin, and *bosons* with an integer value.

1.1.1 Fermions

Fermions, with spin $\frac{1}{2}$, are the particles responsible for the ordinary matter. They are described mathematically by the Fermi-Dirac statistics, therefore they obey the Pauli exclusion principle, the canonical anti-commutation relation and their fundamental particles are the solutions of the Dirac equation (Equation 1.1):

$$(i\partial\!\!\!/ - m)\psi(x) = 0 \tag{1.1}$$

The wave-form of the fermions in the Standard Model, $\psi(x)$, can be written in terms of their two chiral components: left-handed $\psi_L(x)$ and right-handed $\psi_R(x)$. The left-handed fields are $SU(2)$ doublets, while their right-handed partners transform as $SU(2)$ singlets.

The fermionic matter components are leptons and quarks which are organized into three generations, or families, of increasing mass. Table 1.1 shows the different fundamental particles solving the Dirac's equation (Equation 1.1) that have been found so far.

The existence of a fourth or further sequential families is constrained by the measurement of the Z boson decay width [2, 3]. The validity of this result depends on the mass and coupling of the neutrinos with the Z boson and thus, heavier generations cannot be totally ruled out. In the SM, leptonic and baryonic quantum numbers are conserved.

Fermions belonging to the same family have the same fundamental quantum numbers.

Quarks have colour charge, and therefore are the only fermionic particles that can be involved in strong force interactions. The colour charge can take three values, which are commonly known as red (r), green (g) and blue (b). One peculiarity of the strong interaction is the quark confinement, which explains why the free colour-charged particles states have not been observed in nature so far. Thus, it binds the quarks to form colour-neutral composite particles, called hadrons. The simplest particles allowed

	Generation	Name	Symbol	Mass	Charge	Colour
Quarks	1^{st}	Up	u	~ 2.2 MeV	$+2/3$	rgb
		Down	d	~ 4.7 MeV	$-1/3$	rgb
	2^{nd}	Charm	c	1.28 GeV	$+2/3$	rgb
		Strange	s	96 MeV	$-1/3$	rgb
	3^{rd}	Top	t	173.1 GeV	$+2/3$	rgb
		Bottom	b	4.18 GeV	$-1/3$	rgb
Leptons	1^{st}	Electron	e	0.511 MeV	-1	$-$
		Electron neutrino	ν_e	< 2 eV	0	$-$
	2^{nd}	Muon	μ	105.658 MeV	-1	$-$
		Muon neutrino	ν_μ	< 0.19 MeV	0	$-$
	3^{rd}	Tau	τ	1776.86 MeV	-1	$-$
		Tau neutrino	ν_τ	< 18.2 MeV	0	$-$

Table 1.1: Table of the fermionic fundamental particles within the SM with the corresponding mass, electric charge and colour charge options. This table is replicated for the anti-matter particles but with opposite electromagnetic charge [1].

by the confinement are called mesons, which are a combination of quark-antiquark with zero colour charge. The combination of quark-antiquark (semi-integer spin in both cases) gives as result a particle with integer value, hence it behaves as a boson. Other particles that can be created with colourless charge are the baryons, formed by three quarks. Baryons behave as fermions, because of their semi-integer spin.

Leptons are fermions without colour charge, so they are only sensitive to the weak and electromagnetic forces. This is forcedly true just for the electron-type group of leptons that has electromagnetic charge, see Table 1.1. Neutrinos, otherwise, are neutral particles so they are not sensible to the electromagnetic force but they are to the weak force. In the SM, the neutrinos are massless, however experimentally it has been determined that they are massive [4, 5]. One important remark, is that the neutrinos have an extremely small mass and only mass differences between the neutrinos have been measured directly.

1.1.2 Bosons

Fundamental fermions are the constituent of the matter we know, and fundamental bosons are excitements of the fields that describe the fundamental forces of the SM, called carriers or mediators. This excited states of the fields must obey the canonical commutation relation and they are described by the Bose-Einstein statistics because of the integer spin value.

	Symbol	Interaction	Mass (GeV)	Charge	Colours
Bosons	γ	Electromagnetic	$< 10^{-27}$	0	–
	$W^{\pm}$	Weak	80.385 ± 0.015	± 1	–
	Z	Weak	91.1876 ± 0.0021	0	–
	g	Strong	0	0	8
	H	-	124.97 ± 0.24	0	–

Table 1.2: Table of the fermionic fundamental particles within the SM with the corresponding mass, electric charge and colour charge options.

Table 1.2 shows the different fundamental boson particles associated to the Standard Model of particle physics. The photon (γ) is a neutral massless particle that mediates the electromagnetic interactions, and therefore only couples to electrically-charged particles such as quarks and leptons, but not neutrinos.

Another large group of neutral massless particles is formed by the gluons (g), carriers of the strong force. The gluons carry a colour-anticolour charge, allowing eight independent colour combinations, spanning in the Lie algebra of the $SU(3)$ group.

The weak interactions are carried by two different currents: the charged-current mediators $W^{\pm}$ and the neutral-current mediator Z^0. The $W^{\pm}$ are involved in transitions between up-type and down-type quarks or leptons. The Z boson, on the other hand, conserves the fermionic flavour in its interactions according to the SM.

Finally the Higgs boson, H, does not mediate any fundamental gauge interaction, but is an essential piece of the SM, being the responsible for the Spontaneous Symmetry Breaking mechanism. It was discovered at CERN, by the ATLAS and CMS experiments in July 2012 [6, 7]. It has no intrinsic spin, nor charge but its field interactions deliver

mass to the other fundamental particles including itself and therefore it couples to all massive particles.

1.1.3 Standard Model Lagrangian

Nowadays, the Standard Model can be described through a Lagrangian that is composed of the different terms describing the strong interactions, the electroweak interactions, the Higgs sector and the Yukawa interaction of fermions with the Higgs boson.

$$\mathcal{L}_{\text{SM}} = \mathcal{L}_{\text{QCD}} + \mathcal{L}_{\text{EW}} + \mathcal{L}_{\text{H}} + \mathcal{L}_{\text{Yukawa}} \tag{1.2}$$

Each term of Equation 1.2 is briefly described in the following subsections, using the usual convention of summing over repeated indexes.

1.1.4 Strong interactions

Quantum Chromodynamics (QCD) is the name of the strong interaction theory of coloured quarks and gluons and is based on the non-abelian $SU(3)$ gauge theory. Two main properties of the QCD force are: the asymptotic freedom and confinement. The asymptotic freedom is a powerful mathematical feature related to its non-abelian nature. In the QCD, the strong coupling constant, g_s becomes smaller at greater energy scales, allowing the usage of a perturbative approach at high energies whereas at low energies, below 0.5 GeV, the QCD becomes non-perturbative and other phenomenological approaches must be used.

On the other hand, the confinement is a postulate of the QCD theory by the observation that quarks and gluons (charged-colour particles) cannot exist isolated in nature, thus only composite colour-neutral particles (hadrons) can be detected. This postulate is crucial in understanding high energy hadron collider physics and are the responsible of the creation of sprays of hadronic particles, called jets, as products of pp collisions at the LHC.

The Lagrangian expression of the QCD ($\mathcal{L}_{\text{QCD}}$) is described by the covariant derivative operator D^{μ} (Equation 1.3) and the strength tensor field $G^{a}_{\mu\nu}$ (Equation 1.4) constructed

from the gluon fields G^a_μ and G^a_ν.

$$D_\mu = \partial_\mu + ig_s T^a G^a_\mu \tag{1.3}$$

$$G^a_{\mu\nu} = \partial_\mu G^a_\nu - \partial_\nu G^a_\mu - g_s f^a_{bc} G^b_\mu G^c_\nu \tag{1.4}$$

where g_s is the strong coupling constant, $T^a = \lambda^a/2$ and λ^a are the eight Gell-Mann matrices generators of $SU(3)$ [8], the non-abelian a index refers to the colour charge and the f^a_{bc} is the structure constant, which is the result of the commutator of the group generators of $SU(3)$: $[T_a, T_b] = if^c_{ab}T_c$.

Therefore, the QCD Lagrangian can be written in covariant notation as:

$$\mathcal{L}_{\text{QCD}} = \overline{\psi}_Q(i(\gamma^\mu D_\mu) - m)\psi_Q - \frac{1}{4}G^a_{\mu\nu}G^{\mu\nu}_a \tag{1.5}$$

where ψ_Q is the fermion field with a given flavour Q.

1.1.5 Electroweak interactions

Apart from the QCD interactions, two more interactions can be observed at low energy, the electromagnetic force and the weak force. The electromagnetic force is a long-range interaction between elementary particles resulting from their electric and magnetic fields and it is responsible for the atomic and molecular structure, chemical reactions, the attractive and repulsive electromagnetic force associated with electrically charged or magnetically polarized particles, and all other electromagnetic phenomena. The EM force is mediated by photons and acts on charged particles. On the other hand, the weak force is a short-range force. It is responsible for the radioactive decay of nuclei and serves an essential role in nuclear activities.

In 1979 Sheldon Glashow, Abdus Salam and Steven Weinberg were awarded with the Nobel Prize in Physics for their contributions to the unification of the weak and electromagnetic interactions between elementary particles, called electroweak interaction [9–11].

The EW force is based on the gauge symmetry $SU(2)_L \otimes U(1)_Y$. In the SM, the EW symmetry acts for a given left-handed doublet or right-handed singlet and an

hypercharge, Y[1]. Under these conditions, six doublets of left-handed fermions can be defined:

$$\begin{aligned} Q_L \equiv \begin{pmatrix} \psi_u \\ \psi_d \end{pmatrix}_L &= \left\{ \begin{pmatrix} \psi_u \\ \psi_d \end{pmatrix}_L, \begin{pmatrix} \psi_c \\ \psi_s \end{pmatrix}_L, \begin{pmatrix} \psi_t \\ \psi_b \end{pmatrix}_L \right\} \\ L_L \equiv \begin{pmatrix} \psi_\nu \\ \psi_l \end{pmatrix}_L &= \left\{ \begin{pmatrix} \psi_{\nu_e} \\ \psi_e \end{pmatrix}_L, \begin{pmatrix} \psi_{\nu_\mu} \\ \psi_\mu \end{pmatrix}_L, \begin{pmatrix} \psi_{\nu_\tau} \\ \psi_\tau \end{pmatrix}_L \right\} \end{aligned} \tag{1.6}$$

However, just nine singlets need to be defined:

$$\begin{aligned} Q_R &\equiv (\psi_u)_R, (\psi_d)_R, (\psi_c)_R, (\psi_s)_R, (\psi_t)_R, (\psi_b)_R \\ L_R &\equiv (\psi_e)_R, (\psi_\mu)_R, (\psi_\tau)_R \end{aligned} \tag{1.7}$$

In 1961 Glashow proposed the $SU(2)_L \otimes U(1)_Y$ mediators [9], W^a_μ and B_μ, with four fundamental bosons W^1, W^2, W^3 and B. The vector bosons $W^\pm$, Z and γ are not fundamental, but a linear combination of the fundamental fields with a mixing angle, θ_W, defined as $\tan(\theta_W) = g_B/g_W$ where g_B and g_W are the coupling constants of the fundamental fields. The gauge strength tensor terms can be expressed as:

$$\begin{aligned} W^a_{\mu\nu} &= \partial_\mu W^a_\nu - \partial_\nu W^a_\mu + g_{EW}\epsilon^{abc} W^b_\mu W^c_\nu \\ B_{\mu\nu} &= \partial_\mu B_\nu + \partial_\nu B_\mu \end{aligned} \tag{1.8}$$

where ϵ^{abc} is the three dimensional Levi-Civita tensor and g_{EW} the weak isospin coupling constant. In order to obtain the physical observables, the fundamental fields (Equation 1.8) must be rewritten and combined to obtain the physical basis in such a way that their mass terms are totally independent, so:

$$\begin{aligned} W^\pm_\mu &= \frac{1}{\sqrt{2}}(W^1_\mu \mp i W^2_\mu) \\ Z_\mu &= \cos(\theta_W) W^3_\mu - \sin(\theta_W) B_\mu \\ A_\mu &= \cos(\theta_W) B_\mu + \sin(\theta_W) W^3_\mu \end{aligned} \tag{1.9}$$

[1]The hypercharge is a charge operator that accounts for properties of isospin, electric charge and flavour and it is the sum of strangeness S, charmness C, bottomness B', topness T, and baryon number B, $Y = S + C + B' + T + B$. The relation between the isospin, the electric charge and the hypercharge is given by the Gell-Mann Nishijima formula, $Q = I_3 + \frac{1}{2}Y$.

where $W_\mu^\pm$ and Z_μ are the observable bosons of the weak interaction and A_μ is the mediator of the EM force, which is usually referred as photon.

Finally, the electroweak Lagrangian ($\mathcal{L}_{\text{EW}}$) can be written using the fundamental bosons as:

$$\mathcal{L}_{\text{EW}} = i\overline{L}(\gamma^\mu D_\mu)L + i\overline{Q}(\gamma^\mu D_\mu)Q - \frac{1}{4}B^{\mu\nu}B_{\mu\nu} - \frac{1}{4}W^{\mu\nu}W_{\mu\nu} \tag{1.10}$$

where the covariant derivative D_μ with a general left- (right-) handed field, $\psi_L(\psi_R)$ is defined as:

$$\begin{aligned} D_\mu\psi_L &= \delta_\mu\psi_L - ig_{EW}W_\mu^a\tau^a\psi_L - \frac{1}{2}ig'B_\mu\psi_L \\ D_\mu\psi_R &= \delta_\mu\psi_R - \frac{1}{2}ig'B_\mu\psi_R \end{aligned} \tag{1.11}$$

where g' is the coupling constant for the weak hypercharge and τ^a is the canonically normalized $SU(2)$ generators [12].

1.1.6 Spontaneous Symmetry Breaking

Due to gauge invariance, all particles in a Yang-Mills theory need to be massless in contrast with experimental observations. To solve this issue a complex scalar, colourless and doublet under $SU(2)$ field ϕ (Equation 1.12), named Higgs field [13–16], must be added in the SM Lagrangian (Equation 1.13).

$$\phi(x) = \frac{1}{\sqrt{2}}\begin{pmatrix}\phi^+\\ \phi^0\end{pmatrix} = \frac{1}{\sqrt{2}}\begin{pmatrix}\phi_3 + i\phi_4\\ \phi_1 + i\phi_2\end{pmatrix} \tag{1.12}$$

$$\mathcal{L}_{\text{H}} = (D_\mu\phi)^2 - V(\phi) = (D_\mu\phi)^2 + \mu^2\phi^2 - \lambda\phi^4 \tag{1.13}$$

where μ^2 and λ are two free parameters of the Higgs potential. Depending on the conditions of these two parameters different solutions can be achieved. If $\mu^2 < 0$, the state of minimum energy will be $\phi(x) = 0$ and the potential will preserve the symmetries of the Lagrangian. However, if $\mu^2 > 0$, the field $\phi(x)$ will acquire a vacuum

expectation value (VEV), given by:

$$\langle\phi\rangle = \sqrt{\frac{\mu^2}{2\lambda}} = \frac{v}{\sqrt{2}} \tag{1.14}$$

and the global $SU(2)_L \otimes U(1)_Y$ gauge symmetry will be spontaneously broken. This is commonly referred as Spontaneous Symmetry Breaking (SSB) and allows to get the electrodynamic symmetry $U(1)_Q$ at low energies of the electroweak theory.

$$SU(2)_L \otimes U(1)_Y \xrightarrow{SSB} U(1)_Q \tag{1.15}$$

As the minima of the Higgs potential are degenerate, infinite options satisfy the Higgs Lagrangian. Thus, the easiest way to develop the Higgs field in the SSB is by choosing the so-called unitary gauge, in which the degrees of freedom are minimized, by choosing $\phi_3 = \phi_4 = \phi_2 = 0$ in Equation 1.12. Additionally, in order to get physical observables, ϕ_1 must get the minimum of the field and therefore ϕ_1 can be replaced by:

$$\phi(x) = \frac{1}{\sqrt{2}} \begin{pmatrix} 0 \\ v + h(x) \end{pmatrix} \tag{1.16}$$

where $h(x)$ is a new real field.

As in the QFT the mass of the particles are considered the quadratic terms in the Lagrangian and developing the Higgs Lagrangian, Equation 1.13, using the Equation 1.16, the masses of the bosons can be obtained, becoming:

$$\begin{aligned} m_H^2 &= 2\mu^2 \\ m_{W^\pm}^2 &= \frac{g_{EW}^2 v^2}{4} \\ m_Z^2 &= \frac{g_{EW}^2 v^2}{4\cos^2(\theta_W)} = \frac{m_{W^\pm}^2}{\cos^2(\theta_W)} \\ m_\gamma^2 &= 0 \end{aligned} \tag{1.17}$$

where θ_W is the Weinberg mixing angle defined by the condition $\sin\theta_W = g'/\sqrt{g'^2 + g_{EW}}$ and g' is the coupling constant for the weak hypercharge.

The Fermi constant $G_F^0 = g_{EW}^2\sqrt{2}/8m_{W^\pm}^2c^4 = 1.1663787(6) \times 10^{-5}$ GeV^{-2} can be used with the coupling constants to obtain the mass of the different gauge bosons and they can be compared with the experimental observations [17–20]. However, the Higgs boson mass depends on one free parameter μ^2 and it can be measured only experimentally. The measured value with LHC Run 1 and Run 2 data by ATLAS and CMS is [21]:

$$m_H = 124.97 \pm 0.24 \text{ GeV} \tag{1.18}$$

1.1.7 Yukawa interactions

A Yukawa interaction[2] involves the interaction between a scalar field, ϕ, and a Dirac field (Equation 1.6 and 1.7). This is not allowed in the EW Lagrangian because it contains mixed terms of right and left field projections which break the gauge invariance. The Yukawa Lagrangian (Equation 1.19) can be expressed by convention as:

$$-\mathcal{L}_{\text{Yukawa}} = (Y_u)_{ij}\overline{Q}_{Li}u_{Rj}\phi + (Y_d)_{ij}\overline{Q}_{Li}d_{Rj}\phi + (Y_e)_{ij}\overline{L}_{Li}e_{Rj}\phi + h.c. \tag{1.19}$$

where $SU(2)$ indexes are omitted and i and j run over the three families, such that $Y_{u,d,e}$, where $u =$ up-quark, $d =$ down-quark and $e =$ charged-lepton types respectively, are a general complex 3×3 matrices. The Y_f matrix describes the coupling constants in the flavour basis of the electroweak interaction and can be diagonalized to determine the mass-eigenstates (mass basis or physical basis), which are the true observables of the theory. However, if the whole Lagrangian is rewritten in terms of the mass basis, the expressions of the Lagrangian EW interaction loose their diagonality, allowing interactions between different generations and the W boson.

$$-\mathcal{L}_{\text{EW}}^{\text{mass-basis}} = \frac{e}{\sqrt{2}\sin(\theta_W)}\left[W_\mu^+ u_L^i \gamma^\mu (V)^{ij} d_L^i + W_\mu^- d_L^i \gamma^\mu (V^\dagger)^{ij} u_L^j\right] \tag{1.20}$$

[2] In this thesis two analysis are described, the $H \to \tau\tau$ cross-section measurements and a beyond SM search, $H \to \tau l$. For this reason, in this subsection a simple extension of the SM Yukawa coupling is done. To obtain the SM prediction it is required to impose $i = j$ in the leptonic field indexes.

The residual mixing matrix that appears, $V_{CKM} = V^u V^{d\dagger}$:

$$V_{\text{CKM}} = \begin{pmatrix} 0.97446 & 0.22452 & 0.00365 \\ 0.22438 & 0.97356 & 0.04214 \\ 0.00896 & 0.04133 & 0.99105 \end{pmatrix} \tag{1.21}$$

and it is called the Cabibbo-Kobayashi-Maskawa (CKM) matrix. It can be parametrized using three angles and a complex phase [22, 23].

In the Yukawa Lagrangian, fermion mass terms of the kind $m_f \overline{f}_L f_R$ arise upon the breaking of the electroweak symmetry, where m_f is:

$$(m_f)_{ij} = \frac{v}{\sqrt{2}}(Y_f)_{ij}, \qquad f = u, d, e \text{ and } i, j = 1, 2, 3 \tag{1.22}$$

Bruno Pontecorvo predicted in 1957 [24] that if neutrinos were massive particles, they could experience an oscillation effect, where the particle flavour is alternating between the three possible families. This prediction was later confirmed through experimental observations [4,5], indicating that Lepton Flavour Violation (LFV), forbidden in the SM framework, happens in nature.

The parameters that regulate the oscillations between the different neutrino families are summarized in the Pontecorvo-Maki-Nakagawa-Sakata (PMNS) matrix.

The observation of neutrino oscillations indicates that lepton flavour numbers are not conserved. This fact opens the possibility for physics beyond the SM to participate in flavour changing dynamics [25–31], considering the piece of the lepton Yukawa Lagrangian $((-\mathcal{L}_{\text{Yukawa}})_{\text{lepton}})$ as:

$$(-\mathcal{L}_{\text{Yukawa}})_{\text{lepton}} = \frac{1}{\sqrt{2}}(Y_L)_{ij} h \overline{L}_{Li} L_{Rj} + h.c., \qquad i, j = e, \mu, \tau \tag{1.23}$$

where for the SM, $(Y_L^{SM})_{ij} = \delta_{ij}\sqrt{2}m_i/v$.

In principle off-diagonal terms of the Yukawa coupling can give rise to flavour-changing radiative charged-lepton decays, $\mu \to e\gamma$, $\tau \to \mu\gamma$ and $\tau \to e\gamma$, and also to $3-$body charged lepton decays, such as $\mu \to eee$, $\tau \to \mu\mu\mu$ and $\tau \to eee$, which are forbidden in the SM with massless neutrinos. Those decays can only happen via Higgs-lepton loop and two-loop diagrams of the Barr-Zee type [32].

The experimental bounds for those processes are shown in Table 1.3. In simple extensions of the SM incorporating neutrino mass terms, the mechanism makes the Branching Ratios ($\mathcal{BR}$) of these decays very small due to the small mass of the neutrinos. The prediction for the branching ratios of such decays are of the order of 10^{-56}, too small to be observed by experiments. Thus, LFV in the charged lepton sector could be observed at the LHC only if generated by new physics phenomena.

Process	Coupling	Experimental bounds
$H \to \mu e$	$\sqrt{\lvert Y_{e\mu}\rvert^2 + \lvert Y_{\mu e}\rvert^2}$	$< 5.4 \times 10^{-4}$
$\mu \to e\gamma$	$\sqrt{\lvert Y_{e\mu}\rvert^2 + \lvert Y_{\mu e}\rvert^2}$	$< 2.1 \times 10^{-6}$
$\mu \to eee$	$\sqrt{\lvert Y_{e\mu}\rvert^2 + \lvert Y_{\mu e}\rvert^2}$	$< 3.1 \times 10^{-5}$
$H \to \tau e$	$\sqrt{\lvert Y_{\tau e}\rvert^2 + \lvert Y_{e\tau}\rvert^2}$	$< 2.3 \times 10^{-3}$
$\tau \to e\gamma$	$\sqrt{\lvert Y_{\tau e}\rvert^2 + \lvert Y_{e\tau}\rvert^2}$	< 0.014
$\tau \to eee$	$\sqrt{\lvert Y_{\tau e}\rvert^2 + \lvert Y_{e\tau}\rvert^2}$	< 0.12
$H \to \tau\mu$	$\sqrt{\lvert Y_{\tau\mu}\rvert^2 + \lvert Y_{\mu\tau}\rvert^2}$	$< 1.4 \times 10^{-3}$
$\tau \to \mu\gamma$	$\sqrt{\lvert Y_{\tau\mu}\rvert^2 + \lvert Y_{\mu\tau}\rvert^2}$	< 0.016
$\tau \to \mu\mu\mu$	$\sqrt{\lvert Y_{\tau\mu}\rvert^2 + \lvert Y_{\mu\tau}\rvert^2}$	< 0.25

Table 1.3: Experimental bounds of flavour violating Higgs couplings to leptons assuming that the diagonal Yukawa flavour couplings are as predicted by the SM $(Y_L^{SM})_{ii} = \sqrt{2}m_i/v$ [33–35].

2.- Experimental setup

The analyses presented in this thesis use *pp* interaction data produced by the LHC [36, 37] at CERN [38], Switzerland. This chapter introduces the experimental setup describing the ATLAS detector and its sub-systems, as well as the objects used in the physics analyses.

2.1 CERN Laboratory

CERN [38], acronym for *Conseil Européen pour la Recherche Nucléaire*, is the biggest European complex for Nuclear and High energy physics research. This institution was founded in 1954, to restore a strong European scientific community. The twelve founding countries are: Belgium, Denmark, France, the Federal Republic of Germany, Greece, Italy, the Netherlands, Norway, Sweden, Switzerland, the United Kingdom and Yugoslavia. The laboratory is located in the Franco-Swiss border near Geneva because of its central location in Europe and its international tradition. Up to date, and thanks to its successful track record, ten more European member states have joined CERN, as well as some non-European associate and observer countries around the globe. More than thirteen thousand scientists collaborate in experiments conducted at CERN. In particular around three hundred and seventy senior and young physicists and engineers from Spain, which joined CERN in 1983, are involved.

Since its foundation, CERN has achieved remarkable discoveries. For instance, the first observation of the electronic decay of the pion [39], which proved an important prediction of the weak interaction theory, or the muon capture in hydrogen achieved by the Synchro-Cyclotron during its 33 years of operation [40]; the UA1

and UA2 experiments, at the super Sp$\bar{p}$pS Collider, now upgraded and renamed Super Proton-Synchrotron (SPS), discovered the $W^{\pm}$ and the Z bosons [41] in 1983, confirming the unification of weak and electromagnetic forces predicted by the SM in 1968; and, finally, in 2012 the observation of a new scalar massive particle with the predicted properties of the Higgs boson by the ATLAS and CMS experiments currently operating at the LHC [6, 7].

Some of the CERN discoveries have been rewarded with the Nobel Prize: in 1992 G. Charpak who ideated the drift chamber which revolutionized the particle detection; in 1984 S. Van Der Meer for the technique of stochastic cooling of particle beams and C. Rubbia for the discovery of the carriers of the weak interaction. In 2012 P. Higgs and F. Englert received the Nobel prize for the theorisation of the Brout-Englert-Higgs field. In this last case, CERN was mentioned in the Nobel Prize announcement.

CERN achieves success also outside the world of particles physics. The most remarkable example is the development of the World Wide Web. Info.cern.ch was the address of the world's first website and web server, running on a NeXT computer at CERN.

2.1.1 The Large Hadron Collider

The most powerful particle collider made by humans is the Large Hadron Collider (LHC) [36, 37]. It started operating in 2008, located in the same tunnel previously used by the Large Electron Positron collider (LEP). It is planned to continue operating until, at least, 2034 with different upgrade phases.

The accelerator complex is depicted in Figure 2.1. The beams of protons [1] are accelerated in different steps, increasing each time their energy. Firstly, a linear accelerator, the LINAC2, accelerates protons, coming from a bottle of hydrogen gas, up to 50 MeV. The beam is passed to the Proton Synchrotron Booster which increases their energy to 1.4 GeV. The booster is a necessary intermediate step before the Proton Synchrotron (PS), because the low injection energy of 50 MeV would limit the number of protons the PS could accept. Thanks to the Booster, the PS can accept over 100

[1] The LHC can accelerate also heavy ions like Pb and Xe, but for the purpose of this thesis only protons are considered.

times more protons per injection. The PS and SPS synchrotrons are used to increase the energy up to 25 GeV and 450 GeV respectively.

Finally, the SPS supplies the two-ring-superconducting-hadron accelerator called LHC. Acceleration of hadrons in the LHC is achieved through the use of 16 radio frequency cavities tuned to a frequency and field orientation to accelerate the protons to a nominal energy of up to 7 TeV per beam. Almost nine thousand six hundred magnets are placed to squeeze, bend the trajectory and adjust the beams thought the LHC pipes.

The LHC is situated in the west side of Geneva (Switzerland) and it is placed 100 m underground. The accelerator is a ring of roughly 27 km of circumference which is divided in 8 different parts called octants. Each of them has different functions: accelerating, cleaning, dump and colliding the beams. In each of the four colliding points one detector is placed to collect the information from the collisions happening at a frequency of 40 MHz.

Up to date, the *pp* collisions have occurred at centre-of-mass energies of 0.9, 5.02, 7, 8 and 13 TeV, while the design value is 14 TeV. The LHC's first run, Run 1, (2009-2013), was followed by a scheduled long shutdown (LS1). The second run, Run 2 started in 2015 and it ended in 2018. The LHC is now in the second long shutdown (LS2).

ATLAS (A Toroidal LHC ApparatuS) [42] and CMS (Compact Muon Solenoid) [43] experiments are located in the first and fifth octant, shown in Figure 2.2. They are multi-purpose detectors featuring extensive semi-conductor based tracking systems, large-coverage calorimeters and efficient muon detectors optimized for the discovery and measurement of the Higgs boson and the search for new physics, but also to pursue a considerable program of Standard Model measurements. The third experiment, located in the second octant, is ALICE (A Large Ion Collider Experiment) [44], a detector whose focus is the analysis of the heavy-ion collisions to investigate the physics of dense matter and the QCD interaction in the quark-gluon plasma. And finally, located in the eighth octant, the LHCb (LHC-beauty) experiment [45] studies the physics of the B-mesons and CP-violation.

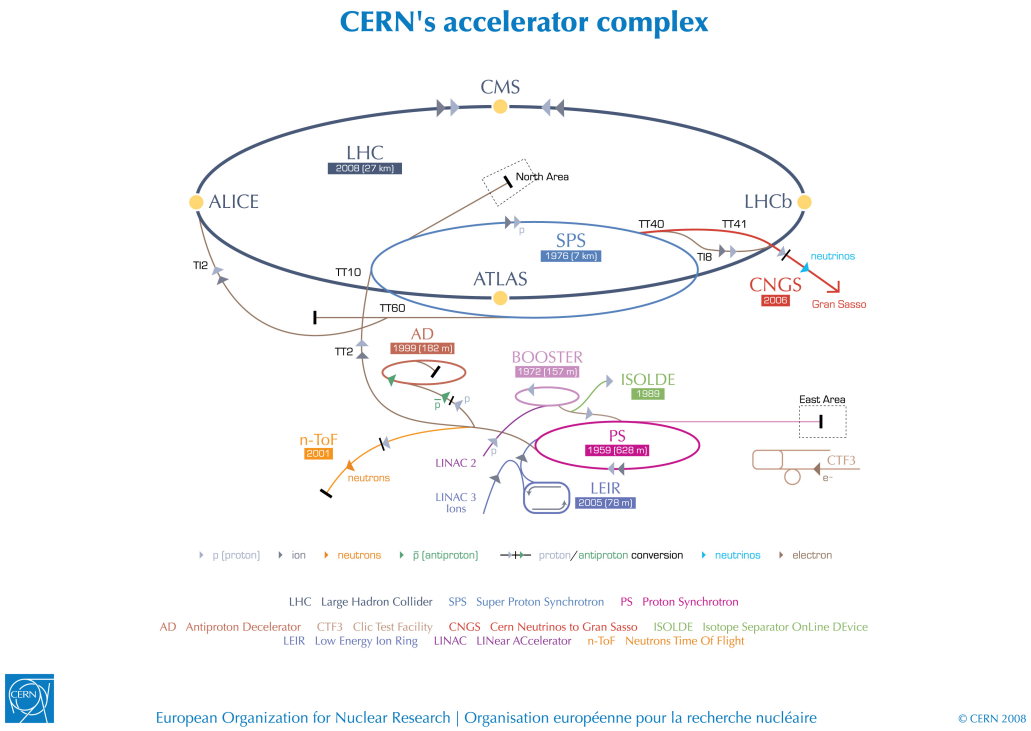

Figure 2.1: CERN accelerator complex.

2.2 The ATLAS detector

ATLAS stands for *A Toroidal LHC ApparatuS* [46]. It is a general-purpose detector designed to cover a wide physics program, including searches for new physics. The detector is located next to the CERN Meyrin site and it was built, and is currently managed, by the ATLAS Collaboration, formed by research groups from 182 different institutions of 38 countries all over the world. ATLAS is the largest LHC detector. It is 44 m long, more than 25 m high and weighting nearly 7000 t, ATLAS has cylindrical symmetry, covering almost a 4π solid angle.

Because several kind of particles can be produced in a pp collision, the ATLAS detector is composed of four layers of sub-detectors, shown in Figure 2.3, each of them designed to help identify and measure the properties of different kind of particles (and their decay products). They are the inner detector, the electromagnetic and hadronic

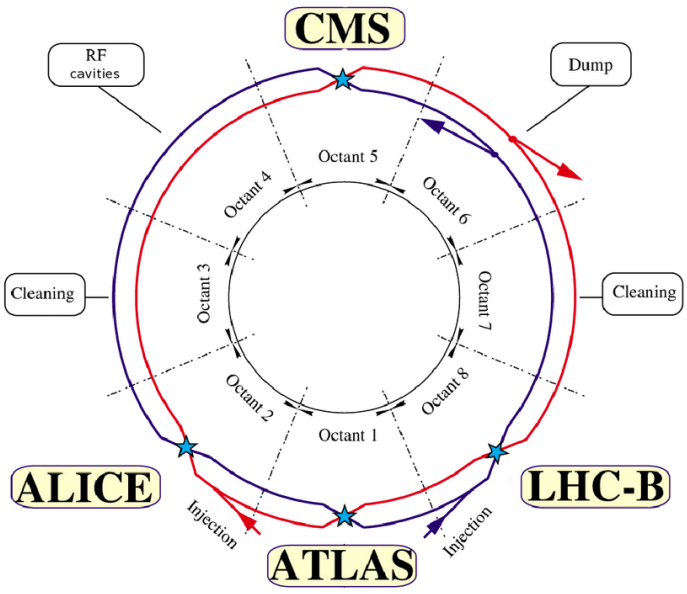

Figure 2.2: LHC layout separated in octants [36].

calorimeters and finally the muon spectrometer. Additionally to the four sub-systems, the ATLAS experiment has a magnet system which bends the trajectories of the charged particles, allowing the determination of their momentum and with a trigger and data acquisition systems that are partitioned into sub-systems, typically associated with sub-detectors, which have the same logical components and building blocks.

A set of Cartesian and cylindrical three-dimensional coordinates, with the origin in the Interaction Point (IP), are used. The *x*-*y* plane, orthogonal to the beam direction is called the transverse plane. The azimuthal angle ϕ is measured around the beam axis, and the polar angle θ, from the beam axis. The rapidity, is defined as:

$$y = \frac{1}{2} \ln \left(\frac{E + p_z}{E - p_z} \right) \tag{2.1}$$

where the E denotes the energy of a particle and p_z the component of its momentum along the beam direction. In the limit where the mass of the particle is negligible,

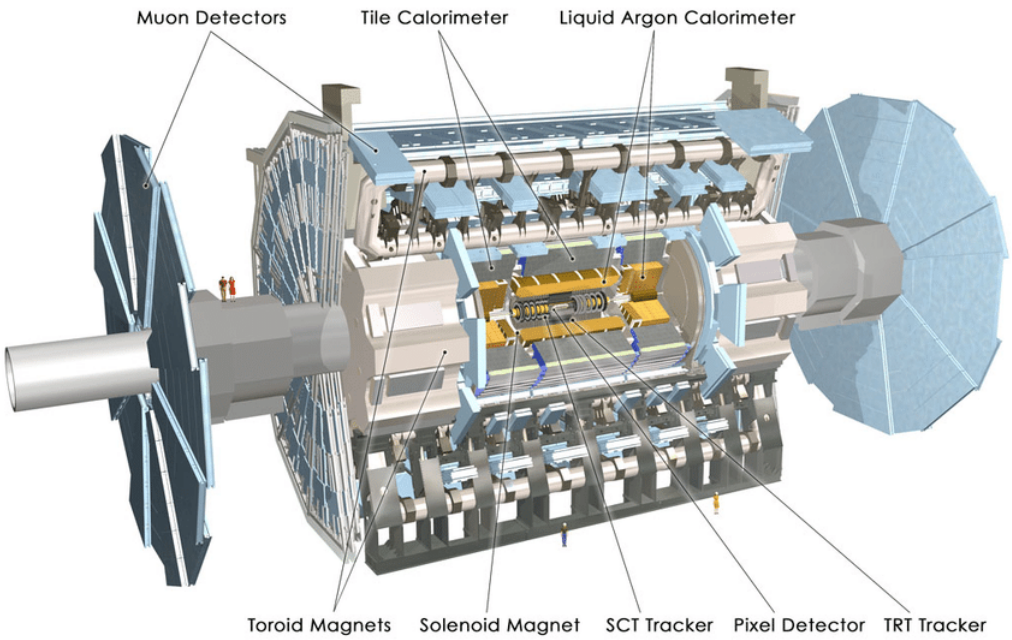

Figure 2.3: Schematic view of the ATLAS detector [36].

$m \ll p \Rightarrow E \approx p$, the rapidity, y, becomes equivalent to the pseudorapidity η:

$$\eta = -\ln \tan\left(\frac{\theta}{2}\right) \tag{2.2}$$

The angular distance between two particles ΔR, is measured in the $\phi - \eta$ plane and is commonly defined as:

$$\Delta R = \sqrt{\Delta\eta^2 + \Delta\phi^2} \tag{2.3}$$

2.2.1 Inner detector

The closest sub-system to the interaction point is the so-called Inner Detector (ID) [47], shown in Figure 2.4. The ID is used as a tracking device and provides a good reconstruction of the trajectory of charged particles. It lends an excellent momentum resolution as well as good measurements of the primary vertices (spacial points where the protons collide around the interaction point) and secondary vertices (spacial points

where particles decay). The inner detector covers a pseudorapidity range of $|\eta| < 2.5$ and it is immersed in a 2 T magnetic field generated by a central solenoid which bends the trajectory of the charged particles coming out of the collisions.

The inner detector is composed of four main sub-systems which decrease in granularity further way from the interaction point. Inside-out they are the Insertable B-layer (IBL) [48], the Pixel Detector, the Semi-Conductor Tracker (SCT) and finally the Transition Radiation Tracker (TRT).

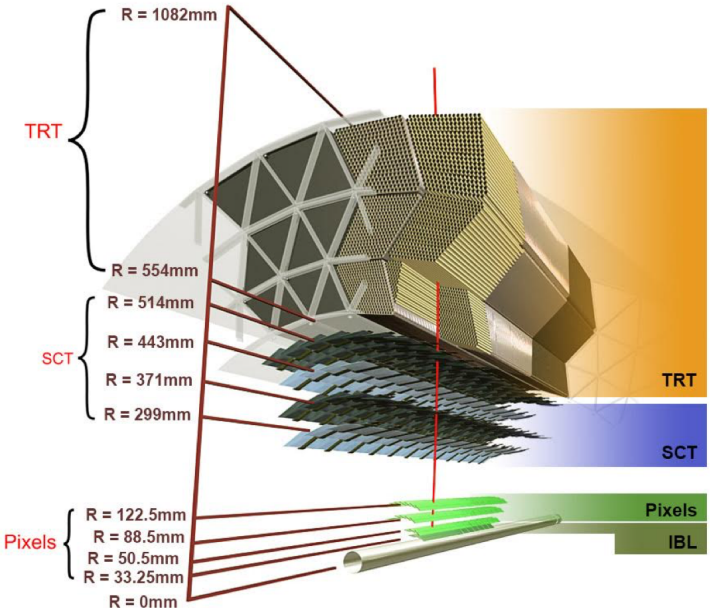

Figure 2.4: 3D visualisation of the structure of the barrel of the ID [49]. In the picture are shown the beam pipe, the IBL, the Pixel layers, the four cylindrical layers of the SCT and the 72 straw layers of the TRT.

The Pixel Detector, with more than 1700 sensors and each of them with 46000 channels, provides a very high-resolution pattern recognition for the particles using discrete space points from the silicon pixel layers. It consists of three concentric cylinders around the beam pipe and two end-caps perpendicular to the z-axis with three disks each. Additionally, in order to improve the ATLAS tracking detector system,

during the LS1, the IBL was installed. This new detector layer is located 33.25 mm away from the beam line and it improves the tracking performance, specially by enhancing the impact parameter resolution, which directly affects b-tagging and vertexing operation. The intrinsic resolution for the IBL and Pixel detectors are 8×40 μm and 10×115 μm, respectively, along the $r\phi$ plane and z-axis. The SCT is composed of 4088 modules in four layers surrounding the Pixel detector and nine disks on each of the end-caps. It was designed to provide eight precision measurements per track in the intermediate radial range, contributing to the measurement of momentum, impact parameter and vertex position with a resolution of 17×580 μm along the $r\phi$ plane and the z-axis. Finally, the TRT is the outermost part of the ID system, composed of around 300.000 straw tubes and filled usually with Xenon gas. Since Run 2, the Xenon gas of several modules has been replaced by Argon because of increasing leaks. The TRT provides electron identification capability and improves the tracking accuracy for $|\eta| < 2$.

The resolution of the inner detector is $\sigma_{p_{\mathrm{T}}}/p_{\mathrm{T}} = 0.05\% p_{\mathrm{T}} \oplus 1\%$ in a pseudorapidity coverage of $|\eta| < 2.5$.

2.2.2 Electromagnetic Calorimeter

The electromagnetic calorimeter of the ATLAS detector is shown in Figure 2.5. It is a lead-liquid argon detector (LAr), whose main purpose is the detection and measurement of the position and energy of electromagnetic interacting particles, such as electrons, positrons and photons. The LAr calorimeter is subdivided in: an electromagnetic barrel (EMB), which covers the region of $|\eta| < 1.5$; an electromagnetic end-cap (EMEC) in each side, covering the region $1.4 < |\eta| < 3.2$; and finally, closest to the beam pipe a forward calorimeter (FCAL) covering the region $3.1 < |\eta| < 4.9$. The active medium is liquid Argon, while the passive material consists of lead arranged in an accordion shape to ensure a complete azimuthal coverage. When an electromagnetic particle passes through the lead absorber, an electromagnetic shower is generated, photons of sufficient energy create e^+e^- pairs and the electrons emit bremsstrahlung photon radiation. The offspring particles interact again and their energy reduces as they penetrate deeper in the calorimeter, producing a shower of electromagnetic particles. The radiation length of the LAr calorimeter is high enough to contain the showers of EM particles produced

by the LHC pp collisions: $24X_0$ for the barrel and $26X_0$ for the end-caps. The EM calorimeter has a design energy resolution of $\sigma/E \approx 10\%/\sqrt{\text{E(GeV)}} \oplus 0.7\%$.

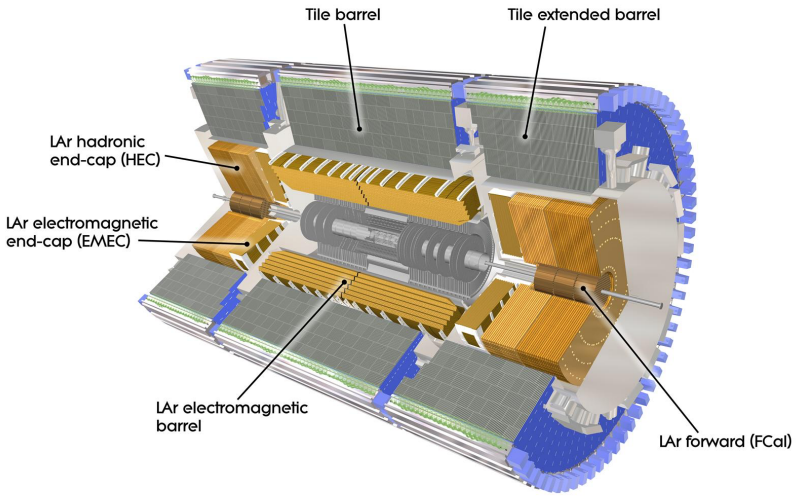

Figure 2.5: 3D visualisation of the Calorimeter system of the ATLAS detector [50]. The ECAL is drawn with orange colour and the HCAL is the surrounding one.

2.2.3 Hadronic Calorimeters

The hadronic calorimeters are the outermost layer of the image of Figure 2.5. The LAr sub-system, despite being an electromagnetic calorimeter, includes also two hadronic end-cap detectors, the Hadronic End-cap Calorimeters (HEC) and the FCAL. The HEC consists of two independent wheels just behind the EMEC which cover the range $1.375 < |\eta| < 3.2$ and uses copper plates as absorbers. The FCAL, already discussed in Section 2.2.2 provides hadronic shower information in addition to electromagnetic coverage.

The Tile Calorimeter (TileCal) is the detector which surrounds the LAr calorimeter in the barrel region. Its main purpose is to measure the energy and the direction of hadronic particles escaping the LAr detector. TileCal is composed of one long barrel (LB), covering the region of $|\eta| < 1$, and two separated extended barrels (EB), covering

the region $0.8 < |\eta| < 1.7$. Furthermore, a gap of 0.6 m between the LB and EB is needed for the services and cabling of the inner and LAr detectors. To maximize the active material in the gap region special scintillators are placed in the region of $1.0 < |\eta| < 1.6$.

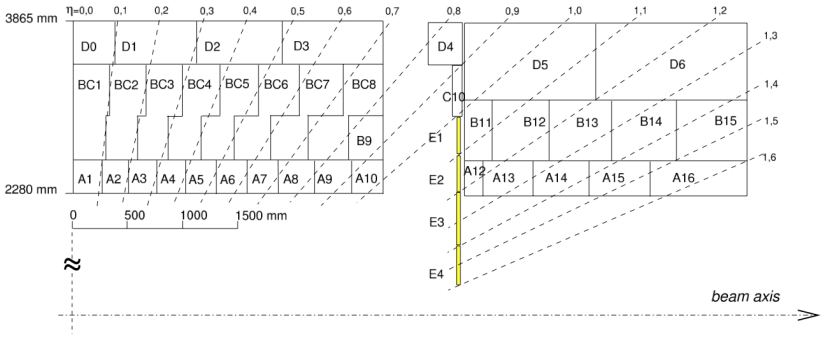

Figure 2.6: Layout of TileCal cells [51] (specular structure for the negative beam axis direction). The A-layer is closest to the beam line, and the A1-cell is the closest to the interaction point.

Figure 2.6 shows the cell structure of TileCal. Each cell is composed of a different amount of iron plates, which are used as a passive medium or absorber, and scintillating tiles used as active medium. Attached to the scintillating tiles, wavelength-shifting fibres carry the light produced in the scintillators to PhotoMultiplier Tubes (PMTs), which convert the light into an electrical signal, see Figure 2.7.

The read-out of the PMTs is commonly referred to as front-end electronics and, among other functions, it converts the analogue signal of the PMTs to a digital signal, using analogue-to-digital converters (ADC) and sends the digital data to the read-out driver (ROD) system with a frequency of up to 100 kHz.

When currents are converted to ADC counts, seven time samples are stored in the pipelines, where each sample corresponds to a 25 ns interval. An internal representation of a PMT pulse is shown in Figure 2.8.

In order to be sensitive to the physics signal of interest, the TileCal energy resolution design value is $\sigma_E/E = 50\%/\sqrt{\mathrm{E(GeV)}} \oplus 3\%$ and the segmentation is $\Delta\eta \times \Delta\phi = 0.1 \times 0.1$ for the central region, $|\eta| < 1.5$. For the forward region, $|\eta| > 1.5$, the HEC

resolution design value is $\sigma_E/E = 100\%/\sqrt{\text{E(GeV)}} \oplus 10\%$ and the segmentation is $\Delta\eta \times \Delta\phi = 0.2 \times 0.2$.

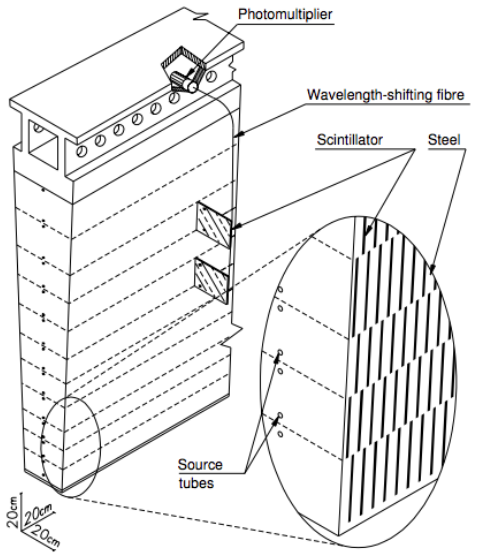

Figure 2.7: Schematic of a Tile Calorimeter module showing the plastic scintillators and the steel absorbers. The front-end electronics drawer is located in the outer radius to read out the PMTs [52].

2.2.4 Muon spectrometer

The outermost ATLAS sub-system is the muon spectrometer (Figure 2.9), used to identify and reconstruct the trajectories of the muons in the pseudorapidity range $|\eta| < 2.7$ and provides projective towers in η and ϕ coordinates. The spectrometer is divided in three different regions: the barrel region for $|\eta| < 1.05$, the transition region for $1.05 < |\eta| < 1.4$ and the end-cap region for $|\eta| > 1.4$. Helped by the magnet system, the muon spectrometer momentum measurement is based on the deflection of the muon trajectories and has a precision of about 2% for 100 GeV and a 8% for 1 TeV muons. The sub-detector consists of Monitored Drift Tubes (MDTs), Resistive Plate Chambers (RPCs), Thin Gap Chambers (TGCs) and Cathode Strip Chambers (CSCs).

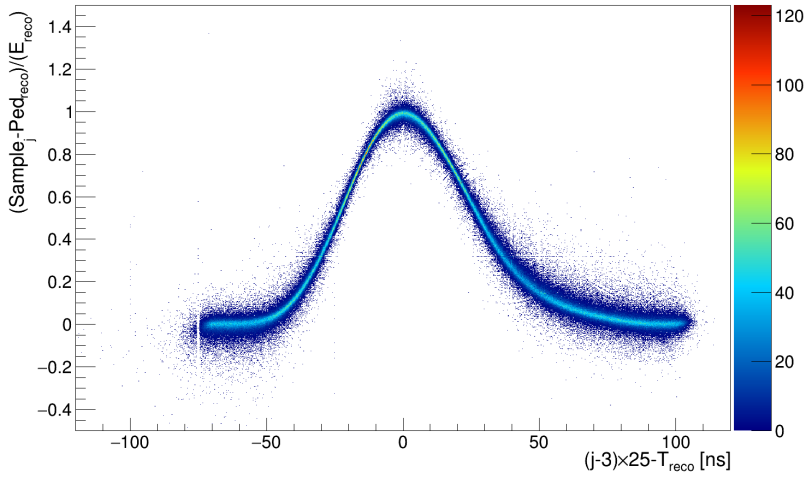

Figure 2.8: Pulse obtained using data for one PMT of the TileCal LB. The measured ADC counts normalized to the pulse amplitude is drawn versus the reconstructed time.

The MDTs are used for precision tracking in the spectrometer bending plane. They are composed of multi-layers of high-pressure drift tubes, made of aluminium, with a central wire of W-Re. The tubes are filled with a mixture of non-flammable Ar-CO_2 at the absolute pressure of 3 bar.

The RPCs and TGCs are used for triggering in barrel and end-cap region, respectively. The RPC is a gaseous $C_2H_2F_4$ parallel plate detector made out of Bakelite. The plates are separated to get a typical space-time resolution of 1 cm $\times$ 1 ns and a uniform electric field produces the avalanche multiplication of ionization electrons. The TGCs are built with wires, separated by 2 mm gap between two graphite cathodes, allowing a fast signal, a typical rise time of 10 ns and a low sensitivity to mechanical deformations.

The CSCs are used for precision measurements in the high-rate end-cap inner layer. They consist of multi-wire proportional chambers operated with a mixture of Ar-CO_2-CF_4 gas. The cathode is segmented into strips orthogonal to the anode wires, achieving a space resolution better than 60 μm .

The design resolution for the muon spectrometer is $\sigma_{p_T}/p_T = 10\%$ at $p_T = 1$ TeV within the pseudorapidity coverage of $|\eta| < 2.7$.

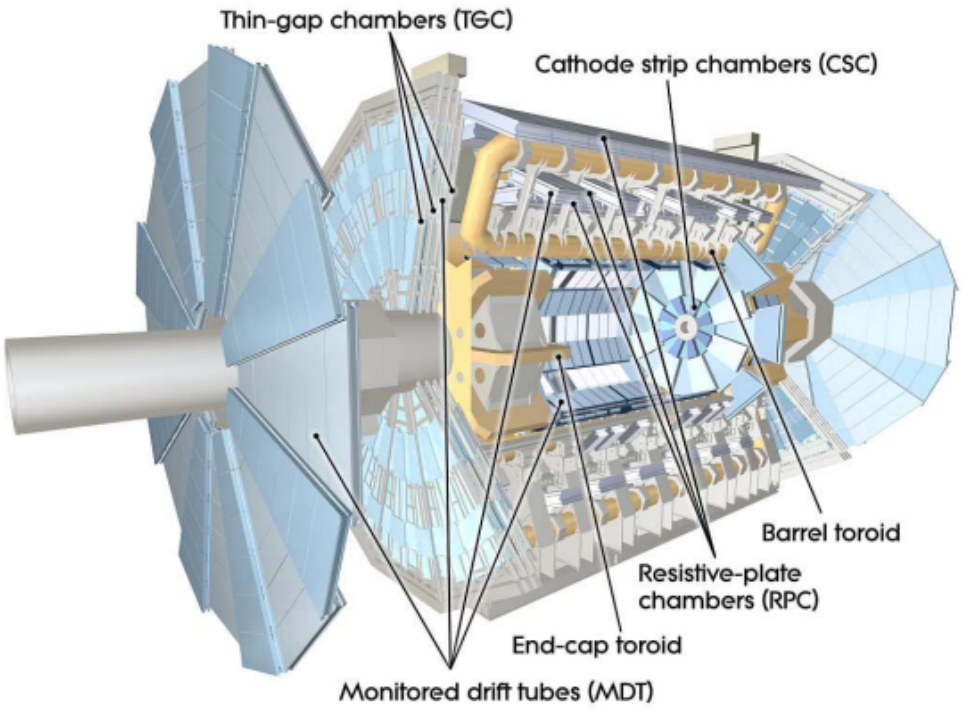

Figure 2.9: A 3D visualization of the muon spectrometer (blue plates) and of the toroidal magnetic system (in yellow) [53].

2.2.5 Magnet system

Due to the challenge of achieving a good momentum resolution for high energy charged particles an unusual configuration of large size superconducting magnet was adopted by ATLAS. The magnet system, shown in Figure 2.9, is 26 m long and approximately 20 m in diameter. It is composed of one central superconducting solenoid, which provides a central field of 2 T around the ID. ATLAS is surrounded also by two end-cap toroids and eight barrel toroids made of Nb-Ti superconductor, providing up to 4.1 T and 3.9 T respectively. Just the magnet system weights nearly 1300 tons and is cooled by liquid He at 4.5 K.

2.2.6 Forward Detectors

To determine the luminosity delivered to ATLAS two smaller detector systems are placed at ± 17 m and ± 240 m respectively. The detectors have to be placed far away from the interaction point and as close as possible to the beam, to capture the particles which scatter at very small angles. The LUminosity measurement using Cherenkov Integrating Detector (LUCID) is the only detector primarily dedicated to online luminosity monitoring. LUCID is a relative luminosity detector. Its main purpose is to detect inelastic pp scattering in the forward direction, in order to both measure the integrated luminosity and to provide online monitoring of the instantaneous luminosity and beam conditions. The furthest luminosity detector is ALFA (Absolute Luminosity For ATLAS) used to know the absolute luminosity via elastic scattering at small angles. ALFA uses the Roman pot (proton-on-target) technique to measure the total cross-section of two particle beams.

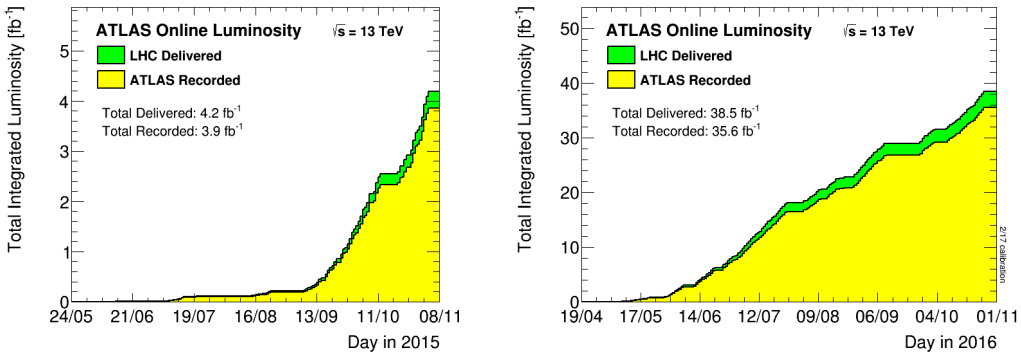

(a) Luminosity for 2015

(b) Luminosity for 2016

Figure 2.10: The total luminosity delivered (green) and recorded (yellow) for the data taking between 2015 and 2016.

2.2.7 The ATLAS Trigger and Data Acquisition System

Forty millions of bunch crossings happen each second in the IPs of the LHC experiments. Due to the high rate and with an instantaneous luminosity of 10^{34} cm^{-2}s^{-1}, the average number of pp interactions is about 35 per bunch crossing

resulting in around 1400 millions of interactions per second. Owing to the limited computing resources for offline storage and data processing, not all the events delivered can be saved. Different selective triggers are required and therefore are in charge of choosing whether an event associated to a bunch-crossing is kept for a later study or not.

One important goal of the trigger system is that it should be able to analyse the data events at the rate of the pp bunch crossings, which is 40 MHz, to avoid an excessive dead time of the detector. During Run 2 ATLAS had two different levels of trigger to achieve these requirements, Figure 2.11. The first level is known as Level-1 (L1), a hardware system placed as close as possible to the detector cavern, to minimize both the length of cables and the time needed for sending the trigger accept signals to the on-detector readout electronics. The L1 trigger analyses the data combining analogue sums of calorimeter signals and signals from dedicated muon trigger chambers (RPC and TGC). During Run 2, the L1 trigger has operated with a maximum acceptance rate of 100 kHz.

If a bunch-crossing event is accepted by the L1 trigger, the data is further scrutinized by a second level of trigger, known as High Level Trigger and uses a fraction of the full precision detector data to reduce the rate further. It is based on conventional CPUs, exploiting custom software to meet the constraints of execution time with multithread processes. At the end of these selection processes around 1.5 GB/s are stored permanently at CERN for offline data analysis.

2.3 Object reconstruction

Signals originating from the sub-detectors are combined and transformed into so-called reconstructed objects. For the precision measurements involving the Higgs boson decaying into a pair of taus, reconstruction of tau decays is specially important. The following subsections will give a brief description of how the physics objects are reconstructed and identified.

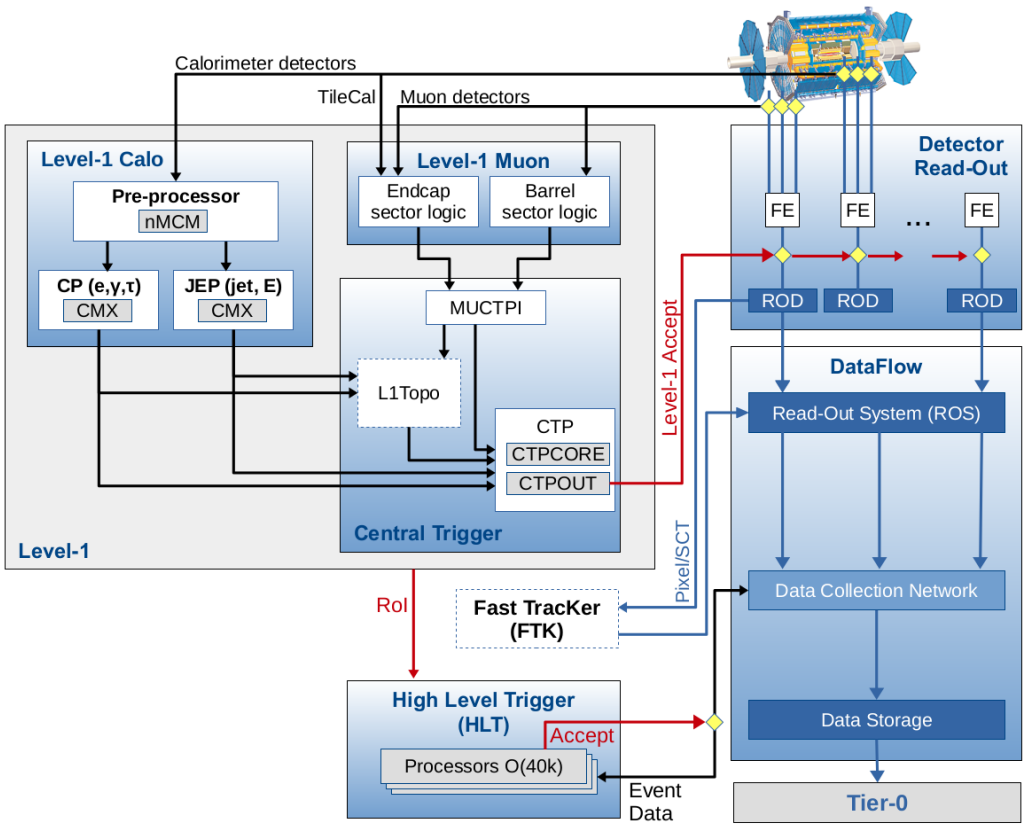

Figure 2.11: Schematic of the trigger systems and data acquisition system of ATLAS.

2.3.1 Tracking and vertexing

The word tracking is the name used by ATLAS for the reconstruction of the trajectories of charged particles. The reconstruction method [54] starts with the conversion of the raw data from the Pixel and SCT into three-dimensional measurements, known as space-points [55]. In principle a single signal or a collection of neighbour signals (clusters) can create a space-point. It can happen that two clusters are close enough to overlap and form a merged cluster. To resolve this ambiguity a neural network (NN) is used. Once all possible space-points are created, track reconstruction begins by combining different space-points from the ID sub-systems. These combinations are known as seeds. Additionally, to maximize the purity and the quality of the

seeds, selection criteria are applied. Once all tracks of good quality have been formed, an ambiguity solver processor is used, where each track is scored using a reward-penalty scheme based on a NN. Moreover, the algorithm gives preferences to longer reconstructed tracks over short segments. Different parts of sub-detectors are weighted according to their space-time resolution. Holes represent a space-point signals which are expected by the algorithm but not observed. The presence of holes and a too big or too small value of the χ^2 reduces considerably the overall track score value. After a track is reconstructed with the pixel and the SCT sub-detectors, the candidates are extended into the TRT volume and combined properly.

Once tracks are formed, the Primary Vertexes (PVs) are reconstructed [56,57] in order to obtain the spatial position of the pp hard-scatter interaction. The PV reconstruction has two stages: the vertex finding and the vertex fitting.

The vertex finding algorithm consists of an association of reconstructed tracks to vertex candidates. After that, the vertex position candidate is estimated via an iterative fit in which the less compatible tracks are down-weighted during each iteration. The tracks incompatible by more than 7σ are used to seed a new vertex, iterating until no tracks are left.

It can occur that unstable particles decay outside the beam interaction region. In that case the corresponding vertex is labelled as secondary vertex.

2.3.2 Electrons

Electron objects are reconstructed by combining the EM calorimeter information with the ID sub-system tracking reconstruction. Electrons can be reconstructed in the central region of the detector within a range of $|\eta| < 2.47$. The reconstruction follows a 4-steps procedure [58–60]. A longitudinal tower is defined using the $\eta \times \phi$ segmentation of the EM calorimeter which is divided into a grid of $N_\eta \times N_\phi = 200 \times 256$ elements of size $\Delta\eta^{tower} \times \Delta\phi^{tower} = 0.025 \times 0.025$. Inside each of these elements, the energy of cells in all longitudinal layers is summed and a seed cluster will be considered when the total cluster energy is above 2.5 GeV. Furthermore, to recover losses from bremsstrahlung, an electron-specific pattern recognition and track fit are used.

Two different sets of electron candidates are reconstructed: prompt electrons originating from the PV such as decay products of the W and Z bosons; and the non-prompt electrons such as the ones produced in the weak decay of b- and c-quarks, whose life time is relatively long and therefore the electron track is displaced from the primary vertex. To determine if an electron is prompt or not, a multivariate technique is used for Run 2 [61]. In this thesis, the electrons from tau decays are considered prompt leptons.

A multivariate analysis (MVA) technique is used to identify the electrons according to three quality identification (ID) categories, with increasing background rejection power: Loose, Medium and Tight [62]. The categories are inclusive for higher tightness, therefore Medium electron candidates are a subset of the Loose category and the Tight electron candidates are a subset of the Medium category.

Isolation criteria [60] are used to evaluate the activity around the electron candidates. This criteria are based on two isolation variables. The first one is the sum of the transverse energies of topological clusters (topo-clusters)[2] [63] within a cone of $\Delta R = 0.2$ around the electron candidate, briefly named as calorimetric isolation energy (E_{T}^{cone20}). The second variable is the sum of the transverse momentum of all tracks in the same cone ($p_{\mathrm{T}}^{varcone20}$), that have passed the quality criteria of a minimum p_{T} of 1 GeV and originating from the reconstructed primary vertex. The selection criteria for the isolated variables are chosen to have an efficiency of 90% (99%) for electrons of the $Z \to ee$ decays with $p_{\mathrm{T}} > 25(60)$ GeV. If all the requirements mentioned are satisfied, the electron is accepted by the Gradient isolation criterion and used as a working point.

In this analysis, electron candidates are required to pass at least the Loose criterion and have a $p_{\mathrm{T}} > 15$ GeV within a range of $|\eta| < 2.47$ region, however in the signal region of the analysis stricter criteria are used to reduce the rate of misidentified objects.

2.3.3 Muons

Different techniques are used to reconstruct the offline muon candidates [64–66]. A muon candidate is reconstructed by combining independent reconstructed track

[2]The collection of the calorimeter signals into clusters of topologically connected cell signals (topo-clusters) is an attempt to extract the significant signal from a background of electronic noise and other sources of fluctuations such as pile-up and allows the resolution of energy-flow structures.

segments in the inner detector and in the muon spectrometer. The reconstruction in the MS is done by fitting hits in the different segments of different layers. Depending on the sub-detectors used, different types of muons can be defined:

- Combined (CB) muons: muon candidates are obtained with a global fit of the hits from tracks reconstructed in the inner detector and in the muon spectrometer.
- Segment-tagged (ST) muons: some muons cross only one MS layer, or because of their low p_{T} or because regions with low MS acceptance. The combined track is formed by extrapolating the ID track up to the muon spectrometer and requiring only one local track segment in the MS.
- Calorimeter-tagged (CM) muons: as its name suggests, the ID track and the information from the calorimeters are used. This kind of reconstruction recovers acceptance in the region ($\eta < 0.1$) where the ATLAS muon spectrometer is only partially instrumented.
- Stand-Alone (SA) or extrapolated (ME) muons: the last option is used when a muon track is reconstructed only in the MS and therefore the track is extrapolated back to the closest point of the beam line, taking into account the estimated energy loss of the muon in the ATLAS calorimeters.

Different levels of muon identification can be defined: Loose, Medium, Tight and a category named as high-p_{T}. The first three categories are inclusive from lower to higher tightness, whereas the high-p_{T} is an independent category where muons passing the Medium selection and having at least three hits in three MS stations are selected.

Isolation criteria are applied in order to suppress contributions from muons produced by heavy-hadron decays. For muons, the following isolation variables are defined: a track-based isolation variable ($p_{\mathrm{T}}^{varcone30}$) which is the scalar sum of the transverse momentum of the tracks with $p_{\mathrm{T}} > 1$ GeV in a cone size of $\Delta R < 0.3$ around the muon track itself and the calorimeter-based isolation variable ($E_{\mathrm{T}}^{topocone20}$) which is defined as the sum of the transverse energy of topological clusters in a cone of $\Delta R = 0.2$, once the energy is corrected for the average energy loss of the muon, it is subtracted. For Run 2, the criteria are chosen to achieve a working point of 95% of efficiency for $p_{\mathrm{T}} = 25$ GeV and 99% for $p_{\mathrm{T}} = 60$ GeV, called Gradient isolation [66].

In the analysis, the technique used to reconstruct the offline muons is the combined muon. In addition, muons must pass the Gradient isolation working point as well as a Medium identification requirement and have $|\eta| < 2.47$ and $p_{\mathrm{T}} > 10$ GeV.

2.3.4 Jets

Due to the colour confinement in quantum chromodynamics, the colour charged particles can not be isolated because they only exist confined in colour neutral states. At the LHC when two protons collide quarks and gluons can be produced, however the strong force binds them to form hadronic particles to conserve the colour neutralness of the final objects. This process is known as hadronisation, and the shower of hadronic particles is called a *jet*.

As for electron reconstruction, the topo-clusters are the entities used to reconstruct jets. The mathematical algorithm for the reconstruction is the anti-k_t algorithm [67] with a distance parameter of 0.4, which determines the size of the jets.

The anti-k_t identifies all the distances between the soft entities and hard entities (pseudojets) (d_{ij}) and distances between an entity and the beam direction B (d_{iB}).

$$\begin{aligned} d_{ij} &= \min(k_{ti}^{-2}, k_{tj}^{-2}) \frac{\Delta_{ij}^2}{R^2} \\ d_{iB} &= k_{tj}^{-2} \end{aligned} \tag{2.4}$$

where $\Delta_{ij}^2 = (y_i - y_j)^2 + (\phi_i - \phi_j)^2$ and k_{ti}, y_i and ϕ_i are respectively the transverse momentum, rapidity and azimuthal angle of the particle i. The radius parameter, R, is the radius of a cone which determines the size of the jets.

The clustering algorithm proceeds identifying the smallest distance with the following criteria: if it is a d_{ij}, the i and j are recombined and if it is a d_{iB} the entity i is called a *jet*, removing it from the list of entities. The distances are then recalculated and the procedure is repeated until no more entities are left.

The clusters used by the anti-k_t algorithm are three dimensional, massless objects with an energy significantly above the noise threshold. Jets are later calibrated to

truth-particle level following three different steps. Firstly, a pile-up[3] correction is applied to remove the energy contributions originated by other pp collisions, reducing significantly the fluctuation from event to event. Additionally to the pile-up correction, the jet energy scale (JES) calibration is applied. The JES calibration is a multiplicative method derived from the MC simulation, and the goal is to restore the jet response to that of truth particle jets, as evaluated in di-jet events. Finally the residual correction is applied to jets in data. It is a correction based on the MC to data ratio in jet energy response, which improves the agreement of the energy response between MC and data, reducing the jet systematic uncertainty.

Nevertheless, as the jets can originate in any of the pp collisions of the bunch crossing, a Jet Vertex Tagger (JVT) algorithm is used. It is a 2D-likelihood discriminant algorithm that reduces the contamination from jets produced in concurrent pp collisions. This method uses as input the Jet Vertex Fraction (JVF) [68] defined as the ratio between the sum of the transverse momentum of the tracks in the jet cone associated to the PV and the sum of the transverse momentum of the tracks associated to any vertex in the event. The condition of the JVT algorithm for the selection of jets was $|\text{JVT}| > 0.64$, applied only to jets with $p_{\text{T}} < 50$ GeV and $|\eta| < 2.4$.

***b*-tagged jets**: One special case of the jet reconstruction is the heavy flavour tagging. ATLAS uses a specific tagging procedure to identify jets containing b-hadrons (b-jets). B-hadrons have a relatively long lifetime and thus they can travel several millimetres away from the PV before decaying.

The identification of b-jets uses different characteristics of the b-hadron decays. Basically it exploits the high mass of the particle and its relative long lifetime, thus the jet often originates from a secondary vertex, and finally the hadrons from the b meson decay retain approximately 70% of the original b-mesons momentum. However c-hadrons also produce a similar signature, except that they have a shorter lifetime and lower mass. Therefore, the algorithm is also prepared to discriminate between the two topologies.

[3] Pile-up: Effect related to the concurrent *pp* interactions happening close in time or position to the collision of interest that triggered the event. Particles from these *pp* interactions contribute to the measured energy, that increases with the number of interactions per bunch crossing.

The b-tagging algorithm used in this thesis is called MV2c20 [69,70] which uses the output of a BDT trained with b-jets as signal and a mixture of 80% light-flavour jets and 20% c-jets as background. The inputs of this BDT are intermediate multivariate algorithms trained for each of the basic features of the b-jets. This approach not only improves the performance but also significantly simplifies the complexity of the algorithm. A 70% operating point efficiency for b-jets is used in this thesis. The b-jet tagging efficiency is measured from the $t\bar{t}$ sample in which the light- and c-jet contribution are reduced by requiring the W boson to decay leptonically. The misidentification rates for c-jets, τ-jets and jets initiated by light quarks or gluons for the same working point and in the same sample of simulated $t\bar{t}$ events are approximately 10%, 4% and 0.2% respectively.

2.3.5 Tau lepton

With a mass $m_\tau = 1.777$ GeV, the τ is the only lepton heavy enough to decay into leptons and hadrons (Table 2.1), therefore two types of τ-lepton decays can be defined: τ_{lep} and τ_{had} respectively. In the case of the τ_{lep} decay, the τ object is not reconstructed as such: the analyses employ directly the final state objects, the light leptons (muons or electrons) and the missing transverse energy $E_{\text{T}}^{\text{miss}}$ (section 2.3.6). However, ATLAS employs a dedicated method to reconstruct the visible part of the τ decays into hadrons, $\tau_{\text{had-vis}}$[4].

The reconstruction method begins with the reconstructed jets seeded by the anti-k_t algorithm with a distance of $R = 0.2$. Only jets with $p_{\text{T}} > 10$ GeV and $|\eta| < 2.5$ are considered. The tau energy is determined using the collected energy in the calorimeters within a cone of $R = 0.2$. The energy measurement is later refined using a multivariate analysis that combines particle flow and calorimeter measurement for the final calibration. Additionally, the tracks inside the jet are used to associate the $\tau_{\text{had-vis}}$ to a PV and to determine the $\tau_{\text{had-vis}}$ directions axis.

The charge of the $\tau_{\text{had-vis}}$ is determined by the sum of the charge of the innermost tracks within the cone of the jet seed. The $\tau_{\text{had-vis}}$ candidates are passed to a multivariate algorithm to discriminate them from parton-initiated jets. The MVA exploits two different

[4] Hadronic decay of the τ is denoted τ_{had}, while $\tau_{\text{had-vis}}$ is the object associated to the reconstruction of its visible part.

Boosted Decision Trees that are trained separately for $\tau_{\text{had-vis}}$ with one (1-prong) or more than one track (multi-prong), where $Z \rightarrow \tau\tau$ simulated events are used as signal and di-jet events from data as background. The boosted decision tree employs variables related with the topology and the energy of the topo-clusters as well as the reconstruction of the π^0 within the $\tau_{\text{had-vis}}$ cone. Three working points are provided for taus: Loose, Medium and Tight with efficiencies designed to be independent from p_{T}. The target efficiencies are 85%, 75% and 60% (75%, 60% and 45%) for 1-(multi-)prong.

In this thesis only $\tau_{\text{had-vis}}$ with 1 or 3 associated tracks and charge of ± 1 are used.

Decay mode	$\mathcal{BR}[\%]$
$\tau \rightarrow e\overline{\nu_e}\nu_\tau$	17.8
$\tau \rightarrow \mu\overline{\nu_\mu}\nu_\tau$	17.4
$\tau \rightarrow h\nu_\tau$	11.5
$\tau \rightarrow h\pi^0\nu_\tau$	26.0
$\tau \rightarrow h\pi^0\pi^0\nu_\tau$	9.5
$\tau \rightarrow hh^+h^-\nu_\tau$	9.8
$\tau \rightarrow hh^+h^-\pi^0\nu_\tau$	4.8
Others	3.2
All had. modes	64.8

Table 2.1: Branching fractions of the main τ decay modes. Charge conservation is assumed.

2.3.6 Missing transverse momentum

Neutrinos are not detected directly by the ATLAS detector, because they are particles interacting weakly with the matter, and thus they escape undetected. The sum of the vector transverse momenta of all products in a collision should be close to zero due to the conservation of the momentum in the transverse plane perpendicular to the beam axis. The missing transverse momentum, $\overrightarrow{p}_{\text{T}}^{\text{miss}}$, is computed as minus the sum of momenta of the reconstructed particles. Its magnitude is called missing transverse energy ($E_{\text{T}}^{\text{miss}}$). Therefore, the $E_{\text{T}}^{\text{miss}}$ can indicate the presence of undetected particles in the final state. Large values of the $E_{\text{T}}^{\text{miss}}$ indicate possible signatures of new physics beyond the SM.

A good measurement of the missing transverse energy has direct consequences in SM measurements and new physics searches. It is an important ingredient in the analyses of this thesis.

The mathematical definition of the $E_{\mathrm{T}}^{\mathrm{miss}}$ is shown in Equation 2.5 [71–74].

$$\begin{aligned} \overrightarrow{p}_{\mathrm{T}}^{\mathrm{miss}} &= -\sum \overrightarrow{p}_{\mathrm{T}}^{e} - \sum \overrightarrow{p}_{\mathrm{T}}^{\gamma} - \sum \overrightarrow{p}_{\mathrm{T}}^{\mu} - \sum \overrightarrow{p}_{\mathrm{T}}^{\tau_{\text{had-vis}}} - \sum \overrightarrow{p}_{\mathrm{T}}^{\mathrm{jet}} - \sum \overrightarrow{p}_{\mathrm{T}}^{\mathrm{soft}} \\ E_{\mathrm{T}}^{\mathrm{miss}} &= \left| \overrightarrow{p}_{\mathrm{T}}^{\mathrm{miss}} \right| \end{aligned} \tag{2.5}$$

where $\overrightarrow{p}_{\mathrm{T}}^{\mathrm{soft}}$ is the sum of the transverse momentum of the inner-detector tracks not associated with any reconstructed hard scattered object [71, 74]. The soft term is reconstructed with the TST method [74] that is relatively insensitive to pile-up effects.

A variant of the $E_{\mathrm{T}}^{\mathrm{miss}}$, called $E_{\mathrm{T}}^{\mathrm{miss,HPTO}}$, is also used in the analysis. This variant is built using only the high p_{T} objects (HPTO) used in the analysis (electrons, muons, $\tau_{\text{had-vis}}$ and jets). $E_{\mathrm{T}}^{\mathrm{miss}}$ and $E_{\mathrm{T}}^{\mathrm{miss,HPTO}}$ are highly correlated for events with undetected particles, while they are less correlated for events with poorly reconstructed objects. Therefore, they can be used to discriminate topologies where the event is not produced by undetected particles.

3.- Data, background and signal samples

The main objectives of this thesis are to understand the Yukawa coupling of the Higgs boson and search for the appearance of physics beyond the SM in the coupling of the Higgs boson to leptons. The Yukawa coupling of the Higgs boson is a new kind of interaction and its understanding is a priority of the particle physics community. This thesis studies the Yukawa interaction of the Higgs boson through the measurement of the following elements of the Yukawa matrix: $Y_{\tau\tau}$, $Y_{\mu\tau}$, $Y_{\mu e}$ among others. The two analyses presented in this thesis have been performed using the data collected by the ATLAS experiment during 2015-2016. This section describes the samples used by the analyses.

3.1 Data samples

The 2015-2016 dataset taken during operations with 25 ns bunch spacing at the LHC is used. It corresponds to a total integrated luminosity of 36.1 fb^{-1} at a centre-of-mass energy of $\sqrt{s} = 13$ TeV. Only events that pass high data-quality standards are analysed in order to reject events recorded during periods with sub-detector failures or defects, such as the periods when IBL was not fully operational or when the detector had a large dead-time or trigger issues.

3.2 Signal samples

At the LHC, neutral Higgs bosons can be produced by different production modes. The computation of production cross-sections have been obtained for the leading production modes.

The dominant Higgs production mechanism at the LHC for $\sqrt{s} = 13$ TeV is the gluon-gluon fusion (ggF), being responsible of approximately 87% of the Higgs bosons produced. This production mode corresponds to the interaction of two gluons mediated by a triangular loop of quarks, shown in Figure 3.1. Since the coupling of the Higgs boson with the fermions is proportional to the mass (Yukawa coupling), the top-quark loop dominates the process.

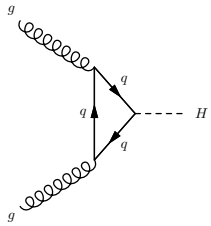

Figure 3.1: Feynman diagram for the gluon fusion process (ggF) at lowest order, showing the production of a Higgs boson via a quark loop.

The second most abundant Higgs boson production mode at the LHC is the Vector Boson Fusion (VBF), shown in Figure 3.2, where the $W^{\pm}$ or the Z bosons fuse to produce a Higgs boson, representing the 6.8% of the total Higgs boson production rate. This process is important because of the outgoing quarks which hadronise forming two energetic jets with large η separation. It is a clear signature of the process serving for background suppression.

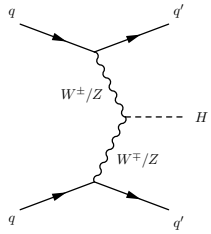

Figure 3.2: Feynman diagram at leading order for the Vector Boson Fusion production process of a Higgs boson with two jets.

Another process with about 4.0% of the total Higgs boson production is the Vector Boson associated production (*VH*), also called Higgs-strahlung. This production is initiated by the collision of a quark-antiquark pair, creating an energetic off-shell vector boson ($W^{\pm}$ or Z) that irradiated a Higgs boson. The processes are shown in Figure 3.3.

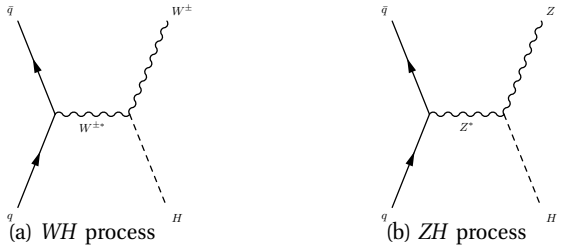

(a) *WH* process (b) *ZH* process

Figure 3.3: Feynman diagrams for the Vector Boson associated production process of the Higgs boson (*VH*) at leading order for (a) the W boson and (b) the Z boson.

Additional Higgs production modes are the associated production with heavy fermions, namely ttH for t-quarks and bbH for b-quarks. These processes account for around 2.2% of the whole Higgs boson production.

The predicted cross-section of the Higgs boson for different production modes as a function of center-of-mass as well as the predicted branching ratios of the Higgs boson are shown Figure 3.4. The predicted values of the cross-section for the most relevant modes of this thesis are summarized in Table 3.1.

Mode	Cross-section [pb]
	13 TeV
ggH	43.920
VBF	3.7480
WH	1.3800
ZH	0.8696
ttH	0.5085
Total	50.935

Table 3.1: Theoretical predictions of the cross-sections for the main production modes of a Higgs boson with a mass of 125 GeV at $\sqrt{s} = 13$ TeV.

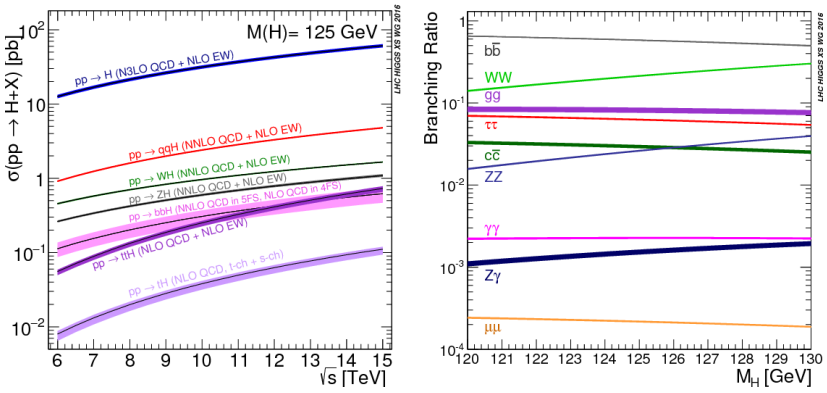

Figure 3.4: Cross-sections (left) for different Higgs boson production processes as a function of center-of-mass energies in the LHC range (6-15 TeV) and the branching ratio of the different Higgs boson decays as a function of the Higgs boson mass. Reproduced from Ref. [75] under CC-BY-4.0 licence.

A combined analysis of the ATLAS and CMS data with a center-of-mass energy of $\sqrt{s} = 7$ and 8 TeV, was performed for the five main Higgs boson production processes and the main decay modes [75]

Figure 3.5 illustrates the signal strengths μ[1] with their total uncertainties as well as the combination of all production modes.

Higgs boson decays ($H \to \gamma\gamma$, $H \to ZZ$,$H \to WW$, $H \to \tau\tau$, and $H \to bb$) are also studied with five independent signal strengths. Figure 3.6 present the best fit signal strength results for the combination of ATLAS and CMS, and separately for each experiment.

The Higgs boson production processes can be associated with Higgs boson couplings to either fermions or vector bosons. Potential deviations of these couplings from the SM predictions can be tested by using a bidimensional parametrisation of the fermion-mediated production processes and the vector-boson-mediated production processes. The combination of the ATLAS and CMS measurements are shown in Figure 3.7 within the 68% confidence limit region for the ten-parameter fit of the five decay channels at a center-of-mass energy of $\sqrt{s} = 7$ and 8 TeV. As shown in Figure 3.7

[1]The signal strength μ represents the signal normalization respect to the SM prediction (see Formula 4.13).

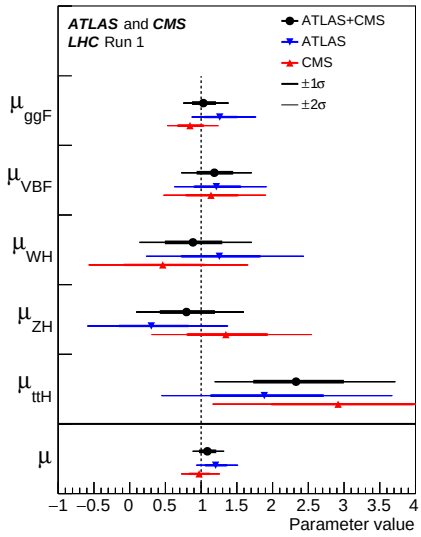

Figure 3.5: Best fit results for the production signal strengths for the combination of ATLAS and CMS data of the Run 1 of the LHC. Also shown are the results from each experiment. The error bars indicate the 1σ (thick lines) and 2σ (thin lines) intervals. The measurements of the global signal strength μ are also shown. Reproduced from Ref. [76] under CC-BY-4.0 licence.

the most sensitive channels to obtain the signal strength of the vector-boson-mediated production processes are the $H \to \tau\tau$ and $H \to WW$ being able to measure with accuracy the σ^{VBF} whereas the $H \to \gamma\gamma$ process is the most sensitive decay mode for the fermion-mediated production processes.

The relation between the fitted couplings and the SM predictions as a function of particle mass is presented in Figure 3.8. In the picture it is assume that there are no new particles entering in the loops of the Higgs boson productions and their decays.

Monte Carlo (MC) samples used by the analyses are produced with the ATLAS simulation infrastructure [78] as part of the ATLAS production campaign. Pythia 8.212 [79] is used to model the τ-lepton decays. Table 3.2 shows the MC samples of the Higgs boson production modes used in the analyses. For the $H \to \tau\tau$ analysis, bbH and other additional production modes of lower cross-section are not considered

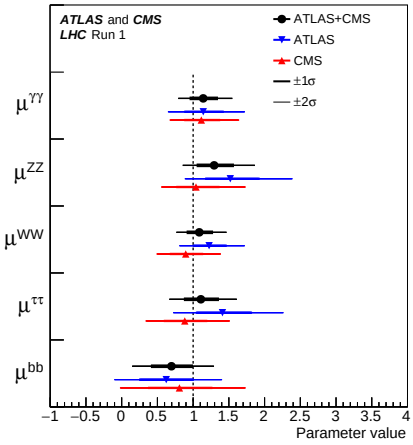

Figure 3.6: Best fit results for the decay signal strengths for the combination of ATLAS and CMS data of the Run 1 of the LHC. Also shown are the results from each experiment. The error bars indicate the 1σ (thick lines) and 2σ (thin lines) intervals. Reproduced from Ref. [76] under CC-BY-4.0 licence.

due to their negligible contribution. For the LFV search negligible contributions from ttH and bbH production modes to the signal are not considered.

Process	MC generator	PDF	UEPS	Order
ggH	Powheg-Box v2 [80–84]	PDF4LHC15 [85] NNLO	Pythia 8.212 [79]	N^{3}LO QCD+NLO EW [86–89]
VBF	Powheg-Box v2	PDF4LHC15 NLO	Pythia 8.212	NNLO QCD+NLO EW [90–92]
VH	Powheg-Box v2	PDF4LHC15 NLO	Pythia 8.212	NNLO QCD+NLO EW [93–95]
ttH	MG5_aMC@NLO v2.2.2 [96]	NNPDF30LO [97]	Pythia 8.212	NLO QCD+NLO EW [98–103]

Table 3.2: Monte Carlo generators used to describe the Higgs boson production processes together with the corresponding parton distribution function (PDF) set and the model of parton showering, hadronisation and underlying event (UEPS). In addition, the order of the total cross-section calculation is given.

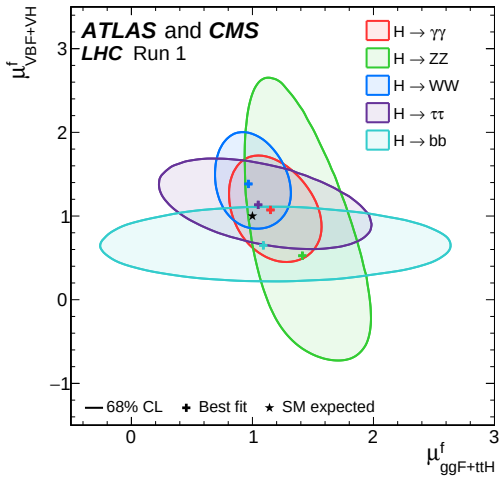

Figure 3.7: Negative log-likelihood contours at 68% confidence limit in the $(\mu_{ggF+ttH}, \mu_{\text{VBF}+VH})$ plane for the combination of ATLAS and CMS data of the Run 1 of the LHC for each of the five decay channels $H \to ZZ$, $H \to WW$, $H \to \gamma\gamma$, $H \to \tau\tau$ and $H \to bb$. The best fit values obtained for each of the five decay channels are also shown, together with the SM expectation. Reproduced from Ref. [76] under CC-BY-4.0 licence.

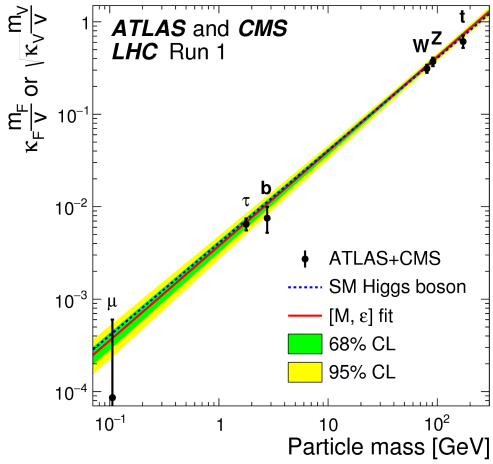

Figure 3.8: Best fit values as a function of particle mass for the combination of ATLAS and CMS data of the Run 1 of the LHC. The dashed (blue) line indicates the predicted dependence on the particle mass in the case of the SM Higgs boson. The solid (red) line indicates the best fit result to the phenomenological model of Ref. [77] with the corresponding 68% and 95% confidence level bands. Reproduced from Ref. [76] under CC-BY-4.0 licence.

3.3 Background samples

Different SM-like processes which can be a source of background for the analyses are summarized in this subsection. The samples used to model each contribution are detailed and given for the fully-leptonic final states. The most important background contributions are the ones in which light leptons can be originated from heavy quarks, tau leptons or boson decays. The main background processes are: $Z \to \tau\tau$, $Z \to \ell\ell$, Top processes, Di-boson production, $H \to WW$, W+jets and multi-jet processes.

The main background is the Z boson decay into a pair of taus ($Z\tau\tau$). It is an irreducible background of the Higgs boson cross-section measurement due to the topology of this decay and because of its similarity with the $H \to \tau\tau$ decay. The main difference lies in the invariant mass of the di-τ system. Despite the reconstructed mass expectation values differ, the two distributions partially overlap. Reducing the amount of $Z\tau\tau$ background is a crucial step in the analysis and a very good modelling is needed.

On the other hand, the Z boson can also decay to light leptons ($Z\ell\ell$, where $\ell = e, \mu$). As the τ objects are reconstructed using their visible leptonic decay products, a $Z\ell\ell$ process can be mis-identified as a $H \to \tau\tau$ event. However, in the $Z\ell\ell$ decay no neutrinos are involved. The amount of $E_{\mathrm{T}}^{\mathrm{miss}}$ in the event is an important discriminant of the process as well as the invariant mass of the two leptons.

In addition to the Z processes, the top-quark decays can be a source of background if leptons are produced via the decay of the W boson. Two different backgrounds are considered here: $t\bar{t}$ and single-t. The top-quark commonly decays into a b-quark and a W boson. Here the b-quark hadronizes forming a jet, more precisely a b-jet. Hence this process can be highly suppressed by vetoing the events containing a b-tagged jet.

Events where two weak bosons are produced (WW, ZZ and WZ) are called conveniently Di-boson processes and they are a source of τ and high energetic light leptons. However, the cross-section of these events is small and their contribution can be estimated with MC simulation.

Table 3.3 lists the different background processes modelled by MC simulation in the analyses, the MC generators, the order of the cross-section calculation of each background and the respective parton distribution function and the parton shower.

Process	MC generator	PDF	UEPS	Order
Z+jets	Sherpa 2.2.1 [104]	NNPDF30NNLO [105]	Sherpa 2.2.1 [106]	NNLO [107,108]
$t\bar{t}$	Powheg-Box v2	CT10 [109]	Pythia 6.428 [110]	NNLO+NNLL [111]
single-t	Powheg-Box v1 [112,113]	CT10	Pythia 6.428	NLO [114–116]
Diboson	Sherpa 2.2.1	NNPDF30NNLO	Sherpa 2.2.1	NLO

Table 3.3: Monte Carlo generators used to describe the background processes together with the PDF set and the UEPS. In addition, the order of the total cross-section calculation is given.

A special case of background processes is the decay of a Higgs boson into two W bosons (HWW). The process is a background for the $H \to \tau\tau$ and LFV analyses. The HWW MC samples are generated using the same MC generators used for the signal samples in Table 3.2.

The $H \to \tau\tau$ process is considered as background for the LFV search. The same MC generators used for the $H \to \tau\tau$ cross-section measurement have been employed. The generators and parton shower models used to simulate the process are summarized in Table 3.2.

Finally, the treatment of the W+jets and multi-jet backgrounds is based on data-driven techniques and is described in Section A.1.

4. Cross-section measurement of the Higgs boson decaying into a pair of τ-leptons

This chapter describes the measurement of the production cross-section of the Higgs boson decaying into a pair of τ-leptons ($H \to \tau\tau$). The measurement is performed by looking for a statistically significant excess of signal-like events over the background expectation in the fully-leptonic channel, $H \to \tau_{\text{lep}}\tau_{\text{lep}}$. The semi-leptonic ($H \to \tau_{\text{lep}}\tau_{\text{had}}$) and fully-hadronic ($H \to \tau_{\text{had}}\tau_{\text{had}}$) channels are also exploited in dedicated analyses. These two channels will be briefly described as they are not the main topic of this thesis. The final results are shown in Section 4.6 and a paper presenting the results of this thesis was published in April 2019 [117]. Previous results concerning the $H \to \tau\tau$ decay can be found in Refs. [118–121].

4.1 Introduction

After the discovery of the Higgs boson, one of the main goals of the LHC experiments is to measure the production cross-section as well as to measure the branching ratios of this new particle. Figure 4.1 shows a Feynman diagram of a Higgs boson decaying into a τ-lepton pair and the possible τ-lepton decays.

This analysis is performed using a cut-based analysis (CBA). The CBA categorization criteria are introduced to define two different signal regions (SRs) to enhance the signal events produced via ggF and VBF processes. Several studies were performed to improve the sensitivity with respect to the Run 1 analysis. Additionally the selection criteria was

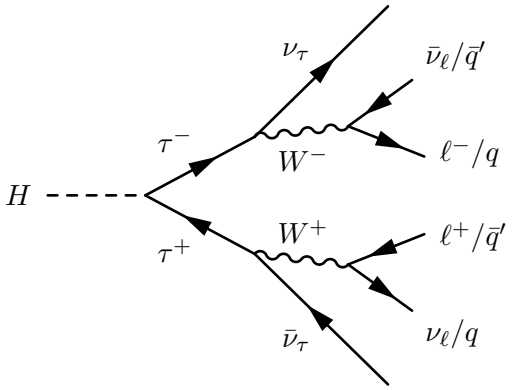

Figure 4.1: Feynman diagram for the decay of a Higgs boson into the $\tau_{\text{lep}}\tau_{\text{lep}}$, $\tau_{\text{lep}}\tau_{\text{had}}$ and $\tau_{\text{had}}\tau_{\text{had}}$ channel combinations. In the case of the Higgs boson decaying into a pair of τ-leptons. The leptonically decaying tau leptons represent light leptons ($\ell \equiv \mu, e$) and their corresponding neutrinos ($\nu_\ell \equiv \nu_\mu, \nu_e$).

optimized by improving the event categorization and harmonizing the requirements among the $H \to \tau\tau$ analysis channels, when no strong impact on the expected significance was observed.

4.2 Event selection and categorization

Several selection criteria are applied to reject background events produced by processes different from the Higgs boson decay into a pair of taus. A first selection, called preselection, is used to select events with a signal-like topology, while retaining enough statistics to verify the background estimates against the data. If an event pass the preselection criteria, it can enter into one of the two signal regions, Tight or Boosted inclusive region. On the other hand, if the event fails the preselection criteria, it can enter into one of the two control regions, Top-quark or $Z\ell\ell$ control region. Figure 4.2 shows the schematic of the signal and control regions used in the analysis.

4.2.1 The $\tau_{\text{lep}}\tau_{\text{lep}}$ selection criteria

The $H \to \tau\tau$ analysis uses the object reconstruction and quality criteria described in Section 2.3. In the $\tau_{\text{lep}}\tau_{\text{lep}}$ channel, Medium identification as well as Gradient isolation

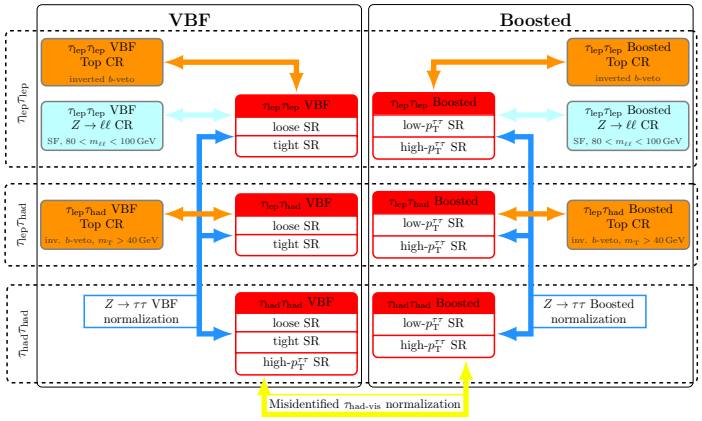

Figure 4.2: Schematic view of the signal and control regions that are used in the fit and their associations to analysis channels and categories. Arrows indicate how the background normalizations are correlated in the fit.

are required for light leptons. Furthermore, Figure 4.3 and Table 4.1 shows a summary of the trigger logic and the offline p_{T} thresholds used at the preselection criteria for the ee, $\mu\mu$ and different flavour (df) channels. The different trigger regions are defined as a function of the leading and subleading[1] lepton p_{T}.

Region	year	ee channel	$\mu\mu$ channel	different flavour channel
$trig1$	2015	$p_{\mathrm{T}}^{e_1}$ [GeV] > 25.0	-	p_{T}^{e} [GeV] > 25.0
	2016	$p_{\mathrm{T}}^{e_1}$ [GeV] > 27.0	-	p_{T}^{e} [GeV] > 27.0
$trig2$	2015	-	$p_{\mathrm{T}}^{\mu_1}$ [GeV] > 21.0	$15.0 < p_{\mathrm{T}}^{e}$ [GeV] < 25.0 and p_{T}^{μ} [GeV] > 21.0
	2016	-	$p_{\mathrm{T}}^{\mu_1}$ [GeV] > 27.3	$18.0 < p_{\mathrm{T}}^{e}$ [GeV] < 27.0 and p_{T}^{μ} [GeV] > 27.3
$trig3$	2015	$15.0 < p_{\mathrm{T}}^{e_1}$ [GeV] < 25.0 $p_{\mathrm{T}}^{e_2}$ [GeV] > 18.0	$18.9 < p_{\mathrm{T}}^{\mu_1}$ [GeV] < 21.0 $p_{\mathrm{T}}^{\mu_2}$ [GeV] > 10.0	$15.0 < p_{\mathrm{T}}^{e}$ [GeV] < 25.0 $14.7 < p_{\mathrm{T}}^{\mu}$ [GeV] > 21.0
	2016	$18.0 < p_{\mathrm{T}}^{e_1}$ [GeV] < 27.0 $p_{\mathrm{T}}^{e_2}$ [GeV] > 18.0	$23.1 < p_{\mathrm{T}}^{\mu_1}$ [GeV] < 27.3 $p_{\mathrm{T}}^{\mu_2}$ [GeV] > 10.0	$18.0 < p_{\mathrm{T}}^{e}$ [GeV] < 27.0 $14.7 < p_{\mathrm{T}}^{\mu}$ [GeV] > 27.3

Table 4.1: Definition of the trigger regions used in the analysis. $Trig1$ is the single electron trigger region, $trig2$ is the single muon trigger region and $trig3$ is the di-lepton trigger region. The $l_{1(2)}$ notation refers to the leading (subleading) lepton.

[1]The decayed lepton of the Higgs boson with highest p_{T} is referred as the leading lepton, whereas the second lepton, with lower p_{T}, is referred as subleading lepton.

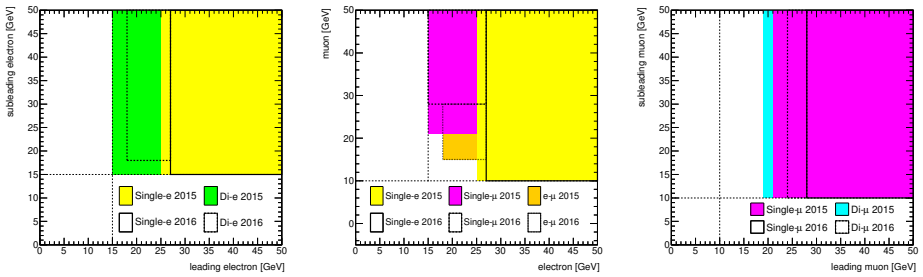

Figure 4.3: The scheme of lepton p_{T} thresholds applied to avoid the overlap between single-lepton and di-lepton triggers. The three plots correspond to individual final states: two electrons (left), electron and muon (middle) and two muons (right).

In the $\tau_{\mathrm{lep}}\tau_{\mathrm{lep}}$ final state, events are required to have at least one reconstructed primary vertex (see Section 2.3.1). The chosen primary vertex candidate is the vertex with the highest sum of the squared transverse momenta of all associated tracks and must have at least two tracks associated to it. These two tracks must belong to the highest p_{T} light leptons in the event. The two leading leptons must have opposite charge. Events with hadronic tau candidates are vetoed. Moreover, the primary vertex must be associated to at least a jet with a $p_{\mathrm{T}} > 40$ GeV, to suppress the irreducible Drell-Yan background.

Only events with $E_{\mathrm{T}}^{\mathrm{miss}} > 20$ GeV are selected to reject background topologies without neutrinos. In the same flavour (sf) channels (ee and $\mu\mu$), this requirement is tightened to reject the Drell-Yan processes, requiring $E_{\mathrm{T}}^{\mathrm{miss}} > 55$ GeV and $E_{\mathrm{T}}^{\mathrm{miss,HPTO}} > 55$ GeV. Another selection criterion to reduce the $Z\ell\ell$ background is that the di-lepton invariant mass has to be 30 GeV $< m_{\ell\ell} <$ 75 GeV for the sf. For the df channel, the di-lepton invariant mass has to be 30 GeV $< m_{\ell\ell} <$ 100 GeV.

Additional criteria are further imposed after the preselection to select signal events where the Higgs boson is boosted[2]. Requirements on the angular distance between the visible decay products of the two selected τ-lepton decays, $\Delta R_{\ell\ell} < 2.0$ and their pseudorapidity difference, $\Delta\eta_{\ell\ell} < 1.5$, are applied to reject non-resonant background events.

[2]A boosted particle is referred to a particle originated with high momentum in the detector reference system.

Another requirement is applied to the momentum fractions carried by the visible τ decay products, restricting the collinear momentum fractions of the leading (x_1) and subleading (x_2) leptons to be $0.1 < x_{1,2} < 1.0$. The fractions of the τ-lepton momenta carried by the visible decay products are calculated using the collinear approximation, assuming that the neutrinos from each τ decay have the same direction as the visible decay products of the τ-leptons. They are defined as:

$$x_{1,2} = \frac{p_{1,2}^{\text{vis}}}{p_{1,2}^{\text{vis}} + E_{\text{T}}^{\text{miss}} \left(\cos\left(\phi_{1,2}^{\text{vis}} - \phi_{E_{\text{T}}^{\text{miss}}} \right) - \sin\left(\phi_{1,2}^{\text{vis}} - \phi_{E_{\text{T}}^{\text{miss}}} \right) \cot\left(\phi_{1,2}^{\text{vis}} - \phi_{2,1}^{\text{vis}} \right) \right)} \tag{4.1}$$

where $p_{1,2}^{\text{vis}}$ is the magnitude of the momentum of the visible τ decay products, $E_{\text{T}}^{\text{miss}}$ is the missing energy and $\phi_{1,2}^{\text{vis}}$ and $\phi_{E_{\text{T}}^{\text{miss}}}$ are the azimuthal angles of the visible τ decay products and the missing energy in the plane perpendicular to the beam line. The collinear momentum fractions are also useful for an estimation of the $m_{\tau\tau}^{\text{coll}}$ mass:

$$m_{\tau\tau}^{\text{coll}} = \frac{m_{\ell\ell}^{\text{vis}}}{\sqrt{x_1 \cdot x_2}} \tag{4.2}$$

where $m_{\ell\ell}^{\text{vis}}$ is the invariant mass of the visible decay products of the taus, and thus in the $\tau_{\text{lep}}\tau_{\text{lep}}$ channel it is equal to the invariant mass of the di-lepton system.

The requirement $m_{\tau\tau}^{\text{coll}} > m_Z - 25$ GeV is applied to ensure that the data is statistically independent of the ATLAS $H \to WW$ analysis [122].

The selection criteria mentioned for the preselection of the $\tau_{\text{lep}}\tau_{\text{lep}}$ channel are summarised in Table 4.2. The yields at the preselection level for the different backgrounds and signals are shown in Table 4.3. The basic kinematic distributions are presented in Figures 4.4 and 4.5.

The invariant mass $m_{\tau\tau}^{\text{MMC}}$ used in the analysis is computed by the Missing Mass Calculator (MMC) algorithm [123]. The $m_{\tau\tau}^{\text{MMC}}$ is one of the most powerful variable to distinguish the Drell-Yan processes from the Higgs boson signal. This algorithm uses a scan of the possible angular positions of the neutrinos to give the most likely value for the invariant mass and it can be applied to all event topologies of $H \to \tau\tau$. The MMC algorithm works by solving an underconstrained system of equations with the assumption that the orientations of the neutrinos and other decay products are

consistent with the mass and decay kinematic of a τ-lepton. The technique assumes that the only source of $E_{\mathrm{T}}^{\mathrm{miss}}$ are the neutrinos coming from the τ-lepton decays. The kinematic of the system is not fully determined due to the unknown momenta of the neutrinos. The value of the invariant mass is computed for all the points in the phase-space of the possible neutrino configurations, with an estimation of their probability. The most probable mass value is used as the final estimator of the MMC mass. The $m_{\tau\tau}^{\mathrm{MMC}}$ variable distributions, shown in Figure 4.6, will be used in the statistical fit.

	$\tau_{\mathrm{lep}}\tau_{\mathrm{lep}}$	
	$df \equiv e\mu/\mu e$	$sf \equiv ee/\mu\mu$
Preselection	Number of $e/\mu = 2$, Number of $\tau_{\text{had-vis}} = 0$ e/μ : Medium, gradient iso. Opposite charge	
	$m_{\tau\tau}^{\mathrm{coll}} > m_Z - 25\,\mathrm{GeV}$ $30\,\mathrm{GeV} < m_{e\mu} < 100\,\mathrm{GeV}$	$30\,\mathrm{GeV} < m_{\ell\ell} < 75\,\mathrm{GeV}$
	b-jet veto	
	$E_{\mathrm{T}}^{\mathrm{miss}} > 20\,\mathrm{GeV}$	$E_{\mathrm{T}}^{\mathrm{miss}} > 55\,\mathrm{GeV}$ $E_{\mathrm{T}}^{\mathrm{miss,HPTO}} > 55\,\mathrm{GeV}$
	Leading jet $p_{\mathrm{T}} > 40\,\mathrm{GeV}$	
	$\Delta R_{\ell\ell} < 2.0$, $\lvert\Delta\eta_{\ell\ell}\rvert < 1.5$ $0.1 < x_1 < 1.0$, $0.1 < x_2 < 1.0$	

Table 4.2: Summary of the event preselection for the $\tau_{\mathrm{lep}}\tau_{\mathrm{lep}}$ channels depending on the final flavour state.

After the preselection, the events are further split into two orthogonal categories, the VBF and Boosted inclusive regions. The aim of this division is the optimization of the analysis for two specific production mechanisms, where a clearer signature of the

Preselection	ee	$\mu\mu$	$e\mu/\mu e$	$\tau_{\text{lep}}\tau_{\text{lep}}$
Fakes	55 ± 4	150 ± 10	610 ± 20	810 ± 30
HWW	7.6 ± 0.5	8.4 ± 0.5	30 ± 1	46 ± 1
Diboson	62 ± 2	80 ± 2	308 ± 5	450 ± 6
Top	93 ± 4	98 ± 5	510 ± 10	700 ± 10
$Z\ell\ell$	240 ± 40	380 ± 80	70 ± 10	690 ± 90
$Z\tau\tau$	910 ± 20	1520 ± 30	5600 ± 50	8030 ± 60
Total background	1370 ± 40	2240 ± 80	7110 ± 60	10700 ± 100
ggF	10.6 ± 0.2	16.3 ± 0.3	45.9 ± 0.4	72.9 ± 0.5
VBF	5.0 ± 0.1	7.23 ± 0.09	18.0 ± 0.2	30.3 ± 0.2
WH	0.72 ± 0.07	1.31 ± 0.09	3.4 ± 0.2	5.4 ± 0.2
ZH	0.50 ± 0.04	0.74 ± 0.06	1.62 ± 0.09	2.9 ± 0.1
ttH	0.34 ± 0.08	0.39 ± 0.08	1.5 ± 0.2	2.3 ± 0.2
Total Signal	17.1 ± 0.3	26.0 ± 0.3	70.5 ± 0.5	113.7 ± 0.7
Data	1265	2299	7066	10630

Table 4.3: Data and expected number of signal and background events of the preselection in the $\tau_{\text{lep}}\tau_{\text{lep}}$ channel for the 2015-2016 dataset divided by flavour. The normalization factors for the main background components listed in Table 4.16 are applied. Only statistical uncertainties are considered.

Higgs boson events can enhance the signal significance. The statistical significance is calculated according to the binned Asimov significance formula [124]:

$$Z = \sqrt{2 \sum_i ((s_i + b_i) \log(1 + s_i/b_i) - s_i)^2} \tag{4.3}$$

where the sum runs over all bins of the chosen distribution for the bin signal and bin background yield.

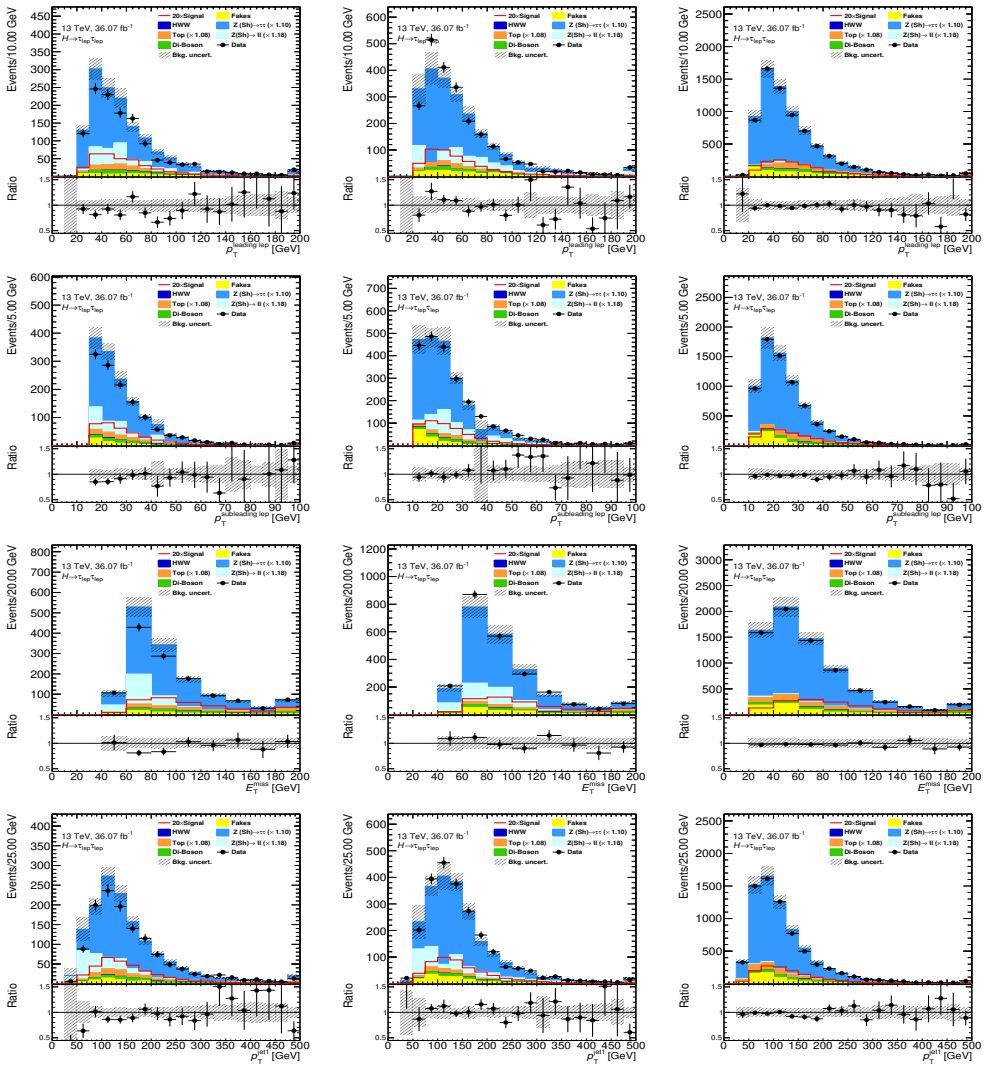

(a) ee channel (b) $\mu\mu$ channel (c) df channel

Figure 4.4: From top to bottom the leading and subleanding lepton momentum, the missing transverse energy, the number of jets and the leading jet momentum after preselection are shown . The ee (left), $\mu\mu$ (middle) and different flavour (right) channels are shown. Error bands include the statistical uncertainties and the systematic uncertainties on the background normalization.

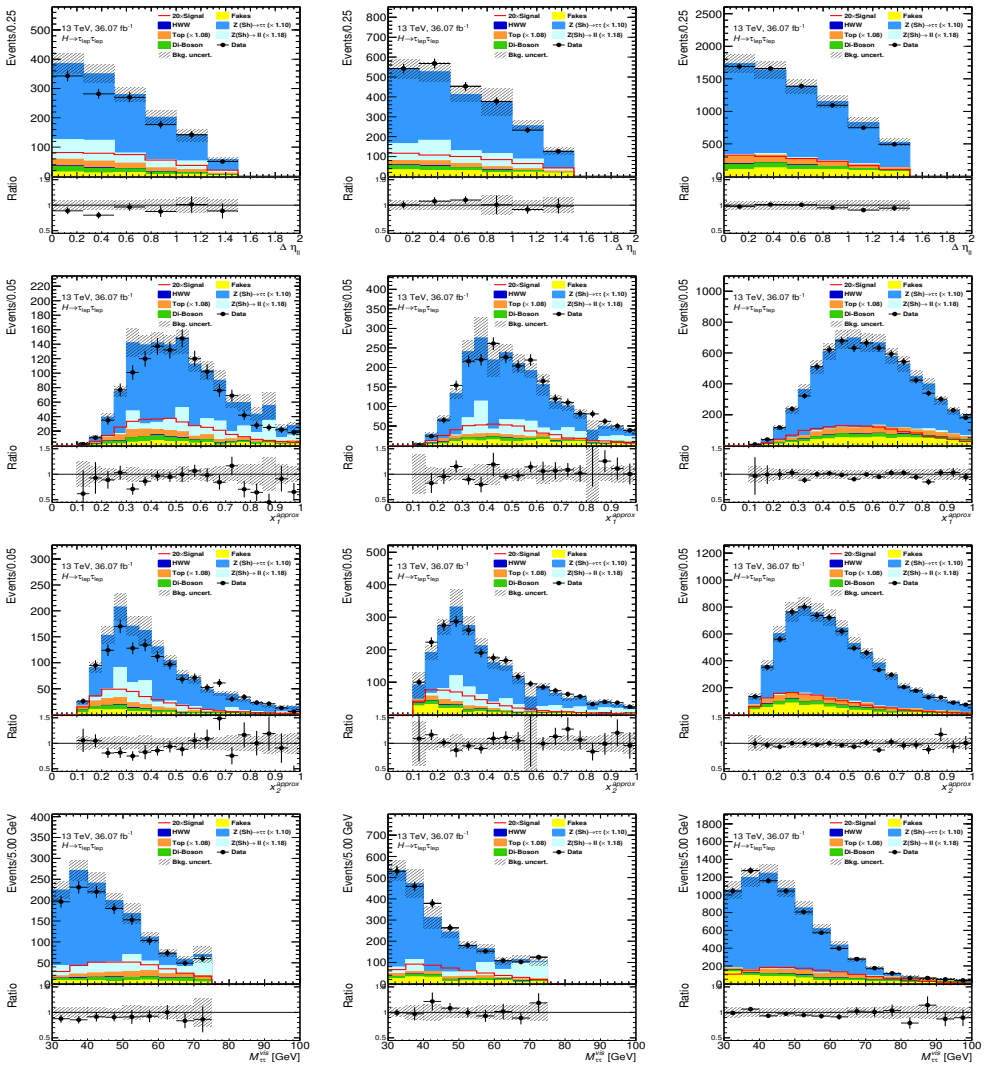

(a) ee channel (b) $\mu\mu$ channel (c) df channel

Figure 4.5: From top to bottom the pseudorapidity separation between the leptons, the collinear momentum fractions of the leptons and the reconstructed mass of the di-lepton system after preselection. The ee (left), $\mu\mu$ (middle) and df channels are ordered from left to right. Error bands include the statistical uncertainties and the systematic uncertainties on the background normalization.

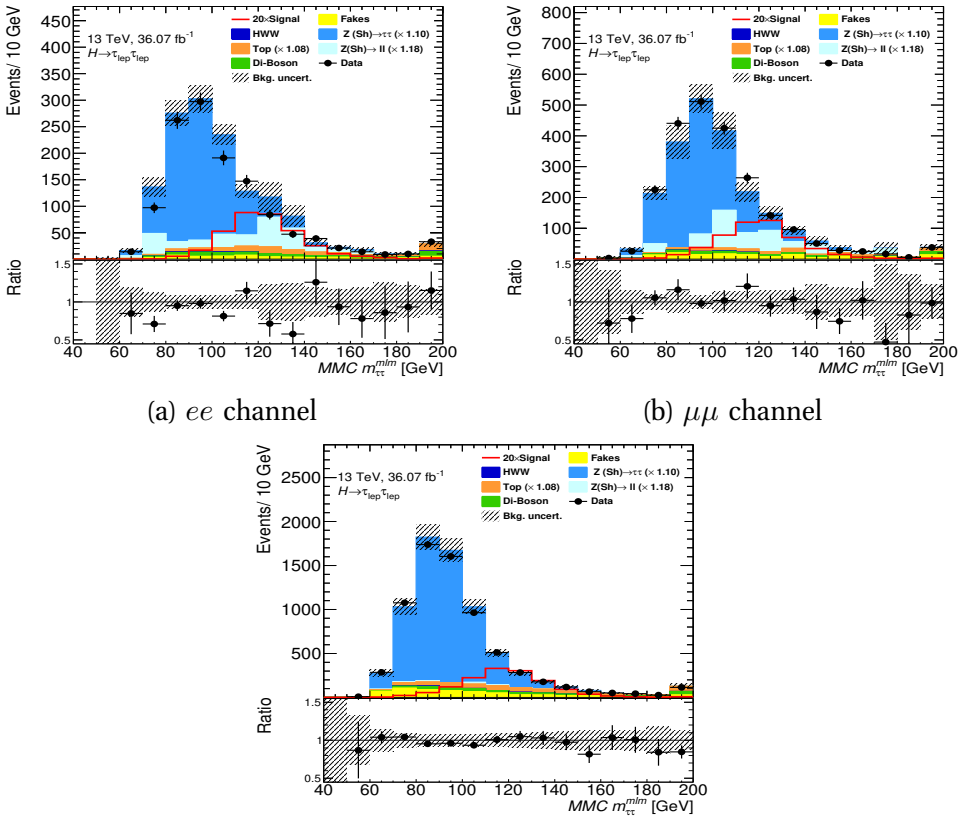

(a) ee channel

(b) $\mu\mu$ channel

(c) df channel

Figure 4.6: The $m_{\tau\tau}^{\text{MMC}}$ distribution after preselection for the different $\tau_{\text{lep}}\tau_{\text{lep}}$ channels. Error bands include the statistical uncertainties and the systematic uncertainties on the background normalization. Signal contributions are scaled by a factor 20 and the pre-fit normalization factors are applied.

.

4.2.2 VBF signal region

The VBF selection criteria require the presence of two forward jets to enhance the Higgs boson signal via the vector boson fusion production process. The Feynman diagram of the VBF production mode is shown in Figure 3.2. The topology production mode of the Higgs boson allows to apply extra requirements to jets. In addition to the leading jet preselection requirement, an extra jet coming from the interaction point is required with a $p_{\mathrm{T}}^{j_2} > 30$ GeV. The requirement of a second jet is motivated because in the Higgs boson VBF production process, two jets are originated from the two interacting quarks. The $p_{\mathrm{T}}^{j_2} > 30$ GeV is chosen to maximize the Asimov significance. The pseudorapidity difference between the two jets must be $|\Delta\eta_{jj}| > 3$, and the product of the pseudorapidities must be negative $\eta_{j_1} \cdot \eta_{j_2} < 0$. Another requirement is applied to the invariant mass of the two leading jets which must be $m_{jj} > 400\,\mathrm{GeV}$. On the other hand, both leptonic tau candidates must lie between the two leading jets in pseudorapidity ($\eta_{j_{1,2}} < \eta_{\ell_{1/2}} < \eta_{j_{2,1}}$).

The VBF region is further split into Tight and Loose subcategories to enhance the sensitivity. In the $\tau_{\mathrm{lep}}\tau_{\mathrm{lep}}$ channel, the Tight subcategory is defined with a requirement of $m_{jj} > 800\,\mathrm{GeV}$, and the remaining events become part of the Loose subcategory. Table 4.4 summarizes the selection criteria mentioned for the VBF region as well as the two subcategories. The event yields of the VBF categories are shown in Table 4.5. The most relevant variables for the VBF category are shown in Figure 4.7. In addition, Figure 4.8(a-c) shows the MMC distributions of the ee, $\mu\mu$ and df channels for the VBF Inclusive selection criteria and in Figure 4.8(d-f) the MMC distributions of the $\tau_{\mathrm{lep}}\tau_{\mathrm{lep}}$ channel for the VBF inclusive category and for the Loose and Tight subcategories.

	$\tau_{\text{lep}}\tau_{\text{lep}}$ All flavours
VBF inclusive	Pass the preselection criteria Subleading jet $p_{\text{T}} > 30\,\text{GeV}$ $m_{jj} > 400\,\text{GeV}$, $\lvert\Delta\eta_{jj}\rvert > 3$ $\eta_{j_1} \cdot \eta_{j_2} < 0$ $\eta_{j_1} < \eta_{\ell_1,\ell_2} < \eta_{j_2}$
VBF Signal Region	Pass VBF inclusive criteria Tight : $m_{jj} > 800\,\text{GeV}$ Loose : $m_{jj} < 800\,\text{GeV}$

Table 4.4: Summary of the event selection for the VBF categories in the $\tau_{\text{lep}}\tau_{\text{lep}}$ channel. The VBF selection criteria are applied after the preselection requirements listed in Table 4.2.

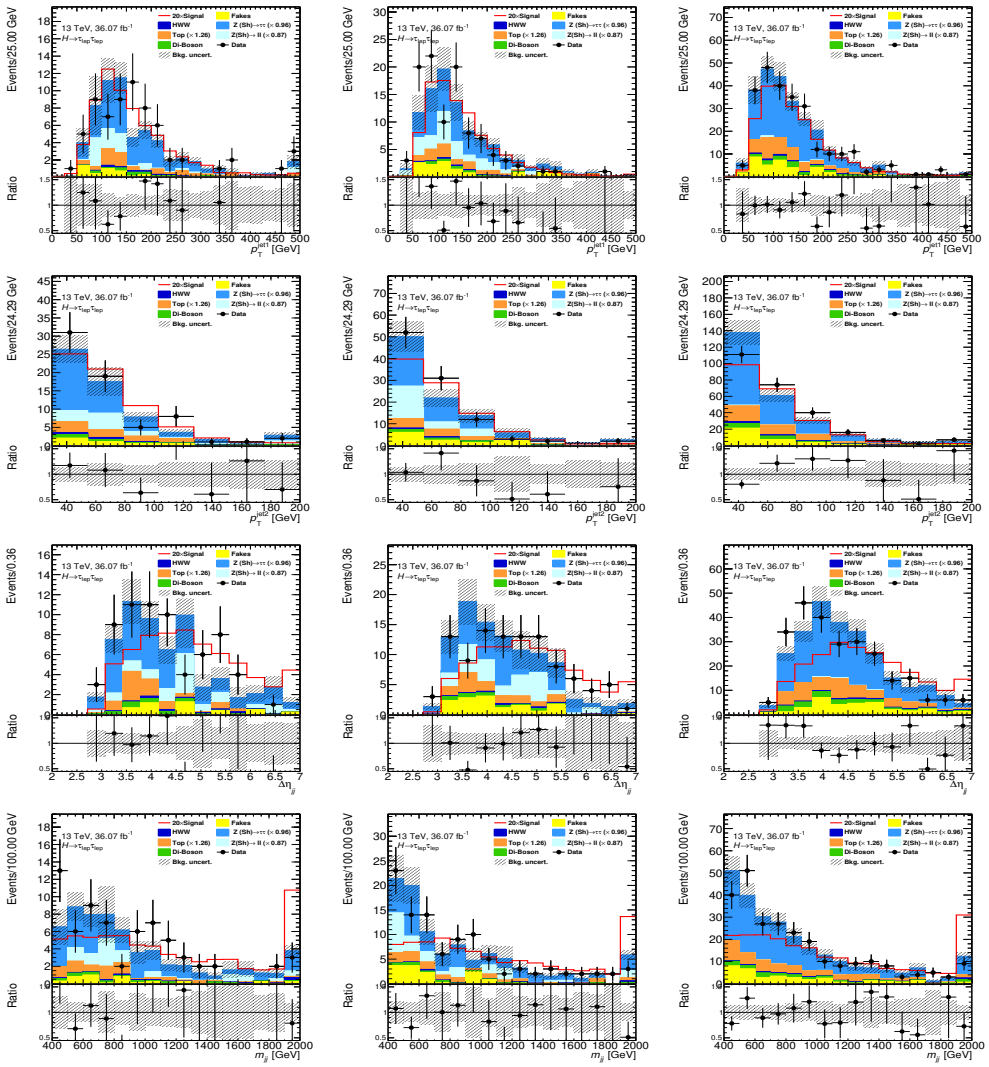

(a) ee channel (b) $\mu\mu$ channel (c) df channel

Figure 4.7: From top to bottom are the leading and subleading jet momentum, $|\Delta\eta_{jj}|$ and m_{jj} distributions for the VBF inclusive region. The ee (left), $\mu\mu$ (right) and df (right) subchannels are shown. Error bands include the statistical uncertainties and the systematic uncertainties on the background normalization. The pre-fit normalizations factors are applied.

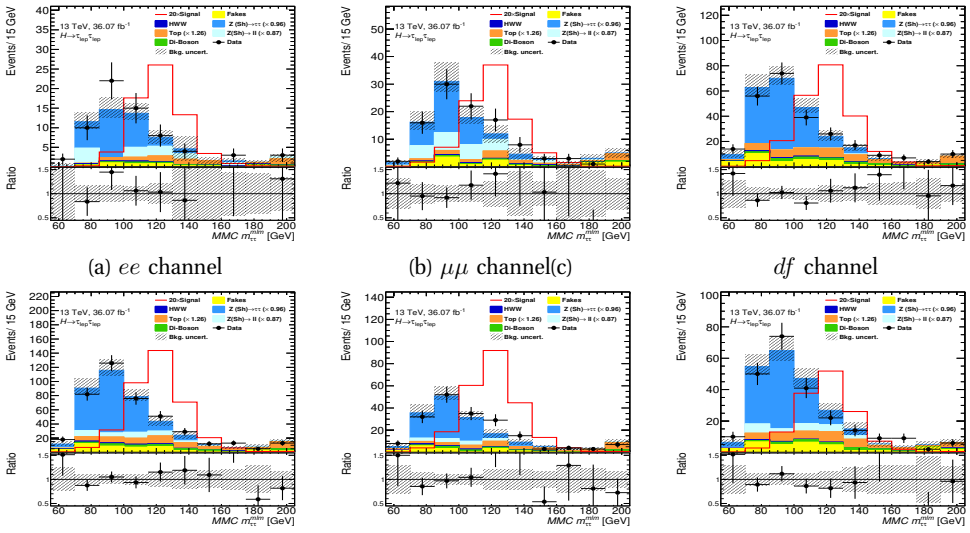

(a) ee channel (b) $\mu\mu$ channel(c) df channel

(d) Incluvive cat. (e) Tight subcat. (f) Loose subcat.

Figure 4.8: The $m_{\tau\tau}^{\text{MMC}}$ distributions for the different $\tau_{\text{lep}}\tau_{\text{lep}}$ subchannels. On the top the histograms (a-c) show the MMC mass distribution for the ee, $\mu\mu$ and df channels after passing the VBF region. On the bottom, the events passing the Loose VBF subcategory . are shown in (d) whereas (e) shows the events passing the Tight VBF subcategory and (f) the events passing the Loose VBF subcategory events. Error bands include the statistical and systematic uncertainties on the background normalization.

VBF	$\tau_{\text{lep}}\tau_{\text{lep}}$		
Preselection	Inclusive	Loose	Tight
Fakes	49 ± 6	32 ± 5	16 ± 3
HWW	8.1 ± 0.3	2.8 ± 0.2	5.4 ± 0.3
Diboson	20 ± 1	10.1 ± 0.7	9.8 ± 0.8
Top	64 ± 4	35 ± 3	29 ± 3
$Z\ell\ell$	36 ± 6	21 ± 5	15 ± 3
$Z\tau\tau$	236 ± 8	134 ± 6	101 ± 5
Total background	410 ± 10	240 ± 10	177 ± 8
ggF	4.4 ± 0.1	2.5 ± 0.1	1.93 ± 0.09
VBF	14.8 ± 0.2	4.52 ± 0.09	10.3 ± 0.1
WH	0.08 ± 0.02	0.04 ± 0.01	0.04 ± 0.01
ZH	0.04 ± 0.01	0.020 ± 0.008	0.017 ± 0.008
ttH	0.10 ± 0.04	0.04 ± 0.02	0.06 ± 0.04
Total Signal	19.5 ± 0.2	7.1 ± 0.1	12.3 ± 0.2
Data	425	237	188

Table 4.5: Expected number of events passing the VBF selections in the $\tau_{\text{lep}}\tau_{\text{lep}}$ channel for the 2015-2016 dataset. The normalization factors for the main background components listed in Table 4.16 are applied. Only statistical uncertainties are shown. Pre-fit normalization factors are applied.

4.2.3 Boosted signal region

The boosted category targets events where the Higgs bosons are produced via ggF, shown in Figure 3.1, with additional recoiling jets, which is motivated by the harder p_{T}-spectrum of the $H \to \tau\tau$ signal compared to the dominant $Z\tau\tau$ background. Events that do not satisfy the VBF selection criteria can enter in the Boosted inclusive region if they pass an additional requirement on the transverse momentum of the Higgs boson candidate of $p_{\mathrm{T}}^{\tau\tau} > 100\,\mathrm{GeV}$ The $p_{\mathrm{T}}^{\tau\tau} > 100\,\mathrm{GeV}$ is chosen to improve the background separation. The p_{T} of the Higgs boson candidate (p_{T}^{H}) is computed as the vector sum of the transverse momenta of the visible decay products of the τ-leptons and the missing transverse momentum vector:

$$p_{\mathrm{T}}^{H} \equiv p_{\mathrm{T}}^{\tau\tau} = |\overrightarrow{p}_{\mathrm{T}}^{\ell_1} + \overrightarrow{p}_{\mathrm{T}}^{\ell_2} + \overrightarrow{p}_{\mathrm{T}}^{\mathrm{miss}}| \tag{4.4}$$

Similarly to the VBF region, the events are further divided into Tight and Loose subcategories. The Tight subcategory requires an angular separation between the two lepton candidates of $\Delta R_{\ell\ell} < 1.5$ and a transverse momentum of the Higgs candidate of $p_{\mathrm{T}}^{H} > 140\,\mathrm{GeV}$. On the other hand, events that have failed the Tight selection enter in the Loose subcategory. Table 4.6 shows the requirements for the Boosted inclusive criteria as well as for each subcategory. The event yields after passing the Boosted categories are shown in Table 4.7. Figure 4.10 shows the $m_{\tau\tau}^{\mathrm{MMC}}$ distributions of the $\tau_{\mathrm{lep}}\tau_{\mathrm{lep}}$ subchannels at the Boosted inclusive region as well as the $m_{\tau\tau}^{\mathrm{MMC}}$ distributions of the Tight and Loose subcategories. The other relevant distributions are shown in Figure 4.9.

	$\tau_{\text{lep}}\tau_{\text{lep}}$ All Flavours
Boosted inclusive	Pass the preselection criteria Fail the VBF selection $p_{\text{T}}^{H} > 100\,\text{GeV}$
Boosted Signal Region	Pass Boosted inclusive criteria Tight : $p_{\text{T}}^{H} > 140\,\text{GeV}$ and $\Delta R_{\ell\ell} < 1.5$ Loose : Otherwise

Table 4.6: Summary of the Boosted event selection for the $\tau_{\text{lep}}\tau_{\text{lep}}$ channel. These criteria must be applied after the preselection criteria.

Boosted	$\tau_{\text{lep}}\tau_{\text{lep}}$		
Preselection	Inclusive	Loose	Tight
Fakes	480 ± 20	340 ± 20	130 ± 10
HWW	33 ± 1	14.2 ± 0.7	18.6 ± 0.8
Diboson	380 ± 5	191 ± 4	189 ± 3
Top	550 ± 10	343 ± 9	208 ± 6
$Z\ell\ell$	600 ± 80	370 ± 80	240 ± 20
$Z\tau\tau$	5660 ± 50	2970 ± 40	2690 ± 40
Total background	7700 ± 100	4230 ± 90	3480 ± 40
ggF	60.2 ± 0.5	30.5 ± 0.3	29.7 ± 0.3
VBF	14.0 ± 0.2	6.8 ± 0.1	7.2 ± 0.1
WH	4.9 ± 0.2	2.1 ± 0.1	2.7 ± 0.1
ZH	2.6 ± 0.1	1.14 ± 0.07	1.49 ± 0.09
ttH	2.1 ± 0.2	1.3 ± 0.1	0.8 ± 0.1
Total Signal	83.9 ± 0.6	41.8 ± 0.4	42.0 ± 0.4
Data	7568	4124	3444

Table 4.7: Event yields passing the Boosted selection in the $\tau_{\text{lep}}\tau_{\text{lep}}$ channel for the 2015-2016 dataset. Only statistical uncertainties are considered. The normalization factors for the main background components listed in Table 4.16 are applied.

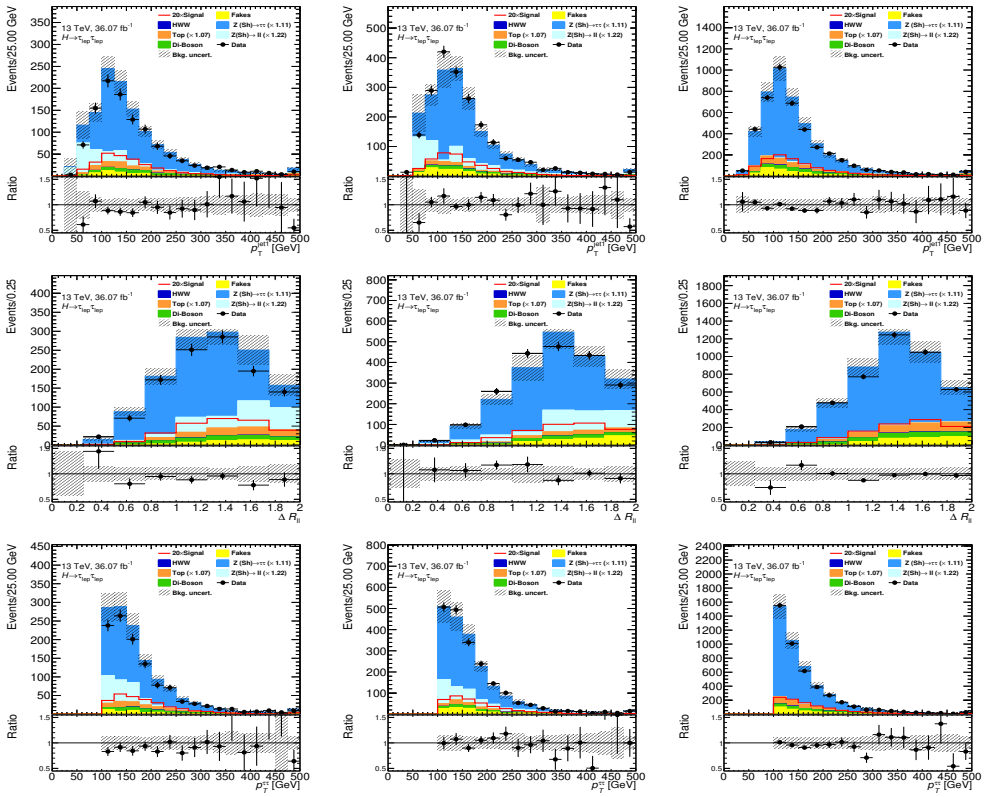

(a) ee channel (b) $\mu\mu$ channel (c) df channel

Figure 4.9: From top to bottom are the distributions of the leading jet momentum, the angular separation between the leptons and the Higgs candidate momentum. The ee (left), $\mu\mu$ (middle) and df (right) subchannels are shown. Error bands include the statistical and systematic uncertainties on the background normalization.

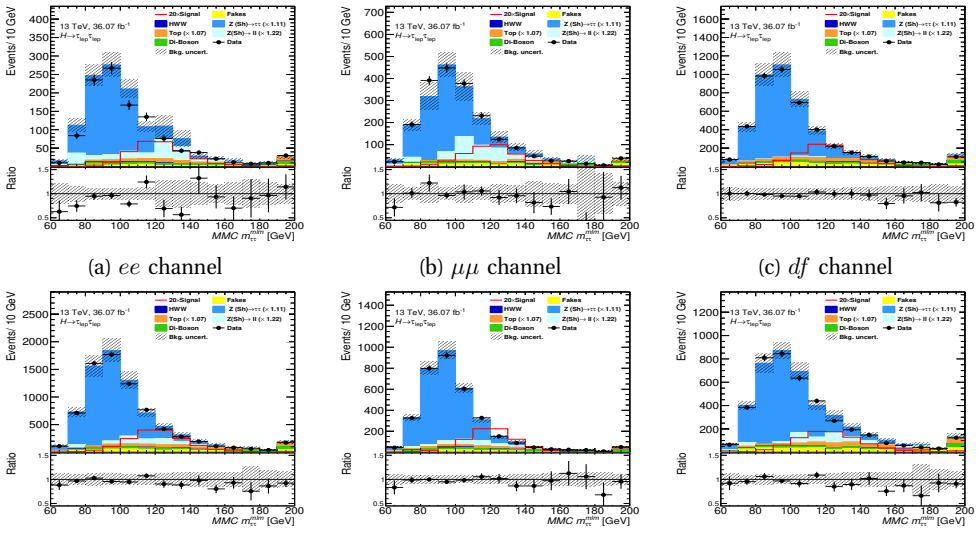

(a) ee channel (b) $\mu\mu$ channel (c) df channel

(d) Inclusive cat. (e) Tight subcat. (f) Loose subcat.

Figure 4.10: The $m_{\tau\tau}^{\text{MMC}}$ mass distributions for the different $\tau_{\text{lep}}\tau_{\text{lep}}$ subchannels. On the top the histograms (a-c) shows the MMC mass distribution for the ee, $\mu\mu$ and df channels after passing the Boosted region. On the bottom, the events passing the Boosted category are shown in (d) whereas (e) shows the events passing the Tight Boosted subcategory and (f) the events passing the Loose Boosted subcategory. Error bands include the statistical and systematic uncertainties on the background normalization.

4.2.4 Fakes transfer factors for the $H \to \tau\tau$ analysis

The background induced by misidentified or non-prompt leptons (known collectively as "Fakes" leptons) is estimated through a special preselection that includes all events in the signal regions as well as in the control regions. The method is described in Appendix A.1. The fakes selection criteria, shown in Table 4.8, includes all requirements related to the trigger regions mentioned in Table 4.1. The composite charge of the leptons is needed to define the four Fakes regions of the ABCD method. Furthermore, to include the top-quark and $Z\ell\ell$ control regions, described in Section 4.3, the b-veto and the $m_{\ell\ell} < 75$ GeV requirements are removed from the fakes selection criteria.

	$\tau_{\text{lep}}\tau_{\text{lep}}$	
	$e\mu/\mu e$	$ee/\mu\mu$
Fake selection	Number of $\tau_{\text{had-vis}} = 0$ $m_{\tau\tau}^{\text{coll}} > m_Z - 25\,\text{GeV}$ $30 < m_{\ell\ell} < 100\,\text{GeV}$ $E_{\text{T}}^{\text{miss}} > 20\,\text{GeV}$	$E_{\text{T}}^{\text{miss}} > 55\,\text{GeV}$ $E_{\text{T}}^{\text{miss,HPTO}} > 55\,\text{GeV}$
	Leading jet $p_{\text{T}} > 40\,\text{GeV}$ $\Delta R_{\ell\ell} < 2.0$, $\lvert\Delta\eta_{\ell\ell}\rvert < 1.5$ $0.1 < x_1 < 1.0$, $0.1 < x_2 < 1.0$	

Table 4.8: Selection criteria applied for the Fakes background of the $\tau_{\text{lep}}\tau_{\text{lep}}$ channel, including all signal as well as control regions.

The transfer factors obtained in different b-tag(-veto) regions, triggers and channels are given in Table 4.9 where only statistical uncertainties are shown.

region		ee	$\mu\mu$	$e\mu$	μe
b-veto	$trig1$	0.24 ± 0.04	—	0.60 ± 0.02	0.15 ± 0.02
	$trig2$	—	0.81 ± 0.04	0.0 ± 0.0	0.21 ± 0.01
	$trig3$	0.35 ± 0.08	1.09 ± 0.09	0.50 ± 0.02	0.37 ± 0.04
b-tag	$trig1$	0.12 ± 0.01	—	0.37 ± 0.01	0.08 ± 0.01
	$trig2$	—	0.41 ± 0.02	0.0 ± 0.0	0.12 ± 0.01
	$trig3$	0.33 ± 0.07	0.45 ± 0.05	0.43 ± 0.03	0.26 ± 0.04

Table 4.9: Transfer factors and their uncertainties in different regions from same-sign (SS) events after applying the selection listed in Table 4.8. The $trig1$, $trig2$ and $trig3$ are single electron, single muon and di-lepton triggers respectively. Only statistical uncertainties are shown.

4.3 Control Regions

A good understanding of the backgrounds is a key aspect of any measurement. The agreement between the background expectation and the data is studied in details in the regions where no Higgs boson signal is expected, because the understanding of the background modelling allows to achieve a more precise cross-section measurement of the $H \to \tau\tau$ process.

The control regions (CRs) are defined with the aim to satisfy three conditions: a negligible contamination from signal events, a phase-space with very high purity in the particular background process of interest and a selection criteria as similar as possible to the signal region. Additionally, the CRs are used to determine the normalization factors of the main background processes (see Section 4.3.3). They are called pre-fit normalization factors (NFs), as they are estimated analytically before the fit. Those pre-fit normalization factors are used only for illustration purposes, while the final values are determined by the statistical analysis, when they appear as free floating parameters.

Two of the main sources of background in the $H \to \tau_{\text{lep}}\tau_{\text{lep}}$ cross-section measurement are the Top-quark and $Z\ell\ell$ processes.

4.3.1 Top-quark control region: yields and control plots

The top-quark control region is a dedicated region to estimate the $t\bar{t}$ and single-t backgrounds. The definition of this CR is obtained by reverting the b-veto requirement in Table 4.2: # of b-jets > 0, the rest of the selection criteria remains unchanged. The event yields in the top-quark CR after preselection, Boosted inclusive and VBF inclusive selection criteria are shown in Tables 4.10-4.12. Figure 4.11 shows the $m_{\tau\tau}^{\text{MMC}}$ distributions for the top-quark control region.

Component	ee	$\mu\mu$	df	Total
Fakes	59 ± 3	108 ± 8	380 ± 10	550 ± 20
HWW	1.2 ± 0.2	1.9 ± 0.3	5.6 ± 0.5	8.8 ± 0.6
Diboson	15.7 ± 0.8	24 ± 1	77 ± 2	117 ± 3
Top	950 ± 10	1160 ± 20	5840 ± 40	7940 ± 40
$Z\ell\ell$	50 ± 10	110 ± 20	13 ± 4	180 ± 20
$Z\tau\tau$	210 ± 10	360 ± 20	1240 ± 30	1810 ± 40
Total background	1290 ± 20	1760 ± 30	7550 ± 50	10600 ± 60
Signal	13.5 ± 0.5	14.3 ± 0.5	53 ± 1	81 ± 1
Data	1293	1776	7564	10633

Table 4.10: Event yields are shown for the top-quark control region at the preselection level. The different $\tau_{\text{lep}}\tau_{\text{lep}}$ flavour combinations are shown. The pre-fit normalization factors are applied. Only statistical uncertainties are shown.

4.3.2 $Z\ell\ell$ control region: yields and control plots

The $Z\ell\ell$ background has a dedicated CR defined requiring the presence of a same-flavour opposite-sign dilepton pair. The selection criteria of this control region is the same as the preselection and signal regions except that the events must satisfy the condition 80 GeV $< m_{\ell\ell} <$ 100 GeV, where the $Z\ell\ell$ background dominates. The event yields after passing the $Z\ell\ell$ CR preselection, Boosted inclusive and VBF inclusive are shown in Tables 4.13-4.15.

The $m_{\tau\tau}^{\text{MMC}}$ distributions are shown in Figure 4.12 for the ee and $\mu\mu$ subchannels. In the distributions the statistical uncertainties are drawn and the corresponding normalization factors are applied for the main backgrounds.

Component	ee	$\mu\mu$	df	Total
Fakes	55 ± 3	101 ± 7	300 ± 10	460 ± 10
HWW	1.0 ± 0.2	1.7 ± 0.3	4.1 ± 0.4	6.8 ± 0.6
Diboson	14.8 ± 0.8	22 ± 1	64 ± 2	100 ± 3
Top	860 ± 10	1050 ± 20	4630 ± 30	6540 ± 40
$Z\ell\ell$	50 ± 10	100 ± 20	9 ± 4	160 ± 20
$Z\tau\tau$	190 ± 10	320 ± 20	820 ± 20	1330 ± 30
Total background	1170 ± 20	1590 ± 30	5830 ± 40	8600 ± 50
Signal	12.5 ± 0.5	13.3 ± 0.5	45.4 ± 0.9	71 ± 1
Data	1170	1611	5841	8622

Table 4.11: Event yields of the top-quark control region for the inclusive Boosted category. The pre-fit normalization factors are applied. Only statistical uncertainties are shown.

Component	ee	$\mu\mu$	df	Total
Fakes	2.1 ± 0.6	5 ± 2	18 ± 3	24 ± 3
HWW	0.15 ± 0.06	0.19 ± 0.04	0.8 ± 0.2	1.1 ± 0.2
Diboson	0.8 ± 0.2	1.5 ± 0.3	3.6 ± 0.4	5.9 ± 0.6
Top	71 ± 4	68 ± 4	297 ± 9	440 ± 10
$Z\ell\ell$	2.1 ± 0.8	4 ± 1	0.7 ± 0.3	7 ± 1
$Z\tau\tau$	10 ± 2	15 ± 3	38 ± 3	63 ± 5
Total background	86 ± 5	93 ± 5	360 ± 10	540 ± 10
Signal	0.80 ± 0.08	0.84 ± 0.08	3.4 ± 0.2	5.0 ± 0.2
Data	85	85	368	538

Table 4.12: Event yields of the top-quark control region for the inclusive VBF category. The pre-fit normalization factors are applied. Only statistical uncertainties are shown.

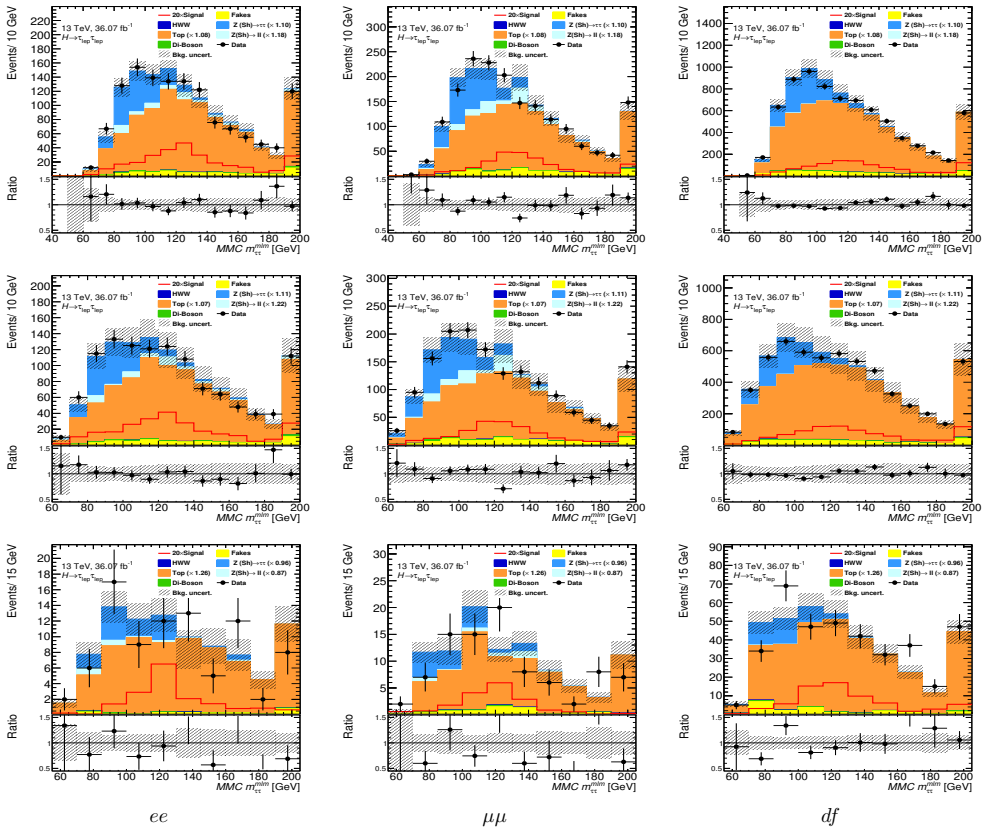

Figure 4.11: Top-quark control region distributions of $m_{\tau\tau}^{\text{MMC}}$ at the preselection (top), Boosted inclusive (middle) and VBF inclusive (bottom) selection criteria. The ee, $\mu\mu$ and df flavour compositions are ordered from left to right respectively. Error bands include the statistical and systematic uncertainties on the background normalization.

Component	ee	$\mu\mu$	Total
Fakes	0.0 ± 0	0.0 ± 0	0.0 ± 0
HWW	0.11 ± 0.05	0.016 ± 0.008	0.13 ± 0.05
Diboson	63 ± 2	57 ± 2	120 ± 2
Top	27 ± 2	25 ± 2	53 ± 3
$Z\ell\ell$	1450 ± 70	1390 ± 70	2850 ± 90
$Z\tau\tau$	4 ± 1	6 ± 1	10 ± 2
Total background	1550 ± 70	1480 ± 70	3030 ± 90
Signal	0.91 ± 0.08	0.65 ± 0.06	1.6 ± 0.1
Data	1473	1564	3037

Table 4.13: Event yields of the $Z\ell\ell$ control region at the preselection level. The contribution of fakes is negligible and is not considered. The pre-fit normalization factors are applied. Only statistical uncertainties are shown.

Component	ee	$\mu\mu$	Total
Fakes	0.0 ± 0	0.0 ± 0	0.0 ± 0
HWW	0.10 ± 0.05	0.016 ± 0.008	0.12 ± 0.05
Diboson	59 ± 2	54 ± 2	114 ± 2
Top	23 ± 2	23 ± 2	47 ± 3
$Z\ell\ell$	1330 ± 60	1310 ± 70	2640 ± 90
$Z\tau\tau$	4 ± 1	6 ± 1	10 ± 2
Total background	1410 ± 60	1400 ± 70	2810 ± 90
Signal	0.72 ± 0.07	0.54 ± 0.06	1.3 ± 0.1
Data	1370	1435	2805

Table 4.14: Event yields of the $Z\ell\ell$ control region for the inclusive Boosted category. The contribution of fakes is negligible and is not considered. The pre-fit normalization factors are applied. Only statistical uncertainties are shown.

Component	ee	$\mu\mu$	Total
Fakes	0.0 ± 0	0.0 ± 0	0.0 ± 0
HWW	0.009 ± 0.007	$(2 \pm 2) \times 10^{-6}$	0.009 ± 0.007
Diboson	3.6 ± 0.3	2.8 ± 0.3	6.3 ± 0.4
Top	5 ± 1	1.9 ± 0.6	6 ± 1
$Z\ell\ell$	130 ± 20	90 ± 10	220 ± 20
$Z\tau\tau$	0.3 ± 0.2	0.3 ± 0.2	0.6 ± 0.3
Total background	130 ± 20	100 ± 10	230 ± 20
Signal	0.18 ± 0.03	0.11 ± 0.01	0.30 ± 0.03
Data	103	129	232

Table 4.15: Event yields of the $Z\ell\ell$ control region for the inclusive VBF category. The contribution of fakes is negligible and is not considered. The pre-fit normalization factors are applied. Only statistical uncertainties are shown.

4.3.3 Pre-fit normalization factors

The pre-fit NFs are determined for the $Z\ell\ell$ and top-quark backgrounds. The selection criteria of each control region are described in Sections 4.3.1 and 4.3.2. However, in the $\tau_{\text{lep}}\tau_{\text{lep}}$ channel there is no $Z\tau\tau$ control region due to the contamination of the other backgrounds and the similarity to the Higgs boson decay, which do not allow the definition of a $Z\tau\tau$ CR with sufficient purity and low signal contamination. Instead, a validation region (VR) is defined to enhance the purity of the $Z\tau\tau$ background. This region uses the same requirements of the signal regions with the additional requirement $m_{\tau\tau}^{\text{MMC}} < 100\,\text{GeV}$. This region is used as $Z\tau\tau$ VR to determine the $Z\tau\tau$ pre-fit NFs.

Therefore three control regions and three normalization factors are defined. This provides a system of three equations with three unknown parameters that can be solved analytically as:

$$\begin{aligned}
&\text{NF}(Z\ell\ell) \cdot \#_{Z\ell\ell}^{\text{Top CR}} + \text{NF}(Z\tau\tau) \cdot \#_{Z\tau\tau}^{\text{Top CR}} + \text{NF}(\text{Top}) \cdot \#_{\text{Top}}^{\text{Top CR}} = \#_{\text{Data}}^{\text{Top CR}} - \#_{\text{other}}^{\text{Top CR}} \\
&\text{NF}(Z\ell\ell) \cdot \#_{Z\ell\ell}^{Z\ell\ell\text{CR}} + \text{NF}(Z\tau\tau) \cdot \#_{Z\tau\tau}^{Z\ell\ell\text{CR}} + \text{NF}(\text{Top}) \cdot \#_{\text{Top}}^{Z\ell\ell\text{CR}} = \#_{\text{Data}}^{Z\ell\ell\text{CR}} - \#_{\text{other}}^{Z\ell\ell\text{CR}} \\
&\text{NF}(Z\ell\ell) \cdot \#_{Z\ell\ell}^{Z\tau\tau\text{VR}} + \text{NF}(Z\tau\tau) \cdot \#_{Z\tau\tau}^{Z\tau\tau\text{VR}} + \text{NF}(\text{Top}) \cdot \#_{\text{Top}}^{Z\tau\tau\text{VR}} = \#_{\text{Data}}^{Z\tau\tau\text{VR}} - \#_{\text{other}}^{Z\tau\tau\text{VR}}
\end{aligned} \tag{4.5}$$

where NF($Z\ell\ell$), NF($Z\tau\tau$) and NF(Top) are the normalization factors for the $Z\ell\ell$, $Z\tau\tau$ and top-quark backgrounds respectively and $\#^{\text{CR}}_{\text{background}}$ are the yields of the control region written in the super-index for the background process written in the sub-index.

The system of equations is solved using the Kramer method for the yields at preselection level as well as for the VBF and Boosted inclusive regions. Table 4.16 summarizes the results of the normalization factors. These values have been applied only for plotting purposes and they are left free floating in the statistical fit.

Selection	Background process		
	$Z\ell\ell$	Top	$Z\tau\tau$
preselection	1.18 ± 0.04	1.08 ± 0.02	1.10 ± 0.02
VBF	0.87 ± 0.11	1.26 ± 0.08	0.96 ± 0.11
Boosted	1.22 ± 0.04	1.07 ± 0.02	1.11 ± 0.03

Table 4.16: Normalization factors obtained from the corresponding control regions for the preselection, VBF and Boosted categories. Only statistical uncertainties are shown.

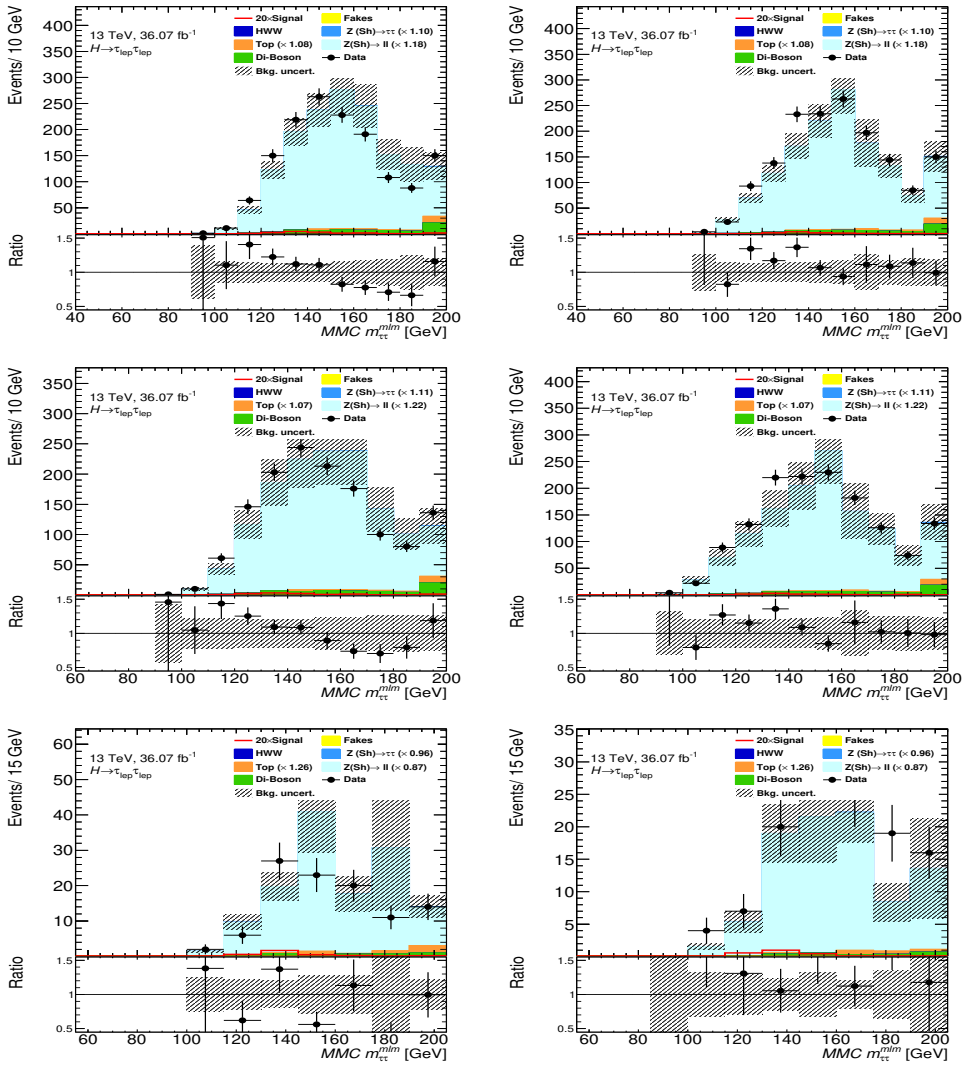

Figure 4.12: The $m_{\tau\tau}^{\text{MMC}}$ distributions of the $Z\ell\ell$ control region at the preselection level (top), Boost inclusive (middle) and VBF inclusive (bottom). The ee (left) and $\mu\mu$ (right) channels are shown. Error bands include the statistical and systematic uncertainties on the background normalization. The pre-fit normalization factors are applied.

4.4 Additional channels of the $H \to \tau\tau$ analysis

As mentioned in Section 2.3.5 two kinds of decay modes are possible for the τ-lepton, τ_{lep} and τ_{had}, allowing the addition of two other channels to the analysis, $\tau_{\text{lep}}\tau_{\text{had}}$ and $\tau_{\text{had}}\tau_{\text{had}}$ channels. A short description will be given in this section.

4.4.1 The $\tau_{\text{lep}}\tau_{\text{had}}$ channel

The $H \to \tau_{\text{lep}}\tau_{\text{had}}$ channel profits from the characteristic signature of an energetic light lepton in addition to the higher probability of a τ_{had} decay.

Like for the $\tau_{\text{lep}}\tau_{\text{lep}}$ channel, a preselection and two signal regions (Boosted and VBF category) are defined. Furthermore, events entering the signal regions are divided in two different subcategories: Tight and Loose. The selection criteria of each category are harmonized with the rest of channels and the same variables are used if no large decrease of significance is observed. Table 4.17 shows the selection criteria for the validation and signal regions. The $m_{\tau\tau}^{\text{MMC}}$ distributions of the VBF and Boosted categories are shown in Figure 4.13.

The SM backgrounds are similar to the $\tau_{\text{lep}}\tau_{\text{lep}}$ channel, however the estimation of the jet faking taus is different. The jet faking lepton background is estimated using MC simulation and it is found to be small.

The $\tau_{\text{lep}}\tau_{\text{had}}$ uses the so-called fake-factor method. The fake-factor method consists of defining an "anti-τ" region where the tau candidate passes all analysis criteria except that the $\tau_{\text{had-vis}}$ must fail the Medium identification requirement. This allows the construction, for each signal region, of an "anti-τ" control region. The estimate of the fakes background in each signal region can be determined by using the data events in the corresponding "anti-τ" region and weight them with a transfer factor to correct the different selection efficiency between the nominal and "anti-τ" criteria. Additionally, events in the fakes region produced by processes yielding a true τ_{had} and a light lepton are subtracted using MC simulation. The fake-factors depend on the quark and gluon composition and therefore they are different for each source of background. The combined fakes factor, F, can be constructed as the sum of the combination fakes factors for each relevant process weighted by the expected contribution in each region,

R:

$$F = R_W F_W + R_Z F_Z + R_{\text{Top}} F_{\text{Top}} + R_{\text{multi-jet}} F_{\text{multi-jet}} \tag{4.6}$$

However, the $Z\ell\ell$ and top-quark background processes are not particularly relevant, their contributions are about $\sim 1-2\%$ after preselection, Boosted and VBF selection. Hence the expression 4.6 can be simplified as:

$$F = R_W F_W + R_{\text{multi-jet}} F_{\text{multi-jet}} \tag{4.7}$$

The fraction of multi-jet events in each region, $R_{\text{multi-jet}}$, is obtained from data as:

$$R_{\text{multi-jet}} = \frac{N^{\text{anti}-\tau \text{ region}}_{\text{multi-jet, data}}}{N^{\text{anti}-\tau}_{\text{Data}} - N^{\text{anti}-\tau}_{\text{MC, not}j\to\tau}} \tag{4.8}$$

where $N^{\text{anti}-\tau \text{ region}}_{\text{multi-jet, data}}$ is the total yield in a chosen region listed in Table 4.17, $N^{\text{anti}-\tau}_{\text{Data}}$ is the data yield and $N^{\text{anti}-\tau}_{\text{MC, not}j\to\tau}$ is the yield of the real τ-leptons of the other background in the "anti-τ" region. Then the fractional contribution from W+jets production is simply $R_W = 1 - R_{\text{multi-jet}}$. And the calculation of the fake-factor for the W and multi-jet backgrounds can be expressed as:

$$F_i = \frac{N^{\text{nomi CR}_i}_{\text{Data}} - N^{\text{nomi CR}_i}_{\text{MC, not } j\to\tau}}{N^{\text{anti-}\tau \text{ CR}_i}_{\text{Data}} - N^{\text{anti-}\tau \text{ CR}_i}_{\text{MC, not}j\to\tau}} \tag{4.9}$$

where i runs over all regions defined in Table 4.18 and the numerator is the data yields in the nominal region and the denominator is the data yields in the "anti-τ" region. MC event yields where the $\tau_{\text{had-vis}}$ is not originated from a jet are denoted as “MC, not $j \to \tau$”.

The control and validation regions are enriched with the corresponding background and their selection criteria are as close as possible to the nominal selection criteria. Table 4.18 lists the control and validation regions used in the $\tau_{\text{lep}}\tau_{\text{had}}$ channel.

	$\tau_{\text{lep}}\tau_{\text{had}}$	
	$e\tau_{\text{had}}$	$\mu\tau_{\text{had}}$
Preselection	# of $e/\mu = 1$, # of $\tau_{\text{had-vis}} = 1$ e/μ : p_{T} cut 21 GeV to 27.3 GeV, e/μ : Medium, gradient iso. $\tau_{\text{had-vis}}$: $p_{\text{T}} > 30$ GeV, Medium 1-prong $\tau_{\text{had-vis}}$: eleBDT e-veto Opposite charge $m_{\text{T}} < 70$ GeV # of b-jets $= 0$ leading jet $p_{\text{T}} > 40$ GeV $\Delta R_{\ell\tau_{\text{had-vis}}} < 2.5$, $\lvert\Delta\eta_{\ell\tau_{\text{had-vis}}}\rvert < 1.5$ $E_{\text{T}}^{\text{miss}} > 20$ GeV $0.1 < x_1 < 1.4$, $0.1 < x_2 < 1.2$	
VBF inclusive	sub-leading jet $p_{\text{T}} > 30$ GeV $m_{jj} > 400$ GeV, $\lvert\Delta\eta_{jj}\rvert > 3$ $\eta_{j_1} \times \eta_{j_2} < 0$ ℓ and $\tau_{\text{had-vis}}$ centrality between jets	
VBF signal regions	Tight : $p_{\text{T}}^{H} > 100$ GeV $m_{jj} > 500$ GeV Loose : otherwise	
Boosted inclusive	Fail VBF requirements $p_{\text{T}}^{T}H > 100$ GeV	
Boosted signal regions	Tight : $p_{\text{T}}^{H} > 140$ GeV $\Delta R_{\ell\tau_{\text{had-vis}}} < 1.5$ Loose : otherwise	

Table 4.17: Summary of the event selection for the $\tau_{\text{lep}}\tau_{\text{had}}$ channel. The signal regions defined in the table are divided into Loose and Tight subcategories to enhance the significance in the final fit.

Sample	Difference from the nominal selection criteria
Top CR	Invert b-veto and require $m_{\mathrm{T}} > 40\,\mathrm{GeV}$
W+jets VR	Invert m_{T} ($m_{\mathrm{T}} > 70\,\mathrm{GeV}$)
Z+jets VR	Two leptons (# of $e/\mu = 2$, # of $\tau_{\text{had-vis}} = 0$)
QCD VR	Inverted lepton isolation

Table 4.18: Definition of the control and validation regions for the $\tau_{\text{lep}}\tau_{\text{had}}$ channel. The criteria mentioned in the table are the only differences with respect to the preselection criteria, the other requirements do not change.

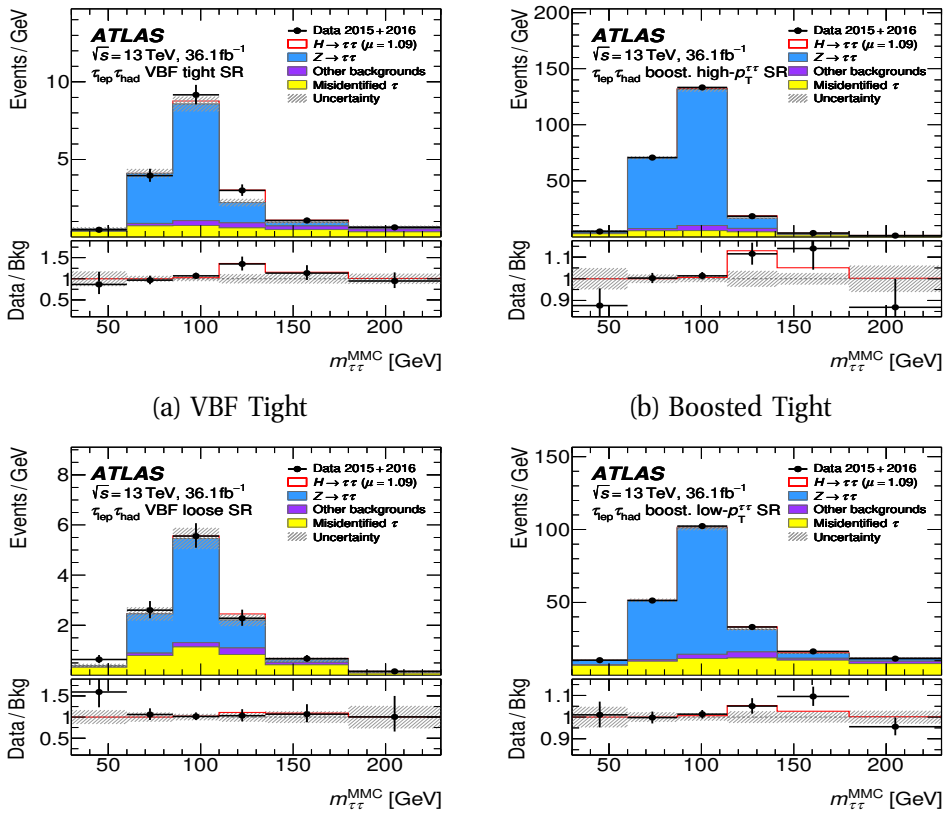

(a) VBF Tight (b) Boosted Tight

(c) VBF Loose (d) Boosted Loose

Figure 4.13: The $m_{\tau\tau}^{\text{MMC}}$ distributions for the $\tau_{\text{lep}}\tau_{\text{had}}$ channel for the Tight and Loose category of the VBF and Boosted selection criteria. The slashed bands include the statistical and systematic uncertainties. Reproduced from Ref. [117] under CC-BY-4.0 licence.

4.4.2 The $\tau_{\text{had}}\tau_{\text{had}}$ channel

The fully-hadronic channel, $\tau_{\text{had}}\tau_{\text{had}}$, aims at detecting events in which both taus decay hadronically. The hadronic decay mode of the τ-lepton is the most probable decay and therefore the $\tau_{\text{had}}\tau_{\text{had}}$ channel has the advantage of large statistics, similar to $\tau_{\text{lep}}\tau_{\text{had}}$. However, the main challenge is the discrimination of the hadronic τ-lepton decays from the multi-jet background faking a $\tau_{\text{had-vis}}$. The source of the multi-jet contribution is treated differently depending on the reconstructed $\tau_{\text{had-vis}}$ matching: events with at least one real tau, such as $W \to \tau\nu$+jets are referred as Other background; events where both tau candidates are jets misidentified as taus are referred as Fakes background. The estimation of the Fakes background is determined by using a data-driven technique, however the Other background is obtained using MC simulation and required to match at least one of the two tau candidates matching a τ_{had} in the truth record simulation. The systematic uncertainties involved in the Fakes background estimation are: the uncertainty on the reweighting procedure because when loosening the tau identification it limits the statistics in the control region severely and incurs a relatively large contamination of real tau events, the uncertainty on the SS region to the OS region extrapolation and the uncertainty on the MC subtraction of the real tau-lepton processes contamination.

In the $\tau_{\text{had}}\tau_{\text{had}}$ channel, a similar strategy is used compared to the other channels. The most significant difference with respect to the other two channels is that in the $\tau_{\text{had}}\tau_{\text{had}}$ channel a Tight identification of the τ candidates is required, since it helps reducing the Fakes background. Another difference is the veto of events which contain a light lepton. On the other hand, the low number of energetic neutrinos originated in the decay allows the $E_{\text{T}}^{\text{miss}}$ selection to be relaxed requiring only $E_{\text{T}}^{\text{miss}} > 20$ GeV.

The inclusive signal regions are later also divided into different subcategories. The $\tau_{\text{had}}\tau_{\text{had}}$ channel has one additional signal region compared with the other channels, the VBF high-p_{T} subcategory. The VBF high-p_{T} selection requires a high momentum of the Higgs boson candidate and therefore a short angular distance between the tau-leptons. The VBF Tight selection is defined for the events that have failed the VBF high-p_{T} selection but satisfy the $m_{jj} > (1550 - 250 \cdot |\Delta\eta_{jj}|)$ GeV requirement and the remaining events of the inclusive VBF selection enter in the VBF Loose category. The Boosted

subcategories have the same definitions as the other $H \to \tau\tau$ channels. Table 4.19 shows the summary of all requirements applied to the preselection, VBF inclusive and Boosted inclusive regions.

Figure 4.14 shows the $m_{\tau\tau}^{\text{MMC}}$ distributions of the different signal regions defined in the $\tau_{\text{had}}\tau_{\text{had}}$ channel. The error bands include the statistical and systematic uncertainties. The backgrounds that are negligible in the SRs are merged in the "Other backgrounds" contribution.

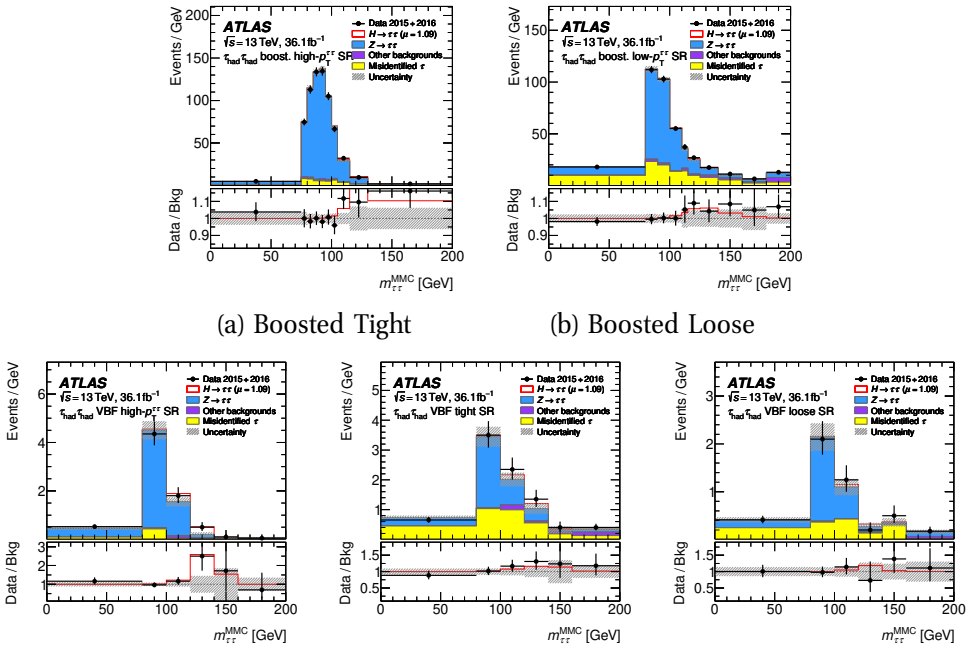

(a) Boosted Tight (b) Boosted Loose

(c) VBF High-p_{T} (d) VBF Tight (e) VBF Loose

Figure 4.14: The $m_{\tau\tau}^{\text{MMC}}$ distributions for the $\tau_{\text{had}}\tau_{\text{had}}$ channel for the Preselection and Tight and Loose subcategories of the Boosted selection and Tight, Boosted and High-p_{T} subcategories of the VBF selection. Statistical and systematic uncertainties are included in the error bands. Reproduced from Ref. [117] under CC-BY-4.0 licence.

	$\tau_{\text{had}}\tau_{\text{had}}$
Preselection	# of e/μ = 0, # of $\tau_{\text{had-vis}} = 2$ $\tau_{\text{had-vis}}$: $p_{\text{T}} > 40, 30\,\text{GeV}$, $\tau_{\text{had-vis}}$: Tight Opposite charge $E_{\text{T}}^{\text{miss}} > 20\,\text{GeV}$ leading jet $p_{\text{T}} > 70\,\text{GeV}$, $\lvert\eta\rvert < 3.2$ $0.8 < \Delta R_{\tau_{\text{had-vis}}\tau_{\text{had-vis}}} < 2.5$ $\lvert\Delta\eta_{\tau_{\text{had-vis}}\tau_{\text{had-vis}}}\rvert < 1.5$ $0.1 < x_1 < 1.4$, $0.1 < x_2 < 1.4$
VBF inclusive	sub-leading jet $p_{\text{T}} > 30\,\text{GeV}$ $m_{jj} > 400\,\text{GeV}$, $\lvert\Delta\eta_{jj}\rvert > 3$ $\eta_{j_1} \times \eta_{j_2} < 0$ ℓ and $\tau_{\text{had-vis}}$ centrality between jets
VBF signal regions	high-p_{T} : $p_{\text{T}}^{H} > 140\,\text{GeV}$ $\Delta R_{\tau_{\text{had-vis}}\tau_{\text{had-vis}}} < 1.5$ Tight : not high-p_{T} $m_{jj} > (1550 - 250 \cdot \lvert\Delta\eta_{jj}\rvert)\,\text{GeV}$ Loose : otherwise
Boosted inclusive	Fail VBF selection criteria $p_{\text{T}}^{T} H > 100\,\text{GeV}$
Boosted signal regions	Tight : $p_{\text{T}}^{H} > 140\,\text{GeV}$ $\Delta R_{\tau_{\text{had-vis}}\tau_{\text{had-vis}}} < 1.5$ Loose : otherwise

Table 4.19: Summary of the event selection for the $\tau_{\text{had}}\tau_{\text{had}}$ subchannel. The signal regions defined in the table are divided into the Loose, Tight and High-p_{T} subcategories to enhance the significance in the final fit.

4.5 Systematic uncertainties

A careful study of the uncertainties affecting the analysis is needed to obtain precise and correct results. Different sources of systematic uncertainties from both theoretical predictions and experimental sources can affect the shape and the yields of the categories used in the analysis. In addition, specific uncertainties related to the background modelling are also considered.

4.5.1 Theoretical uncertainties

The theoretical uncertainties are estimated for the signal and background processes, except for the Fakes background, which is obtained from data.

Theoretical uncertainties for the Higgs boson production modes are arising from three main sources: QCD scale uncertainty due to the missing higher orders in the perturbative theory; the non-perturbative part of the calculation such as underlying event and hadronisation; and finally uncertainties of the parton distribution functions and on the value of the strong coupling constant. The total cross-section uncertainties are provided by the LHC Higgs Cross-Section Working Group (LHCXSWG) [125] and Table 4.20 shows the respective QCD, PDFs and strong coupling uncertainties for each signal production.

Production process	+ QCD scale	- QCD scale	PDF	α_s
ggF	$+3.9\%$	-3.9%	$\pm 1.8\%$	$\pm 2.5\%$
VBF	$+0.4\%$	-0.3%	$\pm 2.1\%$	$\pm 0.5\%$
WH	$+0.5\%$	-0.7%	$\pm 1.7\%$	$\pm 0.9\%$
ZH	$+3.8\%$	-3.1%	$\pm 1.3\%$	$\pm 0.9\%$
ttH	Not considered			

Table 4.20: Total cross-section uncertainties due to the missing high order in QCD scale variation, the PDFs and the strong coupling constant given by the LHCHXSWG for the main Higgs boson production modes.

The QCD scale uncertainties are evaluated by multiplying by a factor 2 and 0.5 the renormalisation and factorization scales around the central value. The impact of

these variations on the fit variable is generally small. However, for gluon-gluon fusion Higgs boson production the theoretical uncertainty could be underestimated due to the experimental selection criteria which impose a binning in the number of jets. This introduces large logarithmic contributions of the order of $\log(p_{\mathrm{T}}/m_{\mathrm{H}})$ which leads to large uncertainties. For this reason QCD scale uncertainties for the gluon-gluon fusion need a specific treatment and nine sources of uncertainties are then evaluated:

- Four scale variations:
  - $\Delta\mu$: Factorization and renormalisation scale variations.
  - $\Delta\phi$: Resummation scale variation.
  - $\Delta_{\mathrm{cut}}^{0/1}$ and $\Delta_{\mathrm{cut}}^{1/2}$[3] Jet bin migration
- Two VBF topology uncertainties:
  - Variation of the VBF phase space
  - Third jet veto
- Two Higgs p_{T}-shape uncertainties:
  - Higgs p_{T} $0 - 60/60 - \infty$ GeV
  - Higgs p_{T} $0 - 120/120 - \infty$ GeV
- Top-quark mass dependence

The first four variations and the VBF topology uncertainties are established using the methods described in the so-called Yellow Report 3 [126] and Yellow Report 4 [75]. The Higgs boson p_{T} shape variations are taken from the QCD scale variations of the Powheg generator and the top mass dependence is derived using the differences from LO to NLO rescaling.

The parton shower uncertainties are evaluated comparing two algorithms, Pythia 8 and Herwig 7. The PDF uncertainties are evaluated using the most recent recommendations of the PDF4LHC collaboration group [85].

[3]The $\Delta_{\mathrm{cut}}^{0/1}$ and $\Delta_{\mathrm{cut}}^{1/2}$ is the yield bin variation of the events that have been moved from a bin "1" to the previous bin "0" and the following bin "2" because of the systematic variation.

A specific uncertainty treatment is considered for the $Z\tau\tau$ background. For this process, two normalization factors are defined controlling the overall normalization of $Z\tau\tau$ across channels in the VBF and Boosted signal regions, respectively. These normalization factors are left free-floating in the analysis fit. The systematic uncertainties are parametrized with the following strategy:

- A set of parameters (one for each inclusive SR and for each channel) to account for the effect of the variation on the discriminant variable as well as the event migration from a subcategory to another within the same inclusive region.
- Two parameters (one for each inclusive SR) will account for the fact that the definition of the inclusive regions are different across the three channels which can therefore be impacted differently by the given systematic uncertainty. It is evaluated as the impact of the variation on the relative normalization of each channel with respect to the total expectation regardless of the decay channel.

The following sources of uncertainty are considered:

- PDF: evaluated using event-weights provided for SHERPA generator.
- Renormalisation and factorisation scales - μ_R/μ_F: The μ_R varies the scale for the running strong coupling constant for the underlying hard process whereas the μ_F varies the scale used for the parton density functions. They are varied in a range of 0.5 and 2 times the nominal scale (Higgs boson scale), with the restriction of $0.5 < \mu_F/\mu_R < 2$.
- Matrix element matching scale (CKKW): the scale taken for the calculation for the overlap between jets from the matrix element and the parton shower. It is evaluated using truth-level parametrisation as a function of jet multiplicity and $p_T(Z)$. The nominal value for this parameter is 20 GeV and the variation are set to ± 5 GeV the nominal value.
- Resummation scale (QSF) : the scale used for the resummation of soft gluon emissions. It is evaluated using truth-level parametrisation as a function of jet multiplicity and p_T of the Z boson.

- Underlying-event: evaluated using samples with different setup of multiple-interactions, however this uncertainty is found to have a negligible effect.

- Parton shower: Estimated as the difference between MadGraph and SHERPA MC generators for the $Z\ell\ell$ process to enhance the available MC statistics. This is validated by comparing the results obtained with $Z\tau\tau$ MC samples for the Boosted category.

For the $Z\ell\ell$ process, which is a sizeable background in the $\tau_{\text{lep}}\tau_{\text{lep}}$ channel, two control regions are used in the fit for the Boosted and VBF signal regions. The same systematic sources used for the $Z\tau\tau$ are considered but they are found to be significantly smaller than the statistical uncertainties on the MC predictions and are therefore neglected.

The $\tau_{\text{lep}}\tau_{\text{lep}}$ and $\tau_{\text{lep}}\tau_{\text{had}}$ channels use dedicated control regions for the normalization of the top-quark background. There are four top-quark CRs in total, one for each Boosted and VBF category of the two channels. Four free-floating normalization factors are used in the fit for the top-quark process. One for each inclusive category of the $\tau_{\text{lep}}\tau_{\text{lep}}$ and $\tau_{\text{lep}}\tau_{\text{had}}$ channels.

4.5.2 Experimental uncertainties

The experimental uncertainties are estimated by the recommendations provided by the combined performance groups. In general, all nuisance parameters are varied within $\pm 1\sigma$ of the given uncertainties and they are used in the fit. The uncertainties considered in the analysis for the different experimental sources are listed below.

- Muon uncertainties

  The muon uncertainties are estimated using the techniques described in Ref. [65], and they take into account the variations in the ID of the muons, the scale variation of their momentum, the efficiency in the triggers, the efficiency in the identification as well as the efficiency in the track to vertex association.

- Electron uncertainties

The electron uncertainties [62] are related to: the variation of the ID, the variation in the energy scale, due to the high voltage or the calibration of the LAr calorimeter, and finally the efficiency of the triggers, the efficiency of the isolation and the efficiency of the reconstruction methods.

- Tau uncertainties

  Tau uncertainties are listed for completeness, because they are not considered in the $\tau_{\text{lep}}\tau_{\text{lep}}$ channel, but they are in the $\tau_{\text{lep}}\tau_{\text{had}}$ and $\tau_{\text{had}}\tau_{\text{had}}$. The uncertainties are related to the scale variation of the energy scale due to the modelling of the detector geometry, the measurement in the tag-and-probe analysis and the Geant4 models. The efficiencies in the identification, in the reconstruction, in the electron overlap removal and in triggers are considered.

- Jet uncertainties

  The jet energy uncertainties depend on the transverse momenta as well as the pseudorapidity of the reconstructed jet. They are determined by comparing data taken in 2015 and 2016 with Monte Carlo simulations [127].

  The uncertainties are summarised in eleven independent components for the jet energy resolution and twenty-one components for the jet energy scale which takes into account the models, the flavour composition and the flavour responses. The efficiency uncertainty for the jet vertex tagger as well as the b-tagging in the extrapolation of the charm or light flavours are also considered.

- Missing transverse momentum uncertainties

  The uncertainty of the missing transverse momentum calculation uses track-soft-term[4] calculations from the total transverse momentum of the hard objects (electrons, muons, taus and jets) reconstructed in the event. It is estimated by comparing data taken in 2015 and 2016 with Monte Carlo simulations [127].

- Pileup reweighting

[4] A track-soft-term is a track within the inner detector that are not associated with high-p_{T} physics objects.

Since the Monte Carlo simulation was performed using a generalized profile for the distribution of the number of interactions per bunch crossing, the simulated events need to be reweighted to describe the observed pile-up profile in the 2015 and 2016 datasets. For the best agreement between data and MC simulation, a correction factor of $1/1.16$ needs to be applied to the simulated number of interactions per bunch crossing [128]. The 1σ uncertainty has been determined to be $1/(1.16 \pm 0.07)$, but the ATLAS recommendation is to use the more conservative estimation of $1/(1.16^{+0.07}_{-0.16})$ which is considered in this analysis. This value is chosen because it best accommodates the experimental number of reconstructed primary vertices in the event.

- Luminosity uncertainty

  The uncertainty on the combined 2015 and 2016 integrated luminosity is 2.1% [129]. It is derived from a preliminary calibration of the luminosity scale using x-y beam-separation scans performed in August 2015 and May 2016. This combined uncertainty assumes fully uncorrelated uncertainties between the years.

The impact on the $\sigma_{H\to\tau\tau}$ of different sources of systematic uncertainties are summarized in Table 4.21 ordered in decreasing order of impact on the cross-section measurement. The impact is evaluated with the methodology described in Section 4.6.1. The most relevant systematic uncertainties come from the theoretical prediction of the signal, the backgrounds statistics and from jet and $E_{\mathrm{T}}^{\mathrm{miss}}$ experimental uncertainties.

On the other hand, the Fakes background uncertainty explained in Appendix A.1.2 is also considered. The values obtained for the $\tau_{\mathrm{lep}}\tau_{\mathrm{lep}}$ channel of the systematic uncertainties are summarized in Table 4.22 for each inclusive category as well as for each p_{T} region of the subleading lepton.

4.6 Statistical analysis and results

A maximum-likelihood function as a product of Poisson and Gaussian probability terms [124] is used to determine the final results of the $H \to \tau\tau$ analysis:

Source of uncertainty	Impact $\Delta\sigma/\sigma_{H\to\tau\tau}$ [%]	
	Observed	Expected
Theoretical uncert. in signal	$+13.4/-8.7$	$+12.0/-7.8$
Background statistics	$+10.8/-9.9$	$+10.1/-9.7$
Jets and $E_{\mathrm{T}}^{\mathrm{miss}}$	$+11.2/-9.1$	$+10.4/-8.4$
Background normalization	$+6.3/-4.4$	$+6.3/-4.4$
Misidentified τ	$+4.5/-4.2$	$+3.4/-3.2$
Theoretical uncert. in background	$+4.6/-3.6$	$+5.0/-4.0$
Hadronic τ decays	$+4.4/-2.9$	$+5.5/-4.0$
Flavour tagging	$+3.4/-3.4$	$+3.0/-2.3$
Luminosity	$+3.3/-2.4$	$+3.1/-2.2$
Electrons and muons	$+1.2/-0.9$	$+1.1/-0.8$
Total systematic uncert.	$+23/-20$	$+22/-19$
Data statistical uncert.	±16	±15
Total	$+28/-25$	$+27/-24$

Table 4.21: Summary of different sources of uncertainty in decreasing order of their impact on $\sigma_{H\to\tau\tau}$. Their observed and expected fractional (%) impacts, both computed by the fit, are given, relative to the $\sigma_{H\to\tau\tau}$ value. Experimental uncertainties in reconstructed objects combine efficiency and energy/momentum scale and resolution uncertainties. Background statistics include the bin-by-bin statistical uncertainties in the simulated backgrounds as well as statistical uncertainties in misidentified τ backgrounds, which are estimated using data. Background normalization describes the combined impact of all background normalization uncertainties.

$$L(\mu, \alpha_p, \phi, \gamma_p) = \prod_{c\in\text{chan.}} \prod_{b\in\text{bins}} \mathrm{P}(n_{cb}|\nu_{cb}) \cdot \mathrm{G}(L|\lambda, \sigma_L) \cdot \prod_{p\in\text{S,NF}} f(\alpha_p, \gamma_p) \tag{4.10}$$

where μ is the parameter of interest, α_p are the parameters related to systematics uncertainties *S*, ϕ the parameters of the normalization factors *NF* determined directly from the fit, α the statistical uncertainties of the expected number of events in each histogram, the $\mathrm{P}(n_{cb}|\nu_{cb})$ is the Poisson probability of observing n_{cb} events in the bin b

Systematics uncertainties	VBF-inclusive category				Boosted-inclusive category			
SS Non-closure	p_{T} [GeV]	10 - 15	15 - 20	20 -	p_{T} (GeV)	10 - 15	15 - 20	20 -
	all	39%	65%		all	26%	44%	21%
Top fake fraction	p_{T} [GeV]	10 - 15	15 - 20	20 -	p_{T} (GeV)	10 - 15	15 - 20	20 -
	ee	—	20.0%		ee	—	20.2%	
	$\mu\mu$	9.6%			$\mu\mu$	11.1%		
	df	6.2%			df	6.1%		
Heavy flavour contents	p_{T} [GeV]	10 - 15	15 - 20	20 -	p_{T} (GeV)	10 - 15	15 - 20	20 -
	ee	—	45.0%	38.9%	ee	—	53.5%	52.9%
	$\mu\mu$	50.0%	50%	50%	$\mu\mu$	51.0%	51.4%	50.7%
	df	38.2%	30.5%	36.4%	df	62.7%	62.4%	59.7%
QCD closure	p_{T} [GeV]	10 - 15	15 - 20	20 -	p_{T} (GeV)	10 - 15	15 - 20	20 -
	df	7.3%	3.2%	4.3%	df	7.2%	4.7%	4.3%
W+jets closure	p_{T} [GeV]	10 - 15	15 - 20	20 -	p_{T} (GeV)	10 - 15	15 - 20	20 -
	all	5.4%			all	6.9%		

Table 4.22: Systematic uncertainties for fakes background estimation in the $H \to \tau_{\mathrm{lep}}\tau_{\mathrm{lep}}$ channel.

of the channel c given the expected number of events ν_{cb}:

$$\mathrm{P}(n|\nu) = \frac{\nu^n e^{-\nu}}{n!} \tag{4.11}$$

where the $\mathrm{G}(L|\lambda, \sigma_L)$ corresponds to the Gaussian probability of measuring the integrated luminosity L, given the true integrated luminosity λ and the measurement uncertainty σ_L:

$$\mathrm{G}(L|\lambda, \sigma_L) = \frac{1}{\sqrt{2\pi\sigma_L^2}} \exp\left[-\frac{(L-\lambda)^2}{2\sigma_L^2}\right] \tag{4.12}$$

and finally, the PDF $f(\alpha_p, \gamma_p)$ determines the constraint on the parameters α_p and γ_p.

Firstly, a single parameter is fitted to measure the total cross-section of the $H \to \tau\tau$ production processes. Then, a two-parameter cross-section fit is presented separating the ggF and the VBF productions. Finally, three one-parameter fits are performed to measure the individual phase spaces regarding the tau decay.

Whereas the 13 MMC mass distributions for the signal region categories are used to infer information in the parameters of interest, six one-bin control regions are used to

constrain the dominant backgrounds through their event yields. As figures of merit to quantify the results, two quantities are considered:

- The significance, Z, which quantifies the rejection of a certain hypothesis with respect to another. Here, two hypotheses are considered: the null hypothesis, H_0, which describes only the known SM background processes and it has to be tested against the alternative hypothesis, H_{a}, which includes the SM backgrounds as well as the signal processes. To quantify the level of agreement a p-value is defined. It gives information about the probability of obtaining test results at least as extreme as the results actually observed during the test, assuming that the null hypothesis is correct. The relation between the p-value and the significance, Z, is $Z = \Phi^{-1}(1-p)$ where Φ^{-1} is the cumulative distribution of a Gaussian. In particle physics, the rejection of the null hypothesis is set to $Z = 5$, which corresponds a p-value of 2.87×10^{-7}.

- The other parameter of interest is the signal strength μ which represents the signal normalization respect to the SM prediction:

$$\mu = \frac{\sigma_H \times \mathcal{BR}(H \to \tau\tau)}{\sigma_H^{\text{SM}} \times \mathcal{BR}^{\text{SM}}(H \to \tau\tau)} \tag{4.13}$$

  where σ_H (σ_H^{SM}) is the fitted (predicted) total cross-section of the considered Higgs boson production modes and $\mathcal{BR}(H \to \tau\tau)$ ($\mathcal{BR}^{\text{SM}}(H \to \tau\tau)$) is the fitted (predicted) $H \to \tau\tau$ branching fraction. The value $\mu = 0$ corresponds to the absence of signal whereas the value of $\mu = 1$ suggests a signal presence as predicted by the SM.

All systematic uncertainties are used in the fit as separate nuisance parameters of the model. However, in the fit model some samples have relatively small event yields and therefore their systematic variations are dominated by statistical fluctuations. This can cause fit instabilities produced by incorrect or anomalous variations. In order to suppress these fluctuations, pruning and smoothing criteria are applied. These criteria consist in symmetrizing the systematic variation with one-sided variation and pruning the variations where the bin-a-bin sum of the significance is smaller than 0.1. The significance is defined as $S_i = |u_i - d_i|/\sigma_i^{tot}$, with $u_i(d_i)$ the upwards (downwards)

systematic variation in bin i for a given sample, while σ_i^{tot} is the statistical uncertainty for the total estimation in bin i.

Additionally, in order to maximise the significance in the final fit a binning optimization strategy is applied in the mass range of 30 GeV $< m_{\text{MMC}}^{\tau\tau} <$ 230 GeV . The optimization has been performed with an Asimov fit, that is obtained replacing data in signal and control regions with the corresponding MC estimation. The three step procedure begins with a scanning to choose the first bin edge and recalculating the significance according to the new binning. The highest significance is chosen. Secondly, after fixing the first bin size, a scan to choose the last bin low edge starts. The value giving the maximum significance is selected. This allows the fit to have a good behaviour avoiding empty bins at the edges of the distributions. Finally, a scan starts to choose the best bin size for the rest of the MMC distributions and for each region the bin size giving the highest significance is chosen.

4.6.1 Data fit

Two fits have been performed for the $H \to \tau\tau$ cross-section measurement: an Asimov and an unblinded data fit. The Asimov fit, where the data are replaced by their signal plus background expectation values, provides the expected values according to the SM predictions whereas the unblinded data fit provides the observed measurement. The observed and expected significance as well as the signal strength computed from the likelihood fit are shown in Table 4.23. Additionally, Table 4.24 summarizes the observed significances per channel and per category for Run 1 and Run 2 data independently. The combined observed (expected) significance of $4.4(4.1)$ standard deviations is compatible with a SM Higgs boson with a mass $m_H = 125$ GeV. The channel uncertainties are correlated because normalization factor constraints across all of the SRs. Tables 4.25-4.27 summarize the expected signal and background yields computed by the fit in each signal region and in each channel for the $\sigma_{H\to\tau\tau}$ measurement. Additionally this result is combined with the result of the search for the $H \to \tau\tau$ decay using 7 and 8 TeV data [130]. The combined observed (expected) significance amounts to $6.4(5.4)\sigma$. The statistical and theory uncertainties on the main background are uncorrelated due to the different procedures to obtain the final results, especially the $Z\tau\tau$ background. However,

the theory and the experimental uncertainties on the signal as well as the other MC backgrounds are correlated. The effects of these correlations are completely negligible. Hence, in this combination, all nuisance parameters are treated as uncorrelated between Run 1 and Run 2.

	Fit type	Combined	Boosted	VBF
Exp. (Obs.) Significance	Asimov	$4.5(4.5)$	$2.9(2.9)$	$2.9(2.9)$
	Unblinded	$4.4(4.1)$	$3.2(2.8)$	$2.6(2.7)$
Signal strength	Asimov	$1.00^{+0.28}_{-0.25}$	$1.00^{+0.42}_{-0.36}$	$1.00^{+0.42}_{-0.37}$
	Unblinded	$1.09^{+0.32}_{-0.28}$	$1.14^{+0.47}_{-0.39}$	$0.98^{+0.47}_{-0.41}$

Table 4.23: Comparison of the significance and the signal strength for the Asimov and data fits. The results of the Boosted and VBF categories are presented independently and combined.

Period	VBF category			Boosted category		
	$\tau_{\text{lep}}\tau_{\text{lep}}$	$\tau_{\text{lep}}\tau_{\text{had}}$	$\tau_{\text{had}}\tau_{\text{had}}$	$\tau_{\text{lep}}\tau_{\text{lep}}$	$\tau_{\text{lep}}\tau_{\text{had}}$	$\tau_{\text{had}}\tau_{\text{had}}$
Run 1	1.88σ	2.23σ	2.23σ	1.72σ	1.01σ	2.56σ
Run 2	1.29σ	1.64σ	1.39σ	1.48σ	1.91σ	1.25σ
Combined	6.4σ					

Table 4.24: Run 1 and Run 2 significance for the data fit. The Boosted and VBF categories are presented independently for each channel. Additionally the combination of all channels and data periods is shown.

The background sources are constrained using the data by the statistical fit to obtain the post-fit normalization factors. Table 4.28 shows the post-fit NFs for the main background sources. Their uncertainties include the statistical and systematic errors.

Firstly, the parameter $\sigma_{H\to\tau\tau} \equiv \sigma_H \cdot \mathcal{BR}(H \to \tau\tau)$ is fitted, where σ_H is the total cross-section of the considered Higgs boson production processes and $\mathcal{BR}(H \to \tau\tau)$ is the $H \to \tau\tau$ branching fraction. For this measurement, the relative contributions from the various Higgs boson production processes are assumed to be as predicted

	$\tau_{\text{lep}}\tau_{\text{lep}}$			
	VBF SR		Boosted SR	
	Loose	Tight	Loose	Tight
Fakes	18 ± 9	9 ± 5	210 ± 90	80 ± 40
HWW	2.9 ± 0.4	5.5 ± 0.9	15 ± 3	19.3 ± 1.8
Diboson	12 ± 2	10.7 ± 1.5	194 ± 9	195 ± 9
Top	33 ± 6	25 ± 5	320 ± 50	190 ± 30
$Z\ell\ell$	15 ± 5	20 ± 7	360 ± 50	240 ± 30
$Z\tau\tau$	181 ± 13	107 ± 12	1980 ± 90	1690 ± 60
Total background	232 ± 13	178 ± 12	4080 ± 60	3410 ± 50
Total Signal	8 ± 2	13 ± 4	47 ± 12	48 ± 12
Data	237	188	4124	3444

Table 4.25: Observed event yields and predictions as computed by the fit in the $\tau_{\text{lep}}\tau_{\text{lep}}$ signal regions. Uncertainties include statistical and systematic components.

by the SM and the uncertainties related to the predicted total signal cross-section are excluded. The measured value of $\sigma_{H\to\tau\tau}$ is $3.77^{+0.60}_{-0.59}(\text{stat})^{+0.87}_{-0.74}(\text{syst})$ pb, consistent with the standard model prediction $\sigma_H^{\text{SM}} = 3.46 \pm 0.13$ pb [125]. The signal strength of the total cross-section is computed by a fit including all uncertainties in the predicted signal cross-section and is evaluated to be $1.09^{+0.18}_{-0.17}(\text{stat})^{+0.26}_{-0.22}(\text{syst})^{+0.11}_{-0.16}(\text{theory syst})$. The different signal strengths of each channel are shown in Table 4.23.

A summary of the dominant uncertainties of the total $H \to \tau\tau$ cross-section are listed in Table 4.21. Additionally, Figure 4.15 shows the systematic uncertainties with the largest impact. To compare the impact for each nuisance parameter, a separate fit is performed fixing the value to the one fitted in the unconstrained fit, and the resulting uncertainty on the cross-section is subtracted from the uncertainty obtained in the original fit via variance subtraction.

The majority of the dominant uncertainties are related to the limited statistics in the simulated samples, the QCD higher order correction in the signal process cross-section prediction, the jet energy resolution, the identification of τ_{had} and the normalization of the irreducible backgrounds, $Z\ell\ell$ and $Z\tau\tau$. Furthermore, Figure 4.15 shows that in most

	$\tau_{\text{lep}}\tau_{\text{had}}$			
	VBF SR		Boosted SR	
	Loose	Tight	Loose	Tight
Fakes	103 ± 16	101 ± 15	1900 ± 80	610 ± 30
Other background	4.0 ± 1.6	9.3 ± 1.9	115 ± 8	129 ± 9
Top	5.8 ± 1.6	18 ± 5	120 ± 20	57 ± 10
$Z\ell\ell$	10 ± 3	13 ± 3	130 ± 40	115 ± 16
$Z\tau\tau$	178 ± 18	320 ± 20	4190 ± 90	5350 ± 80
Total background	301 ± 17	460 ± 20	6450 ± 80	6250 ± 80
Total Signal	12 ± 3	32 ± 8	80 ± 20	90 ± 30
Data	318	496	6556	6347

Table 4.26: Observed event yields and predictions as computed by the fit in the $\tau_{\text{lep}}\tau_{\text{had}}$ signal regions. Uncertainties include statistical and systematic components.

of the cases the fitted impact parameters are in agreement with the pre-fit values. The pulls, referring to the bottom x-axis of the figure, are compatible with 0 within 1σ.

Moreover, the results of the fit when only the data of an individual channel or of an individual category are used and in Figure 4.16.

The $m_{\tau\tau}^{\text{MMC}}$ distributions for the combined signal regions of $\tau_{\text{had}}\tau_{\text{had}}$, $\tau_{\text{lep}}\tau_{\text{had}}$ and $\tau_{\text{lep}}\tau_{\text{lep}}$ analysis channels with background predictions adjusted by the likelihood fit are shown in Figures 4.17(a-c) and separately Figures 4.17(d-e) show the combined VBF and Boosted signal regions. Finally the MMC distribution of the combination of all signal regions as well as all channels are shown in Figure 4.18.

Figure 4.16 (bottom) illustrates that the VBF and Boosted category provides a good sensitivity to the VBF and ggF Higgs boson production modes, respectively. A two-parameter fit is therefore performed to determine the cross-sections of these production processes by exploiting the sensitivity offered by the categories of the channels. Two cross-section parameters $\sigma_{H\to\tau\tau}^{\text{VBF}}$ and $\sigma_{H\to\tau\tau}^{\text{ggF}}$ are introduced and the data are fitted to those parameters. The other contributions of the Higgs boson production processes are set to their SM prediction values. The best fit values of $\sigma_{H\to\tau\tau}^{\text{VBF}} = 0.25 \pm 0.09(\text{stat})^{+0.11}_{-0.9}(\text{syst})$ pb and $\sigma_{H\to\tau\tau}^{\text{ggF}} = 3.1 \pm 1.0(\text{stat})^{+1.6}_{-1.3}(\text{syst})$ pb are

	$\tau_{\text{had}}\tau_{\text{had}}$				
	VBF SR			Boosted SR	
	Loose	Tight	High-p_{T}	Loose	Tight
Fakes	45 ± 5	96 ± 9	20 ± 3	1870 ± 140	360 ± 50
Other background	4.4 ± 1.4	11.6 ± 1.7	4.4 ± 0.7	280 ± 20	110 ± 9
$Z\tau\tau$	67 ± 9	100 ± 12	141 ± 12	3250 ± 130	3580 ± 80
Total background	117 ± 9	208 ± 12	165 ± 12	5400 ± 80	4060 ± 60
Total Signal	2.6 ± 0.8	9 ± 2	15 ± 4	57 ± 15	68 ± 18
Data	121	220	179	5455	4103

Table 4.27: Observed event yields and predictions as computed by the fit in the $\tau_{\text{had}}\tau_{\text{had}}$ signal regions. Uncertainties include statistical and systematic components.

in agreement with the standard model predicted values $\sigma^{\text{SM, VBF}}_{H\to\tau\tau} = 0.237 \pm 0.006$ pb and $\sigma^{\text{SM, ggF}}_{H\to\tau\tau} = 3.1 \pm 1.0$ pb. The two results are anti-correlated as shown in Figure 4.19.

Background	Channel	Normalization factors	
		VBF	Boosted
$Z \to \ell\ell$ (CR)	$\tau_{\text{lep}}\tau_{\text{lep}}$	$0.88^{+0.34}_{-0.30}$	$1.27^{+0.30}_{-0.25}$
Top (CR)	$\tau_{\text{lep}}\tau_{\text{lep}}$	1.19 ± 0.09	1.07 ± 0.05
Top (CR)	$\tau_{\text{lep}}\tau_{\text{had}}$	$1.53^{+0.30}_{-0.27}$	1.13 ± 0.07
Fake-$\tau_{\text{had-vis}}$ (data-driven)	$\tau_{\text{had}}\tau_{\text{had}}$	1.12 ± 0.12	
$Z \to \tau\tau$ (fit in each SR)	all	$1.04^{+0.10}_{-0.09}$	1.11 ± 0.05

Table 4.28: Normalization factors for backgrounds that have their normalization constrained using data in the fit, including all statistical and systematic uncertainties, but without uncertainties in total simulated cross-sections extrapolated to the selected phase space. Systematic uncertainties are the dominant contribution to the normalization factor uncertainties. Also shown are the analysis channels to which the normalization factors are applied.

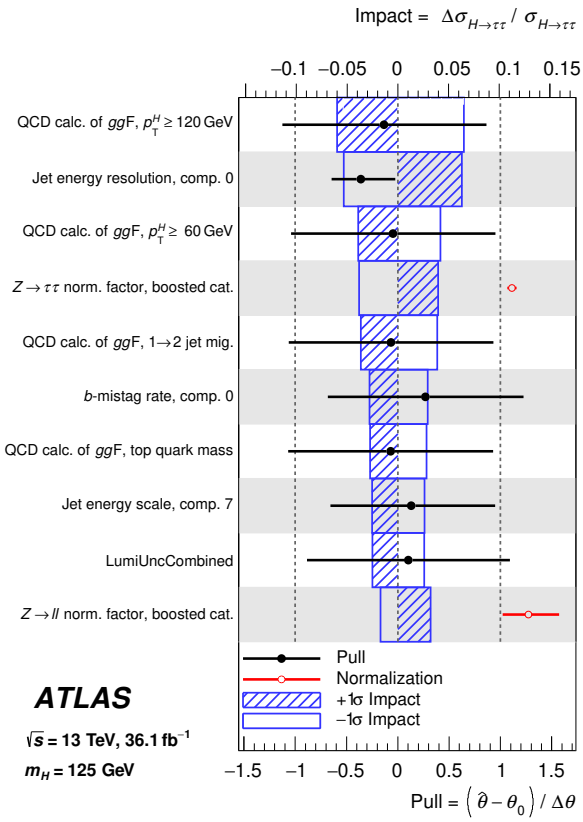

Figure 4.15: Fractional impact of systematic uncertainties in $\sigma_{H\to\tau\tau}$ as computed by the fit. The systematic uncertainties are listed in decreasing order of their impact on $\sigma_{H\to\tau\tau}$ on the y-axis. The hatched blue and open blue boxes show the variations of $\sigma_{H\to\tau\tau}$ referring to the top x-axis (impact). The filled circles, referring to the bottom x-axis, show the pulls of the fitted nuisance parameters, i.e. the deviations of the fitted parameters $\hat{\theta}$ from their nominal values θ_0, normalized to their nominal uncertainties $\Delta\theta$. The black lines show the uncertainties of the nuisance parameters resulting from the fit. Several sources of uncertainties such as the jet energy scale and resolution as well as the b-mistag rate are described by their principal components in the fit. The open circles, also referring to the bottom x-axis, show the values of the fitted $Z \to \tau\tau$ and $Z \to \ell\ell$ normalization factors in the boosted category. Their uncertainties do not include uncertainties in total simulated cross-sections extrapolated to the selected phase space. Reproduced from Ref. [117] under CC-BY-4.0 licence.

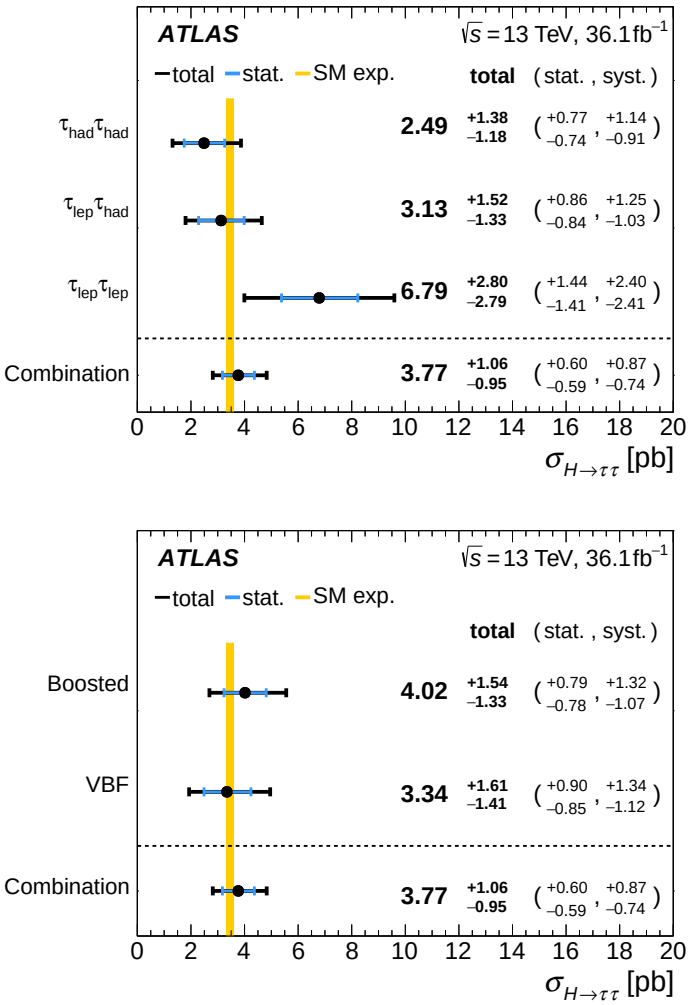

Figure 4.16: The measured values for $\sigma_{H\to\tau\tau}$ when only the data of individual channels (top) or individual categories (bottom) are used. Also shown is the result from the combined fit. The total $\pm 1\sigma$ uncertainty in the measurement is indicated by the black error bars, with the individual contribution from the statistical uncertainty in blue. The theory uncertainty in the predicted signal cross-section is shown by the yellow band. Reproduced from Ref. [117] under CC-BY-4.0 licence.

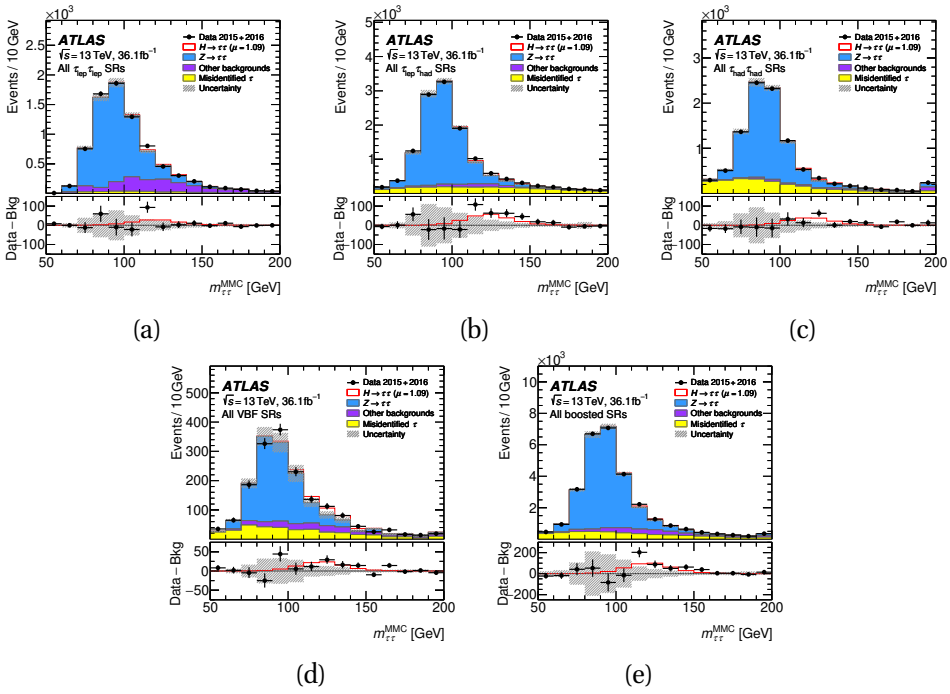

Figure 4.17: Distributions of the reconstructed di-τ invariant mass ($m_{\tau\tau}^{\mathrm{MMC}}$) for the sum of (a) all $\tau_{\mathrm{lep}}\tau_{\mathrm{lep}}$, (b) all $\tau_{\mathrm{lep}}\tau_{\mathrm{had}}$ and (c) all $\tau_{\mathrm{had}}\tau_{\mathrm{had}}$ (d) all VBF and (e) all boosted signal regions. The bottom panels show the differences between observed data events and expected background events (black points). The observed Higgs-boson signal ($\mu = 1.09$) is shown with the solid red line. Entries with values that would exceed the x-axis range are shown in the last bin of each distribution. The signal and background predictions are determined in the likelihood fit. The size of the combined statistical, experimental and theoretical uncertainties in the background is indicated by the hatched bands. Reproduced from Ref. [117] under CC-BY-4.0 licence.

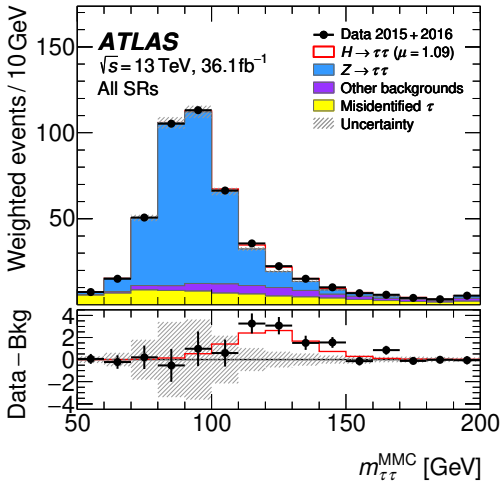

Figure 4.18: Distribution of the reconstructed di-τ invariant mass ($m_{\tau\tau}^{\text{MMC}}$) for the sum of all signal regions. The contributions of the different SRs are weighted by a factor of $\ln(1 + S/B)$, where S and B are the expected numbers of signal and background events in that region, respectively. The size of the combined statistical, experimental and theoretical uncertainties in the background is indicated by the hatched bands. Reproduced from Ref. [117] under CC-BY-4.0 licence.

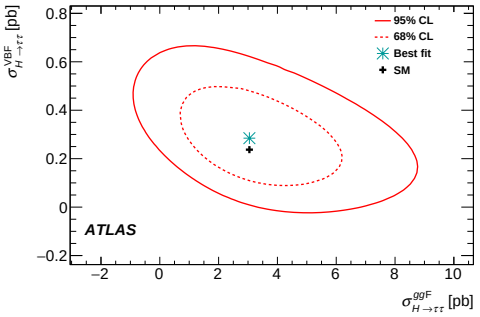

Figure 4.19: Likelihood contours for the combination of all channels in the ($\sigma_{H\to\tau\tau}^{VBF}$, $\sigma_{H\to\tau\tau}^{ggF}$) plane. The 68% and 95% CL contours are shown as dashed and solid lines, respectively, for $m_H = 125\,\text{GeV}$. The SM expectation is indicated by a plus symbol and the best fit to the data is shown as a star. Reproduced from Ref. [117] under CC-BY-4.0 licence.

5.- Search for Lepton Flavour Violation in the Higgs sector

This chapter describes the search for lepton flavour violation in the Higgs sector. The analysis is performed by looking for the decay of the Higgs boson into the final states $H \to \tau\ell$. The search is done using the data collected by the ATLAS experiment during the years 2015 and 2016 of the LHC Run 2 period corresponding to an integrated luminosity of 36.1 fb^{-1}.

This analysis searches for two decays of the Higgs boson: $H \to \mu\tau$ and $H \to e\tau$ and therefore it is sensitive to two off-diagonal terms of the Yukawa matrix, $Y_{\mu\tau}$ and $Y_{e\tau}$.

Previous ATLAS searches [131, 132] placed upper limits of $1.04\%(1.43\%)$ on the $H \to e\tau(H \to \mu\tau)$ branching ratio with a 95% confidence level (CL) using Run 1 data, corresponding to an integrated luminosity of 20.3 fb^{-1}. The CMS Collaboration recently provided 95% CL upper limits on the $H \to e\tau(H \to \mu\tau)$ branching ratio of $0.61\%(0.25\%)$, using an integrated luminosity of 35.9 fb^{-1} taken during the Run 2 [133]. The work of this thesis is incorporated in the ATLAS paper of reference [134] published in November 2019.

5.1 Introduction

One of the main goals of the LHC programme at CERN is the search for processes beyond the SM. Modifications of the Yukawa coupling to leptons can give rise to processes where the lepton flavour is violated, such as $H \to \tau\ell$, as shown in Figure 5.1.

Due to neutrino oscillations, these decays are possible, but in the absence of beyond the SM, their branching ratios are much smaller than the sensitivity of the LHC experiments.

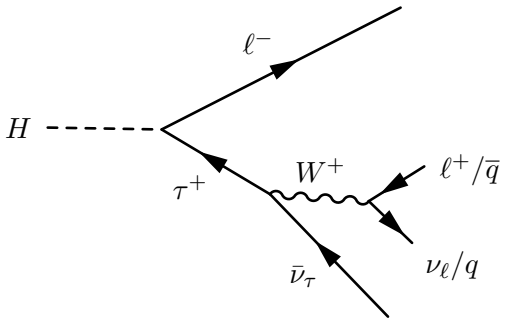

Figure 5.1: Feynman diagram for a possible decay of the Higgs boson $H \to \tau\ell$, if the Yukawa coupling $Y_{e\tau}$ or $Y_{\mu\tau}$ are not zero.

The existence of LFV decays of the Higgs boson with a branching fraction lower than 1% would not change significantly the Higgs boson production processes. Hence, similarly to the $H \to \tau\tau$ cross-section measurement, the LFV search exploits two signal regions to tag the most probable processes of the Higgs boson production at the LHC: the ggF and VBF productions. The signal regions are defined by common preselection criteria, which select the kinematics of the LFV decays. This selection is also used to study the agreement between data and MC predictions. Most of the selection criteria are inspired by the Run 1 publication [132], although for Run 2 those criteria have been optimized to achieve the highest significance.

5.2 Event selection and categorization

In this section the requirements used to achieve a good signal over background ratio for the $H \to \ell\tau_{\ell'}$ channel are described. Three different selections are used: the baseline preselection, and the VBF and non-VBF selections. Figure 5.2 shows the schematic of the signal and control regions used in the analysis.

All SM backgrounds described in section 3.3 are considered in this search. The most relevant backgrounds are the top-quark and the $Z \to \tau\tau$ processes and two control

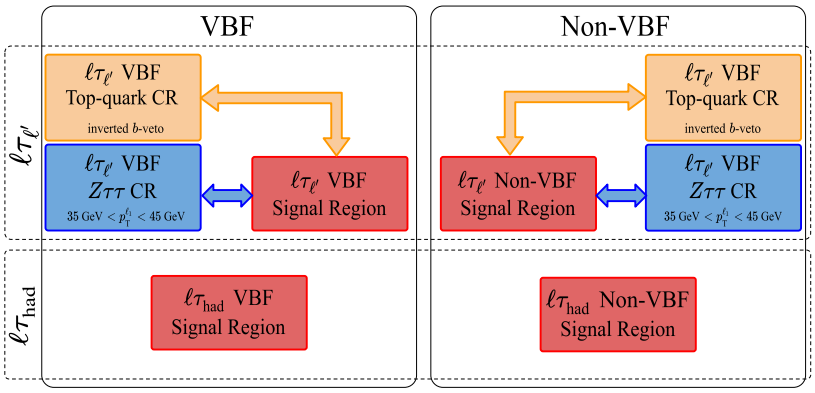

Figure 5.2: Schematic view of the signal and control regions that are used in the fit and their associations to analysis channels and categories. Arrows indicate how the background normalizations are correlated in the fit.

regions are defined to constrain them. On the other hand, the $Z \to \ell\ell$ process is, in this case, mostly negligible due to the selection requirement of different flavour leptons. In addition, the fakes transfer factors obtained from the fakes estimation (see section A.1) are shown in the subsection 5.2.4.

5.2.1 The $\ell\tau_{\ell'}$ selection criteria

For an event to be selected in the $\ell\tau_{\ell'}$ channel it must contain exactly two opposite-sign leptons of different flavour. In addition, these two leptons must be an electron and a muon[1], where the lepton with higher p_{T} is indicated as leading lepton, ℓ_1, and the other as subleading lepton, ℓ_2. Because of the topology of the LFV decay, the prompt lepton carries on average a bigger portion of the Higgs boson energy than the lepton originated from the τ decay. Hence, the leading lepton momentum must be $p_{\mathrm{T}}^{\ell_1} > 45\,\mathrm{GeV}$ whereas the subleading lepton momenta has to satisfy $p_{\mathrm{T}}^{\ell_2} > 15\,\mathrm{GeV}$. The requirement of the subleading lepton p_{T} is the lowest common trigger threshold

[1]The $\tau_{\ell'}$ object candidates are constructed and identified by the algorithms used for electron and muon objects.

between 2015 and 2016 datasets. The trigger thresholds are shown in Table 4.1 as well as in Figure 4.3.

The asymmetry in the lepton momentum criteria allows to discriminate and reduce the presence of the $Z \to \tau\tau$ background, the $H \to \tau\tau$ contribution and the eventual presence of $H \to \tau\mu(H \to \tau e)$ events in the $H \to \tau e(H \to \tau\mu)$ final state. Finally, the events are required to have no b-jets and a visible mass of the two light leptons between, $30\,\text{GeV} < m_{\ell\ell} < 150\,\text{GeV}$ to reduce the top-quark backgrounds.

In the $\mu\tau_e$ channel there is a sizeable background contribution from the $Z \to \mu\mu$ decay due to one of the muons being misidentified as an electron, when if it deposits a significant energy in the EM calorimeter. To reduce this source of background, a restriction on the ratio between the electron ID track momentum and the electron cluster transverse energy is applied, $p_{\text{T}}^{\text{track}}(\ell_2)/p_{\text{T}}^{\text{cluster}}(\ell_2) < 1.2$. Figure 5.3 shows the distribution of this ratio before applying the criteria to reduce the $Z \to \mu\mu$ background (light blue histogram) and it shows how this background with a misidentified muon concentrates in the right part of the distribution.

	$\ell\tau_{\ell'}$	
	$e\tau_\mu$	$\mu\tau_e$
Baseline	$p_{\text{T}}(e) > p_{\text{T}}(\mu)$	$p_{\text{T}}(\mu) > p_{\text{T}}(e)$
	$p_{\text{T}}^{\ell_1} > 45\,\text{GeV}$	
	$p_{\text{T}}^{\ell_2} > 15\,\text{GeV}$	
	$30\,\text{GeV} < m_{\ell\ell} < 150\,\text{GeV}$	
	# of b-jets $= 0$	
	$p_{\text{T}}^{\text{track}}(\ell_2)/p_{\text{T}}^{\text{cluster}}(\ell_2) < 1.2$	

Table 5.1: Summary of the baseline event selection for the $\ell\tau_{\ell'}$ final states.

All selection criteria mentioned above are summarized in Table 5.1 for the two different channels, $e\tau_\mu$ and $\mu\tau_e$. Figures 5.4 and 5.5 show the most relevant kinematic distributions for the baseline selection of each one of the two independent $\ell\tau_{\ell'}$ analyses.

For the LFV search, the missing mass calculator is adapted to the LFV decay [123], because of the difference in the final number of neutrinos and τ-leptons with respect

to the di-τ final states. The MMC distributions are shown in Figure 5.6 for $e\tau_\mu$ and $\mu\tau_e$ channels and the respective yields are reported in Table 5.2 where the LFV pre-fit NFs are applied as derived from the $Z\tau\tau$ and top-quark control regions (see section 5.4.3).

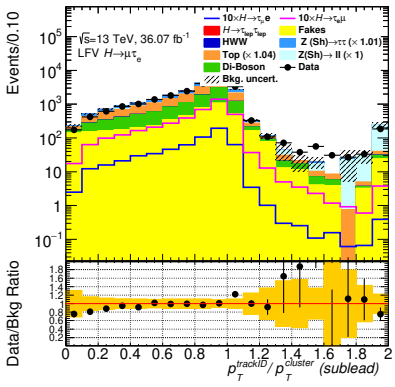

Figure 5.3: Distributions for the ratio between the electron ID track p_{T} and the electron cluster transverse energy. The baseline selection criteria, shown in Table 5.1, are applied except the $p_{\mathrm{T}}^{\mathrm{track}}(\ell_2)/p_{\mathrm{T}}^{\mathrm{cluster}}(\ell_2) < 1.2$ requirement. Error bands include the statistical uncertainties and the systematic uncertainties on the background normalization.

Sample	Baseline selection	
	$\mu\tau_e$	$e\tau_\mu$
$H \to \tau\tau$	99.6 ± 0.8	131.7 ± 0.9
$H \to WW$	178 ± 3	227 ± 3
$Z \to \tau\tau$+jets	4990 ± 40	6330 ± 50
$Z \to ee\,, \mu\mu$+jets	210 ± 60	280 ± 50
$t\bar{t}$	8210 ± 40	10450 ± 40
Diboson	6070 ± 30	7650 ± 30
Fakes	4470 ± 50	4400 ± 60
Total background	24230 ± 100	29475 ± 110
$H \to \mu\tau_e$ signal	397.9 ± 1.9	71.0 ± 0.7
$H \to e\tau_\mu$ signal	59.3 ± 0.6	523 ± 2
Data	23840	30250

Table 5.2: Yields of the $\mu\tau_e$ and $e\tau_\mu$ channels for the baseline selection. $\mathcal{BR}(H \to \mu\tau_e)$ and $\mathcal{BR}(H \to e\tau_\mu)$ are assumed to be 1%. Only statistical uncertainties are shown.

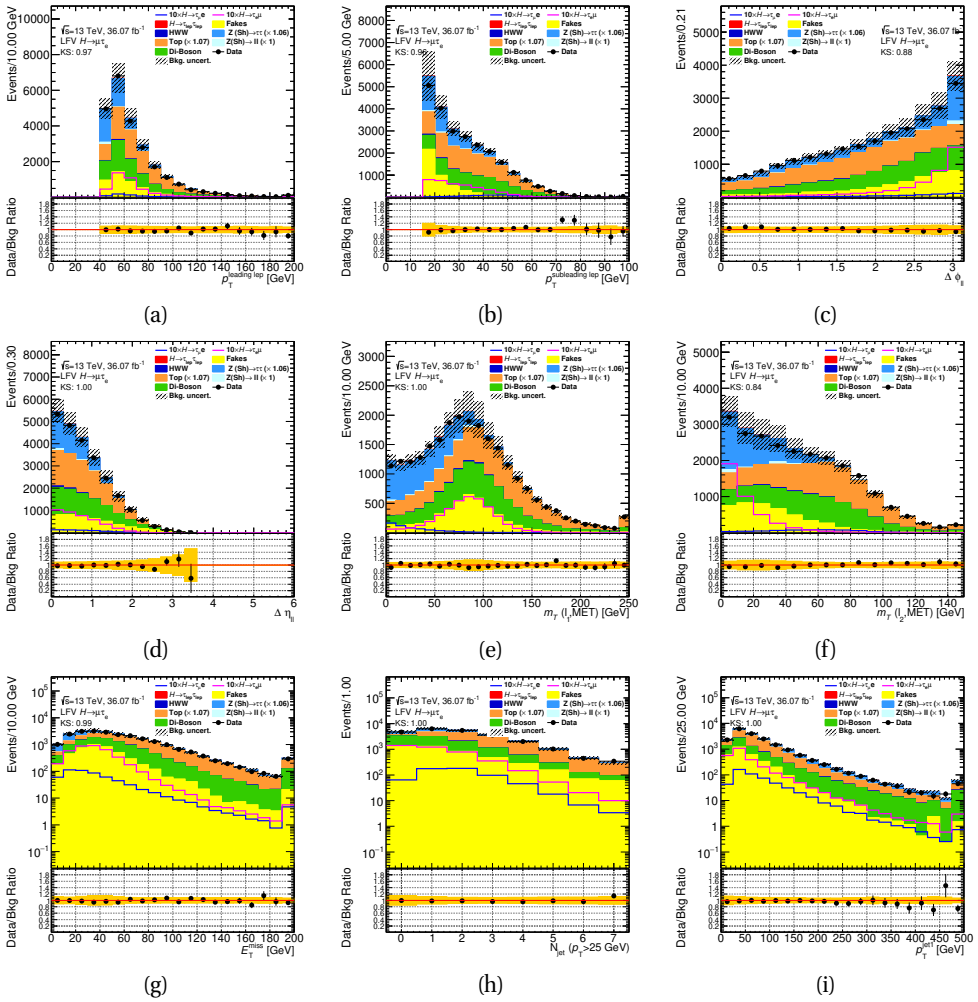

Figure 5.4: Kinematic distributions for the $\mu\tau_e$ final state for events passing the baseline selection. Shown are the distributions of $p_{\mathrm{T}}^{\ell_1}$ (a), $p_{\mathrm{T}}^{\ell_2}$ (b), $\Delta\phi_{\ell\ell}$ (c), $\Delta\eta_{\ell\ell}$ (d), $m_{\mathrm{T}}(\ell_1, E_{\mathrm{T}}^{\mathrm{miss}})$ (e), $m_{\mathrm{T}}(\ell_2, E_{\mathrm{T}}^{\mathrm{miss}})$ (f), $E_{\mathrm{T}}^{\mathrm{miss}}$ (g), $\mathrm{N_{jets}}$ (h) and $p_{\mathrm{T}}^{j_1}$ (i). Error bands include the statistical uncertainties and the systematic uncertainties on the background normalization.

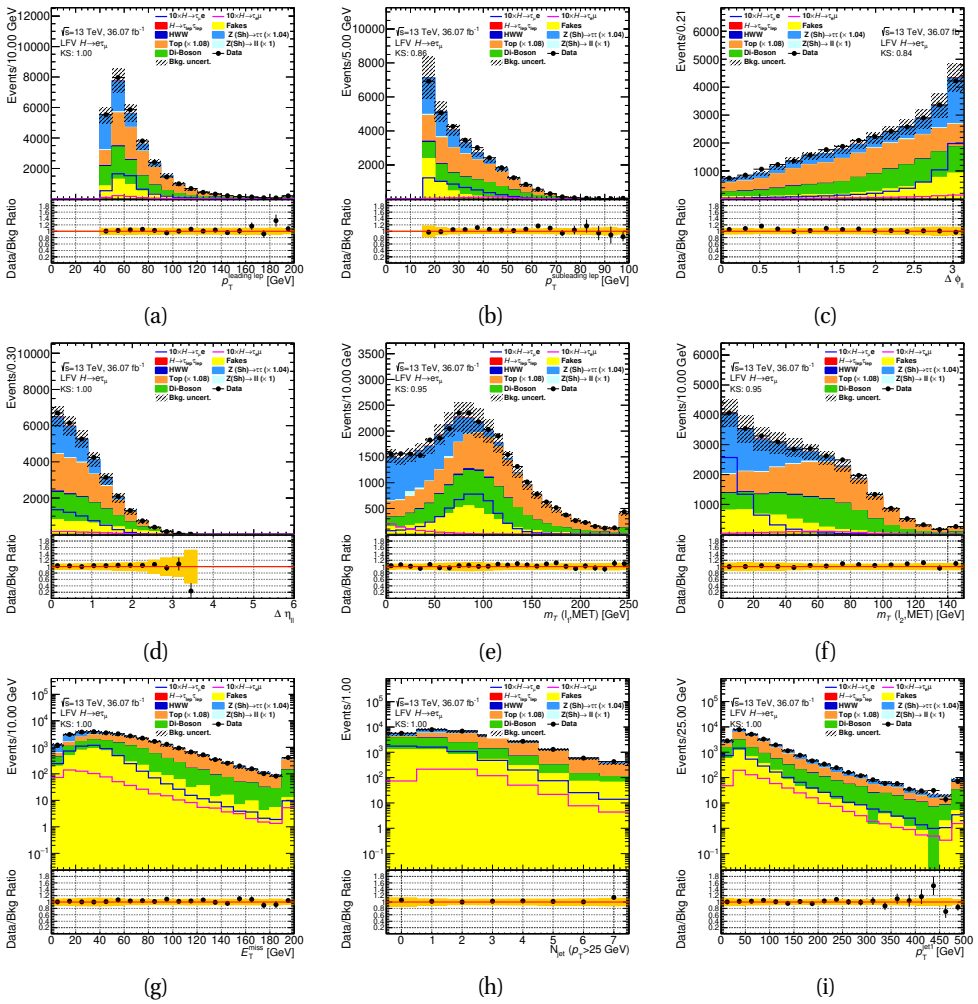

Figure 5.5: Kinematic distributions for the $e\tau_\mu$ final state for events passing the baseline selection. Shown are the distributions of $p_{\mathrm{T}}^{\ell_1}$ (a), $p_{\mathrm{T}}^{\ell_2}$ (b), $\Delta\phi_{\ell\ell}$ (c), $\Delta\eta_{\ell\ell}$ (d), $m_{\mathrm{T}}(\ell_1, E_{\mathrm{T}}^{\mathrm{miss}})$ (e), $m_{\mathrm{T}}(\ell_2, E_{\mathrm{T}}^{\mathrm{miss}})$ (f), $E_{\mathrm{T}}^{\mathrm{miss}}$ (g), $\mathrm{N}_{\mathrm{jets}}$ (h) and $p_{\mathrm{T}}^{j_1}$ (i). Error bands include the statistical uncertainties and the systematic uncertainties on the background normalization.

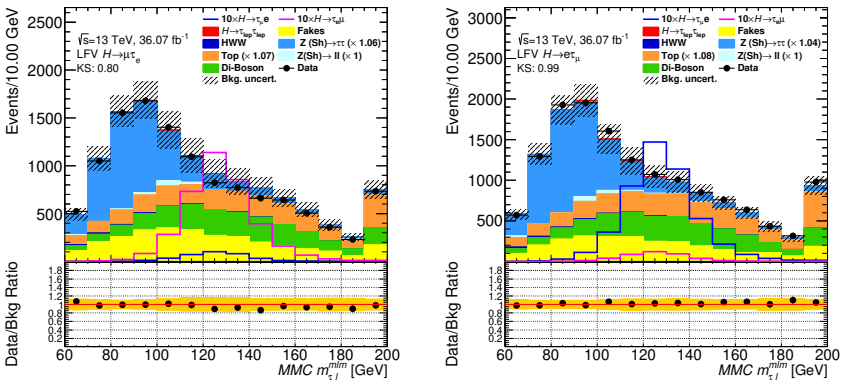

Figure 5.6: MMC mass distributions for the $\mu\tau_e$ (left) and $e\tau_\mu$ (right) final state for events passing the baseline selection. Error bands include the statistical uncertainties and the systematic uncertainties on the background normalization.

5.2.2 VBF signal region

The VBF signal region, like in the $H \to \tau\tau$ cross-section measurement, is used to select events produced by the VBF production mode applying restrictions in the most relevant kinematic parameters of the jets.

After the baseline selection, the VBF criteria require at least two jets with a $p_{\mathrm{T}}^{j_1} > 40\,\mathrm{GeV}$ and $p_{\mathrm{T}}^{j_2} > 30\,\mathrm{GeV}$ for the leading and subleading jet momentum respectively. Those jets are also expected to have a large η separation and a large energy due to the recoil of the quarks involved in the exchange of the heavy vector bosons. Therefore the invariant mass of the system of the jets must be $m_{jj} > 400\,\mathrm{GeV}$ and have a pseudorapidity separation $|\Delta\eta_{jj}| > 3$. A summary of the selection criteria used in the VBF category are shown in Table 5.3.

The events yields of the VBF selection criteria are in Table 5.4 for each $\ell\tau_{\ell'}$ channel. The pre-fit NFs extracted at preselection level are applied to the top-quark and $Z \to \tau\tau$ backgrounds only for displaying purpose. In addition, the most relevant kinematic distributions of both searches are reported in Figures 5.7, 5.8 and 5.9.

	$\ell\tau_{\ell'}$ $e\tau_\mu/\mu\tau_e$
VBF Signal Region	Pass Baseline selection # of jets $\geqslant 2$ $p_{\mathrm{T}}^{j_1} > 40\,\mathrm{GeV}$ $p_{\mathrm{T}}^{j_2} > 30\,\mathrm{GeV}$ $m_{jj} > 400\,\mathrm{GeV}$ $\lvert\Delta\eta_{jj}\rvert > 3$

Table 5.3: Summary of the event selection for the $\ell\tau_{\ell'}$ channel at the VBF signal region after applying the baseline selection shown in Table 5.1.

Sample	VBF selection	
	$\mu\tau_e$	$e\tau_\mu$
$H \to \tau\tau$	7.08 ± 0.16	9.9 ± 0.2
$H \to WW$	16.7 ± 0.6	20.5 ± 0.6
$Z \to \tau\tau$+jets	138 ± 6	190 ± 9
$Z \to ee\,, \mu\mu$+jets	2.3 ± 1.1	6.6 ± 1.8
$t\bar{t}$	404 ± 8	529 ± 10
Diboson	125 ± 5	161 ± 3
Fakes	84 ± 6	101 ± 9
Total background	785 ± 13	1017 ± 16
$H \to \mu\tau_e$ signal	14.9 ± 0.2	6.15 ± 0.13
$H \to e\tau_\mu$ signal	5.07 ± 0.13	19.8 ± 0.3
Data	723	990

Table 5.4: Yields of the $\mu\tau_e$ and $e\tau_\mu$ final states for the VBF selection. $\mathcal{BR}(H \to \mu\tau_e)$ and $\mathcal{BR}(H \to e\tau_\mu)$ are assumed to be 1%. Only statistical uncertainties are shown and the normalization factors derived from the control regions are applied to the relevant backgrounds, see section 5.4.3.

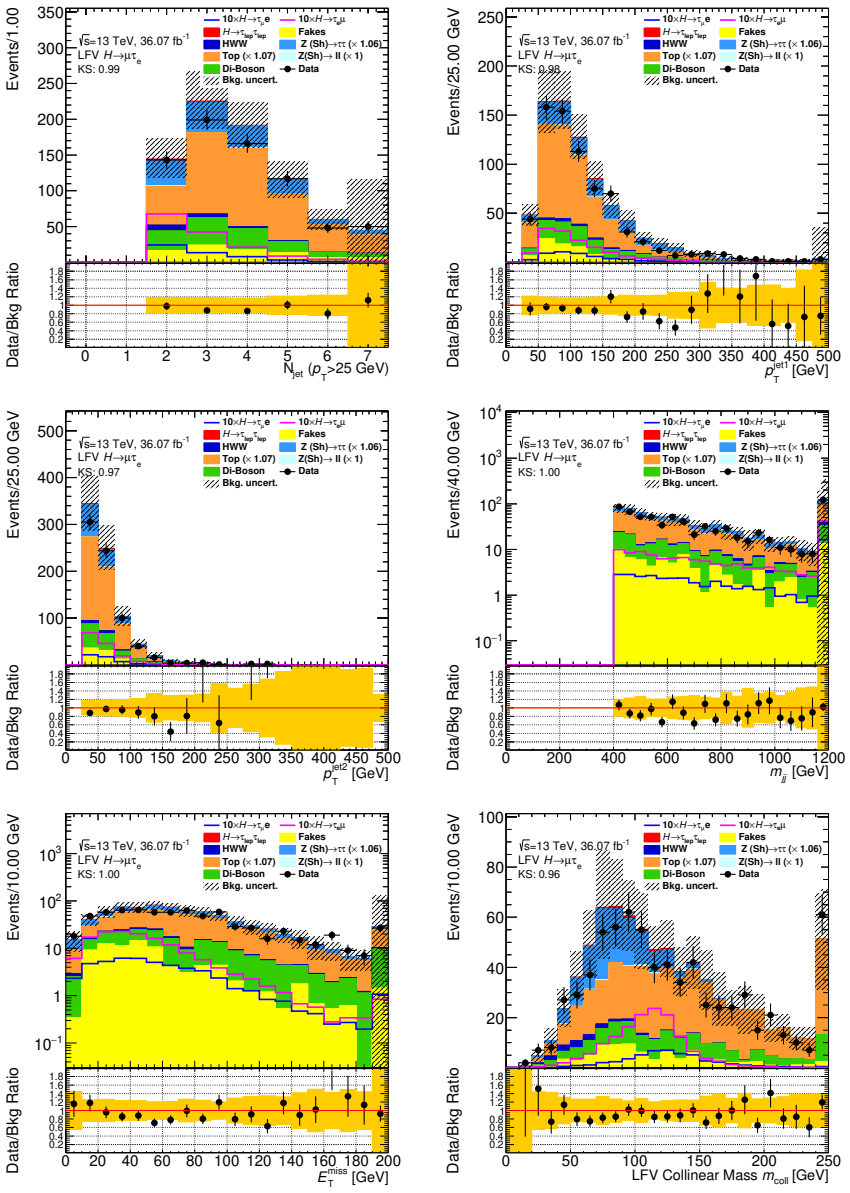

Figure 5.7: Kinematic distributions for the $\mu\tau_e$ final state after passing the VBF selection criteria. Error bands include the statistical uncertainties and the systematic uncertainties on the background normalization.

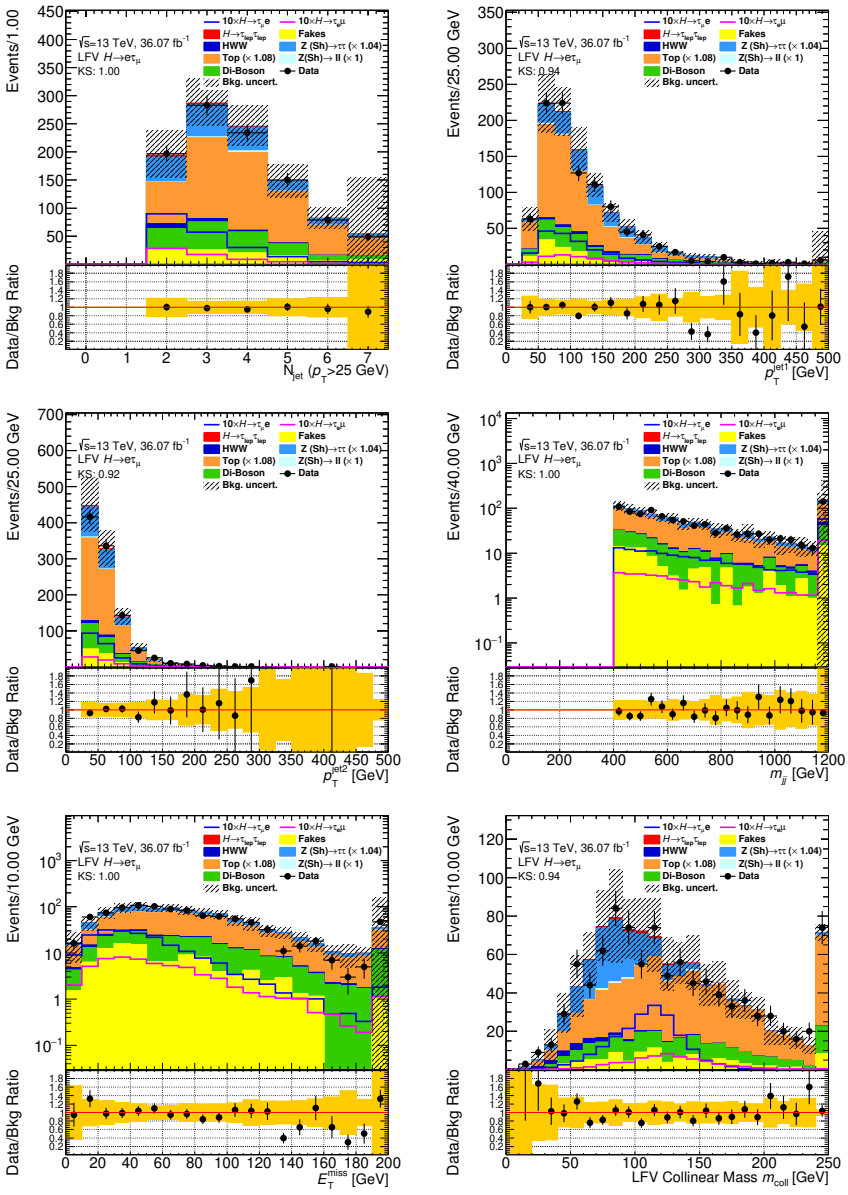

Figure 5.8: Kinematic distributions for the $e\tau_\mu$ final state after passing the VBF selection criteria. Error bands include the statistical uncertainties and the systematic uncertainties on the background normalization.

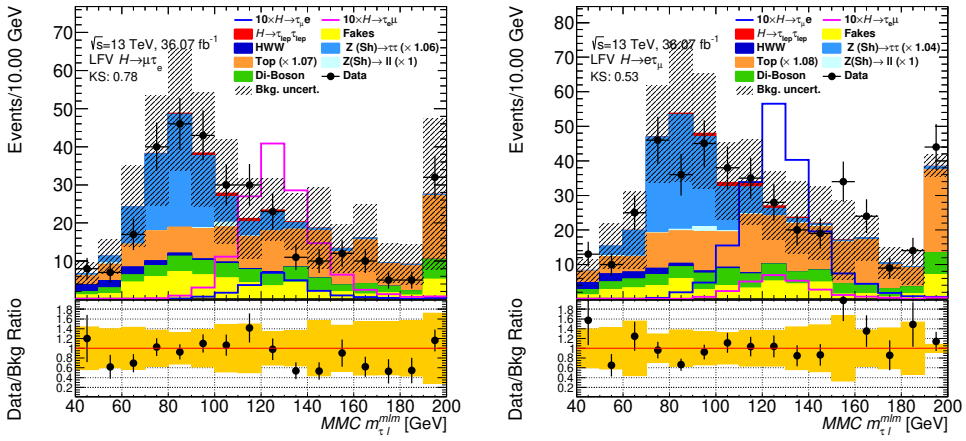

Figure 5.9: MMC distribution for the $\mu\tau_e$ (left) and $e\tau_\mu$ (right) final states after passing the VBF selection criteria. Error bands include the statistical uncertainties and the systematic uncertainties on the background normalization.

5.2.3 Non-VBF signal region

The events not passing the VBF selection are considered for the non-VBF category, which is a set of selection criteria chosen to increase the signal to background ratio for the ggF Higgs boson production mode. In addition to the baseline requirements, four more criteria are applied to reject the backgrounds which do not have a similar LFV topology.

The non-VBF selection requires the transverse mass between the leading (subleading) lepton and $E_{\mathrm{T}}^{\mathrm{miss}}$ to be: $m_{\mathrm{T}}^{\ell_1} > 50\,\mathrm{GeV}$ ($m_{\mathrm{T}}^{\ell_2} < 40\,\mathrm{GeV}$). The angular difference between the subleading lepton and $E_{\mathrm{T}}^{\mathrm{miss}}$ must be $\Delta\phi(\ell_2, E_{\mathrm{T}}^{\mathrm{miss}}) < 1.0$. The $\Delta\phi(\ell_2, E_{\mathrm{T}}^{\mathrm{miss}})$ requirement is used to constrain the $H \to \mu\tau_e$ ($H \to e\tau_\mu$) process in the $e\tau_\mu$ ($\mu\tau_e$) channel.

Additionally, a criterion is applied to suppress the fake leptons contamination at low energies and reduce the overall systematic uncertainty due to the fakes background procedure: the momentum ratio between the tau and the light-lepton must be $p_{\mathrm{T}}^{\tau}/p_{\mathrm{T}}^{\ell_1} > 0.5$, where the tau momentum is defined as $\overrightarrow{p}_{\mathrm{T}}^{\tau} = \overrightarrow{p}_{\mathrm{T}}^{\mathrm{miss}} + \overrightarrow{p}_{\mathrm{T}}^{\ell_2}$. The $p_{\mathrm{T}}^{\tau}/p_{\mathrm{T}}^{\ell_1}$ distribution is shown in Figure 5.10 before applying the criterion.

Table 5.5 summarizes all the criteria used for the non-VBF region. The yields obtained are shown in Table 5.6 for the $\mu\tau_e$ and $e\tau_\mu$ channels and the most relevant kinematic distributions are in Figures 5.11 and 5.12, whereas the missing mass distributions are shown in Figure 5.13.

	$\ell\tau_{\ell'}$ $e\tau_\mu/\mu\tau_e$
Non-VBF Signal Region	Pass Baseline selection Fail VBF category selection $\Delta\phi(\ell_2, E_{\mathrm{T}}^{\mathrm{miss}}) < 1.0$ $m_{\mathrm{T}}^{\ell_1} > 50\,\mathrm{GeV}$ $m_{\mathrm{T}}^{\ell_2} < 40\,\mathrm{GeV}$ $\frac{p_{\mathrm{T}}^{\tau}}{p_{\mathrm{T}}^{\ell_1}} > 0.5$

Table 5.5: Summary of the event selection for the non-VBF signal region.

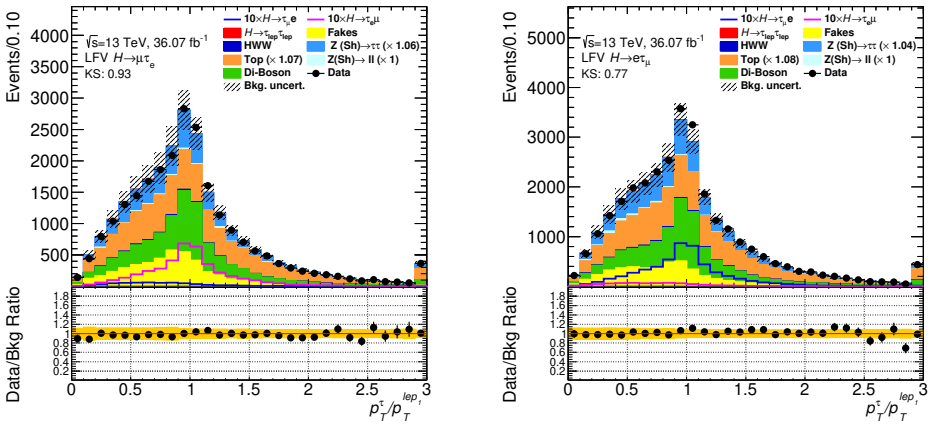

Figure 5.10: Kinematic distribution for the $\mu\tau_e$ (left) and $e\tau_\mu$ (right) final state for events passing the baseline selection. The $p_{\mathrm{T}}^{\tau}/p_{\mathrm{T}}^{\ell_1}$ distributions are shown. Error bands include the statistical uncertainties and the systematic uncertainties on the background normalization.

Sample	Non-VBF selection	
	$\mu\tau_e$	$e\tau_\mu$
$H \to \tau\tau$	37.6 ± 0.5	50.8 ± 0.6
$H \to WW$	25.0 ± 1.0	31.9 ± 1.1
$Z \to \tau\tau$+jets	1580 ± 20	2120 ± 30
$Z \to ee\,, \mu\mu$+jets	90 ± 40	20 ± 30
$t\bar{t}$	1351 ± 15	1767 ± 18
Diboson	1119 ± 12	1494 ± 15
Fakes	1720 ± 30	1540 ± 40
Total background	6010 ± 60	7010 ± 60
$H \to \mu\tau_e$ signal	287.0 ± 1.6	4.7 ± 0.2
$H \to e\tau_\mu$ signal	3.98 ± 0.17	379.2 ± 1.9
Data	5660	7120

Table 5.6: Yields of the $\mu\tau_e$ and $e\tau_\mu$ final states for the non-VBF selection. $\mathcal{BR}(H \to \mu\tau_e)$ and $\mathcal{BR}(H \to e\tau_\mu)$ are assumed to be 1%. Only statistical uncertainties are shown and the normalization factors derived from the control regions are applied to the relevant backgrounds, see section 5.4.3.

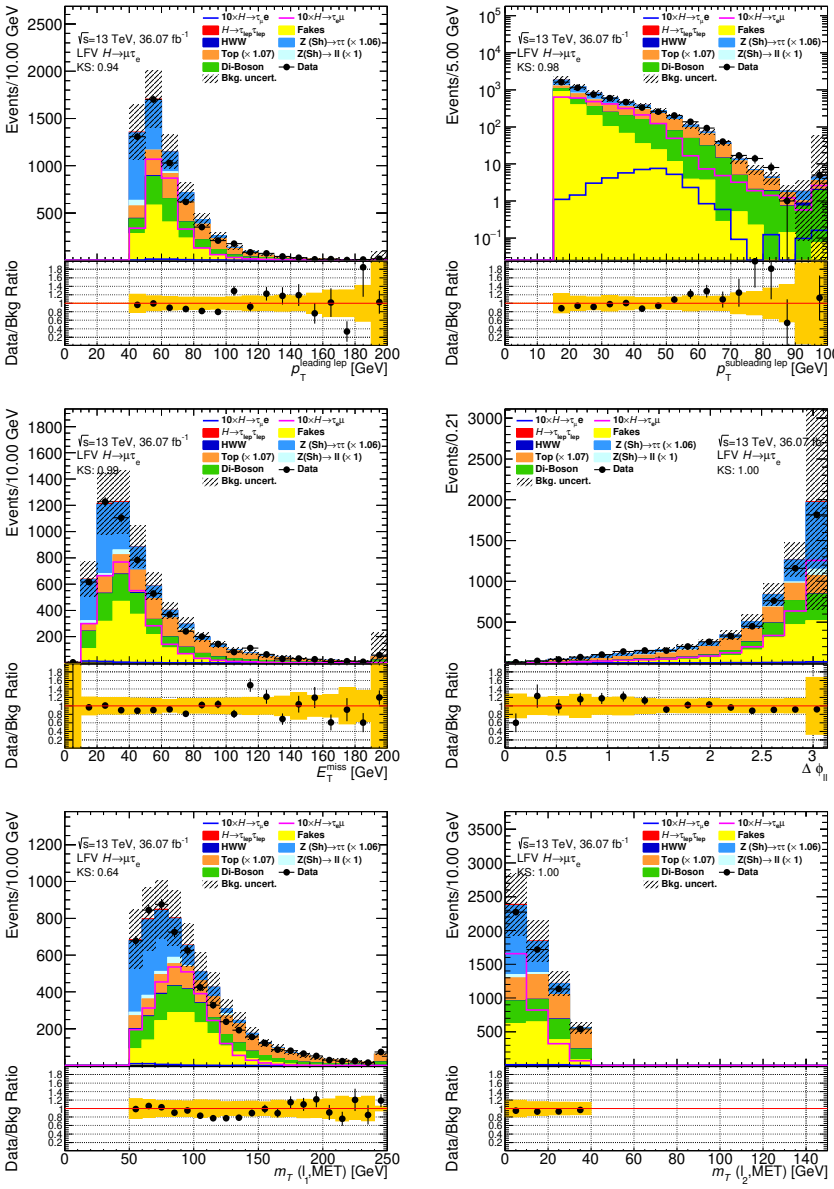

Figure 5.11: Kinematic distributions for the $\mu\tau_e$ final state events passing the non-VBF selection criteria. Error bands include the statistical uncertainties and the systematic uncertainties on the background normalization.

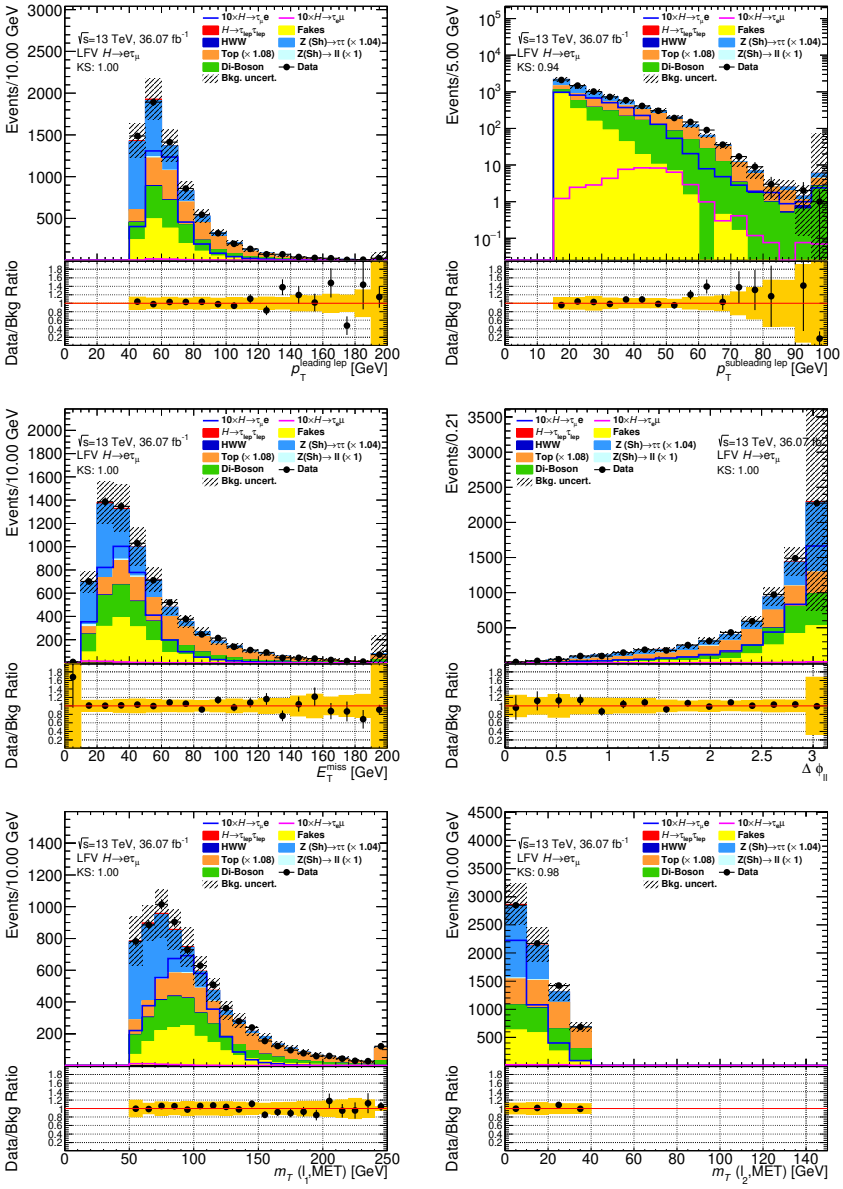

Figure 5.12: Kinematic distributions for the $e\tau_\mu$ final state events passing the non-VBF selection criteria. Error bands include the statistical uncertainties and the systematic uncertainties on the background normalization.

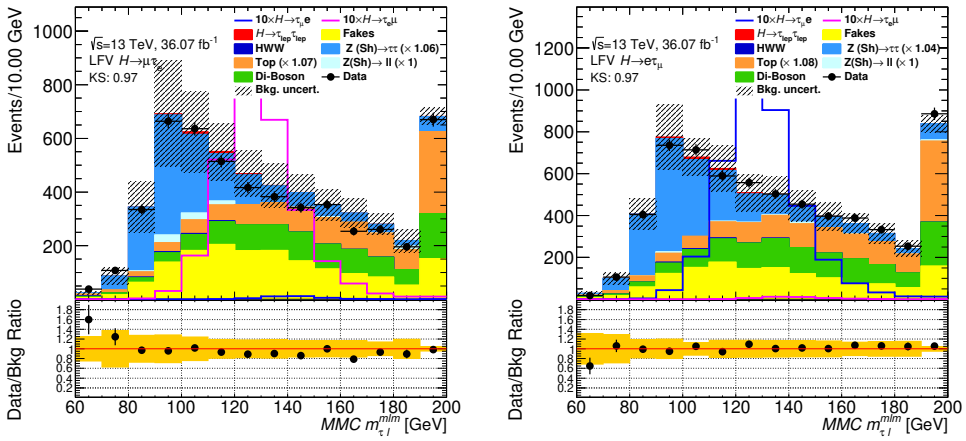

Figure 5.13: MMC distribution for the events in the $\mu\tau_e$ (left) and $e\tau_\mu$ (right) final states after passing the non-VBF selection criteria. Error bands include the statistical uncertainties and the systematic uncertainties on the background normalization.

5.2.4 Fakes transfer factors for the $H \to \ell\tau_{\ell'}$ search

As for the $H \to \tau\tau$ cross-section measurement, a special selection is defined for the estimation of the fakes transfer factors and the method is described in Appendix A.1. The baseline selection criteria are required, however to include as well the events corresponding to control regions defined in Section 5.4 two criteria have been modified: the momentum of the leading lepton, $p_{\mathrm{T}}^{\ell_1} > 35\,\mathrm{GeV}$, and the restriction of events without b-jets.

The transfer factors in different b-jet regions, triggers and channels, according to the method described in appendix A.1, are given in Table 5.7.

region		$e\mu$	μe
b-veto	$trig1$	0.549 ± 0.014	0.260 ± 0.017
	$trig2$	—	0.307 ± 0.006
	$trig3$	—	—
b-tag	$trig1$	0.244 ± 0.011	0.082 ± 0.009
	$trig2$	—	0.135 ± 0.006
	$trig3$	—	—

Table 5.7: Transfer factors and their uncertainties in different regions calculated from SS events after the LFV baseline selection. $trig1$, $trig2$ and $trig3$ corresponds to a single electron, single muon and di-lepton triggers respectively. Due to the selection criteria on the p_{T} of the leptons just the single electron and single muon triggers are used. Only statistical uncertainties are considered.

5.3 Multivariate Analysis

No further categorization is applied to the signal regions. In this case, in view of the signal-to-background condition, and in order to exploit correlations between final-state observables, a MultiVariate Analysis technique (MVA), based on Boosted Decision Tree (BDT) gradient boosting [135–137] of the TMVA package [138], is used to extract the final results. The BDT algorithm was chosen over other tested methods because it gave the highest signal acceptance over the background rejection.

The algorithm divides the phase space into signal-like and background-like regions and assign a BDT score to each event depending on which region it falls into. The BDTs are trained on the statistically independent samples described in Section 3.2 for LFV signal-like events and Section 3.3 and A.1 for background-like events.

The MVA analysis exploits the events entering in the selection used for the non-VBF and VBF signal regions. The variables given to the BDTs allow them to discriminate further the signal-like events from the background-like events. The complete list of variables used is shown in Table 5.8.

The strategy involved in the Training-Test part uses a 5-fold strategy where 5 BDTs are trained using 80% of the statistics and applied to the remaining 20% of the events, and are statistically independent for each BDT. The events have been randomly split based on their event number.

Variables	Non-VBF	VBF
The angular distance between the two leptons: $\Delta R(\ell_1, \ell_2)$	•	•
The momentum of the leading lepton: $p_{\mathrm{T}}^{\ell_1}$	•	•
The momentum of the subleading lepton: $p_{\mathrm{T}}^{\ell_2}$	•	•
The angular difference between the leading lepton and $E_{\mathrm{T}}^{\mathrm{miss}}$: $\Delta\phi(\ell_1, E_{\mathrm{T}}^{\mathrm{miss}})$	•	•
The angular difference between the subleading lepton and $E_{\mathrm{T}}^{\mathrm{miss}}$: $\Delta\phi(\ell_2, E_{\mathrm{T}}^{\mathrm{miss}})$	•	•
The transverse mass of the leading lepton and $E_{\mathrm{T}}^{\mathrm{miss}}$: $m_{\mathrm{T}}^{\ell_1}$	•	•
The transverse mass of the subleading leptons and $E_{\mathrm{T}}^{\mathrm{miss}}$: $m_{\mathrm{T}}^{\ell_2}$	•	•
The MMC reconstructed mass: $m_{\ell\tau}^{\mathrm{MMC}}$	•	•
The momentum ratio between the tau and the leading lepton: $\frac{p_{\mathrm{T}}^{\tau}}{p_{\mathrm{T}}^{\ell_1}}$	•	
The invariant mass of the two leading jets: m_{jj}		•
The eta distance two leading jets: $\lvert\Delta\eta_{jj}\rvert$		•

Table 5.8: List of variables for the MVA analysis in the non-VBF and VBF categories. The variables are listed in no particular order.

Non-VBF category						
Variable	1 fold	2 fold	3 fold	4 fold	5 fold	Average
$m_{\ell_\tau}^{\text{MMC}}$	0.20520	0.19390	0.19760	0.18590	0.20080	0.19668
$p_{\text{T}}^{\ell_2}$	0.12130	0.12980	0.12440	0.13200	0.12870	0.12724
$\Delta\phi(\ell_2, E_{\text{T}}^{\text{miss}})$	0.11870	0.11510	0.10420	0.10580	0.10740	0.11024
$m_{\text{T}}^{\ell_1}$	0.09866	0.10530	0.11140	0.11380	0.10410	0.10665
$p_{\text{T}}^{\tau}/p_{\text{T}}^{\ell_1}$	0.09279	0.09864	0.09627	0.09754	0.09670	0.09639
$p_{\text{T}}^{\ell_1}$	0.10020	0.09299	0.09688	0.09629	0.09311	0.09589
$m_{\text{T}}^{\ell_2}$	0.09039	0.09421	0.09314	0.09685	0.09102	0.09312
$\Delta R(\ell_1, \ell_2)$	0.09065	0.08905	0.09251	0.09213	0.08850	0.09057
$\Delta\phi(\ell_1, E_{\text{T}}^{\text{miss}})$	0.08215	0.08101	0.08358	0.07973	0.08968	0.08323

Table 5.9: Ranking of the variables for the non-VBF category provided by the algorithm. The variables are sorted by the highest to the lowest importance according to the average value.

After the training, the variables are ranked in order of importance by the algorithm. The ranking is derived by counting how often the variables are used to split decision tree nodes, and by weighting each split occurrence by the separation-gain squared it has achieved and by the number of events in the node. Table 5.9 and 5.10 show the variable ranking of each fold as well as the average for the non-VBF and VBF signal regions. The normalised distributions for the variables used by the MVA algorithm are shown in Figures 5.14, 5.15, 5.16 and 5.17 for signal and background events. The correlation of the variables for both signal regions are shown in Figure 5.18. The high correlation between the transverse mass and the angular difference between the leptons and $E_{\mathrm{T}}^{\mathrm{miss}}$ is expected due to the definition of the transverse mass. Additionally, to check the BDT over-training, Figures 5.19 and 5.20 show the output distributions for 5-fold BDTs used for the non-VBF and VBF category as well as the ratio of the testing and training samples.

VBF category						
Variable	1 fold	2 fold	3 fold	4 fold	5 fold	Average
$m_{\ell\tau}^{\mathrm{MMC}}$	0.16550	0.16490	0.16650	0.16430	0.16660	0.16556
$\Delta R(\ell_1, \ell_2)$	0.12370	0.12100	0.12540	0.12440	0.12390	0.12368
$m_{\mathrm{T}}^{\ell_2}$	0.11220	0.10990	0.10620	0.11040	0.11900	0.11154
$\Delta\eta_{jj}$	0.09775	0.09436	0.10310	0.09733	0.09559	0.09763
$p_{\mathrm{T}}^{\ell_1}$	0.09552	0.09610	0.09962	0.09607	0.09411	0.09628
$p_{\mathrm{T}}^{\ell_2}$	0.09588	0.09788	0.09679	0.09400	0.09139	0.09519
$m_{\mathrm{T}}^{\ell_1}$	0.09534	0.09205	0.09060	0.09473	0.09477	0.09350
$\Delta\phi(\ell_1, E_{\mathrm{T}}^{\mathrm{miss}})$	0.09351	0.09483	0.08591	0.09137	0.08239	0.08960
m_{jj}	0.06108	0.06459	0.06716	0.06369	0.06713	0.06473
$\Delta\phi(\ell_2, E_{\mathrm{T}}^{\mathrm{miss}})$	0.05950	0.06436	0.05865	0.06375	0.06517	0.06229

Table 5.10: Ranking of the variables for the VBF category provided by the algorithm. The variables are sorted by the highest to the lowest importance according to the average value.

Table 5.11 shows a comparison of the statistical significance of the MVA analysis (using the BDT score distribution) vs CBA analysis (using the MMC mass distribution).

Even if CBA and MVA employ the same selection, the MVA obtains a better statistical significance by about $15\%(20\%)$ for the $\mu\tau_e(e\tau_\mu)$ channel thanks to the BDT algorithm.

	Search	nonVBF	VBF	Combined
CBA	$\mu\tau_e$	5.81	1.26	5.95
	$e\tau_\mu$	7.18	1.54	7.34
MVA	$\mu\tau_e$	6.84	1.86	7.09
	$e\tau_\mu$	8.23	2.31	8.55

Table 5.11: Table of the binned significance for the final discriminant distribution in each region. The Combined column is the quadratic sum of significance of the two signal regions. The signal branching ratio is assumed to be 1% for the significance calculation.

The BDT parameters have been optimized independently of the category and they are determined by looking at the number of trees and the complexity of each tree. The $e\tau_\mu$ and $\mu\tau_e$ event samples have been merged for the purpose of the BDT training. This allows a better discrimination of the background-like events, thanks to the higher statistics. The best combination obtained for the BDT parameters is shown in Table 5.12. The Ntrees variable is the total number of steps the MVA uses to separate the events. The rest of variables are used to modify the complexity of each tree. MaxDepth is used to define the maximum number of selection steps the MVA must do whereas the MinNodeSize and Shrinkage are used to define the percentage of training events required in a node and the learning rate of the algorithm respectively.

NTrees=1000	MaxDepth=2	MinNodeSize=2.5%	nCuts=20
BoostType=Grad	UseBaggedBoost=true	Shrinkage=0.1	BaggedSampleFraction=0.5

Table 5.12: BDT parameters used in the MVA analysis.

After optimizing the BDT parameters to obtain the highest significance, the output score of each channel and category is shown in Figure 5.21. The algorithm assigns a value of -1 to the most background-like events and a value of $+1$ to the most signal-like events. The distributions include the statistical and systematic uncertainties. The BDT distributions are the ones considered in the statistical fit to obtain the final results.

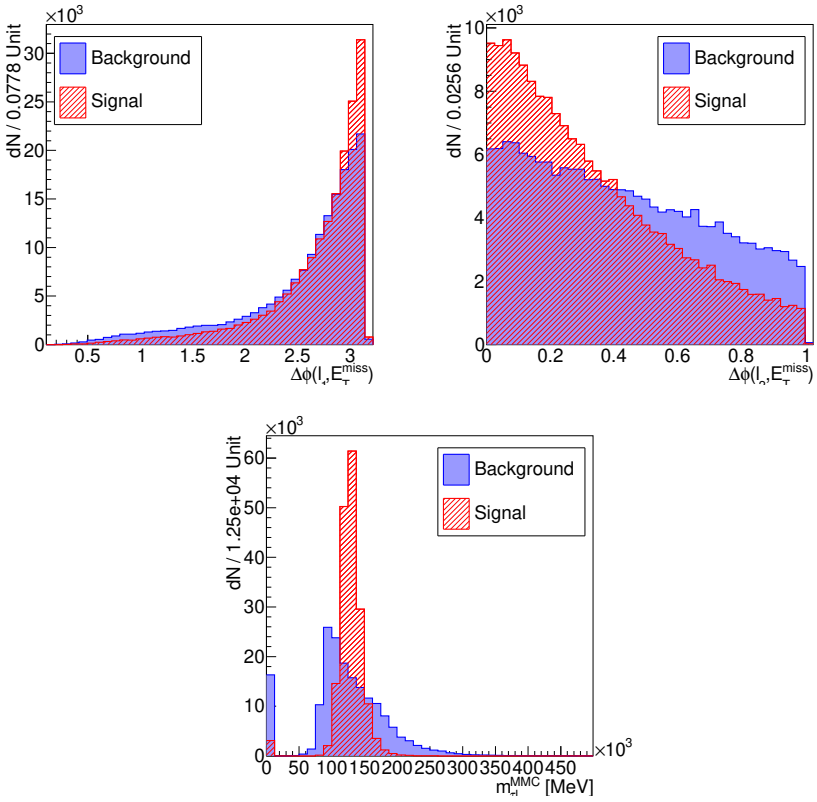

Figure 5.14: Distributions of the signal (red) and background (blue) events for the BDT input variables of the non-VBF category.

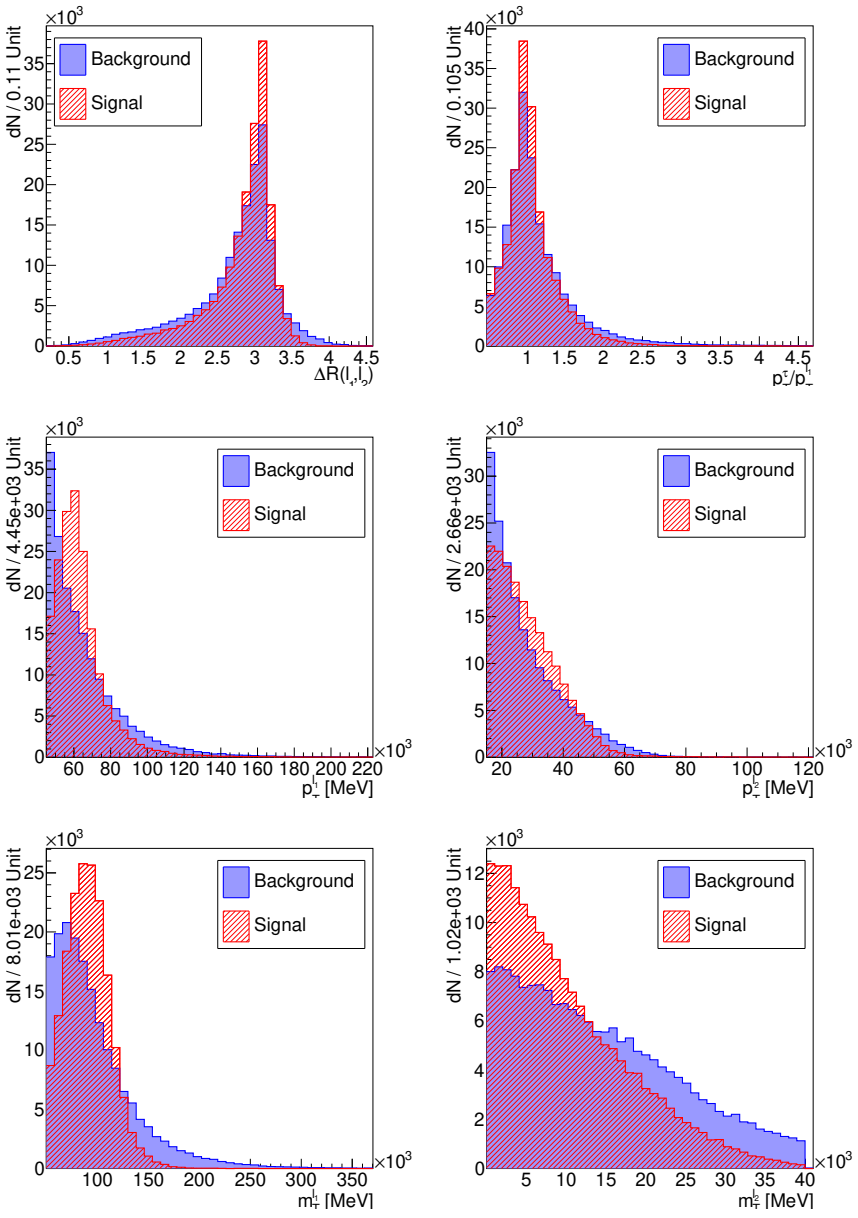

Figure 5.15: Distributions of the signal (red) and background (blue) events for the BDT input variables of the non-VBF category.

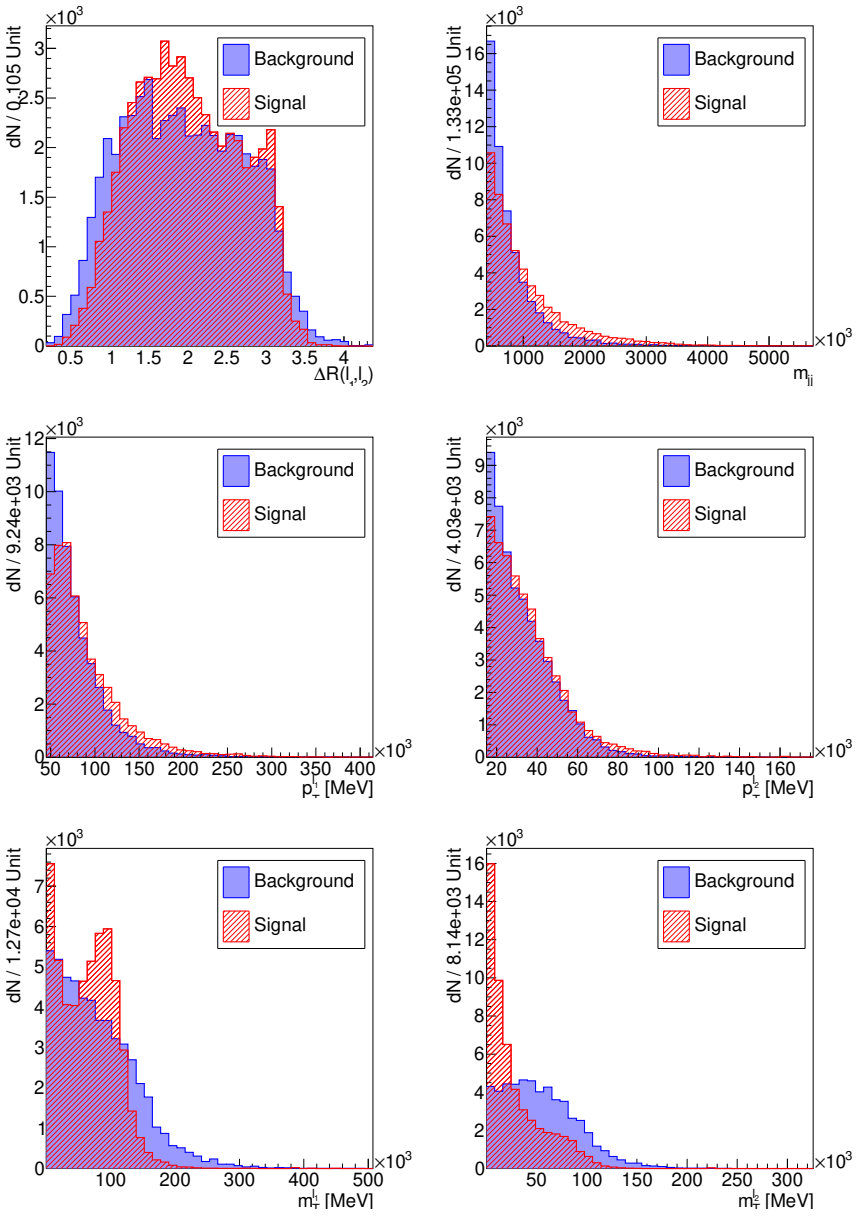

Figure 5.16: Distributions of the signal (red) and background (blue) events for the BDT input variables of the VBF category.

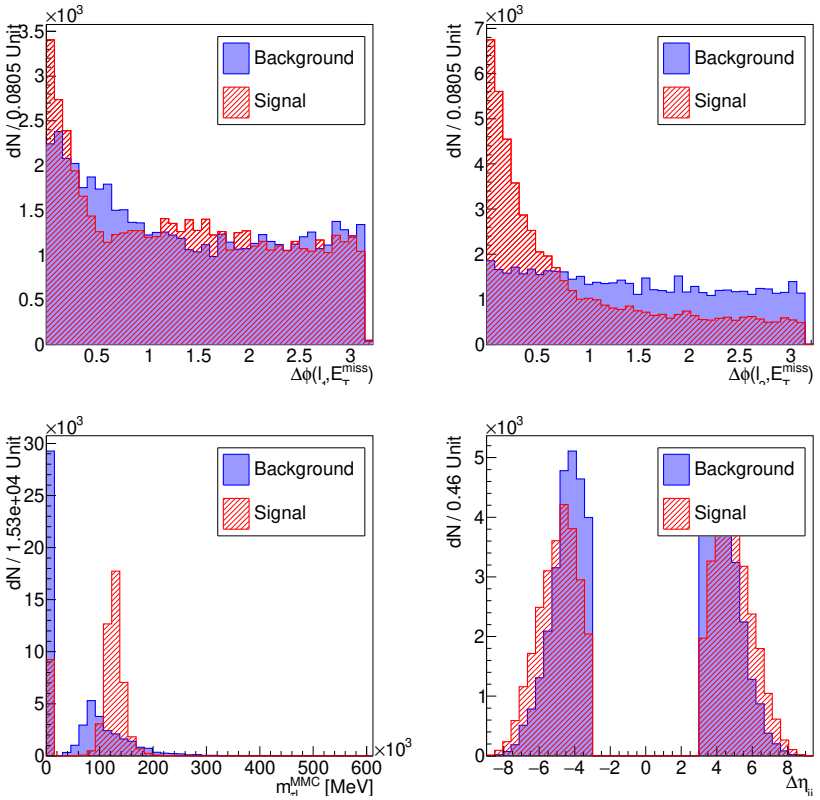

Figure 5.17: Distributions of the signal (red) and background (blue) events for the BDT input variables of the VBF category.

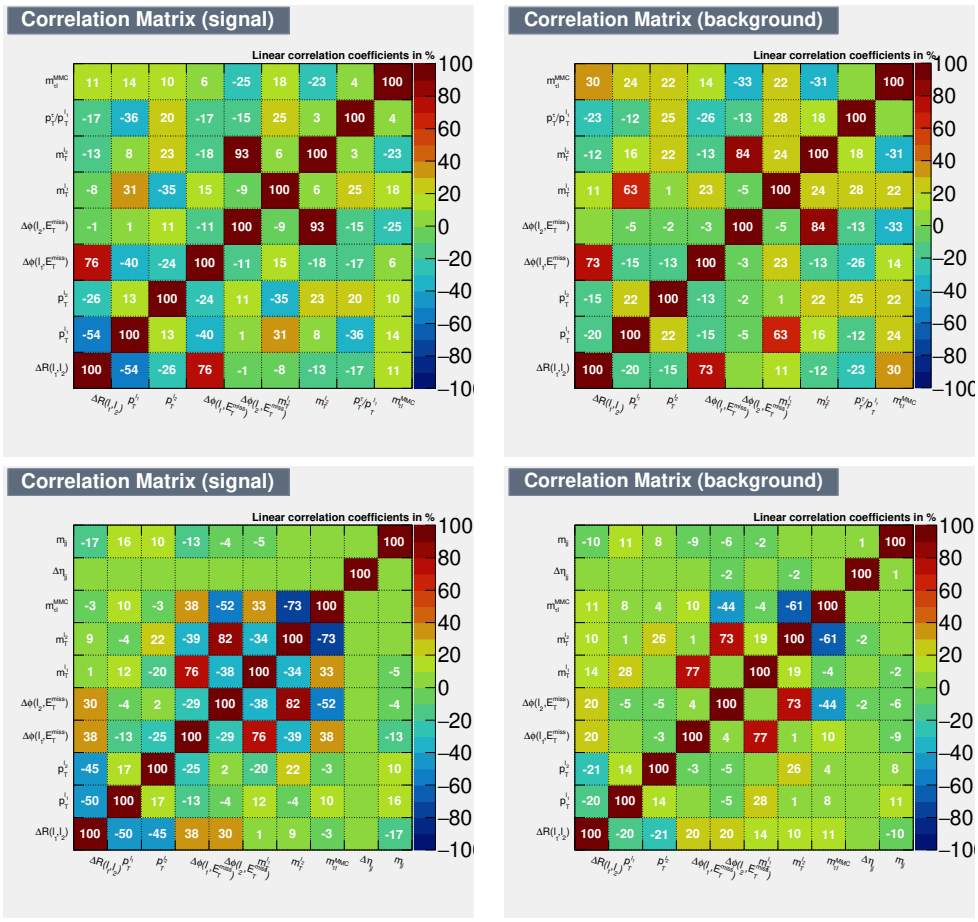

Figure 5.18: Correlation of the variables used for the non-VBF (top) and VBF (bottom) category for both the signal (left) and background (right) events.

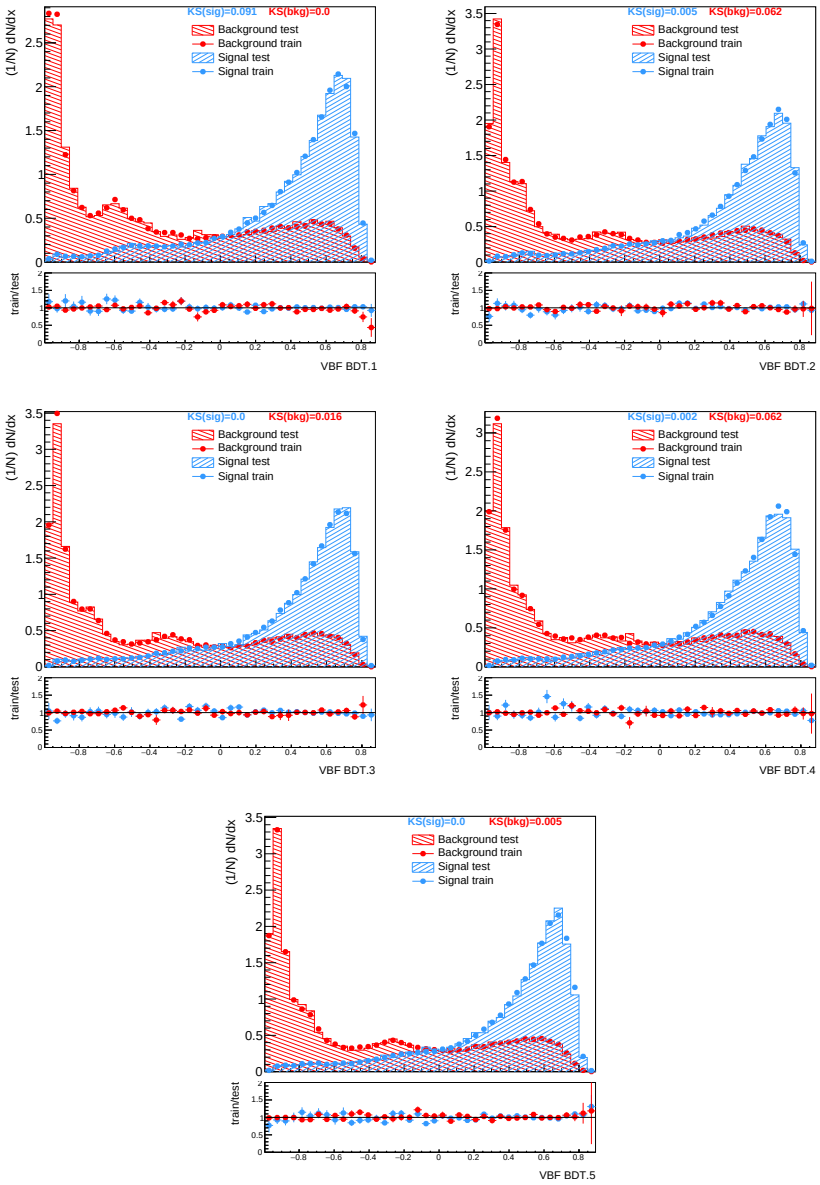

Figure 5.19: Classifier TMVA output distribution for all BDTs of the non-VBF category. The low pad of each canvas shows the ratio of the test and training samples for signal (red) and background (blue) events.

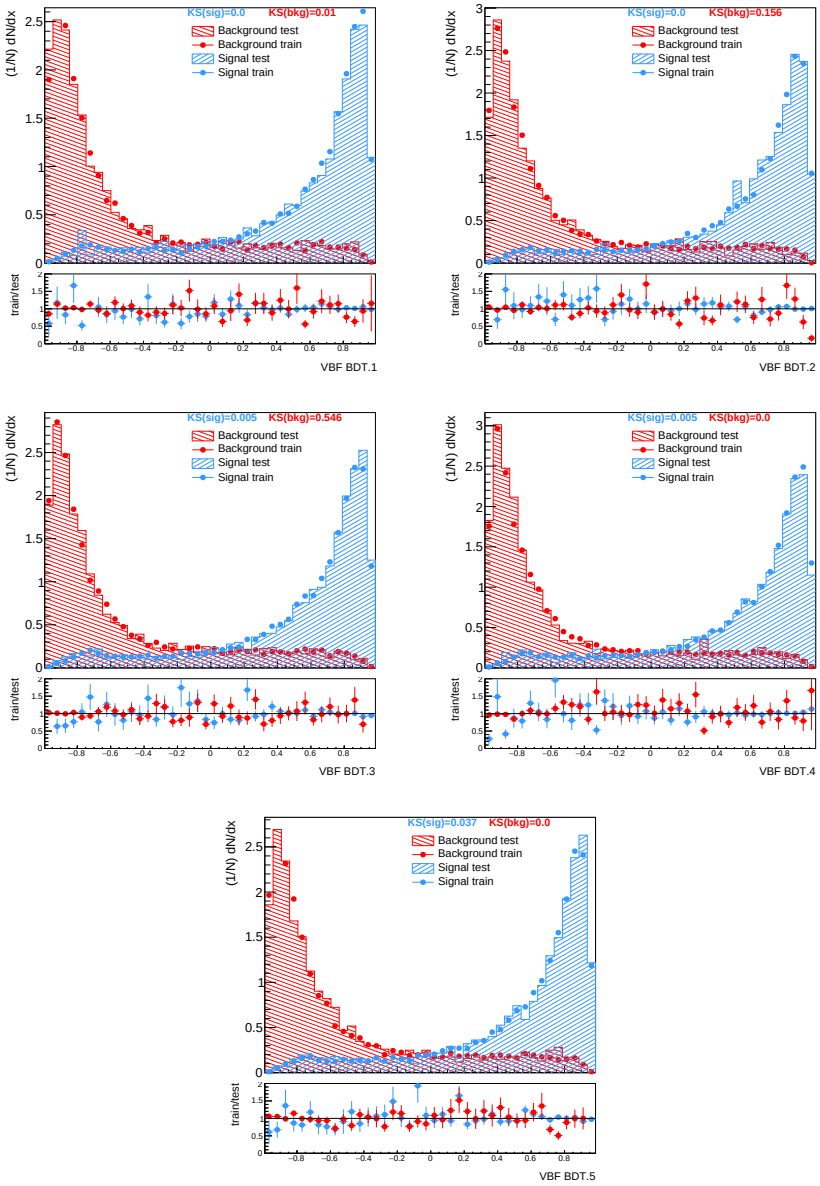

Figure 5.20: Classifier TMVA output distribution for all BDTs of the VBF category. The low pad of each canvas shows the ratio of the test and training samples for signal (red) and background (blue) events.

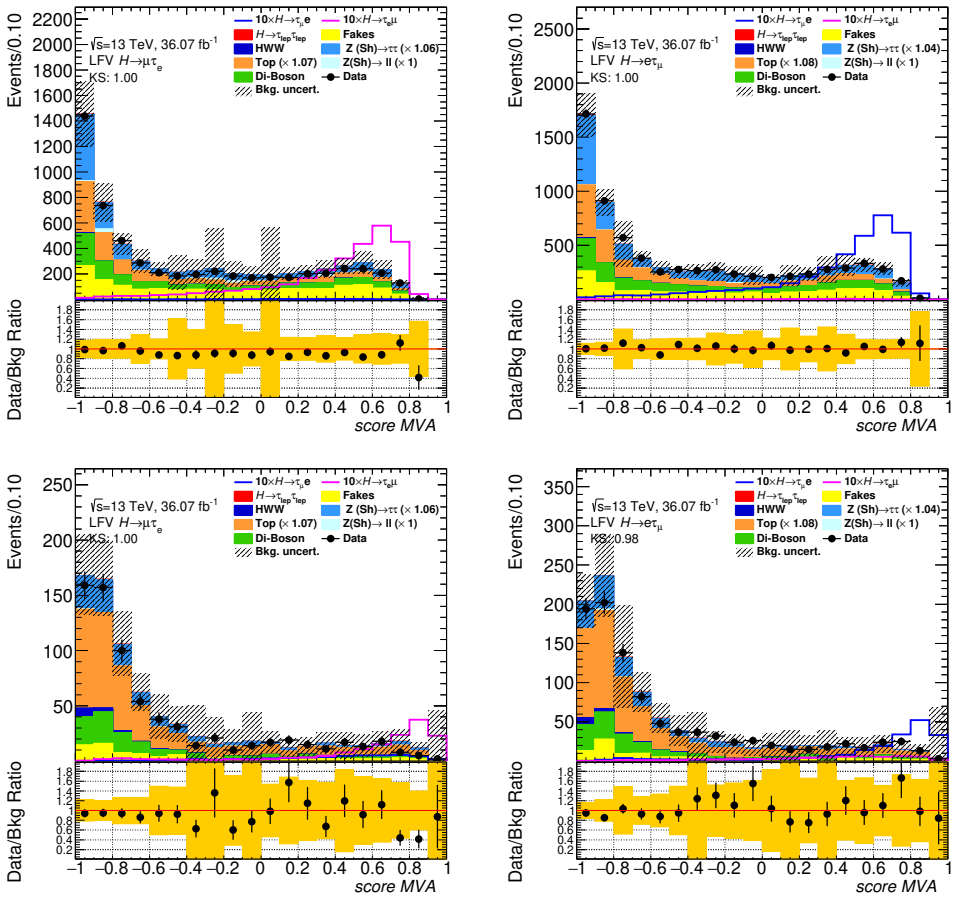

Figure 5.21: BDT output distribution for the $\mu\tau_e$ (left) and $e\tau_\mu$ (right) final states after passing the non-VBF (top) and VBF (bottom) selection criteria. Error bands include the statistical uncertainties and the systematic uncertainties on the background normalization.

5.4 Control Regions

The most significant backgrounds of the $H \to \ell\tau_{\ell'}$ searches are the $Z \to \tau\tau$ process and the single and pair-produced top-quarks. Therefore two sets of CRs are used to constrain the normalization of the $Z \to \tau\tau$ and top-quark background components. These CRs inherit their definitions from the corresponding categories but invert one requirement to ensure orthogonality with the nominal selection. They are used in the statistical fit by fitting the event yields in the control regions simultaneously to the BDT spectra of the signal regions.

5.4.1 Top-quark control region: yields and control plots

The top-quark CR is used to enhance the top events in a orthogonal region as close as possible to the signal regions. These regions are obtained from the signal regions by inverting the b-jet veto requirement, so at least one b-jet has to be present in the event.

Tables 5.13 and 5.14 show the yields of the top-quark control region of the baseline and signal regions of the two searches. The top-quark CRs are almost exclusively composed of top-quark backgrounds, with a purity of approximately 95% across both searches and categories. Figures 5.22 and 5.23 show the distributions of the kinematic variables at preselection level and Figures 5.24 and 5.25 show the invariant mass using the MMC algorithm as well as the BDT output for the VBF and non-VBF selection criteria.

Sample	Top Control Region, $\mu\tau_e$		
	Baseline	VBF	non-VBF
$H \to \tau\tau$	310 ± 3	13.4 ± 0.5	52.9 ± 1.0
$H \to WW$	17.9 ± 1.0	2.8 ± 3	2.5 ± 0.4
$Z \to \tau\tau$+jets	680 ± 20	33 ± 3	119 ± 9
$Z \to ee\,, \mu\mu$+jets	36 ± 18	0.2 ± 0.3	7 ± 4
$t\bar{t}$	66550 ± 120	3110 ± 30	10040 ± 50
Diboson	497 ± 8	32.0 ± 1.8	69 ± 3
Fake leptons	1141 ± 17	71 ± 4	283 ± 7
Total background	69230 ± 120	3260 ± 30	10570 ± 50
$H \to \mu\tau_e$ signal	26.3 ± 0.5	2.22 ± 0.11	14.7 ± 0.4
$H \to e\tau_\mu$ signal	7.85 ± 0.5	0.80 ± 0.06	0.36 ± 0.07
Data	69200	3490	10570

Table 5.13: Yields of the $\mu\tau_e$ channels for the Baseline, VBF and non-VBF selections. $\mathcal{BR}(H \to \mu\tau_e)$ and $\mathcal{BR}(H \to e\tau_\mu)$ are assumed to be 1%. The top-quark and $Z \to \tau\tau$ predictions are scaled by the normalization factors obtained in the corresponding baseline control regions.

Sample	Top Control Region, $e\tau_\mu$		
	Baseline	VBF	Non-VBF
$H \to \tau\tau$	419 ± 3	19.7 ± 0.6	72.7 ± 1.3
$H \to WW$	24.4 ± 1.2	3.1 ± 0.3	2.8 ± 0.4
$Z \to \tau\tau$+jets	910 ± 20	49 ± 4	163 ± 12
$Z \to ee\,, \mu\mu$+jets	33 ± 12	2.4 ± 0.9	3 ± 4
$t\bar{t}$	84930 ± 140	4140 ± 30	13480 ± 50
Diboson	634 ± 10	35.3 ± 1.9	94 ± 4
Fake leptons	1260 ± 40	56 ± 7	311 ± 13
Total background	88200 ± 140	4310 ± 30	14130 ± 60
$H \to \mu\tau_e$ signal	9.5 ± 0.3	0.95 ± 0.08	0.33 ± 0.05
$H \to e\tau_\mu$ signal	35.6 ± 0.6	2.96 ± 0.13	20.3 ± 0.5
Data	88203	4330	13980

Table 5.14: Yields of the $e\tau_\mu$ search for the Baseline, VBF and Non-VBF selections. $\mathcal{BR}(H \to \mu\tau_e)$ and $\mathcal{BR}(H \to e\tau_\mu)$ are assumed to be 1%. The top-quark and $Z \to \tau\tau$ predictions are scaled by the normalization factors obtained for the baseline control regions.

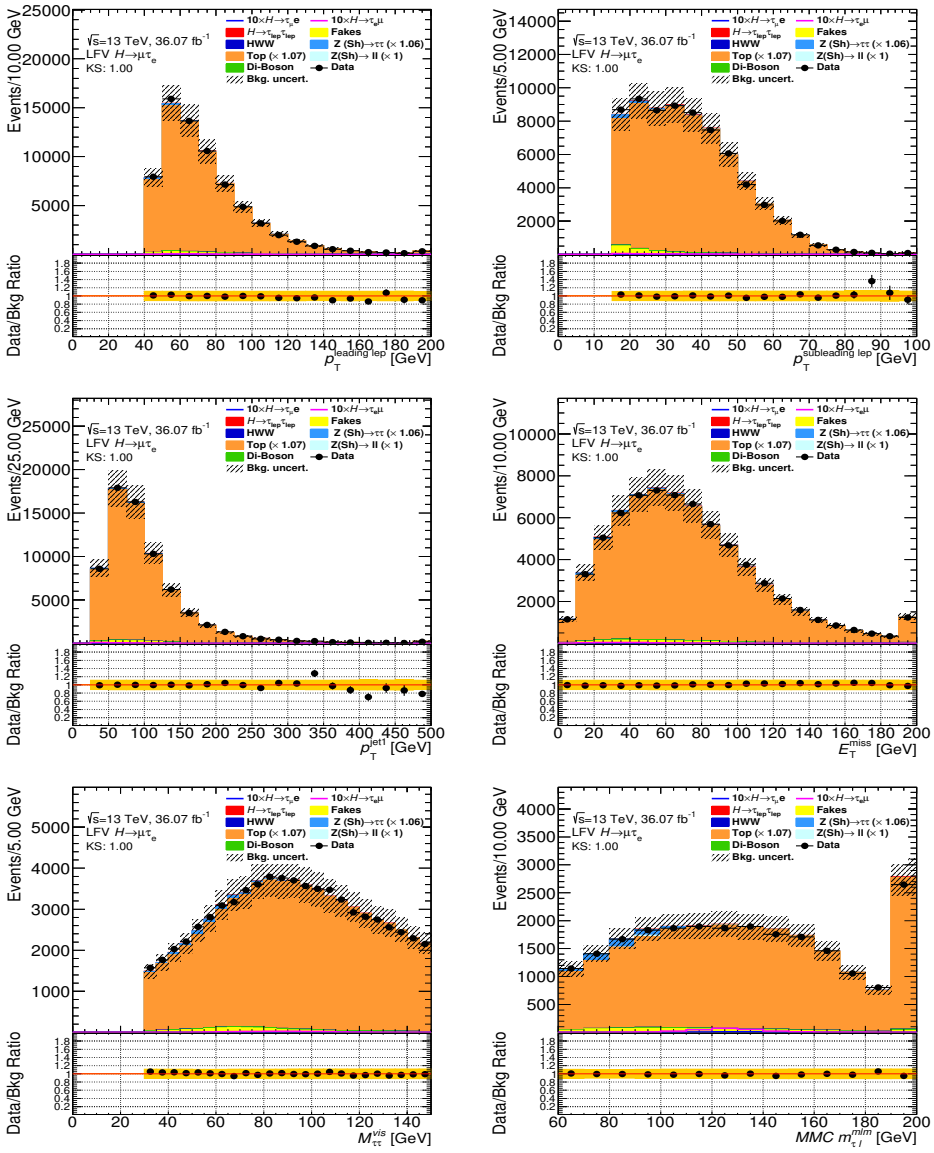

Figure 5.22: Top control region distributions for $\mu\tau_e$ events after baseline selection. Pre-fit normalization factors obtained in the baseline top-quark control region have been applied. Error bands include the statistical uncertainties and the systematic uncertainties on the background normalization.

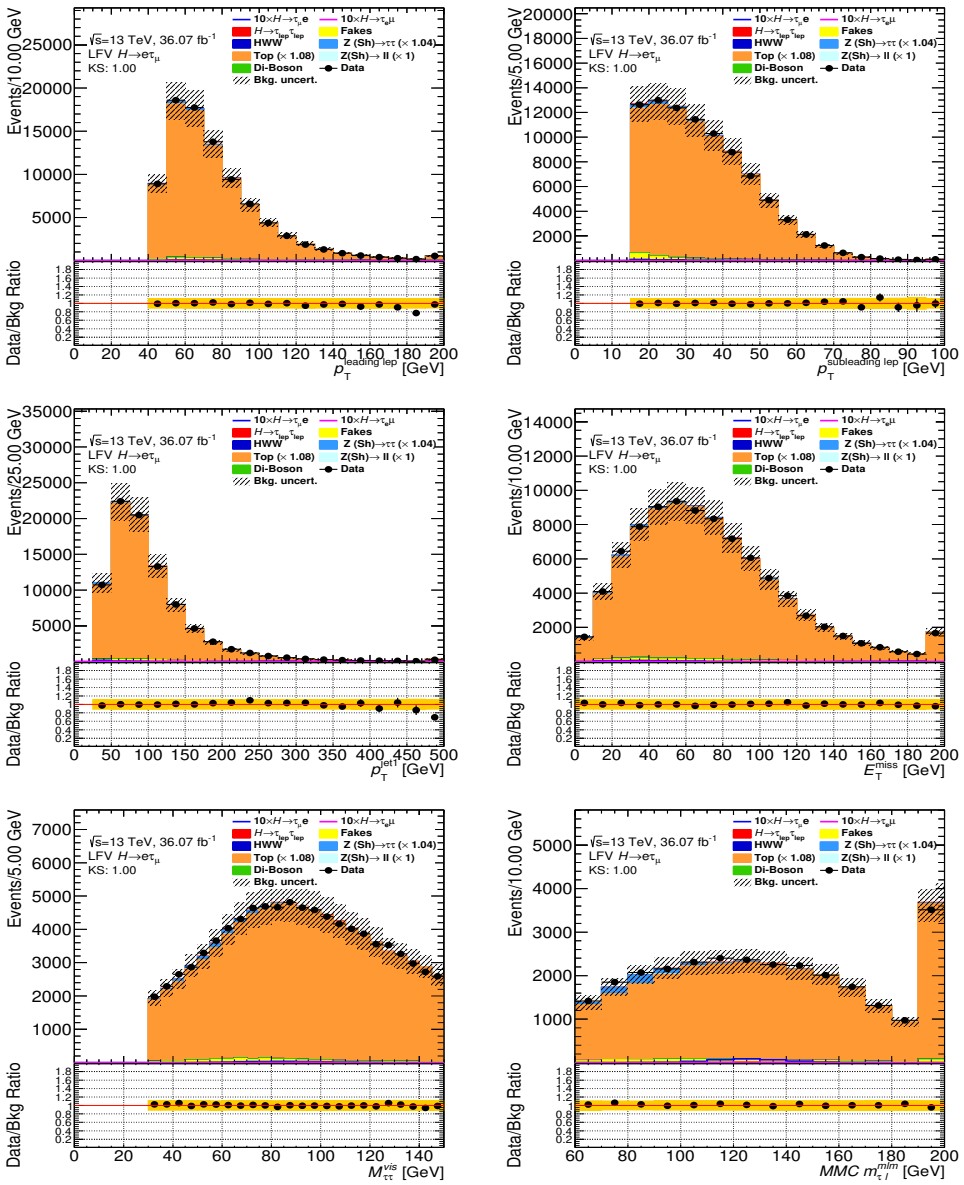

Figure 5.23: Top control region distributions for $e\tau_\mu$ events after baseline selection. Pre-fit normalization factors obtained in the baseline top-quark control region have been applied. Error bands include the statistical uncertainties and the systematic uncertainties on the background normalization.

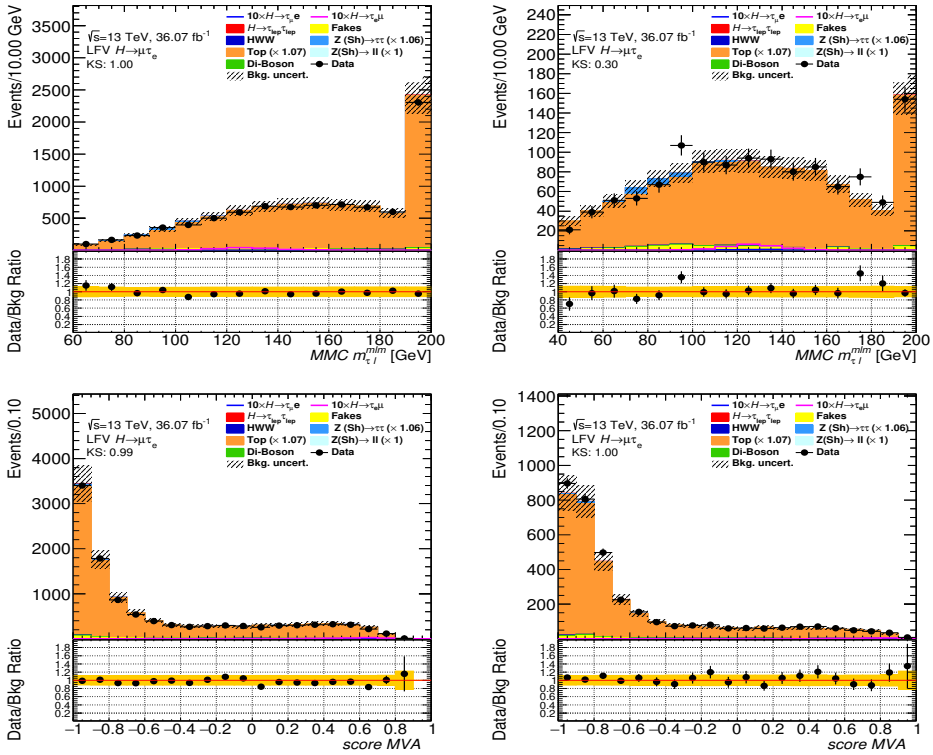

Figure 5.24: Top-quark control region distributions of the MMC mass and the BDT score for $\mu\tau_e$ events after non-VBF (left) and VBF (right) selection. Pre-fit normalization factors obtained in the baseline top control region have been applied. Error bands include the statistical uncertainties and the systematic uncertainties on the background normalization.

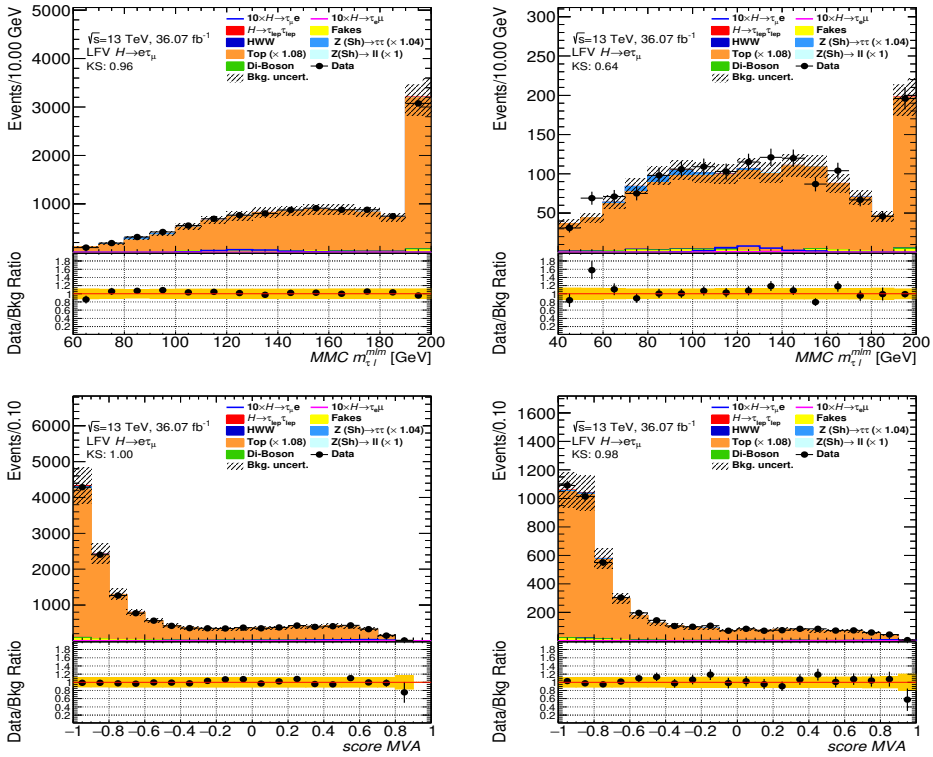

Figure 5.25: Top control region distributions of the MMC mass and the BDT score for $e\tau_\mu$ events after non-VBF (left) and VBF (right) selection. Pre-fit normalization factors obtained in the baseline top control region have been applied. Error bands include the statistical uncertainties and the systematic uncertainties on the background normalization.

5.4.2 $Z\tau\tau$ control region: yields and control plots

A control region is defined to constrain the $Z \to \tau\tau$ process. This control region is enriched in $Z \to \tau\tau$ background with a selection very close to the signal regions. The selection criteria is the same of the nominal selection, except that the transverse momentum of the leading lepton has to be $35\,\text{GeV} < p_{\text{T}}^{\ell_1} < 45\,\text{GeV}$. The $Z \to \tau\tau$ CR, has a purity of $\sim 80\%$ in the non-VBF category, while a lower purity of $\sim 60\%$ is observed in the VBF category. Yields of the $Z\tau\tau$ CR are shown in Tables 5.15 and 5.16. The most important kinematic distributions are shown in Figures 5.26 and 5.27 for the $\mu\tau_e$ and in Figures 5.28 and 5.29 for the $e\tau_\mu$.

Sample	$Z \to \tau\tau$ Control Region, $\mu\tau_e$		
	Baseline	VBF	Non-VBF
$H \to \tau\tau$	68.0 ± 0.6	1.63 ± 0.07	27.4 ± 0.4
$H \to WW$	53.9 ± 1.4	1.40 ± 0.10	14.4 ± 0.7
$Z \to \tau\tau$+jets	11650 ± 70	69 ± 5	3840 ± 30
$Z \to ee\,, \mu\mu$+jets	350 ± 70	1.6 ± 1.0	32 ± 20
$t\bar{t}$	496 ± 9	19.2 ± 1.9	167 ± 6
Diboson	1022 ± 13	7.1 ± 0.7	260 ± 6
Fake leptons	1770 ± 30	16 ± 2	598 ± 19
Total background	15410 ± 110	105 ± 6	4940 ± 40
$H \to \mu\tau_e$ signal	50.9 ± 0.6	1.31 ± 0.06	34.9 ± 0.6
$H \to e\tau_\mu$ signal	6.5 ± 0.2	0.19 ± 0.02	0.36 ± 0.08
Data	15410	102	5150

Table 5.15: $Z \to \tau\tau$ CR yields of the $\mu\tau_e$ channel for the baseline, VBF and non-VBF selections. $\mathcal{BR}(H \to \mu\tau_e)$ and $\mathcal{BR}(H \to e\tau_\mu)$ are assumed to be 1%. The top-quark and $Z \to \tau\tau$ predictions are scaled by the normalization factor obtained in the corresponding baseline control regions.

Sample	$Z \to \tau\tau$ Control Region, $e\tau_\mu$		
	Baseline	VBF	Non-VBF
$H \to \tau\tau$	82.3 ± 0.7	1.82 ± 0.08	33.9 ± 0.5
$H \to WW$	61.2 ± 1.6	1.7 ± 0.2	18.6 ± 0.8
$Z \to \tau\tau$+jets	13400 ± 70	69 ± 5	4750 ± 40
$Z \to ee\,, \mu\mu$+jets	210 ± 60	1.1 ± 0.5	27 ± 11
$t\bar{t}$	564 ± 10	25 ± 2	194 ± 6
Diboson	1131 ± 14	8.1 ± 0.7	296 ± 7
Fake leptons	1760 ± 40	17 ± 4	610 ± 20
Total background	17210 ± 100	123 ± 7	5930 ± 50
$H \to \mu\tau_e$ signal	4.5 ± 0.3	0.18 ± 0.02	0.49 ± 0.07
$H \to e\tau_\mu$ signal	59.3 ± 0.7	1.63 ± 0.07	40.8 ± 0.6
Data	17210	123	5880

Table 5.16: $Z \to \tau\tau$ CR yields of the $e\tau_\mu$ channel for the baseline, VBF and non-VBF selections. $\mathcal{BR}(H \to \mu\tau_e)$ and $\mathcal{BR}(H \to e\tau_\mu)$ are assumed to be 1%. The top-quark and $Z \to \tau\tau$ predictions are scaled by the normalization factor obtained in the corresponding baseline control regions.

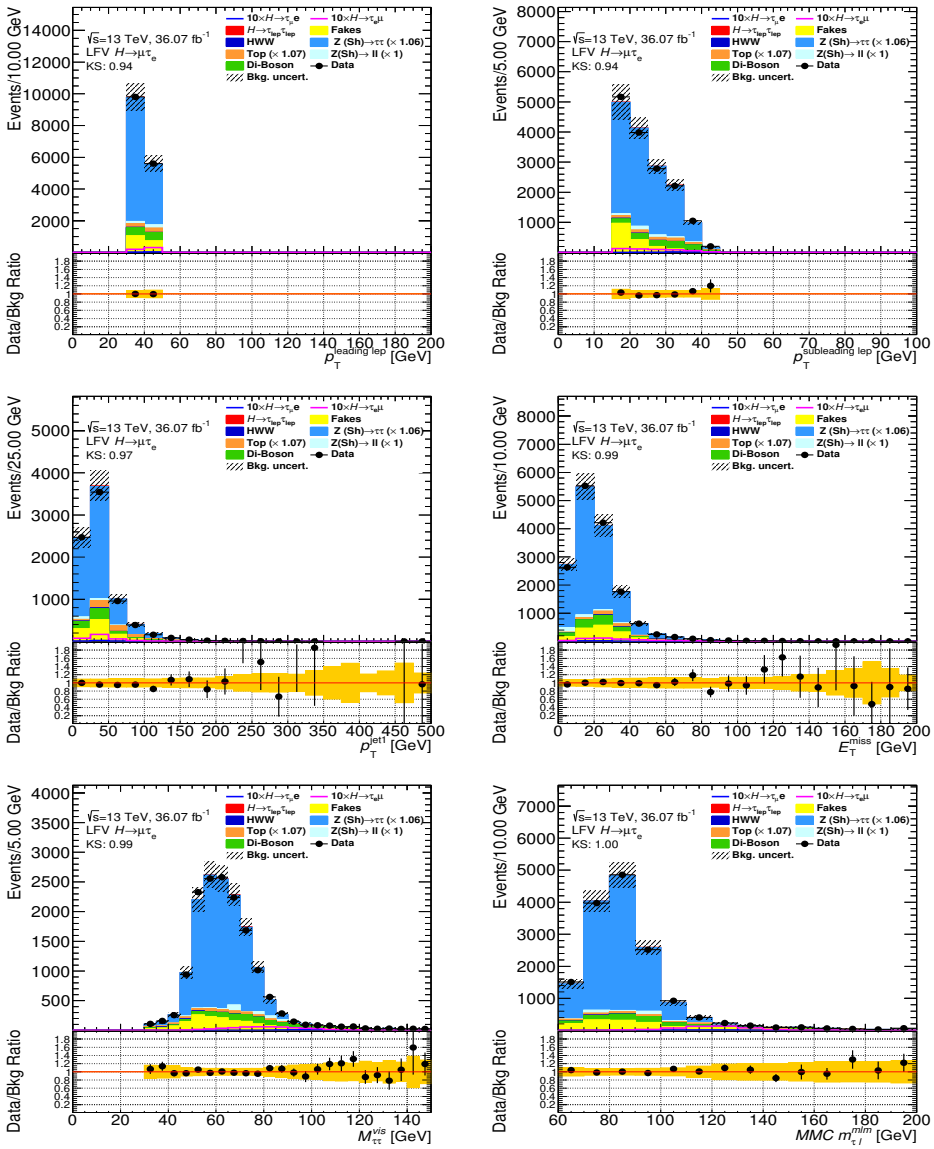

Figure 5.26: $Z \to \tau\tau$ control region distributions for $\mu\tau_e$ events after baseline selection. Pre-fit normalization factors obtained in the $Z\tau\tau$ CR have been applied, as described in section 5.4.3. Error bands include the statistical uncertainties and the systematic uncertainties on the background normalization.

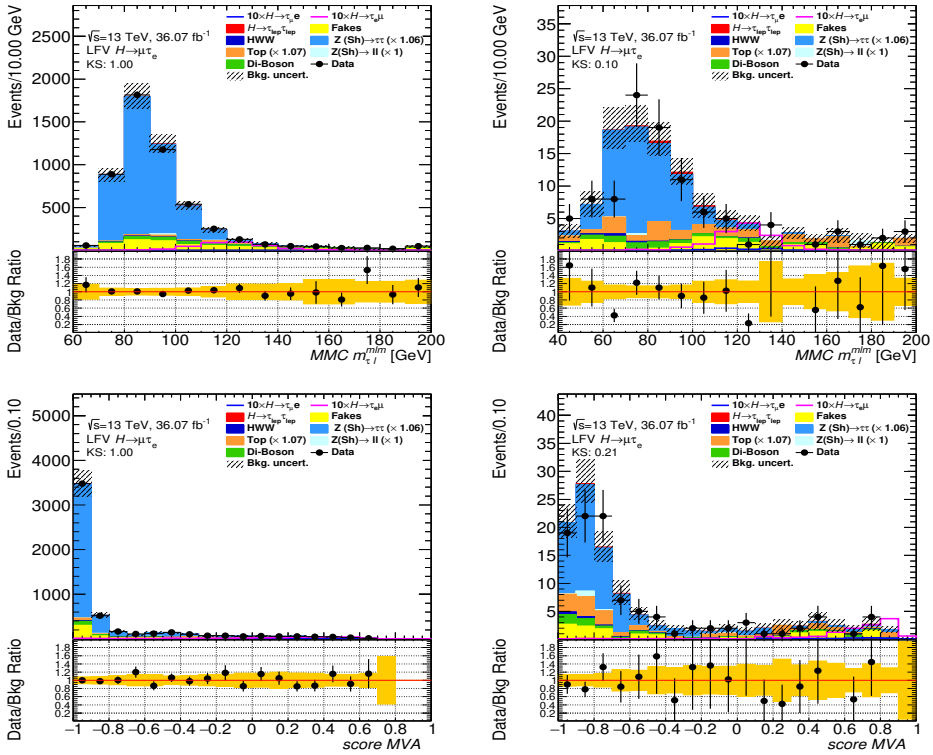

Figure 5.27: Distributions of the MMC mass and the BDT score for $\mu\tau_e$ events in the $Z \to \tau\tau$ control region after non-VBF (left) and VBF (right) selection. Pre-fit normalization factors obtained in the baseline $Z\tau\tau$ CR have been applied. Error bands include the statistical uncertainties and the systematic uncertainties on the background normalization.

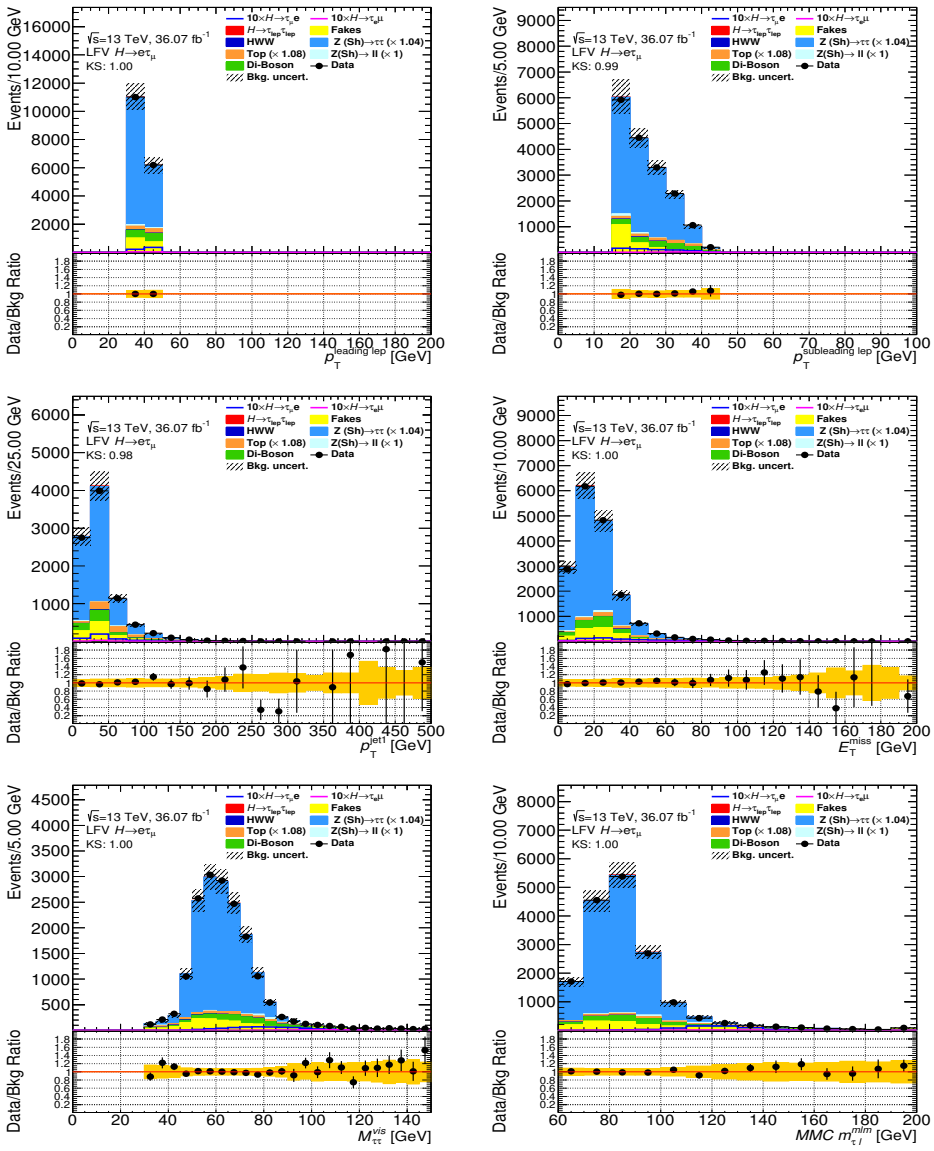

Figure 5.28: $Z \to \tau\tau$ control region distributions for $e\tau_\mu$ events after baseline selection. Pre-fit normalization factors obtained in the baseline $Z\tau\tau$ CR have been applied. Error bands include the statistical uncertainties and the systematic uncertainties on the background normalization.

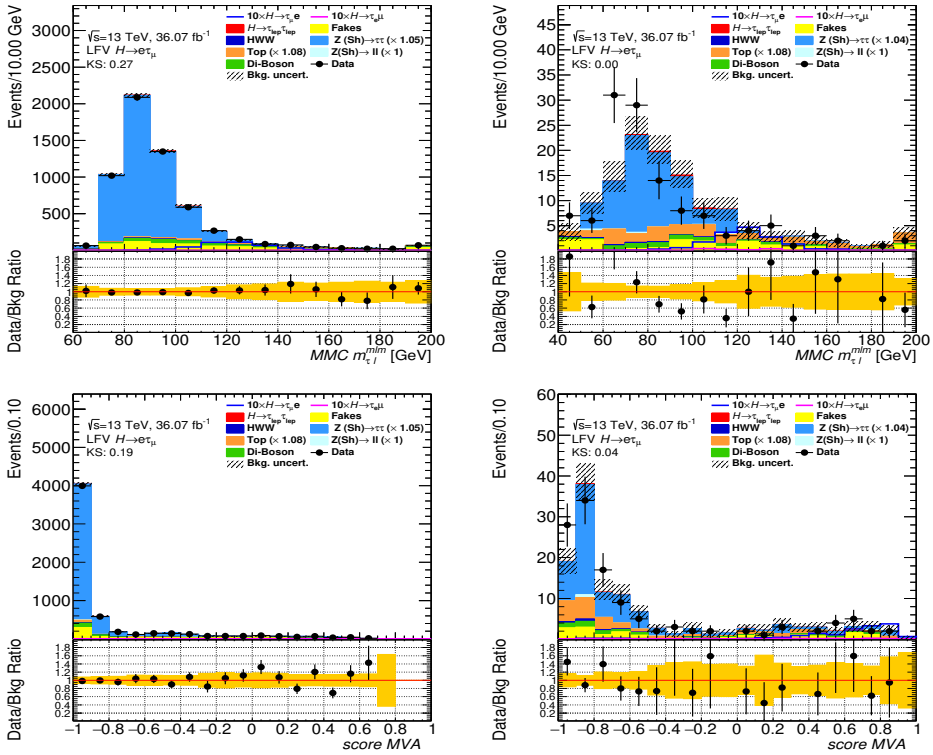

Figure 5.29: Distributions of the MMC mass and the BDT score for $e\tau_\mu$ events of the $Z \to \tau\tau$ control region after non-VBF (left) and VBF (right) selections. Pre-fit normalization factors obtained in the baseline $Z\tau\tau$ CR have been applied. Error bands include the statistical uncertainties and the systematic uncertainties on the background normalization.

5.4.3 Pre-fit normalization factors

Pre-fit normalization factors for the $Z \to \tau\tau$ and top-quark processes are extracted from the CRs of the baseline selection and applied to the events of the baseline selection as well as signal regions. Those pre-fit NFs are used only for plotting purpose while a different approach is used in the statistical fit, as discussed in 5.7.

To obtain the pre-fit normalization factors a linear system of two equations with two unknown variables is solved, using the yields of the CRs shown in 5.4.1 and 5.4.2. The system of equations 5.1, can be solved analytically by the Kramer technique,

$$\begin{aligned} \text{NF}(Z\tau\tau) \cdot \#_{Z\tau\tau}^{Top\text{CR}} + \text{NF}(\text{Top}) \cdot \#_{Top}^{Top\text{CR}} &= \#_{\text{Data}}^{Top\text{CR}} - \#_{\text{other}}^{Top\text{CR}} \\ \text{NF}(Z\tau\tau) \cdot \#_{Z\tau\tau}^{Z\tau\tau\text{CR}} + \text{NF}(\text{Top}) \cdot \#_{Top}^{Z\tau\tau\text{CR}} &= \#_{\text{Data}}^{Z\tau\tau\text{CR}} - \#_{\text{other}}^{Z\tau\tau\text{CR}} \end{aligned} \tag{5.1}$$

where $\text{NF}(Z\tau\tau)$ and $\text{NF}(\text{Top})$ are the normalization factors for the $Z\tau\tau$ and Top backgrounds respectively and $\#_{\text{background}}^{\text{CR}}$ is the event yield of the control region in the super-index for the background process written in the sub-index.

This system of equations has been solved for the $e\tau_\mu$ and $\mu\tau_e$ channel independently, and the results, considering only statistical uncertainties, are shown in Table 5.17.

Sample	Pre-fit NFs	
	$\mu\tau_e$	$e\tau_\mu$
$Z \to \tau\tau$+jets	1.0689 ± 0.0015	1.0474 ± 0.0011
Top-quark	1.0748 ± 0.0004	1.0801 ± 0.0003

Table 5.17: Pre-fit normalization factors of the $\mu\tau_e$ and $e\tau_\mu$ channels for the baseline selection.

5.5 The $H \to \ell\tau_{\text{had}}$ channel

An additional channel is exploited in the $H \to \ell\tau$ searches: the semi-leptonic channel, $H \to \ell\tau_{\text{had}}$. In this channel, a high energetic light-lepton and a τ_{had} shower are expected in the final state. The hadronic decays of the tau lepton are more common in nature and therefore a higher statistics is expected than in the fully-leptonic decay channel.

Similarly to $H \to \ell\tau_{\ell'}$, two independent final states are considered: $H \to e\tau_{\text{had}}$ and $H \to \mu\tau_{\text{had}}$. The strategy used in this search to enhance the signal over the background is similar to the fully-leptonic case where selection criteria are applied to reduce the background and later in the signal regions a multivariate approach using boosted decision trees is employed in order to separate the LFV Higgs boson signal from other processes. Contrary to the $\ell\tau_{\ell'}$ channel, in the $\ell\tau_{\text{had}}$ no control regions are used, but two validation regions are defined to cross-check the agreement between data and MC.

The fakes background originates from multi-jet events and W-boson production in association with jets, where the jets are misidentified as $\tau_{\text{had-vis}}$. As in the $\tau_{\text{lep}}\tau_{\text{had}}$ channel of the $H \to \tau\tau$ analysis, explained in 4.4.1, a fake-factor method [117] is used to estimate the contribution of each component separately. The fake factor consists of the ratio of the number of events where the highest-p_{T} jet is identified as a Tight $\tau_{\text{had-vis}}$ candidate to the number of events where the highest-p_{T} jet fails the nominal τ identification criterion, but satisfies a looser criterion in a CR.

The $H \to \ell\tau_{\text{had}}$ selection consists in a preselection and two orthogonal signal regions, VBF and non-VBF, that are later exploited in the statistical fit. The selection uses the topology of the Higgs boson decay to apply requirements in the kinematic variables.

The two leptons must have opposite charge and the p_{T} of the light-lepton and the tau must be $p_{\text{T}}^{\ell} > 27.3\,\text{GeV}$ and $p_{\text{T}}^{\tau_{\text{had-vis}}} > 25\,\text{GeV}$ respectively. To reduce the W+jets background the sum of the azimuthal separation must be $\sum_{i=\ell,\tau_{\text{had-vis}}} \cos\Delta\phi(i, E_{\text{T}}^{\text{miss}}) > -0.35$. Moreover, for the baseline selection, a criterion based on the pseudorapidity difference between the leptons is applied $|\Delta\eta(\ell, \tau_{\text{had-vis}})| <$

2. This allows to reduce the misidentified $\tau_{\text{had-vis}}$ candidates. Finally, to reduce the top processes a b-veto requirement is applied.

The VBF category exploits the jet kinematic variables. The selection is harmonized with the $\ell\tau_{\ell'}$ channel, shown in Table 5.3 with an additional criteria in the tau momentum that must be $p_{\text{T}}^{\tau_{\text{had-vis}}} > 45\,\text{GeV}$. On the other hand, the non-VBF category accepts events that have passed the baseline, but have failed the VBF criteria.

The summary of the $\ell\tau_{\text{had}}$ selection is shown in Table 5.18 and relevant distributions of the channel are shown in Figure 5.30.

	$\ell\tau_{\text{had}}$
Baseline	exactly 1ℓ and $1\tau_{\text{had-vis}}$ with OS $p_{\text{T}}^{\ell} > 27.3\,\text{GeV}$ $p_{\text{T}}^{\tau_{\text{had-vis}}} > 25\,\text{GeV}$, $\lvert\eta^{\tau_{\text{had-vis}}}\rvert < 2.4$ $\sum_{i=\ell,\tau_{\text{had-vis}}} \cos\Delta\phi(i, E_{\text{T}}^{\text{miss}}) > -0.35$ # of b-jets $= 0$ $\lvert\Delta\eta(\ell, \tau_{\text{had-vis}})\rvert < 2$
VBF SR	Pass preselection # of jets $\geqslant 2$ $p_{\text{T}}^{j_1} > 40\,\text{GeV}$ $p_{\text{T}}^{j_2} > 30\,\text{GeV}$ $m_{jj} > 400\,\text{GeV}$ $\lvert\Delta\eta_{jj}\rvert > 3$ $p_{\text{T}}^{\tau_{\text{had-vis}}} > 45\,\text{GeV}$
Non-VBF SR	Pass preselection but fail VBF

Table 5.18: Summary of the event selection for the $\ell\tau_{\text{had}}$ channel at the baseline region.

After the baseline selection criteria, the events are used also to train and validate the BDT algorithms to enhance the signal separation from the background in the individual

channels and categories. Table 5.20 summarizes the variables used in the training of the BDT algorithm.

One difference between the $\ell\tau_{\ell'}$ and $\ell\tau_{\text{had}}$ channels is the choice of the mass reconstruction algorithm. While in the $\ell\tau_{\ell'}$ case the MMC mass reconstruction is used, the $\ell\tau_{\text{had}}$ channel employs the collinear mass, m_{coll}, defined in equation 5.2. It assumes that the momentum of the τ-lepton is $\overrightarrow{p}_{\text{T}}^{\,\tau} = \overrightarrow{p}_{\text{T}}^{\,\tau_{\text{had-vis}}} + \overrightarrow{E}_{\text{T}}^{\text{miss}}$ and the direction of the tau in the polar plane is the same of its visible decay products.

$$m_{\text{coll}} = \sqrt{2p_{\text{T}}^{\ell}\left(p_{\text{T}}^{\tau_{\text{had-vis}}} + E_{\text{T}}^{\text{miss}}\right)\left(\cosh(\Delta\eta)\cos(\Delta\phi)\right)} \tag{5.2}$$

A table comparing the performance of the MVA to the CBA is presented in Table 5.19 for the signal regions of the $\ell\tau_{\text{had}}$ channel. In the MVA analysis the BDT output is used as final discriminant while the m_{coll} is used by the cut-based analysis. The BDT achieves an improvement of $23\%(36\%)$ over the CBA for the $\mu\tau_{\text{had}}(e\tau_{\text{had}})$ channel. These values are calculated from the quadratic sum of the Asimov significance of each bin (Equation 4.3).

	Search	Non-VBF	VBF	Combined
CBA	$\mu\tau_{\text{had}}$	7.20	2.29	7.56
	$e\tau_{\text{had}}$	6.32	2.32	6.73
MVA	$\mu\tau_{\text{had}}$	8.79	3.16	9.34
	$e\tau_{\text{had}}$	8.59	3.29	9.20

Table 5.19: Binned significance values in the $\ell\tau_{\text{had}}$ signal regions. The improvement by using the BDT output distribution in the signal region is approximately $23\%(36\%)$ over the use of m_{coll} for the $\mu\tau_{\text{had}}$ and $e\tau_{\text{had}}$ respectively.

Variables	Non-VBF	VBF
Collinear mass approximation m_{coll}	•	•
The momentum of the leading lepton: p_{T}^{ℓ}	•	•
The momentum of the tau leptons: $p_{\text{T}}^{\tau_{\text{had-vis}}}$	•	•
The angular difference between the leptons $\Delta R(\ell, \tau_{\text{had-vis}})$	•	•
Transverse mass between leading lepton and $E_{\text{T}}^{\text{miss}}$: $m_{\text{T}}(\ell, E_{\text{T}}^{\text{miss}})$	•	•
Transverse mass between tau and $E_{\text{T}}^{\text{miss}}$: $m_{\text{T}}(\tau_{\text{had-vis}}, E_{\text{T}}^{\text{miss}})$	•	•
$\sum_{i=\ell,\tau_{\text{had-vis}}} \cos\Delta\phi(i, E_{\text{T}}^{\text{miss}})$	•	•
The missing transverse momentum: $E_{\text{T}}^{\text{miss}}$	•	•
The angular difference between the light-leptons and $E_{\text{T}}^{\text{miss}}$: $\Delta\phi(\ell, E_{\text{T}}^{\text{miss}})$	•	
The visible mass: m_{vis}	•	
Pseudorapidity difference between the leptons $\Delta\eta(\ell, \tau_{\text{had-vis}})$	•	
The pseudorapidity of the leptons η^{ℓ} and $\eta^{\tau}_{\text{had-vis}}$	•	
The angular distance of the leading lepton : ϕ^{ℓ}	•	
The angular distance of the tau : $\phi^{\tau_{\text{had-vis}}}$	•	
The angular distance of the $E_{\text{T}}^{\text{miss}}$: $\phi(E_{\text{T}}^{\text{miss}})$	•	
The angular difference between the tau and $E_{\text{T}}^{\text{miss}}$: $\Delta\phi(\tau_{\text{had-vis}}, E_{\text{T}}^{\text{miss}})$		•
The invariant mass of the leading jets: m_{jj}		•
The pseudorapidity difference between the leading jets $\Delta\eta_{jj}$		•

Table 5.20: List of variables for the MVA analysis in the non-VBF and VBF categories for the $\ell\tau_{\text{had}}$ channel. The variables are listed in no particular order.

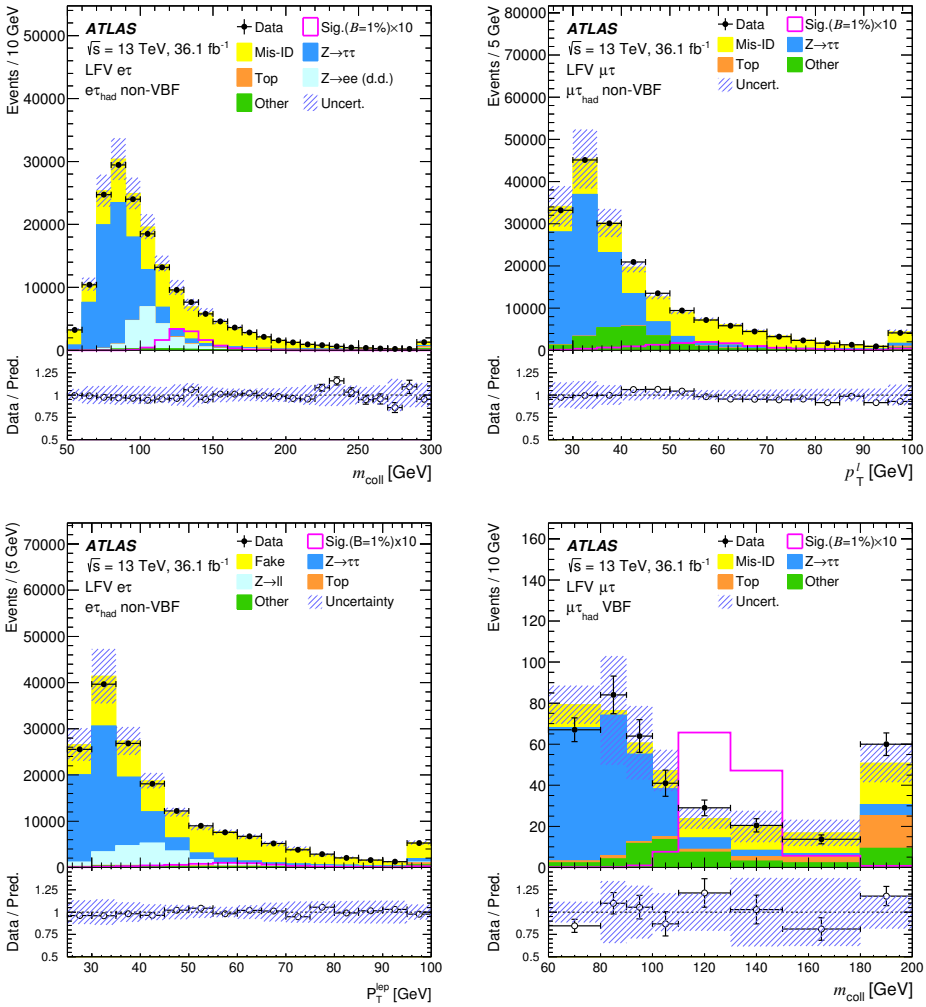

Figure 5.30: Post-fit distributions of representative kinematic quantities for different channels and categories before the fit. Entries with values that would exceed the x-axis range are included in the last bin of each distribution. The size of the combined statistical, experimental and theoretical uncertainties in the background is indicated by the hatched bands. The $H \to e\tau$ ($H \to \mu\tau$) signal overlaid in top (bottom) plots assumes $\mathcal{BR}(H \to \ell\tau) = 1\%$ and is enhanced by a factor 10. In the data/background prediction ratio plots, points outside the displayed y-axis range are shown by arrows. Reproduced from Ref. [134] under CC-BY-4.0 licence.

5.6 Systematics

The systematic uncertainties considered in the LFV search are the same discussed in Section 4.5. In particular, the uncertainty of the LFV signal production are estimated with the same procedure used in the Higgs boson cross-section measurement and follows the recommendations of the LHC Higgs Cross-Section Working Group [125]. The systematic uncertainties and their impact on the best-fit value of $\mathcal{BR}$ in the $H \to \ell\tau$ searches are summarized in Table 5.21.

Source of uncertainty	Impact on $\mathcal{B}(H \to e\tau)$ [%]		Impact on $\mathcal{B}(H \to \mu\tau)$ [%]	
	Measured	Expected	Measured	Expected
Electron	$+0.05/-0.05$	$+0.06/-0.06$	$+0.03/-0.03$	$+0.02/-0.02$
Muon	$+0.04/-0.04$	$+0.04/-0.04$	$+0.10/-0.10$	$+0.08/-0.10$
$\tau_{\text{had-vis}}$	$+0.02/-0.02$	$+0.02/-0.02$	$+0.04/-0.04$	$+0.04/-0.05$
Jet	$+0.09/-0.08$	$+0.09/-0.09$	$+0.11/-0.12$	$+0.11/-0.12$
$E_{\text{T}}^{\text{miss}}$	$+0.02/-0.02$	$+0.02/-0.03$	$+0.05/-0.08$	$+0.03/-0.05$
b-tag	$+0.02/-0.03$	$+0.03/-0.03$	$+0.01/-0.01$	$+0.01/-0.01$
Mis-ID backg. ($\tau_{\text{lep}}\tau_{\text{lep}}$)	$+0.08/-0.07$	$+0.09/-0.08$	$+0.07/-0.07$	$+0.07/-0.07$
Mis-ID backg. ($\tau_{\text{lep}}\tau_{\text{had}}$)	$+0.12/-0.11$	$+0.11/-0.12$	$+0.11/-0.11$	$+0.10/-0.10$
Pile-up modelling	$+0.02/-0.01$	$+0.01/-0.01$	$+0.05/-0.03$	$+0.08/-0.06$
Luminosity	< 0.01	< 0.01	< 0.01	< 0.01
Background norm.	$+0.05/-0.04$	$+0.05/-0.03$	$+0.04/-0.02$	$+0.05/-0.03$
Theor. uncert. (backg.)	$+0.04/-0.03$	$+0.04/-0.03$	$+0.08/-0.07$	$+0.09/-0.09$
Theor. uncert. (signal)	$+0.01/-0.01$	$+0.01/-0.01$	$+0.04/-0.02$	$+0.02/-0.02$
MC statistics	$+0.04/-0.04$	$+0.03/-0.03$	$+0.04/-0.04$	$+0.05/-0.04$
Full systematic	$+0.17/-0.16$	$+0.17/-0.17$	$+0.18/-0.18$	$+0.19/-0.20$
Data statistics	$+0.07/-0.07$	$+0.07/-0.07$	$+0.07/-0.07$	$+0.08/-0.08$
Total	$+0.18/-0.17$	$+0.18/-0.18$	$+0.19/-0.19$	$+0.20/-0.21$

Table 5.21: Summary of the systematic uncertainties and their impact on the best-fit value of the branching ratios of $H \to e\tau$ and $H \to \mu\tau$. The measured values are obtained by the fit to data, while the expected values are determined by the fit to a background-only sample, see 5.7.

The fakes uncertainties are discussed in Section A.1 and their values in percentage are summarized in Table 5.22 for each category as a function of the p_{T} of the subleading lepton.

Systematics uncertainties (%)	VBF category				Non-VBF category			
SS Non-closure	p_{T} (GeV)	15 - 20	20 - 25	25 -	p_{T} (GeV)	15 - 20	20 - 25	25 -
	$e\mu$	36%	$^{+183}_{-100}$%		$e\mu$	9.9%	27.8%	28.2%
	μe	44%	86%		μe	12.1%	13.2%	11.1%
Top fake fraction	p_{T} (GeV)	15 - 20	20 - 25	25 -	p_{T} (GeV)	15 - 20	20 - 25	25 -
	$e\mu$		4.8%		$e\mu$		4.9%	
	μ		7.3%		μe		7.3%	
Heavy flavour contents	p_{T} (GeV)	15 - 20	20 - 25	25 -	p_{T} (GeV)	15 - 20	20 - 25	25 -
	$e\mu$	30%	31%		$e\mu$	20.5%	31.1%	79.2%
	μe	20%	36%		μe	33.6%	19.8%	26.6%
QCD closure	p_{T} (GeV)	15 - 20	20 - 25	25 -	p_{T} (GeV)	15 - 20	20 - 25	25 -
	$e\mu$		1.4%		$e\mu$		1.4%	
	μe		0.5%		μe		0.5%	
$\Delta\phi$ Corrections	p_{T} (GeV)	15 - 20	20 - 25	25 -	p_{T} (GeV)	15 - 20	20 - 25	25 -
	$e\mu$	15.3%	24.1%	34.5%	$e\mu$	15.6%	16.8%	17.1%
	μe	15.3%	20.6%	17.0%	μe	14.2%	15.8%	16.6%

Table 5.22: Systematic uncertainties for the fakes background estimation in the $H \to \tau\ell$ search. The correction in the angular difference between the leptons and the $E_{\mathrm{T}}^{\mathrm{miss}}$ is also considered.

5.7 Statistical analysis and results

The statistical analysis uses a binned likelihood function [124], constructed as a product of Gaussian and Poisson probability terms over all bins considered in the search. This function depends on the branching ratio $\mathcal{BR}(H \to \tau\ell)$, and a set of nuisance parameters θ that encode the effect of systematic uncertainties in the signal and background expectations. All nuisance parameters are implemented in the likelihood function as Gaussian or log-normal constraints. The normalization factors of the Top-quark and $Z \to \tau\tau$ background components in the $\ell\tau_{\ell'}$ channel are unconstrained parameters of the fit.

The searches for $H \to e\tau$ and $H \to \mu\tau$ are treated independently because either of the two can have a branching ratio large enough to be observed. In each search, the analysis exploits the four signal regions ($\ell\tau_{\ell'}$ and $\ell\tau_{\mathrm{had}}$ VBF and non-VBF SRs) and the two control regions used to constrain the major backgrounds ($\ell\tau_{\ell'}$ $Z\tau\tau$ and Top CRs). The BDT output distributions of all signal regions are analysed to test the presence of signal, simultaneously with the event yields in the control regions.

The estimation of the parameter of interest, the branching ratio of the LFV decay, is calculated with the profile likelihood ratio test statistic [124,139].

In order to maximise the significance in the final fit a binning optimization was performed in the BDT score distribution between the range $-1 <$ BDT score< 1. The procedure follows the same three steps used in the $H \to \tau\tau$ cross-section measurement, described in section 4.6.

5.7.1 Data fit

The discriminant distributions after the statistical fit in each channel are shown in Figures 5.31 and 5.32, where a good agreement between data and the expected backgrounds is observed. The event yields provided by the fit are summarized in Tables 5.23 and 5.24 for each search. The smaller yields in the non-VBF category for $\ell\tau_{\ell'}$ than for $\ell\tau_{\text{had}}$ are due to the tighter selection criteria defined for the channel.

	$\mu\tau_e$		$\mu\tau_{\text{had}}$	
	Non-VBF	VBF	Non-VBF	Non-VBF
$Z \to \tau\tau$	1860 ± 130	144 ± 26	96100 ± 2000	274 ± 33
Top-quark	1260 ± 130	390 ± 34	1620 ± 210	51 ± 10
Mis-identify	1340 ± 210	41 ± 21	63900 ± 1600	149 ± 33
Other	1180 ± 140	168 ± 18	23000 ± 1000	104 ± 15
Total	5640 ± 100	743 ± 29	184500 ± 1200	580 ± 30
Signal	287 ± 23	14.6 ± 1.9	1200 ± 120	25 ± 5
Data	5664	723	184508	58324

Table 5.23: Event yields and predictions as determined by the background-only fit in different signal regions of the $H \to \mu\tau$ analysis. Uncertainties include both the statistical and systematic contributions. "Other" contains diboson, $Z \to \ell\ell$, $H \to \tau\tau$ and $H \to WW$ background processes. The normalization factors ($\ell\tau_{\ell'}$ channel only) of top-quark and $Z \to \tau\tau$ background components are determined by the fit. The expected signal yields are given for $\mathcal{BR}(H \to \mu\tau) = 1\%$.

The best fit $\mathcal{BR}$ and upper limits are computed assuming $\mathcal{BR}(H \to \mu\tau) = 0$ for the $H \to e\tau$ search and $\mathcal{BR}(H \to e\tau) = 0$ for the $H \to \mu\tau$ search. The impact of the systematic uncertainties in the determination of the branching ratio of the LFV decays

	$e\tau_\mu$		$e\tau_{\text{had}}$	
	Non-VBF	VBF	Non-VBF	Non-VBF
$Z \to \tau\tau$	2470 ± 230	221 ± 34	73800 ± 1900	290 ± 40
Top-quark	1640 ± 140	490 ± 40	1580 ± 190	56 ± 12
Mis-identify	1330 ± 250	73 ± 33	74400 ± 1600	140 ± 50
Other	1700 ± 80	220 ± 15	18960 ± 2000	82 ± 13
Total	7130 ± 100	1003 ± 33	168700 ± 1000	570 ± 40
Signal	379 ± 31	19.8 ± 2.7	1180 ± 110	25 ± 4
Data	7128	992	168883	572

Table 5.24: Event yields and predictions as determined by the background-only fit in different signal regions of the $H \to e\tau$ analysis. Uncertainties include both the statistical and systematic contributions. "Other" contains diboson, $Z \to \ell\ell$, $H \to \tau\tau$ and $H \to WW$ background processes. The uncertainty of the total background includes all correlations between channels. The normalizations ($\ell\tau_{\ell'}$ channel only) of top-quark and $Z \to \tau\tau$ background components are determined by the fit. The expected signal yields are given for $\mathcal{BR}(H \to e\tau) = 1\%$.

are shown in Table 5.21 of section 5.6 and the combined impact of all systematic and statistical uncertainties ranges from 0.17% to 0.19%. The highest impact uncertainties in the parameter of interest are the ones related with the misidentified backgrounds for both channels and those related to the jet energy scale and resolution.

The best-fit values of the LFV decays branching ratios of the Higgs boson are $0.15^{+0.18}_{-0.17}\%$ and $-0.22 \pm 0.19\%$, for the $H \to e\tau$ and $H \to \mu\tau$ respectively. Due to the absence of significant excess, upper limits on the LFV branching ratios are set for a Higgs boson with $m_H = 125$ GeV. The observed (expected) 95% CL upper limits are $0.47\%(0.34^{+0.13}_{-0.10}\%)$ and $0.28\%(0.37^{+0.14}_{-0.10}\%)$ for the $H \to e\tau$ and $H \to \mu\tau$ decay respectively. The upper limits obtained for the 2015-2016 period are significantly lower than the corresponding ATLAS Run 1 limits [132], which were $\mathcal{BR}(H \to e\tau) < 1.04\%$ and $\mathcal{BR}(H \to \mu\tau) < 1.43\%$. Figure 5.33 shows upper limits for both searches and the best-fit branching ratios denoted by $\widehat{\mu}$. Besides, the CMS collaboration has also provided 95% CL upper limits on the $H \to e\tau$ and $H \to \mu\tau$ branching ratios of 0.61% and 0.25%, respectively, using CMS Run 2 data for an integrated luminosity of

35.9 fb^{-1} [133]. The summary of 95% CL upper limits obtained by ATLAS and CMS experiments is shown in Table 5.25.

The non-diagonal terms of the Yukawa matrix, Y_L, equation 1.22, are related with the $\mathcal{BR}$ of the LFV Higgs boson decay, by the formula:

$$\sqrt{|Y_{\ell\tau}|^2 + |Y_{\tau\ell}|^2} = \frac{8\pi}{m_H} \frac{\mathcal{BR}(H \to \ell\tau)}{1 - \mathcal{BR}(H \to \ell\tau)} \Gamma_H^{\text{SM}} \tag{5.3}$$

where $\Gamma_H^{\text{SM}} = 4.07$ MeV stands for the Higgs boson width as predicted by the SM. The observed limits on the branching ratio correspond to the following limits on the coupling matrix elements, $\sqrt{|Y_{e\tau}|^2 + |Y_{\tau e}|^2} = 0.0020$ and $\sqrt{|Y_{\mu\tau}|^2 + |Y_{\tau\mu}|^2} = 0.0015$. Those limits are shown in Figure 5.34, together with the limits from the ATLAS Run 1 search.

	95% CL upper limits	
	$\mathcal{BR}(H \to \tau\mu)[\%]$	$\mathcal{BR}(H \to \tau e)[\%]$
ATLAS Run 1	1.43	1.04
ATLAS Run 2	0.28	0.47
CMS Run 2	0.25	0.61

Table 5.25: Comparison of the 95% CL upper limits on the branching ratio of the $H \to \mu\tau$ and $H \to e\tau$ decays for the ATLAS and CMS experiments.

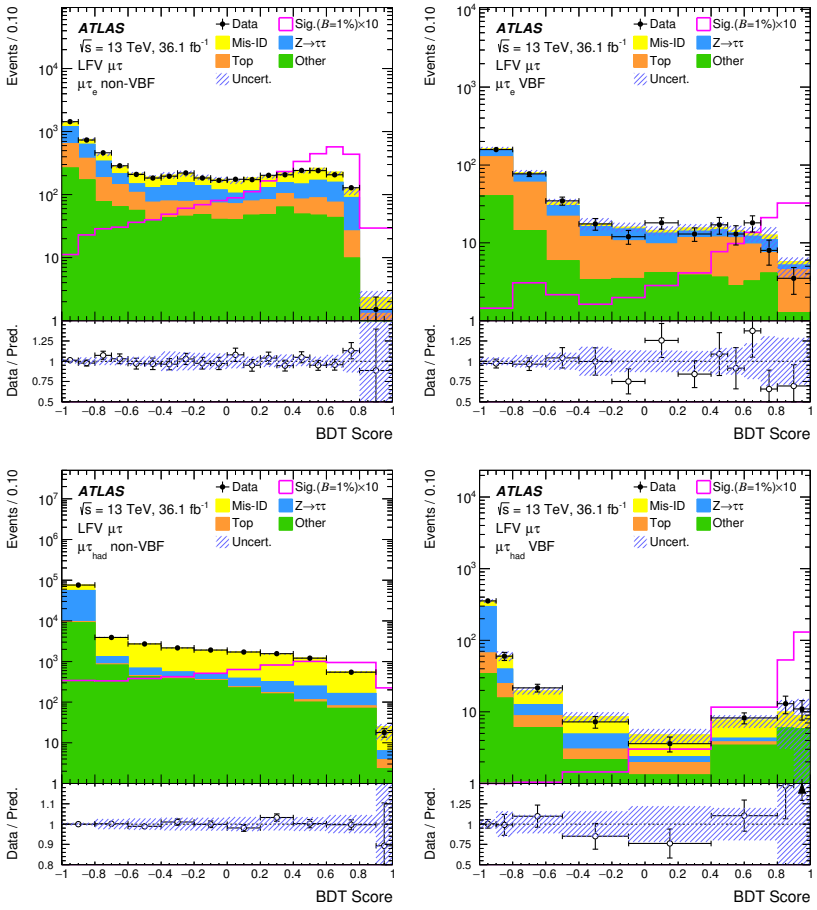

Figure 5.31: Distributions of the BDT score after the background+signal fit in each signal region of the $\mu\tau$ search. The LFV signal is overlaid, normalized to $\mathcal{BR}(H \to \mu\tau) = 1\%$ and enhanced by a factor 10 for visibility. The top and bottom plots display $\mu\tau_e$ and $\mu\tau_{\text{had}}$ BDT scores respectively, the left (right) column corresponds to the non-VBF (VBF) category. The size of the combined statistical, experimental and theoretical uncertainties of the background is indicated by the hatched bands. The binning is shown as in the statistical analysis. In the data/background prediction ratio plots, points outside the displayed y-axis range are shown by arrows. Reproduced from Ref. [117] under CC-BY-4.0 licence.

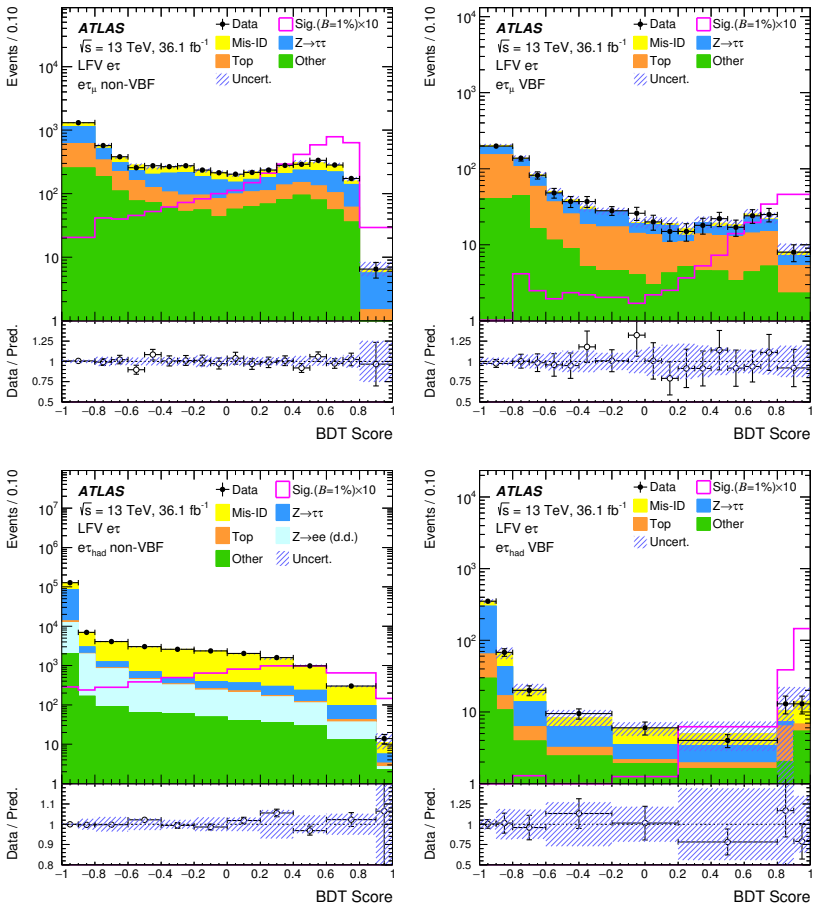

Figure 5.32: Distributions of the BDT score after the background+signal fit in each signal region of the $e\tau$ search. The LFV signal is overlaid, normalized to $\mathcal{BR}(H \to e\tau) = 1\%$ and enhanced by a factor 10 for visibility. The top and bottom plots display $e\tau_\mu$ and $e\tau_{\text{had}}$ BDT scores respectively, the left (right) column corresponds to the non-VBF (VBF) category. The size of the combined statistical, experimental and theoretical uncertainties of the background is indicated by the hatched bands. The binning is shown as in the statistical analysis. Reproduced from Ref. [117] under CC-BY-4.0 licence.

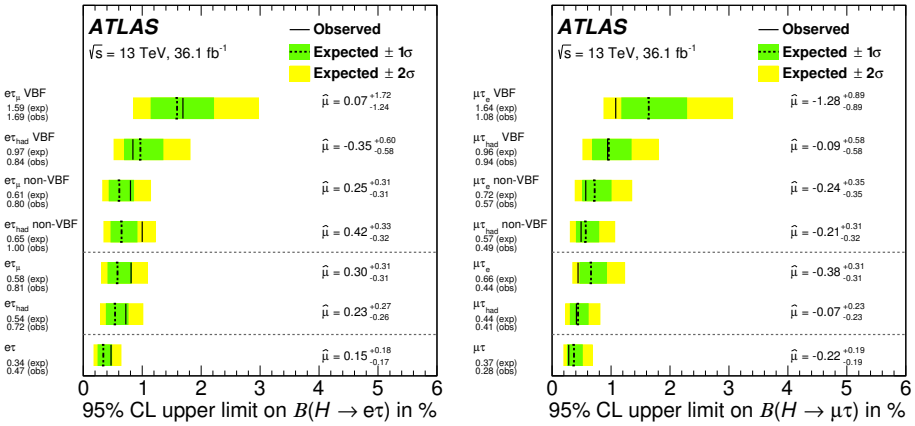

Figure 5.33: Upper limits at 95% CL on the LFV branching ratios of the Higgs boson, $H \to e\tau$ (left) and $H \to \mu\tau$ (right), indicated by solid and dashed lines. Best-fit values of the branching ratios ($\hat{\mu}$) are also given, in %. The limits are computed while assuming that $\mathcal{BR}(H \to \mu\tau) = 0$ (left) and $\mathcal{BR}(H \to e\tau) = 0$ (right). On the top part, the results of the fits are shown when only the data of an individual channel, or of an individual category, are used. In these cases, the signal and control regions from all other channels/categories are removed from the fit. These results are finally compared with the full fit displayed in the last row. Reproduced from Ref. [117] under CC-BY-4.0 licence.

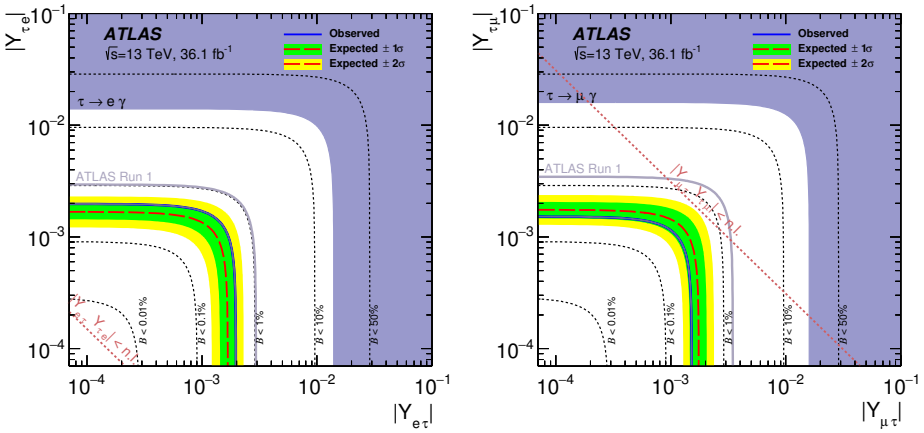

Figure 5.34: Upper limits on the absolute value of the couplings $Y_{\tau\ell}$ and $Y_{\ell\tau}$ together with the limits from the ATLAS Run 1 analysis (light grey line) and the most stringent indirect limits from $\tau \to \ell\gamma$ searches (dark purple region). Also indicated are the lines corresponding to different branching ratios (0.01%, 0.1%, 1%, 10% and 50%) and the naturalness limit (denoted n.l.) $|Y_{\tau\ell}Y_{\ell\tau}| \lesssim \frac{m_\tau m_\ell}{v^2}$ [35] where v is the vacuum expectation value of the Higgs field. Reproduced from Ref. [117] under CC-BY-4.0 licence.

6. Conclusions

One of the most powerful framework to describe the subatomic world of particle physics is the Standard Model. It have been tested up to the TeV scale giving satisfactory results in a wide variety of phenomena. However, many questions are still unanswered.

The work of this thesis is devoted to search for new physics beyond the Standard Model and to measure the Higgs boson cross-section in the di-τ final state. The thesis employs 36.1 fb^{-1} of data collected at $\sqrt{s} = 13$ TeV recorded by the ATLAS experiment.

Firstly, a measurement of the production cross-section of the Higgs boson decaying into a pair of tau leptons was presented. This measurement is important because at the present LHC running conditions this is the only possible measure of the lepton Yukawa coupling.

The analysis measured the ggF and the VBF production modes of the Higgs boson. After the event selection, a maximum-likelihood fit is performed to measure the cross-section of the $H \to \tau\tau$ process. The first parameter fitted has been the total cross-section of the $H \to \tau\tau$ production process and a value of $\sigma_{H\to\tau\tau} = 3.77^{+0.60}_{-0.59}(\text{stat})^{+0.87}_{-0.74}(\text{syst})$ pb is obtained. Additionally, the ggF and the VBF production mode cross-section have been fitted independently The best fit values obtained are $\sigma^{VBF}_{H\to\tau\tau} = 0.25 \pm 0.09(\text{stat})^{+0.11}_{-0.9}(\text{syst})$ pb and $\sigma^{ggF}_{H\to\tau\tau} = 3.1 \pm 1.0(\text{stat})^{-1.3}_{+1.6}(\text{syst})$ pb for the two production precesses. All measurement are consistent with the predictions for a SM Higgs boson of 125 GeV of mass and the measured signal strength is $\mu_{H\to\tau\tau} = 1.09^{+0.18}_{-0.17}(\text{stat})^{+0.26}_{-0.22}(\text{syst})^{+0.11}_{-0.16}(\text{theory syst})$.

The other analysis presented in this thesis has been the direct search for Higgs boson decays where the lepton flavour is violated, $H \to e\tau$ and $H \to \mu\tau$. Similarly to the $H \to \tau\tau$ cross-section measurement, two signal categories have been defined

for the ggF and VBF production modes of the Higgs boson. Moreover, to enhance the signal to background separation, the analysis used MVA algorithms. After the selection criteria, a maximum-likelihood fit has been performed to measure the branching ratio of the two decays. The best fit values obtained for the branching ratios are $0.15^{+0.18}_{-0.17}\%$ and $-0.22 \pm 0.19\%$ for the $H \to e\tau$ and $H \to \mu\tau$ decay, respectively. In the absence of a significant excess, upper limits at 95% confidence level are found to be $0.47\%(0.34^{+0.13}_{-0.10}\%)$ and $0.28\%(0.37^{+0.14}_{-0.10}\%)$, respectively. These limits are more stringent than the corresponding limits determined by ATLAS with Run 1 data.

Additional searches have been performed by the ATLAS collaboration, such as the di-electron ($H \to ee$), the di-muon ($H \to \mu\mu$) and the electron-muon ($H \to \mu e$) decay of the Higgs boson. These analyses have been performed using data corresponding to an integrated luminosity of 139 fb^{-1}, the total luminosity collected by ATLAS during Run 2. Despite the lack of a significant excess, the results of these searches represent a big improvement with respect to the previous limits on the parameters of interest.

The $H \to \mu\mu$ search [140] obtains a best fit signal strength of $\mu = 0.5 \pm 0.7$, corresponding to an observed (expected) significance of 0.8σ (1.5σ) with respect to the null hypothesis. Figure 6.1 shows the reconstructed di-muon mass distribution. The uncertainty on μ is dominated by the statistical uncertainty on data. The observed (expected) upper limit on μ at 95% CL is found to be 1.7 (1.3), corresponding to a branching ratio upper limit at 95% CL of $\mathcal{BR}(H \to \mu\mu) < 3.8 \times 10^{-4}$. This results represents an improvement of about 50% with the previous ATLAS results [141]. This improvement comes from the increase of integrated luminosity as well as the refinements in the analysis techniques.

On the other hand, the best fit value of the $H \to ee$ branching fraction of the ATLAS search [142] is $(0.0 \pm 1.7(\text{stat}) \pm 0.6(\text{syst})) \times 10^{-4}$. Figure 6.2 shows the reconstructed di-electron mass distribution. The main uncertainty of the result comes from the statistical uncertainty in the data. The observed (expected) upper limit on the branching fraction with a 95% CL is found to be 3.6×10^{-4} (3.5×10^{-4}). This result is a significant improvement of the previous limit by CMS of 1.9×10^{-3} based on Run 1 data [143].

Concerning the $H \to e\mu$ search [142], the best fit value of the branching fraction is $(0.4 \pm 2.9(\text{stat}) \pm 0.3(\text{syst})) \times 10^{-5}$. Figure 6.3 shows the reconstruction di-lepton mass

distribution. The uncertainties are dominated by the statistical uncertainty on the data and the Higgs boson production cross-section uncertainty. The observed (expected) upper limit at the 95% CL is 6.2×10^{-5} (5.9×10^{-5}). This result is a significant improvement on the previous limit by CMS of 3.5×10^{-4} based on Run 1 data [33].

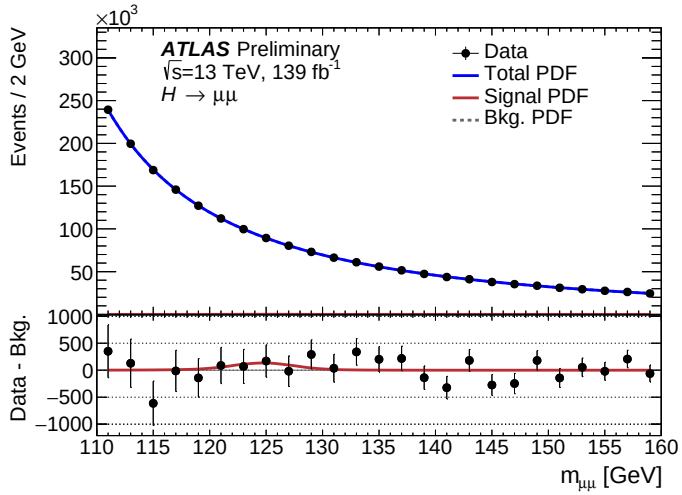

Figure 6.1: Di-muon invariant mass spectrum observed in data. The unweighted sum of all events and signal plus background probability density functions (PDF) are shown. The signal parametrisation is shown with a red line. The bottom panel shows the difference between data and the background-only fit. Reproduced from Ref. [140] under CC-BY-4.0 licence.

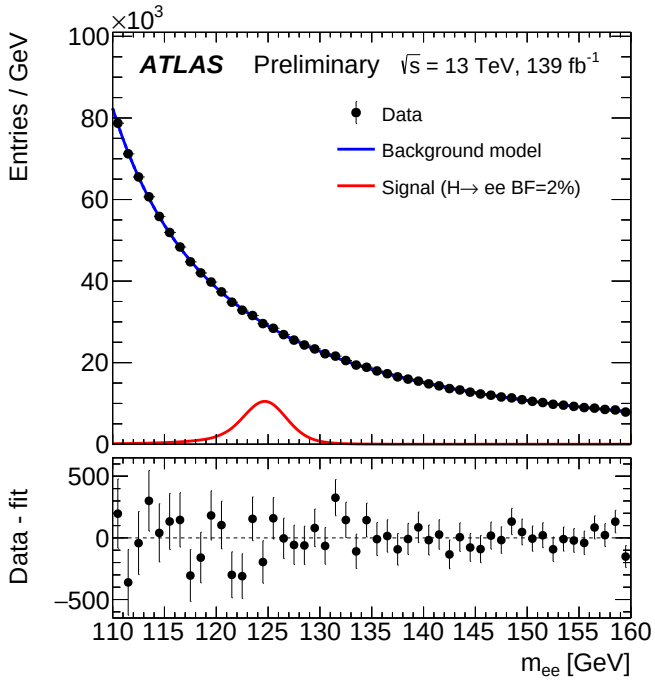

Figure 6.2: Dielectron invariant mass m_{ee} compared with the background-only model. The signal parametrisation with branching fraction set to $\mathcal{BR}(H \to ee) = 2\%$ is shown with a red line. The bottom panel shows the difference between data and the background-only fit. Reproduced from Ref. [142] under CC-BY-4.0 licence.

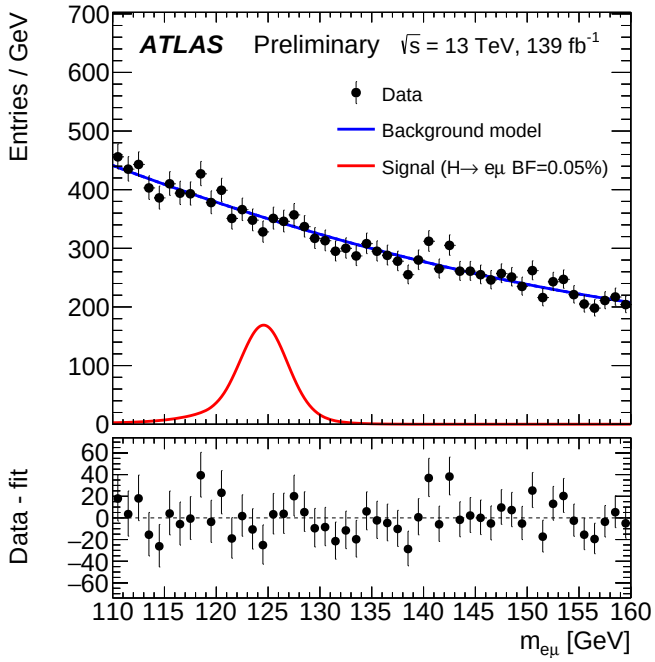

Figure 6.3: Dilepton invariant mass $m_{e\mu}$ compared with the background-only model. The signal parametrisation with branching fraction set to $\mathcal{BR}(H \to e\mu) = 0.5\%$ is shown with a red line. The bottom panel shows the difference between data and the background-only fit. Reproduced from Ref. [142] under CC-BY-4.0 licence.

Resum en Valencià

Introducció

El treball presentat en aquesta tesi s'ha desenvolupat durant els anys 2015 fins a finals de 2019 a l'experiment ATLAS, un dels detectors instal·lat a l'accelerador de LHC en Ginebra (Suïssa). En ella es descriurà dos anàlisis per a la millor comprensió del bosó de Higgs, una partícula descoberta en Juliol del 2012 per ATLAS i CMS.

La motivació fonamental d'aquesta tesi és la comprensió de l'acoblament del bosó de Higgs amb partícules leptòniques, anomenat acoblament de Yukawa. El model estàndard és la ferramenta matemàtica desenvolupada fins al moment que descriu el comportament de les partícules sub-atòmiques. Malauradament, presenta encara incongruències amb el que passa al mon real. Algunes de les preguntes encara obertes són: Per què el model estàndard no dona massa als neutrins quan s'ha descobert que sí en tenen? Per què el món està fet de matèria i no de antimatèria? O per què al model estàndard es conserva el sabor leptònic, però a la natura està lleugerament trencat?

Aquestes preguntes encara sense resoldre obrin portes per a nova física més enllà del model estàndard, així com intentar esbrinar quines son les peces mancants en aquesta teoria. Tot açò fa possible que a la investigació siga encara puntera l'estudi dels acoblaments amb bona precisió d'unes partícules a altres.

Fonamentalment, s'han fet dos estudis en aquesta tesi. Un d'ells està dins del marc del model estàndard i consisteix en mesurar la secció transversal del bosó de Higgs a un parell de leptons τ. L'altre, acull el marc de física més enllà del model estàndard i consisteix en calcular quina és la probabilitat de trobar, mitjançant col·lisions protó-protó, bosons de Higgs que han decaigut a un leptó lleuger (electró o muó) i un

leptó τ, violant així la conservació d'acoblament a partícules de la mateixa generació predita pel model estàndard.

Model Estàndard

En física de partícules la teoria quàntica de camps que descriu aquests objectes fonamentals i les seues interaccions s'anomena Model Estàndard, amb acrònim SM per les seues paraules en anglès. Aquesta teoria unifica tres de les quatre forces de la natura: la electromagnètica, la nuclear feble i la nuclear forta.

El SM està construït dins del grup de simetria de Lie, causant de que moltes de les simetries observades en la natura tinguen cabuda. En compte, a baixes energies les simetries es trenquen, donant com a resultat la separació de les forces esmentades anteriorment.

Aquest formalisme matemàtic descriu el comportament de dos tipus de partícules, les anomenades partícules fermiòniques i les partícules bosòniques. La figura R.1 mostra el conjunt de totes les partícules fonamentals descrites pel model estàndard. La diferència entre els dos tipus de partícules és l'espín, un nombre quàntic que ens dirà com es comportarà dita partícula sota un camp magnètic.

La matèria fermiònica està formada per leptons i quarks, amb espín semi-enter $1/2$. S'agrupen en tres generacions de massa creixent, cadascun compost per dos element. Els leptons son parelles d'elements on un està carregat elèctricament i l'altre és neutre. Per altra banda, els quarks són doblets on cadascun té carrega elèctrica diferent. Aquestes partícules fermiòniques estan descrites per l'estadística de Fermi-Dirac i obeeixen el principi d'exclusió de Pauli.

L'altre grup de partícules, les bosòniques, són les que tenen espín enter i sorgeixen com a manifestació de la simetria del grup de Lie. Són excitaments dels camps quàntics que descriuen les forces fonamentals i per tant són els anomenats mediadors d'aquestes forces.

El bosó de Higgs és també un partícula bosònica, però en canvi, no és mediadora de cap força fonamental. Aquesta partícula es va descobrir experimentalment el 4 de Juliol de 2012, per l'experiment ATLAS i CMS. El descobriment va marcar un punt d'inflexió a

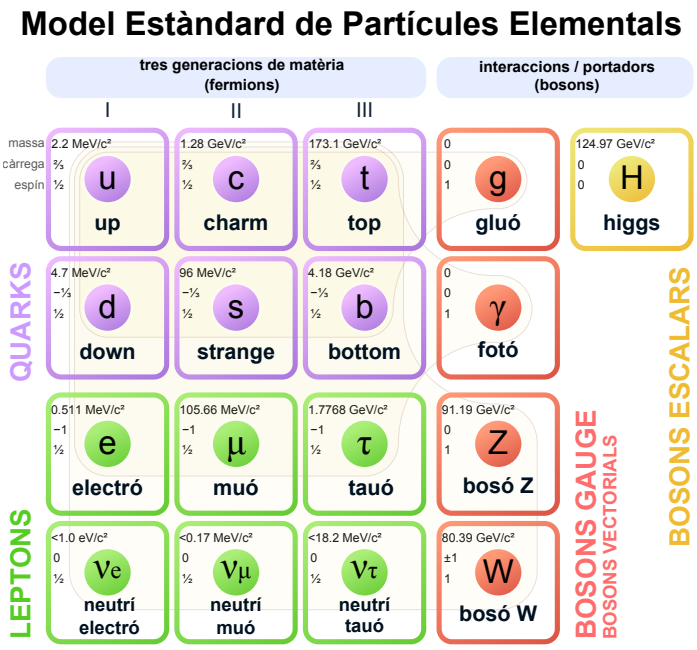

Figura R.1: Conjunt de partícules elementals descrites pel model estàndard. A la part de dalt esquerra de cada partícula està posada la seua massa aproximada, la càrrega i l'espín corresponent.

l'hora de comprendre per què les partícules descobertes tenien massa. Fins al moment, el model estàndard predeia que cap partícula podia tindre massa.

El bosó de Higgs s'origina pel trencament espontani de simetria del SM amb els mateixos nombres quàntics que el buit físic, sense carrega elèctrica ni carrega de color. És un camp que impregna tot l'espai-temps i redueix el moviment de les partícules que hi interactuen, de manera que aquestes adquireixen massa. L'auto-interacció del camp de Higgs amb si mateix genera també una massa per al bosó de Higgs, que està al voltant d'uns 125 GeV.

El formalisme matemàtic del SM està regit per l'anomenat formalisme de lagrangians, on de forma additiva es pot anar sumant els termes de les forces d'interaccions, la creació del bosó de Higgs i la interacció del bosó de Higgs amb les partícules

fermiòniques. Aquest últim terme és el lagrangià on estaran focalitzats els resultats d'aquesta tesi.

En aquest formalisme hi apareixen termes de matrius de mescla entre els leptons o quarks amb al bosó de Higgs. Aquesta unió entre quarks o leptons amb el bosó s'anomenen acoblaments de Yukawa. Per a la unió dels quarks amb el bosó la matriu de mescla s'anomena Cabibbo-Kobayashi-Maskawa (CKM) i pot ser parametritzada per tan sols tres angles i una fase complexa. Per altra banda, malgrat que al lagrangià hi ha una matriu leptònica de mescla, aquesta és proporcional a les masses, i com les masses dels neutrins són extremadament xicotetes, la mescla entre leptons està extremadament restringida.

Pontecorvo en 1957 va descobrir experimentalment la violació del sabor leptònic, prohibit al formalisme matemàtic del SM. Per tant, permetent la hipòtesi que partícules, com per exemple el bosó de Higgs, decaigueren a leptons de distintes generacions de família (mescla de sabor leptònic). Una bona precisió dels acoblaments entre els leptons ens donarà informació sobre la possibilitat de trobar nova física més enllà del model estàndard.

L'accelerador LHC i l'experiment ATLAS

El gran col·lisionador de partícules hadròniques, amb acrònim LHC, és l'accelerador de partícules més gran del món. L'accelerador té una circumferència d'uns 27 km soterrat uns 100 m, situat entre les fronteres de França i Suïssa, prop de la ciutat de Ginebra. S'ha dissenyat per a assolir energies de 14 TeV al centre de masses i una lluminositat de 10^{34} cm^{-2} s^{-1}, on cada 25 ns es produeix una col·lisió.

Al ser un accelerador hadrònic, els principal modes de producció de la partícula estudiada són, per ordre d'importància, la fusió gluó-gluó (ggF), la fusió de bosons vectorials (VBF), la producció associada a un bosó vectorial (VH) i la producció del bosó mitjançant els quarks t (ttH), amb unes taxes de producció del 87%, 7%, 5% i 1% respectivament.

Aquests esdeveniments, poden ser detectats a quatre punt de l'anell, on dos feixos d'hadrons col·lideixen en el centre de cada detector: ATLAS, CMS, ALICE i LHCb.

L'experiment ATLAS, acrònim de *'A Toroidal LHC Apparatus*' és un dels detectors més grans del món construït amb un objectiu general, tant per a trobar nova física com per a estudiar amb més deteniment el SM. Mesura 45 m de llargària i 25 m de d'alçada, pesa més de 7000 tones i està constituït amb les tecnologies més sofisticades i els materials més especialitzats de l'època.

ATLAS pot dividir-se en quatre detectors més menuts, cadascun amb una funció diferent, i un sistema d'imants optimitzat per desviar les trajectòries de les partícules creades en la col·lisió.

El detector més proper a la col·lisió s'anomena detector intern (ID) està dissenyat per a reconstruir les traces i els vèrtex primaris de desintegració amb alta eficiència. Està format per quatre subsistemes que disminueixen la granularitat a mesura que t'allunyes del punt de col·lisió. Aquests són: la capa inserible B (IBL), el detector de píxels (PD), el detector de traces mitjançant semi-conductors (SCT) i el detector de radiació de transició (TRT). Els tres primers estan basats en silici, mentre que l'últim usa tubs de deriva. El ID esta immers en un camp magnètic de 2 T creat per un solenoide que corba la trajectòria de les partícules carregades.

Seguidament hi ha dos calorímetres que serveixen per a mesurar la energia depositada de les partícules creades en les col·lisions i les desintegracions. A la part més interna d'aquest està el calorímetre electromagnètic, anomenat LAr, amb el qual es mesura l'energia depositada per les partícules que interaccionen de manera electromagnètica (electrons i fotons). Utilitza argó líquid com a mitjà ionitzant i té una geometria en forma d'acordió. Al voltant del calorímetre electromagnètic, està el calorímetre hadrònic (TileCal), utilitzat per mesurar l'energia depositada per les partícules hadròniques (protons, neutrons, pions, kaons, etc). Està format per un material d'escintil·lació com a medi actiu i ferro com a medi passiu. Finalment, a la part exterior, està el detector de muons, dissenyat per a identificar i reconstruir les trajectòries dels muons. A més, tot el detector ATLAS està immers en un intens camp magnètic toroïdal que proporciona al voltant de 4 T.

Reconstrucció d'esdeveniments

La detecció de partícules en ATLAS es fa mitjançant un conjunt d'algoritmes especialitzats que converteixen les dades provinents del detector en objectes, els quals tenen les característiques de les partícules fonamentals del model estàndard. Aquests conjunt d'algorismes reben el nom de reconstrucció d'esdeveniments.

La reconstrucció comença amb reconèixer les traces de les partícules carregades que han passat pel detector intern. Aquesta reconstrucció utilitza xarxes neuronals per a distingir senyals que estan properes les unes amb les altres per formar la traça. Aquestes es combinen amb la deposició d'energia obtinguda als calorímetres per a reconstruir els objectes finals.

Els electrons es reconstrueixen combinant una traça amb un depòsit d'energia en el calorímetre electromagnètic. Els muons, al no depositar quasi energia als calorímetres, es reconstrueixen utilitzant les traces del detector intern amb les traces del detector de muons.

Els *jets* són cascades de partícules que s'han originat per la interacció amb els calorímetres o la desintegració de partícules pesades. Aquests es reconstrueixen a partir d'agregats topològics en el calorímetre utilitzant l'algoritme "anti-k_t". Als candidats a *jet* se'ls aplica una sèrie de correccions per tal de reduir els efectes d'apilament, soroll electrònic o la variació del moment segons la regió del detector, entre d'altres. Un tipus especial de *jet* són els originats per quarks-*b*, pels quals s'utilitzen diferents algoritmes que exploten la topologia d'aquestes partícules per tal d'identificar-lo.

Finalment, un dels objectes reconstruïts més importants és l'energia reconstruïda mancant. Degut a que els neutrins són partícules que interaccionen poc amb la matèria, aquests escapen del detector sense interaccionar i per tant sense detectar-los. Com a conseqüència de la conservació de moment en el pla transvers al feix, la suma vectorial del moment transvers de tots els productes ha de ser zero. La no detecció dels neutrins crea un desequilibri en aquesta quantitat i indica la presència de partícules que només interaccionen feblement. Al valor que equilibra el moment transvers s'anomena energia reconstruïda mancant.

Fons del model estàndard

Al SM hi ha diferents processos que no corresponen al tipus de decaïment que volem mesurar, però que l'estat final d'aquest processos és semblant a la senyal que volem considerar. En ambdós recerques, a l'estat final hi haurà una parella de leptons lleugers. Processos com $Z \to \tau\tau$, $Z \to \ell\ell$, $t\bar{t}$, Di-bosons, múltiples *jets* o inclús $H \to WW$, contaminaran la nostra recerca per a trobar el procés $H \to \tau\ell$ o el procés $H \to \tau\tau$.

La majoria d'aquests fons tenen una topologia diferent a la de la senyal, no obstant això els fons de $Z \to \tau\tau$ i $Z \to \ell\ell$ són pràcticament irrecognoscibles amb la nostra senyal. Tant és així, que són dos fons irreductibles, i per tant una bona comprensió d'ells es necessària. L'única diferencia entre ells i el decaïment del bosó del Higgs roman a la reconstrucció de la massa invariant dels dos leptons τ, ja que al primer cas és una distribució de Gauss centrada en 90 GeV mentre que a la senyal està centrada a 125 GeV.

Tots aquests fons es tindran en compte mitjançant tècniques de simulació a l'anàlisi i estan predits pel model estàndard.

Fals fons de leptons

Un dels fons més importants d'aquesta anàlisi és l'anomenat fals fons de leptons. Aquest fons no està predit pel model estàndard, ja que són objectes que s'han reconstruït malament. Aquests falsos positius venen donats a l'hora de la reconstrucció, i normalment són partícules que han deixat senyal semblants a les partícules en les que s'han confós. En aquesta anàlisi, la majoria de vegades són *jets* que s'han reconstruït com a leptons lleugers (electrons o muons). L'única manera de poder estimar aquest fons és mitjançant el desenvolupament de tècniques basades en les dades i a més cada tècnica és especifica per a cada estudi.

Per a determinar el fals fons s'han determinat quatre regions mirant l'aïllament dels leptons i la carrega entre ells. Als estudis s'utilitzaran leptons on la carrega entre ells siga negativa, és a dir, els dos leptons tenen signe contrari, a més, han de estar aïllats. La regió que s'utilitzarà per a l'anàlisi haurà de contindre les parelles de leptons que tinguen signe contrari però que no estiguen aïllades (degut a la topologia dels *jets*).

Finalment, com al SM no hi ha distinció entre matèria i antimatèria, les regions on els leptons tenen el mateix signe, s'utilitzaran per a determinar quina és la fracció d'esdeveniment per a passar de la regió on els leptons no estan aïllats de la que si ho estan. Aquest factor s'anomena factor de transmissió.

El factor de transmissió dependrà se la selecció que s'usa, del tipus de *jets* que hi ha haja a l'esdeveniment i al moment transvers que porta el leptó. Diferents incerteses s'han estimat relacionades amb la estimació del fals fons. Aquestes consideren incerteses basades en la extrapolació dels esdeveniments des de la selecció més bàsica a la regió de senyal; continguts de fals fons on hi ha d'esdeveniments de quarks pesats, com el quark-t o el quark-b; la composició del fals fons; i una incertesa especial associada sols a l'anàlisi de la violació del sabor leptònic per la correcció d'un incorrecte modelatge de les dades i l'estimació del fons.

Mesura de la secció transversal del bosó de Higgs desintegrant-se a leptons τ

Aquesta anàlisi està dins del model estàndard, i consisteix en calcular la secció transversal de dos tipus de creació del bosó de Higgs, mitjançant la fusió gluó-gluó i mitjançant la fusió de bosons vectorials, que decau a un parell de leptons τ. Per realitzar l'anàlisi s'han utilitzat les dades obtingudes durant els anys 2015 i 2016 al detector ATLAS, a una energia en el centre de masses de 13 TeV. Llevat que els resultats d'aquest treball estan realitzats per tres canals de desintegració dels taus diferents, aquesta tesi sols és centra en la metodologia del canal $\tau_{\text{lep}}\tau_{\text{lep}}$, on cadascun dels leptons τ decauen a leptons lleugers, electrons o muons. Els altres dos canals, $\tau_{\text{lep}}\tau_{\text{had}}$ i $\tau_{\text{had}}\tau_{\text{had}}$, on un o els dos leptons τ decauen a partícules hadròniques, seguiran una metodologia completament similar, tant és així que la selecció utilitzada per a arribar als resultats està completament harmonitzada.

Per a aplegar als resultats finals, s'han utilitzat una sèrie de talls cinemàtics enfocats a la topologia de l'esdeveniment. Primerament, s'aplica una preselecció d'esdeveniment per a comprovar si la simulació, donada pel model estàndard, s'ajusta a les dades. Si

hi ha alguna mancança o dèficit de cert fons, aquest es corregeix utilitzant factors de normalització.

Dos regions, anomenades regions de senyal, es defineixen per a afavorir esdeveniments de creació del bosó de Higgs mitjançant ggF i VBF, anomenades regió d'alt moment i regió VBF respectivament. La selecció d'aquestes regions s'afavoreix de la topologia de l'estat final de l'esdeveniment, aplicant talls cinemàtics després de passar la preselecció. Aquestes categories són completament independents sense cap solapament en l'espai de fases.

A la regió de VBF, la selecció està encarada a la cinemàtica dels dos *jets* que es formen a la producció del Higgs, mentre que a la regió d'alt moment seran esdeveniments que haguen passat la preselecció, però fallen els requisits de la regió de VBF.

Per altra banda, dos regions de control es defineixen per a poder constrènyer la normalització dels dos fons predominants de l'anàlisi, el fons de quark-t i el del bosó neutre Z que decau a dos leptons lleugers. La selecció de l'espai fàsic de les dos regions de control estan definides de manera que siguen el més semblants possibles a les regions de senyal i sols canvien un criteri cadascun.

Resultats

En aquesta anàlisi s'ha mesurat la secció transversal del bosó de Higgs de tres maneres distintes mitjançant un estudi estadístic. El mètode estadístic utilitzat és el de *maximum-likelihood*, on productes de probabilitats de Poisson i de Gauss estimen els resultats finals de l'anàlisi de $H \to \tau\tau$. L'ajust consta de tres parts, on en total 13 regions de senyal i 6 regions de control (incloent-hi els altres dos canals) són utilitzades per a traure els paràmetres d'interès. Primerament, s'ha realitzat un ajust a un sol paràmetre per a calcular la secció transversal total del processes $H \to \tau\tau$. Després, s'has ajustat les dades a dos paràmetres per a calcular independentment les dos seccions transversals totals depenent de la producció del Higgs, per a separar el ggF i el VBF. Finalment, s'han ajustat a dades tres paràmetres en els quals s'han diferenciat els tres canals independentment.

La significança observada(esperada) d'un excés de senyal relatiu a suposar solament fons obtinguda a l'ajust estadístic és de $4.4(4.1)$ desviacions estàndard, compatible amb la partícula del bosó de Higgs predit pel model estàndard amb massa de $m_H = 125$ GeV. Aquest resultat combinant-lo amb l'obtingut utilitzant les dades de 7 i 8 TeV d'energia al centre de masses augmenta fins al valor de $6.4(5.4)$ desviacions estàndard.

El paràmetre $\sigma_{H\to\tau\tau} \equiv \sigma_H \cdot \mathcal{BR}(H \to \tau\tau)$, on $\sigma_{H\to\tau\tau}$ és la secció transversal total de la creació del bosó de Higgs mitjançant el processos de ggF, VBF, VH i ttH; i on la fracció de decaïment, $\mathcal{BR}(H \to \tau\tau)$, és el percentatge de vegades que el bosó de Higgs decau a un parell de leptons τ. El valor obtingut a l'anàlisi estadístic és de $\sigma_{H\to\tau\tau} = 3.77^{+0.60}_{-0.59}(\text{stat})^{+0.87}_{-0.74}(\text{syst})$ pb, consistent amb la predicció del model estàndard $\sigma^{\text{SM}}_{H\to\tau\tau} = 3.46 \pm 0.13$ pb. Per a comparar la desviació amb el model estàndard s'utilitza la fracció $\mu = \frac{\sigma_H \times \mathcal{BR}(H\to\tau\tau)}{\sigma^{\text{SM}}_H \times \mathcal{BR}^{\text{SM}}(H\to\tau\tau)}$, on el denominador són els valors esperats pel SM. El valor obtingut és de $\mu = 1.09^{+0.18}_{-0.17}(\text{stat})^{+0.26}_{-0.22}(\text{syst})^{+0.11}_{-0.16}(\text{theory syst})$. La Figura R.2 estan representades les diferents distribucions de les masses per als canals considerats a l'anàlisi, a més de la unió de tot ells per categories.

L'ajust als dos paràmetres permet obtindre la secció transversal dels dos modes de producció del Higgs més probables a l'accelerador LHC, $\sigma^{VBF}_{H\to\tau\tau}$ i $\sigma^{ggF}_{H\to\tau\tau}$. Els valor calcular a l'ajust són de $\sigma^{VBF}_{H\to\tau\tau} = 0.25 \pm 0.09(\text{stat})^{+0.11}_{-0.9}(\text{syst})$ pb i $\sigma^{ggF}_{H\to\tau\tau} = 3.1 \pm 1.0(\text{stat})^{-1.3}_{+1.6}(\text{syst})$ pb. Els valor són completament compatibles amb l'esperat pel model estàndard $\sigma^{\text{SM},VBF}_{H\to\tau\tau} = 0.237 \pm 0.006$ pb i $\sigma^{\text{SM},ggF}_{H\to\tau\tau} = 3.1 \pm 1.0$ pb. La Figura R.3 mostra l'espai del pla de ($\sigma^{VBF}_{H\to\tau\tau}$, $\sigma^{ggF}_{H\to\tau\tau}$) per a comparar el valor obtingut experimentalment i teòricament.

Violació del sabor leptònic en el bosó de Higgs

Aquesta anàlisi descriu la recerca de física més enllà del model estàndard, com la violació del sabor leptònic (LFV) en decaïments del bosó de Higgs. La recerca és similar a la del anàlisi $H \to \tau\tau$, on es busca un excés estadístic d'esdeveniments de senyal sobre el fons predit pel model estàndard. Els bosó de Higgs decau a un leptó τ i a un leptó lleuger (electró o muó), $H \to \tau\ell$. S'han considerat dos canals, el completament leptònic ($\ell\tau_{\ell'}$) i el semi-leptònic ($\ell\tau_{\text{had}}$), d'on en aquesta tesi es centra purament en el

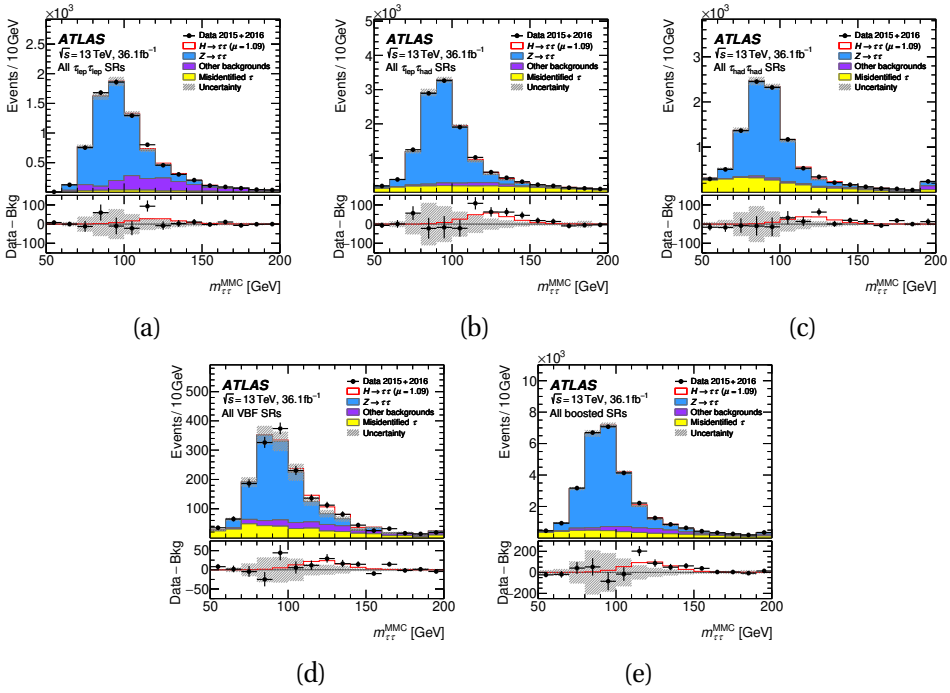

Figura R.2: Distribucions de la massa reconstruïda dels dos leptons τ ($m_{\tau\tau}^{\mathrm{MMC}}$) per als canals $\tau_{\mathrm{lep}}\tau_{\mathrm{lep}}$ (a), $\tau_{\mathrm{lep}}\tau_{\mathrm{had}}$ (b), $\tau_{\mathrm{had}}\tau_{\mathrm{had}}$ (c) independentment i per a les regions de senyal VBF (d) i d'alt moment (e). Els punt negres són les dades observades, mentre que l'histograma és la predicció del model estàndard. El panell de baix és la diferencia entre l'observació i el fons predit pel SM. L'histograma a ratlles mostra la incertesa estadística i experimental sumada.

desenvolupament del canal completament leptònic, encara que als resultats, tots dos canals estan considerats.

Al canal completament leptònic s'han estudiat dos possibilitats on sempre hi ha un leptó lleuger primari i d'un secundari. Quan l'electró és primari i el muó secundari, l'estat final és del tipus $e\tau_{\mu}$, mentre que a l'invers hi tenim $\mu\tau_{e}$. Aquestes dues possibilitats són completament excloents entre elles, és a dir, l'observació d'una d'elles exclou l'altra. El límit superior predit pels diferent models teòrics per a la fracció de decaïment és de l'ordre de l'1%.

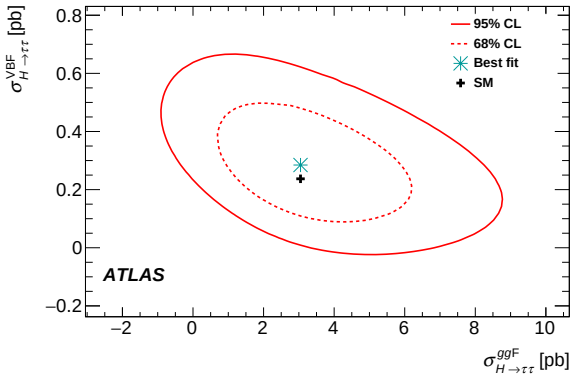

Figura R.3: Contorns de probabilitat per a la suma de tots els canals al pla ($\sigma^{VBF}_{H\to\tau\tau}$, $\sigma^{ggF}_{H\to\tau\tau}$). La línia discontinua i la línia sòlida són el 68% i el 95% de nivell de confiança, respectivament, per a un bosó de Higgs amb una massa de $m_H = 125\,\mathrm{GeV}$. La predicció del model estàndard s'indica com a símbol '+', mentre que el millor valor de l'ajust a les dades és el símbol '$*$'

Les dades utilitzades són les mateixes que a l'anàlisi anterior, llevat de la senyal, que en aquest cas està considerada com a fons degut a l'observació experimental del procés. Per a veure si les prediccions del model estàndard estan d'acord amb les dades, s'apliquen una sèrie de talls cinemàtics bàsics on el fons es predominant. Aquesta regió s'anomena preselecció o selecció bàsica. Seguidament, per a reduir considerablement els fons i afavorir la senyal, es defineixen dos categories estadísticament independents, la VBF i la no-VBF, on cada regió contindrà els dos tipus predominants de la producció del bosó de Higgs: la fusió de bosons vectorial (VBF) i la fusió de gluons (ggF) respectivament. A més, dos regions de control, del quark-t i la del $Z \to \tau\tau$, es defineixen per a restringir els fons predominants de la part completament leptònica de l'anàlisi.

Com la fracció de decaïment de la violació de sabor leptònic s'estima que serà menor de l'1%, s'utilitzarà una anàlisi multivariable mitjançant l'anomenat *Boosted Decision Tree* (BDT). Aquesta tècnica anirà després de les regions de senyal. L'algoritme divideix els esdeveniment depenent de si són amb una topologia semblant a la senyal o al fons. Per a això, les BDTs s'entrenen amb el 80% de les mostres predites, mentre que el 20%

restant, s'empra per a validar que el procediment seguit a l'entrenament s'ha efectuat correctament.

Una vegada entrenats els algoritmes, s'aplica la selecció. Els esdeveniments passen per l'anàlisi multivariable i el valor d'eixida és el que s'utilitza a l'ajust estadístic.

Resultats

L'ajust consta de funcions de probabilitat de Poisson i de Gauss que recorren la distribució del valor d'eixida per a treure la fracció de decaïment del procés $H \to \tau\ell$. Els millors resultats de l'ajust s'obtenen quan els dos canals, $H \to \mu\tau$ i $H \to e\tau$ s'assumeixen nuls l'un de l'altre, és a dir, quan $\mathcal{BR}(H \to \mu\tau) = 0$ per a la recerca de $H \to e\tau$ i viceversa.

Les incerteses estan compreses entre el 0.17% i el 0.19% de la mesura, i la incertesa que dona major contribució està relacionada amb el fals fons, així com la resolució i l'escala dels *jets*.

Els valors obtinguts per a la fracció de decaïment són $0.15^{+0.18}_{-0.17}\%$ i $-0.22 \pm 0.19\%$ per a la recerca de $H \to e\tau$ i $H \to \mu\tau$ respectivament. Com s'observa, degut a l'absència de senyal, i sent valors compatibles amb zero, un límit superior s'obté per a cada recerca en l'anàlisi per a un bosó de Higgs amb massa 125 GeV. Els límits superiors observats(esperats) per a la recerca de $H \to e\tau$ i $H \to \mu\tau$ són de $0.47\%(0.34^{+0.13}_{-0.10}\%)$ i de $0.28\%(0.37^{+0.14}_{-0.10}\%)$ respectivament. Aquests valors per als límits superiors són significativament més menuts que els obtinguts durant el període del Run 1.

Els valors no-diagonals de la matriu de Yukawa, estan directament relacionats amb les fraccions de decaïment calculades a l'ajust per l'equació R.1.

$$\sqrt{|Y_{\ell\tau}|^2 + |Y_{\tau\ell}|^2} = \frac{8\pi}{m_H} \frac{\mathcal{BR}(H \to \ell\tau)}{1 - \mathcal{BR}(H \to \ell\tau)} \Gamma_H^{\text{SM}} \tag{R.1}$$

on $\Gamma_H^{\text{SM}} = 4.07$ MeV és l'amplada del bosó de Higgs predita pel model estàndard. Els límits observats de la fracció de decaïment correspon a el següents límits per als acoblaments dels elements de matriu $\sqrt{|Y_{e\tau}|^2 + |Y_{\tau e}|^2} = 0.0020$ i $\sqrt{|Y_{\mu\tau}|^2 + |Y_{\tau\mu}|^2} = 0.0015$. La figura R.4 s'exposen els límits individualment per

a cada recerca junts amb els límits proporcionats per l'anàlisi fet per ATLAS durant el Run 1.

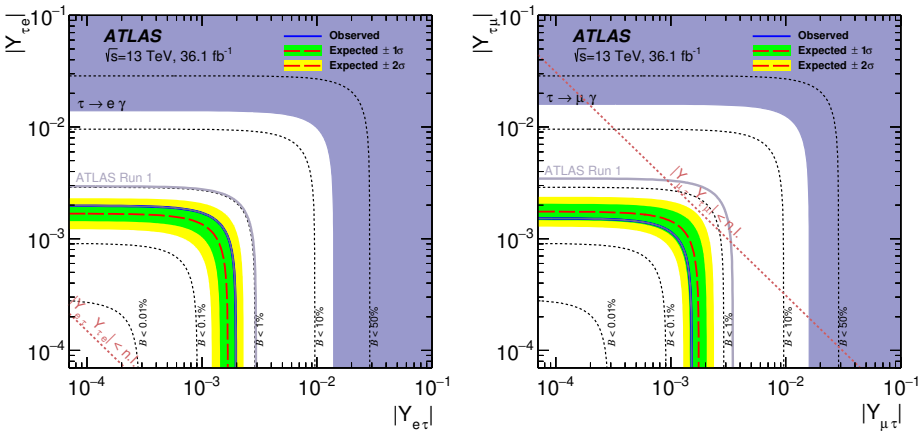

Figura R.4: Límits superiors per al valor absolut dels acoblaments $Y_{\tau\ell}$ i $Y_{\ell\tau}$ junt amb els límits obtinguts pel Run 1 (línia gris) i el valor més restrictiu per a recerques de $\tau \to \ell\gamma$ (regió morada). S'indica també els límits corresponents a diferents fraccions de decaïment (0.01%, 0.1%, 1%, 10% i 50%) i els límits donats per la natura de $|Y_{\tau\ell}Y_{\ell\tau}| \lesssim \frac{m_\tau m_\ell}{v^2}$ [35] on v és el valor esperat del buit del camp de Higgs.

Conclusions

En aquesta tesi s'han presentat dos recerques de física fonamental. Les dades per a realitzar-la s'han pres al detector ATLAS, ubicat en l'anell del l'accelerador LHC al CERN en Ginebra (Suïssa). L'energia al centre de masses és de 13 TeV amb un total de dades de 36.1 fb^{-1}.

La primera recerca està compresa dins del marc del model estàndard i calcula la secció transversal del bosó de Higgs que decau a un parell de leptons τ. Aquesta secció s'ha calculat mitjançant dos creacions del bosó anomenades ggF i VBF, a més de la secció transversal total incloent-hi tots els processos de creació. Els valors obtinguts són $\sigma^{VBF}_{H\to\tau\tau} = 0.25 \pm 0.09(\text{stat})^{+0.11}_{-0.9}(\text{syst})$ pb i $\sigma^{ggF}_{H\to\tau\tau} = 3.1 \pm 1.0(\text{stat})^{-1.3}_{+1.6}(\text{syst})$ pb per a la creació mitjançant VBF i ggF respectivament, mentre que la secció transversal total calculada és de $\sigma_{H\to\tau\tau} = 3.77^{+0.60}_{-0.59}(\text{stat})^{+0.87}_{-0.74}(\text{syst})$ pb. Ambdós ajusts són

completament compatibles amb el model estàndard i estan dins dels valors esperats calculats teòricament.

L'altra recerca està encarada en el marc de més enllà del model estàndard. Consisteix en mesurar els acoblaments no-diagonals de la matriu leptònica de mescla. Degut a la massa dels leptons lleugers, aquests elements estan molt restringits, tant i tot que dins del model estàndard està prohibit. Malgrat no estar permès a la teoria, s'ha comprovat experimentalment que aquests elements no són nuls per al neutrins. Una manera de comprovar els elements no-diagonals de la matriu d'acoblament és mitjançant els decaïment $H \to \tau\ell$, on ℓ pot ser o electró o muó. Aquest decaïment viola el valor del numero leptònic, ja que el bosó de Higgs decau a dos leptons de distinta família. El procediment emprat és semblant a l'anterior, s'hi defineixen dos regions independents on en cada una d'elles predomina una producció del bosó. A més, sabent que els valors dels elements no-diagonals són molt xicotets, una vegada passada la preselecció, les dades s'han analitzat amb una anàlisi multivariable per a incrementar la separació del fons i la senyal. Els resultats obtinguts per a la fracció de decaïment per a cada processes és $0.15^{+0.18}_{-0.17}\%$ i $-0.22 \pm 0.19\%$ per a la recerca de $H \to e\tau$ i $H \to \mu\tau$ respectivament. A causa de l'absència de senyal, s'hi calculen els límits superiors, obtenint 0.47% i de 0.28% respectivament, molt per avall dels valors obtinguts al Run 1.

Appendix

A.1 Mis-identified leptons background

The backgrounds described in Section 3 have final states with two prompt leptons and MC simulation is used to model them in the analyses. However, reconstructed leptons can originate from mis-identified objects as well. This background is referred as *Fake lepton* background or *Fakes*, and is important for the analyses. The source of this background originates mostly from jets mis-identified as light leptons, for instance background processes like QCD multi-jet and W+jets.

This background is difficult to model with MC simulation and originates from processes with large cross-sections. This led to the development of data-driven methods for its estimation. Two different kind of Fakes can be distinguished: events with one fake lepton and one prompt lepton and events where both leptons are fakes. In the $H \to \tau\tau$ and LFV analyses the main source of Fakes background are of the former. Multi-jet and processes where both leptons are fakes are less relevant, despite that both sources are treated and estimated together.

The technique used to estimate the contribution of the Fakes background consists of dedicated control regions (CRs) called Fakes CRs. The method used for both analyses is called ABCD, because four statistically independent regions are used. To define these regions, the relative charge of the leptons (same-sign (SS) and opposite-sign (OS)) and their isolation are exploited. As the main source of fakes background has one fake and one prompt lepton, the isolation requirement applies only to the lepton with lower p_{T}[1].

[1]Empirically, it is found that only in a negligible fraction of cases the fake lepton is the one of higher p_{T}.

So the p_{T} distribution of the subleading lepton in the fakes control region is used to validate the fake background modelling.

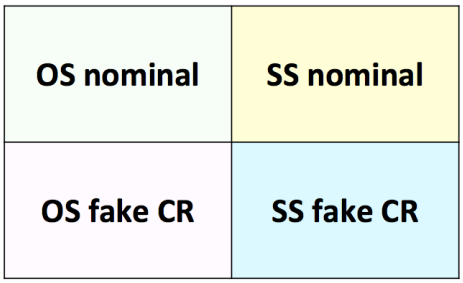

Figure A.1.1: Sketch of the different regions considered in the fakes background estimation.

Basically, the method lies in the independence of the SS and OS regions. The behaviour of the fakes in these two regions is assumed to be the same and a systematic uncertainty is associated to residual differences between the regions. The regions are defined as follows:

- SS nominal region where both leptons are isolated, but the charge requirement is reverted.
- SS Fakes CR is obtained by reverting the isolation requirement.
- OS Fakes CR is the region used as control region to build the template of the variables to model and where the isolation requirements are reverted.
- OS nominal region containing the events of the signal regions (SRs).

Figure A.1.1 shows the four independent regions where the charge product is in the x-axis and the lepton isolation criteria is in the y-axis.

The isolation criteria for both fake control regions depend on the final state of the two leptons: ee, $\mu\mu$, $e\mu$ and μe channels. The Medium identification (ID) and Gradient isolation (ISO) requirements are always applied to the leading lepton. While the subleading lepton criteria vary. For the ee channel the subleading lepton must always fail the Gradient ISO in addition of failing the Medium ID. If it passes the

Medium ID it is required to fail the Gradient ISO but passes the relative isolation criteria $p_{\mathrm{T}}^{varcone20}/p_{\mathrm{T}} > 0.1$. In the $\mu\mu$ channel the subleading lepton will always pass the Medium ID, fail the Gradient ISO and pass relative isolation criterion $p_{\mathrm{T}}^{varcone30}/p_{\mathrm{T}} > 0.1$. In the μe channel the subleading lepton must fail the Medium ID and the Gradient ISO. In the $e\mu$ channel, the subleading lepton must fail the Gradient ISO but the lepton must pass the Medium ID. Table A.1.1 shows the summary of the requirements of the fakes CRs.

Channel	Selection criteria for the subleading lepton
ee	Fail Gradient ISO and fail Medium ID
	Pass Medium ID and Fail Gradient ISO but pass $p_{\mathrm{T}}^{\mathrm{varcone20}}/p_{\mathrm{T}} > 0.1$
$\mu\mu$	Pass Medium ID and Fail Gradient ISO but pass $p_{\mathrm{T}}^{\mathrm{varcone30}}/p_{\mathrm{T}} > 0.1$
$e\mu$	Fail Gradient ISO and pass Medium ID
μe	Fail Gradient ISO and fails Medium ID

Table A.1.1: Selection criteria applied for the Fakes CRs for each channel. The word *fail* means that the subleading lepton does not pass the requirement and the word *pass* means that the subleading lepton satisfies the chosen requirement. In the LFV analysis only the different flavour channels are used.

The normalization of OS Fake CR to the OS nominal region is done by applying transfer factors. These factors are obtained from the ratio of the SS regions and applied and validated in the OS regions.

To achieve a good fakes background estimation different numbers of regions are defined by different lepton flavour combinations, trigger strategies and number of b-jets. The regions are driven by the trigger strategy of the analysis, shown in Table 4.1 and Figure 4.3, which are defined as a function of the lepton p_{T}. The three regions are called $trig1$, $trig2$ and $trig3$ which refer to single electron triggers, single muon triggers and di-lepton triggers, respectively.

To improve the statistics in the Fakes CR for the different flavour (df) channel, a logical OR between the single electron ($trig1$) and single muon ($trig2$) triggers is used.

A.1.1 Transfer factors

The transfer factors are derived from the SS events as:

$$f_{\text{trans}} = \frac{N^{\text{SS}}_{\text{nominal}}}{N^{\text{SS}}_{\text{fake CR}}} \tag{A.1.1}$$

where $N^{\text{SS}}_{\text{nominal}}$ and $N^{\text{SS}}_{\text{fake CR}}$ are the yields of events in the SS nominal and SS fake regions, where the estimation of other backgrounds with two prompt leptons is subtracted, as obtained from MC simulation. These background components, in the fake CR are due to the prompt lepton processes such as $Z\ell\ell$ and leptonically decaying top-quark. Figure A.1.2 shows the reconstructed mass of the di-τ system (defined in Section 4.2.1) in the OS fake CR at the preselection level, described in the subsections 4.2.4 and 5.2.4.

Additionally to the trigger regions defined by the lepton flavour combinations, channel selection criteria and number of b-jets, preselection criteria are applied as described in the subsections 4.2.4 and 5.2.4.

A.1.2 Fakes background estimation uncertainties

In this section the systematic uncertainties related to the fake-lepton background estimation are discussed. The same procedure is used for the $H \to \tau\tau$ cross-section measurement and the LFV search. However, one extra systematic uncertainty is considered for the $H \to \tau\ell$ search related to the correction in the $\Delta\phi(l_1, E_{\text{T}}^{\text{miss}})$ and $\Delta\phi(l_2, E_{\text{T}}^{\text{miss}})$ distributions, explained in section 5.2.4 and another extra systematic uncertainty for the $H \to \tau\tau$ cross-section measurement for the difference in the extrapolation efficiencies between OS and SS regions based on the W+jets MC is contemplated.

• The SS non-closure systematic uncertainties are based on the SS nominal region extrapolation from the fake CR preselection to the signal region, after going through the same set of selection criteria used in the analysis. The non-closure systematics are given in different $p_{\text{T}}^{l_2}$ bins and, to be conservative, the statistical errors from both samples as well as the difference between data and MC in yields in each $p_{\text{T}}^{l_2}$ bin are summed in quadrature. However, in the VBF signal region, the $Z\ell\ell$+jets background is

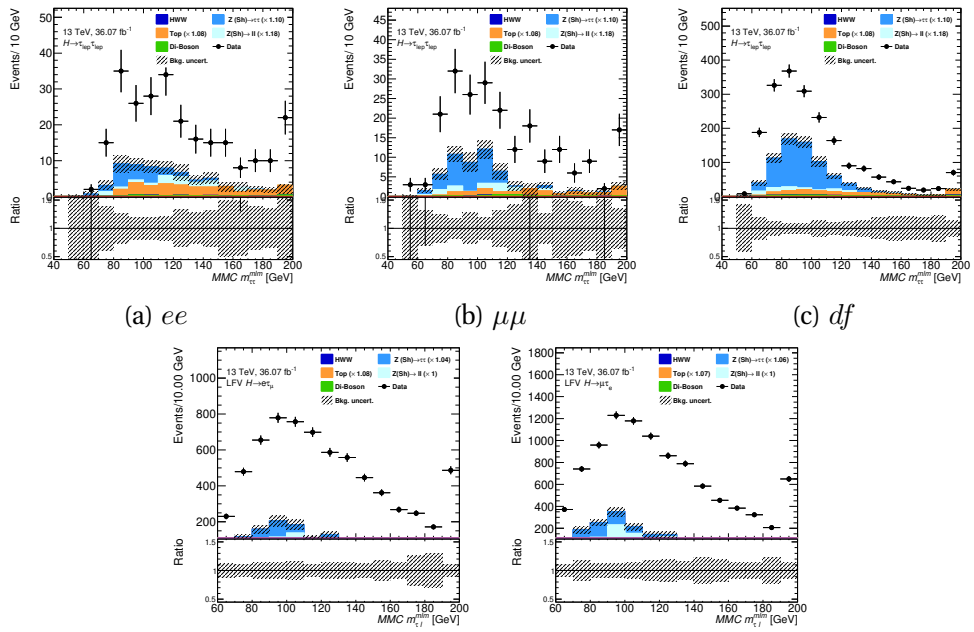

(a) ee (b) $\mu\mu$ (c) df

(d) $e\mu$ (e) μe

Figure A.1.2: The $m_{\tau\tau}^{MMC}$ distributions in the OS fake b-veto region after the $H \to \tau\tau$ analysis preselection (a), (b) and (c) and for the LFV preselection (d) and (e). They are used to show the contamination of the real lepton processes in the OS fake CR. The uncertainties are statistical only.

relatively small in both the SS nominal and SS fake samples, and some events have a very large weights due to the limited statistics of the lowest $Z\ell\ell$+jets MC slices. Thus, this component is not subtracted from neither the SS fake sample nor SS nominal sample.

• The fraction of fakes from top-quark processes is important to determine the relative contributions of QCD multi-jet, W+jets and top events in the different regions. Tables A.1.2 and A.1.3 show the relative fraction of the top processes (top fakes) to the total fakes events. The relative contribution of the top fakes events are taken from the semi-leptonic $t\bar{t}$ MC sample. The fractions of top fakes in the OS and SS nominal regions are small and similar, whereas this fraction is slightly higher in SS fakes than in

OS fakes region. Despite that, the Top processes are not the main source of fake lepton background, thus the relative impact on the uncertainty is small. To check the impact of this difference, the top fakes events are subtracted from SS fakes CR, and the transfer factors are recalculated. The impact is added as a systematic uncertainty.

The composition of the fake lepton background can be further checked using the transverse mass distribution. The W+jets background peaks close to the W boson mass value while the multi-jet background tends to peak at lower values. Hence, this distribution is indicative of the relative fraction of W+jets and multi-jet backgrounds. The shapes of the distributions are similar between the nominal and fakes CRs as well as between OS and SS regions. This indicates that the relative fractions of multi-jets are similar in all four regions. Tables A.1.4 and A.1.5 show the fraction of multi-jets background in the OS and SS regions, whose difference is included as QCD non-closure systematic uncertainty.

	OS nominal	OS fake	SS nominal	SS fake
ee	19.1 ± 2.7	35.2 ± 1.8	20.9 ± 3.9	46.1 ± 2.5
$\mu\mu$	10.8 ± 0.9	23.4 ± 1.3	14.4 ± 1.6	30.9 ± 2.0
df	9.4 ± 0.5	14.5 ± 0.3	9.8 ± 0.6	19.6 ± 0.5
total	10.2 ± 0.4	16.9 ± 0.3	11.0 ± 0.5	22.4 ± 0.5

Table A.1.2: The fraction (in %) of top-quark fakes events in the total fakes background after the $H \to \tau\tau$ cross-section preselection criteria in each region.

	OS nominal	OS fake	SS nominal	SS fake
$e\mu$	3.2 ± 0.2	7.4 ± 0.2	4.7 ± 0.4	11.7 ± 0.3
μe	3.4 ± 0.2	10.6 ± 0.2	4.8 ± 0.3	16.7 ± 0.3

Table A.1.3: The fraction (in %) of top-quark fakes events in the total fake lepton background after the LFV search preselection criteria in each region.

• Additionally, to consider the heavy flavour content in the systematic uncertainties, two different procedures have been followed for each analysis. In the $H \to \tau\tau$ cross-section measurement, the procedure is similar to the top fake fraction procedure. The transfer factors are derived from the b-tag SS regions to later be applied to the b-veto

	OS	SS
ee	-25.2 ± 27.8	12.9 ± 6.5
$\mu\mu$	5.5 ± 9.6	-4.0 ± 3.0
df	34.4 ± 2.6	32.0 ± 2.6

Table A.1.4: The fraction (in %) of multi-jet fakes in OS and SS regions for the $H \to \tau\tau$ cross-section measurement, averaged over nominal and fakes regions for different channels.

	OS	SS
$e\mu$	1.5 ± 4.3	10.5 ± 4.9
μe	7.9 ± 4.0	5.4 ± 4.3

Table A.1.5: The fraction (in %) of multi-jet fakes in OS and SS regions for the $H \to \tau\ell$ search, averaged over nominal and fakes regions for different flavour channels.

OS fakes CR. This is a conservative estimation of the impact of different heavy flavour fractions in OS and SS regions based on data. The total difference of the yields between the analysis signal region and the nominal region when the b-tag transfer factors are applied, is used for the $H \to \tau\tau$ cross-section measurement systematic uncertainties.

On the other hand, the systematic uncertainty due to the heavy flavour content of the LFV search is computed following a different procedure because it is not fully covered by the SS non-closure systematics. This systematic uncertainty is derived from an orthogonal OS b-veto region close to the SRs. The selection criteria of those regions are the same as shown in Table 5.3, except in the VBF category where the following criteria are changed:

- $m_{jj} < 400$ GeV or $|\Delta\eta_{jj}| < 3$

instead of $m_{jj} > 400$ GeV and $|\Delta\eta_{jj}| < 3$. Moreover, the following criteria 50 [GeV] $< m_{\mathrm{T}}^{l_1} < 120$ [GeV] and $m_{\mathrm{T}}^{l_2} < 70$ GeV are added to enrich the fakes contribution. For the non-VBF category, the selection criteria are shown in Table 5.5 except for the change in the angular difference:

- $\Delta\phi(l_2, E_{\mathrm{T}}^{\mathrm{miss}}) > 1.0$

The control regions have similar flavour contents as the OS nominal b-veto regions because they have been formed using the same isolation and b-veto criteria. They serve

as a closure test for the extrapolation systematics from the LFV preselection to the SRs. The subleading lepton momentum distributions are shown in Figure A.1.3.

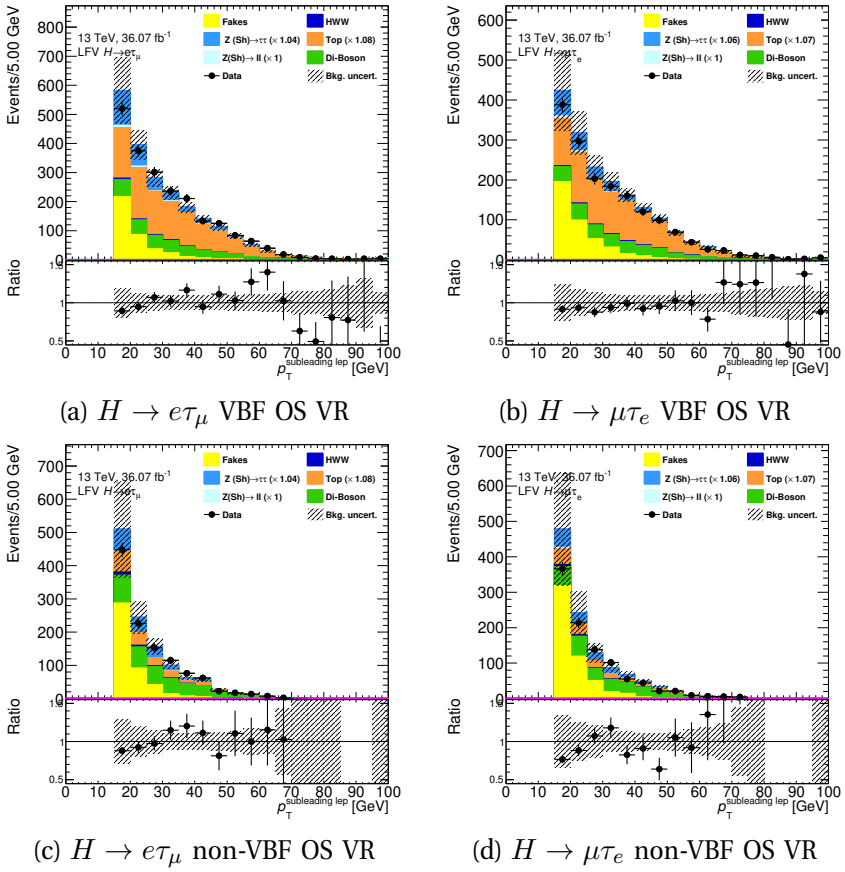

(a) $H \to e\tau_\mu$ VBF OS VR

(b) $H \to \mu\tau_e$ VBF OS VR

(c) $H \to e\tau_\mu$ non-VBF OS VR

(d) $H \to \mu\tau_e$ non-VBF OS VR

Figure A.1.3: The distributions of $p_{\mathrm{T}}^{l_2}$ in in the VBF (top) and non-VBF (bottom) OS VRs in the two channels of the LFV search.

• The QCD closure systematic uncertainty takes into account the variation of the transfer factors using a control region where the fake leptons are enriched. The transfer factors will reflect the difference between QCD and non-QCD fake events, and they are derived from the b-veto SS regions, with an extra criteria of $m_{\mathrm{T}}^{l_1} < 120$ GeV. Then they

are applied to the b-veto OS fake CR. The difference between the analyses criteria and the nominal QCD non-closure region is added as systematic.

• Only for the $H \to \tau\tau$ analysis the relative contributions of heavy flavour in the Sherpa W+jets MC events, is studied and implemented as a W+jets systematic uncertainty. The lepton objects are classified according to their origin: real prompt leptons, non-prompt from heavy hadron decays, hadron fakes, etc.). The heavy flavour uncertainty is used to validate the fake extrapolation from the preselection to the final SR and to see the compatibility between SS and OS regions. This closure test is a MC-MC comparison and, due to the low statistics, no trigger requirement is applied. As for data, the transfer factors are first derived in the SS regions and applied to the OS fake events. The ratio of SS nominal to fakes event yields are given in Table A.1.6. The consistency of these ratios between OS and SS samples indicates that the systematic uncertainty from the SS events covers the difference for the OS events.

		preselection	VBF	Boosted
W+jets	OS	0.84±0.05	0.88±0.19	0.77±0.08
	SS	1.04±0.06	0.93±0.23	0.72±0.08
Top	OS	0.98±0.02	1.01±0.09	1.00±0.03
	SS	1.00±0.02	1.07±0.09	1.08±0.04

Table A.1.6: The ratios of nominal to fakes CR yields in the OS and SS regions for preselection, VBF and non-VBF categories derived from the W+jets and top MC, with the transfer factors derived from the SS regions of the $H \to \tau\tau$ cross-section measurement preselection.

• One additional systematic uncertainty is used in the LFV search because of a mismodeling in the $\Delta\phi(l_1, E_{\mathrm{T}}^{\mathrm{miss}})$ and $\Delta\phi(l_2, E_{\mathrm{T}}^{\mathrm{miss}})$ distributions. To correct this mismodeling, shown in Figures A.1.4 and A.1.6, corrections are derived in the SS regions and applied to the OS regions. Figures A.1.5 and A.1.7 show the relevant distributions after the correction, where the agreement between the SS and OS regions improve. To be conservative, the full effect of the correction is considered and the difference between with and without the corrections is assigned as a systematic uncertainty. For the rest of the variables, a good agreement is achieved between data and the fake-lepton estimation in the SS fakes and nominal regions.

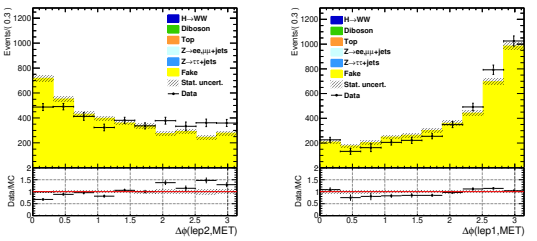

(a1) SS $\Delta\phi(l_2, E_{\mathrm{T}}^{\mathrm{miss}})$ (b1) SS $\Delta\phi(l_1, E_{\mathrm{T}}^{\mathrm{miss}})$

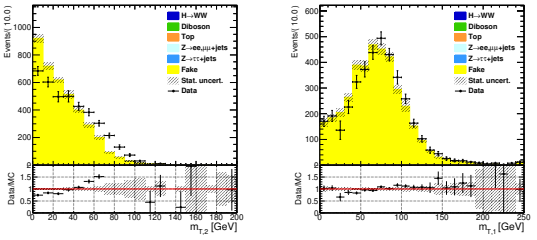

(c1) SS $m_{\mathrm{T}}^{l_2}$ (d1) SS $m_{\mathrm{T}}^{l_1}$

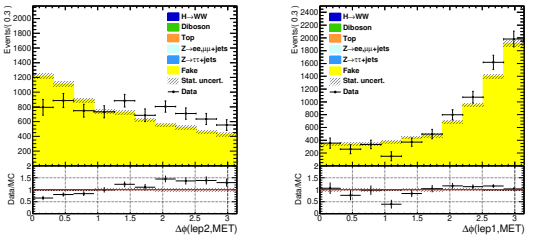

(e1) OS $\Delta\phi(l_2, E_{\mathrm{T}}^{\mathrm{miss}})$ (f1) OS $\Delta\phi(l_1, E_{\mathrm{T}}^{\mathrm{miss}})$

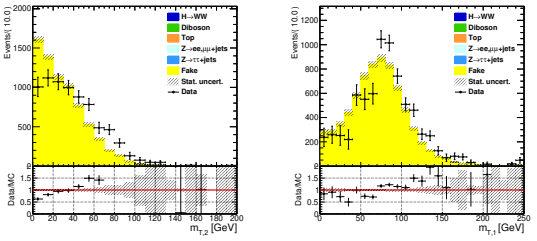

(g1) OS $m_{\mathrm{T}}^{l_2}$ (h1) OS $m_{\mathrm{T}}^{l_1}$

Figure A.1.4: The $\Delta\phi(l_2, E_{\mathrm{T}}^{\mathrm{miss}})$, $\Delta\phi(l_1, E_{\mathrm{T}}^{\mathrm{miss}})$, $m_{\mathrm{T}}^{l_2}$ and $m_{\mathrm{T}}^{l_1}$ distributions before the corrections in the $e\mu$ channel SS (a1-d1) and OS (e1-h1) nominal b-veto region after the preselection. The errors are statistical only.

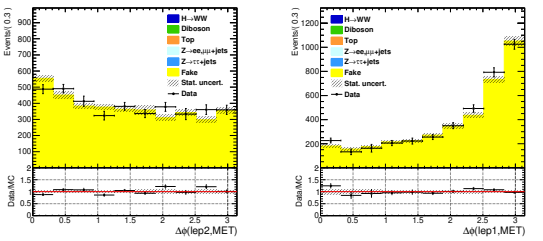

(a2) SS $\Delta\phi(l_2, E_{\mathrm{T}}^{\mathrm{miss}})$

(b2) SS $\Delta\phi(l_1, E_{\mathrm{T}}^{\mathrm{miss}})$

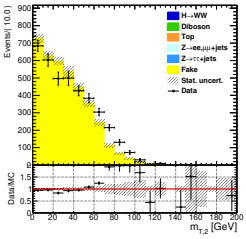

(c2) SS $m_{\mathrm{T}}^{l_2}$

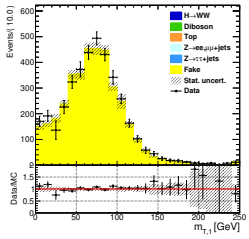

(d2) SS $m_{\mathrm{T}}^{l_1}$

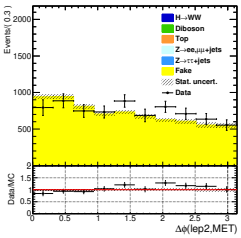

(e2) OS $\Delta\phi(l_2, E_{\mathrm{T}}^{\mathrm{miss}})$

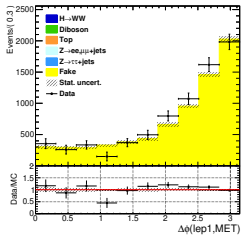

(f2) OS $\Delta\phi(l_1, E_{\mathrm{T}}^{\mathrm{miss}})$

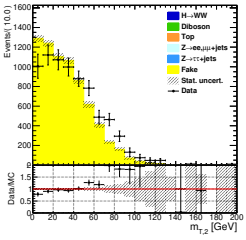

(g2) OS $m_{\mathrm{T}}^{l_2}$

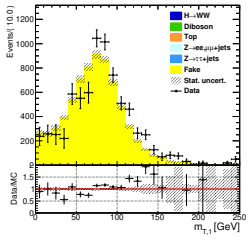

(h2) OS $m_{\mathrm{T}}^{l_1}$

Figure A.1.5: The $\Delta\phi(l_2, E_{\mathrm{T}}^{\mathrm{miss}})$, $\Delta\phi(l_1, E_{\mathrm{T}}^{\mathrm{miss}})$, $m_{\mathrm{T}}^{l_2}$ and $m_{\mathrm{T}}^{l_1}$ distributions after the corrections in the $e\mu$ channel SS (a2-d2) and OS (e2-h2) nominal b-veto region after the preselection. The errors are statistical only.

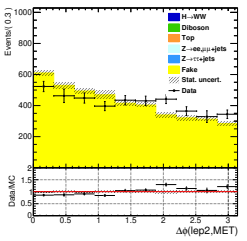

(al) SS $\Delta\phi(l_2, E_{\mathrm{T}}^{\mathrm{miss}})$

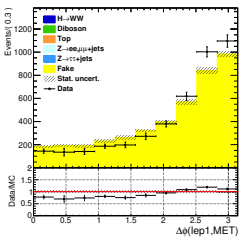

(bl) SS $\Delta\phi(l_1, E_{\mathrm{T}}^{\mathrm{miss}})$

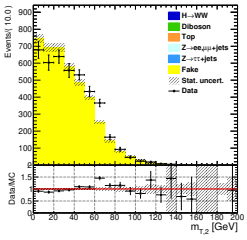

(cl) SS $m_{\mathrm{T}}^{l_2}$

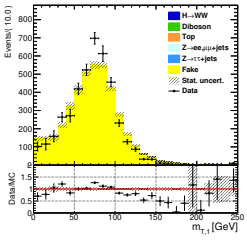

(dl) SS $m_{\mathrm{T}}^{l_1}$

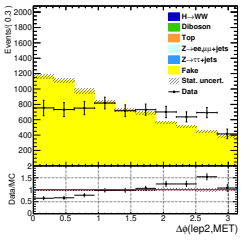

(el) OS $\Delta\phi(l_2, E_{\mathrm{T}}^{\mathrm{miss}})$

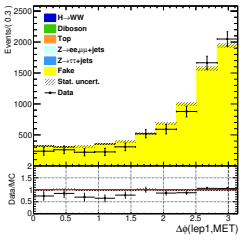

(fl) OS $\Delta\phi(l_1, E_{\mathrm{T}}^{\mathrm{miss}})$

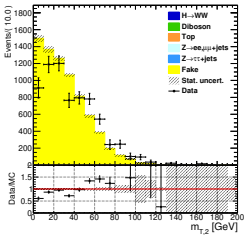

(gl) OS $m_{\mathrm{T}}^{l_2}$

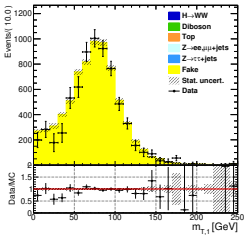

(hl) OS $m_{\mathrm{T}}^{l_1}$

Figure A.1.6: The $\Delta\phi(l_2, E_{\mathrm{T}}^{\mathrm{miss}})$, $\Delta\phi(l_1, E_{\mathrm{T}}^{\mathrm{miss}})$, $m_{\mathrm{T}}^{l_2}$ and $m_{\mathrm{T}}^{l_1}$ distributions before the corrections in the μe channel SS (a1-dl) and OS (e1-hl) nominal b-veto region after the preselection. The errors are statistical only.

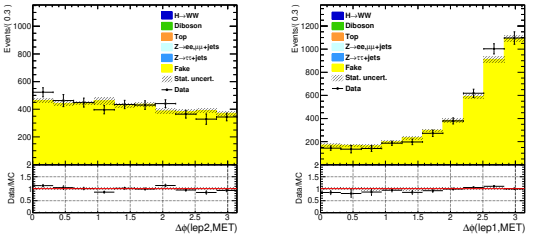

(a2) SS $\Delta\phi(l_2, E_{\mathrm{T}}^{\mathrm{miss}})$

(b2) SS $\Delta\phi(l_1, E_{\mathrm{T}}^{\mathrm{miss}})$

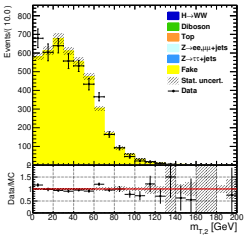

(c2) SS $m_{\mathrm{T}}^{l_2}$

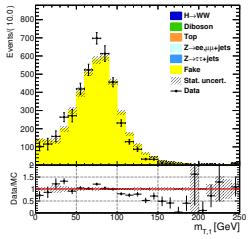

(d2) SS $m_{\mathrm{T}}^{l_1}$

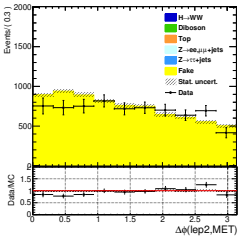

(e2) OS $\Delta\phi(l_2, E_{\mathrm{T}}^{\mathrm{miss}})$

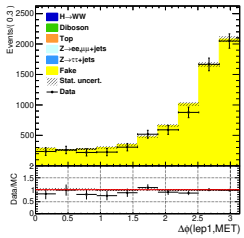

(f2) OS $\Delta\phi(l_1, E_{\mathrm{T}}^{\mathrm{miss}})$

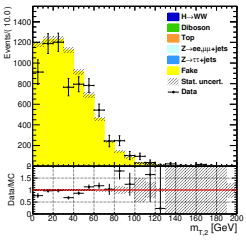

(g2) OS $m_{\mathrm{T}}^{l_2}$

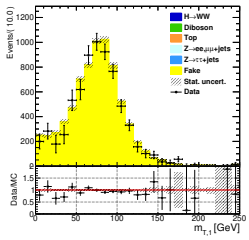

(h2) OS $m_{\mathrm{T}}^{l_1}$

Figure A.1.7: The $\Delta\phi(l_2, E_{\mathrm{T}}^{\mathrm{miss}})$, $\Delta\phi(l_1, E_{\mathrm{T}}^{\mathrm{miss}})$, $m_{\mathrm{T}}^{l_2}$ and $m_{\mathrm{T}}^{l_1}$ distributions after the corrections in the μe channel SS (a2-d2) and OS (e2-h2) nominal b-veto region after the preselection. The errors are statistical only.

Bibliography

[1] Particle Data Group Collaboration, C. Patrignani et al., *Review of Particle Physics*, Chin. Phys. **C40** (2016) 100001.

[2] ALEPH Collaboration, D. Decamp et al., *Determination of the Number of Light Neutrino Species*, Phys. Lett. **B231** (1989) 519–529.

[3] Particle Data Group Collaboration, C. Amsler et al., *Review of Particle Physics*, Phys. Lett. **B667** (2008) 1–1340.

[4] SNO Collaboration, Q. R. Ahmad et al., *Direct evidence for neutrino flavor transformation from neutral current interactions in the Sudbury Neutrino Observatory*, Phys. Rev. Lett. **89** (2002) 011301, arXiv:nucl-ex/0204008 [nucl-ex].

[5] Super-Kamiokande Collaboration, Y. Fukuda et al., *Evidence for oscillation of atmospheric neutrinos*, Phys. Rev. Lett. **81** (1998) 1562–1567, arXiv:hep-ex/9807003 [hep-ex].

[6] ATLAS Collaboration, *Observation of a new particle in the search for the Standard Model Higgs boson with the ATLAS detector at the LHC*, Phys. Lett. **B716** (2012) 1–29, arXiv:1207.7214 [hep-ex].

[7] CMS Collaboration, S. Chatrchyan et al., *Observation of a new boson at a mass of 125 GeV with the CMS experiment at the LHC*, Phys. Lett. **B716** (2012) 30–61, arXiv:1207.7235 [hep-ex].

[8] M. Gell-Mann, *Model of the Strong Couplings*, Phys. Rev. **106** (1957) 1296–1300.

[9] S. L. Glashow, *Partial Symmetries of Weak Interactions*, Nucl. Phys. **22** (1961) 579–588.

[10] A. Salam, *Weak and Electromagnetic Interactions*, Conf. Proc. **C680519** (1968) 367–377.

[11] S. Weinberg, *A Model of Leptons*, Phys. Rev. Lett. **19** (1967) 1264–1266.

[12] A. Pich, *The Standard model of electroweak interactions*, arXiv:hep-ph/9412274 [hep-ph].

[13] P. W. Higgs, *Broken Symmetries and the Masses of Gauge Bosons*, Phys. Rev. Lett. **13** (1964) 508–509, [,160(1964)].

[14] P. W. Higgs, *Spontaneous Symmetry Breakdown without Massless Bosons*, Phys. Rev. **145** (1966) 1156–1163.

[15] F. Englert and R. Brout, *Broken Symmetry and the Mass of Gauge Vector Mesons*, Phys. Rev. Lett. **13** (1964) 321–323, [,157(1964)].

[16] G. S. Guralnik, C. R. Hagen, and T. W. B. Kibble, *Global Conservation Laws and Massless Particles*, Phys. Rev. Lett. **13** (1964) 585–587, [,162(1964)].

[17] UA1 Collaboration, G. Arnison et al., *Experimental Observation of Isolated Large Transverse Energy Electrons with Associated Missing Energy at s**(1/2) = 540-GeV*, Phys. Lett. **B122** (1983) 103–116, [,611(1983)].

[18] UA2 Collaboration, M. Banner et al., *Observation of Single Isolated Electrons of High Transverse Momentum in Events with Missing Transverse Energy at the CERN anti-p p Collider*, Phys. Lett. **B122** (1983) 476–485, [,7.45(1983)].

[19] UA1 Collaboration, G. T. J. Arnison et al., *Experimental observation of lepton pairs of invariant mass around* $95 GeV/c^2$ *at the CERN SPS collider*, Phys. Lett. B **126** (1985) 398–410. 17 p, https://cds.cern.ch/record/163857.

[20] UA2 Collaboration, P. Bagnaia et al., *Evidence for Z0 —> e+ e- at the CERN anti-p p Collider*, Phys. Lett. **B129** (1983) 130–140, [,7.69(1983)].

[21] ATLAS Collaboration, M. Aaboud et al., *Measurement of the Higgs boson mass in the $H \to ZZ^* \to 4\ell$ and $H \to \gamma\gamma$ channels with $\sqrt{s} = 13$ TeV pp collisions using the ATLAS detector*, Phys. Lett. **B784** (2018) 345–366, arXiv:1806.00242 [hep-ex].

[22] N. Cabibbo, *Unitary Symmetry and Leptonic Decays*, Phys. Rev. Lett. **10** (1963) 531–533, [,648(1963)].

[23] M. Kobayashi and T. Maskawa, *CP Violation in the Renormalizable Theory of Weak Interaction*, Prog. Theor. Phys. **49** (1973) 652–657.

[24] B. Pontecorvo, *Mesonium and anti-mesonium*, Sov. Phys. JETP **6** (1957) 429, [Zh. Eksp. Teor. Fiz.33,549(1957)].

[25] J. D. Bjorken and S. Weinberg, *Mechanism for Nonconservation of Muon Number*, Phys. Rev. Lett. **38** (1977) 622–625, https://link.aps.org/doi/10.1103/PhysRevLett.38.622.

[26] J. L. Diaz-Cruz and J. J. Toscano, *Lepton flavor violating decays of Higgs bosons beyond the standard model*, Phys. Rev. D **62** (2000) 116005, https://link.aps.org/doi/10.1103/PhysRevD.62.116005.

[27] M. Arana-Catania, E. Arganda, and M. J. Herrero, *Non-decoupling SUSY in LFV Higgs decays: a window to new physics at the LHC*, JHEP **09** (2013) 160, arXiv:1304.3371 [hep-ph], [Erratum: JHEP10,192(2015)].

[28] A. Arhrib, Y. Cheng, and O. C. W. Kong, *Comprehensive analysis on lepton flavor violating Higgs boson to $\mu^{\mp}\tau^{\pm}$ decay in supersymmetry without R parity*, Phys. Rev. **D87** (2013) 015025, arXiv:1210.8241 [hep-ph].

[29] G. Perez and L. Randall, *Natural Neutrino Masses and Mixings from Warped Geometry*, JHEP **01** (2009) 077, arXiv:0805.4652 [hep-ph].

[30] A. Goudelis, O. Lebedev, and J.-h. Park, *Higgs-induced lepton flavor violation*, Phys. Lett. **B707** (2012) 369–374, arXiv:1111.1715 [hep-ph].

[31] D. McKeen, M. Pospelov, and A. Ritz, *Modified Higgs branching ratios versus CP and lepton flavor violation*, Phys. Rev. **D86** (2012) 113004, arXiv:1208.4597 [hep-ph].

[32] A. Crivellin, S. Najjari, and J. Rosiek, *Lepton Flavor Violation in the Standard Model with general Dimension-Six Operators*, JHEP **04** (2014) 167, arXiv:1312.0634 [hep-ph].

[33] CMS Collaboration, V. Khachatryan et al., *Search for lepton flavour violating decays of the Higgs boson to $e\tau$ and $e\mu$ in proton–proton collisions at $\sqrt{s} = 8$ TeV*, Phys. Lett. **B763** (2016) 472–500, arXiv:1607.03561 [hep-ex].

[34] CMS Collaboration, A. M. Sirunyan et al., *Search for lepton flavour violating decays of the Higgs boson to $\mu\tau$ and $e\tau$ in proton-proton collisions at $\sqrt{s} = 13$ TeV*, JHEP **06** (2018) 001, arXiv:1712.07173 [hep-ex].

[35] R. Harnik, J. Kopp, and J. Zupan, *Flavor Violating Higgs Decays*, JHEP **03** (2013) 026, arXiv:1209.1397 [hep-ph].

[36] L. Evans and P. Bryant, *LHC Machine*, JINST **3** (2008) S08001.

[37] M. Benedikt, P. Collier, V. Mertens, J. Poole, and K. Schindl, *LHC Design Report*. CERN Yellow Reports: Monographs. CERN, Geneva, 2004. https://cds.cern.ch/record/823808.

[38] *CERN: Accelerating science*, https://home.cern/.

[39] T. Fazzini, G. Fidecaro, A. W. Merrison, H. Paul, and A. V. Tollestrup, *Electron Decay of the Pion*, Phys. Rev. Lett. **1** (1958) 247–249, https://link.aps.org/doi/10.1103/PhysRevLett.1.247.

[40] V. A. Andreev, T. I. Banks, and Case, *Measurement of the Rate of Muon Capture in Hydrogen Gas and Determination of the Proton's Pseudoscalar Coupling g_P*, Tech. Rep. arXiv:0704.2072, Apr, 2007. http://cds.cern.ch/record/1030410. Comments: submitted to Phys.Rev.Lett.

[41] L. Di Lella and C. Rubbia, *The Discovery of the W and Z Particles*, Adv. Ser. Dir. High Energy Phys. **23** (2015) 137–163, https://cds.cern.ch/record/2103277.

[42] ATLAS Collaboration, *The ATLAS Experiment at the CERN Large Hadron Collider*, JINST **3** (2008) S08003.

[43] CMS Collaboration, S. Chatrchyan et al., *The CMS Experiment at the CERN LHC*, JINST **3** (2008) S08004.

[44] ALICE Collaboration, K. Aamodt et al., *The ALICE experiment at the CERN LHC*, JINST **3** (2008) S08002.

[45] LHCb Collaboration, A. A. Alves, Jr. et al., *The LHCb Detector at the LHC*, JINST **3** (2008) S08005.

[46] ATLAS Collaboration, A. Airapetian et al., *ATLAS detector and physics performance: Technical Design Report, 1.* Technical Design Report ATLAS. CERN, Geneva, 1999. https://cds.cern.ch/record/391176.

[47] ATLAS Collaboration Collaboration,, *ATLAS inner detector: Technical Design Report, 1.* Technical Design Report ATLAS. CERN, Geneva, 1997. https://cds.cern.ch/record/331063.

[48] ATLAS Collaboration, *ATLAS Insertable B-Layer Technical Design Report*, Tech. Rep. CERN-LHCC-2010-013. ATLAS-TDR-19, Sep, 2010. https://cds.cern.ch/record/1291633.

[49] ATLAS Collaboration Collaboration, K. Potamianos, *The upgraded Pixel detector and the commissioning of the Inner Detector tracking of the ATLAS experiment for Run-2 at the Large Hadron Collider*, Tech. Rep. ATL-PHYS-PROC-2016-104, CERN, Geneva, Aug, 2016. http://cds.cern.ch/record/2209070. 15 pages, EPS-HEP 2015 Proceedings.

[50] J. Pequenao, *Computer Generated image of the ATLAS calorimeter*, Mar, 2008.

[51] ATLAS Collaboration, M. Aaboud et al., *Operation and performance of the ATLAS Tile Calorimeter in Run 1*, Eur. Phys. J. **C78** (2018) 987, arXiv:1806.02129 [hep-ex].

[52] ATLAS Collaboration, *The ATLAS Experiment at the CERN Large Hadron Collider*, J. Inst. **3** (2008) S08003.

[53] ATLAS Muon Collaboration, E. Diehl, *ATLAS Muon Detector Commissioning*, in *Particles and fields. Proceedings, Meeting of the Division of the American Physical Society, DPF 2009, Detroit, USA, July 26-31, 2009*. 10, 2009. arXiv:0910.2767 [physics.ins-det].

[54] ATLAS Collaboration Collaboration,, *Performance of the ATLAS Inner Detector Track and Vertex Reconstruction in the High Pile-Up LHC Environment*, Tech. Rep. ATLAS-CONF-2012-042, CERN, Geneva, Mar, 2012. http://cds.cern.ch/record/1435196.

[55] T. Cornelissen, M. Elsing, S. Fleischmann, W. Liebig, E. Moyse, and A. Salzburger, *Concepts, Design and Implementation of the ATLAS New Tracking (NEWT)*, Tech. Rep. ATL-SOFT-PUB-2007-007. ATL-COM-SOFT-2007-002, CERN, Geneva, Mar, 2007. https://cds.cern.ch/record/1020106.

[56] ATLAS Collaboration, *Reconstruction of primary vertices at the ATLAS experiment in Run 1 proton–proton collisions at the LHC*, Eur. Phys. J. **C77** (2017) 332, arXiv:1611.10235 [physics.ins-det].

[57] *Vertex Reconstruction Performance of the ATLAS Detector at* $\sqrt{s}$ *= 13 TeV*, Tech. Rep. ATL-PHYS-PUB-2015-026, CERN, Geneva, Jul, 2015. http://cds.cern.ch/record/2037717.

[58] ATLAS Collaboration, *Electron reconstruction and identification efficiency measurements with the ATLAS detector using the 2011 LHC proton-proton collision data*, Eur. Phys. J. **C74** (2014) 2941, arXiv:1404.2240 [hep-ex].

[59] *Electron efficiency measurements with the ATLAS detector using the 2012 LHC proton-proton collision data*, Tech. Rep. ATLAS-CONF-2014-032, CERN, Geneva, Jun, 2014. https://cds.cern.ch/record/1706245.

[60] ATLAS Collaboration, *Electron efficiency measurements with the ATLAS detector using the 2015 LHC proton-proton collision data*, Tech. Rep. ATLAS-CONF-2016-024, CERN, Geneva, Jun, 2016. https://cds.cern.ch/record/2157687.

[61] ATLAS Collaboration, G. Aad et al., *Expected Performance of the ATLAS Experiment - Detector, Trigger and Physics*, arXiv:0901.0512 [hep-ex].

[62] ATLAS Collaboration, M. Aaboud et al., *Electron reconstruction and identification in the ATLAS experiment using the 2015 and 2016 LHC proton-proton collision data at $\sqrt{s}$ = 13 TeV*, Eur. Phys. J. **C79** (2019) 639, arXiv:1902.04655 [physics.ins-det].

[63] ATLAS Collaboration, G. Aad et al., *Topological cell clustering in the ATLAS calorimeters and its performance in LHC Run 1*, Eur. Phys. J. **C77** (2017) 490, arXiv:1603.02934 [hep-ex].

[64] ATLAS Collaboration, *Muon reconstruction efficiency and momentum resolution of the ATLAS experiment in proton-proton collisions at $\sqrt{s}$ = 7 TeV in 2010*, Eur. Phys. J. **C74** (2014) 3034, arXiv:1404.4562 [hep-ex].

[65] ATLAS Collaboration, *Measurement of the muon reconstruction performance of the ATLAS detector using 2011 and 2012 LHC proton–proton collision data*, Eur. Phys. J. **C74** (2014) 3130, arXiv:1407.3935 [hep-ex].

[66] ATLAS Collaboration, *Muon reconstruction performance of the ATLAS detector in proton–proton collision data at $\sqrt{s}$ =13 TeV*, Eur. Phys. J. **C76** (2016) 292, arXiv:1603.05598 [hep-ex].

[67] M. Cacciari, G. P. Salam, and G. Soyez, *The Anti-k(t) jet clustering algorithm*, JHEP **04** (2008) 063, arXiv:0802.1189 [hep-ph].

[68] ATLAS Collaboration, T. A. collaboration, *Pile-up subtraction and suppression for jets in ATLAS*,.

[69] ATLAS Collaboration, *Expected performance of the ATLAS b-tagging algorithms in Run-2*, Tech. Rep. ATL-PHYS-PUB-2015-022, CERN, Geneva, Jul, 2015. https://cds.cern.ch/record/2037697.

[70] ATLAS Collaboration Collaboration,, *Optimisation of the ATLAS b-tagging performance for the 2016 LHC Run*, Tech. Rep. ATL-PHYS-PUB-2016-012, CERN, Geneva, Jun, 2016. https://cds.cern.ch/record/2160731.

[71] ATLAS Collaboration, *Performance of Missing Transverse Momentum Reconstruction in Proton-Proton Collisions at 7 TeV with ATLAS*, Eur. Phys. J. **C72** (2012) 1844, arXiv:1108.5602 [hep-ex].

[72] *Performance of Missing Transverse Momentum Reconstruction in ATLAS studied in Proton-Proton Collisions recorded in 2012 at 8 TeV*, Tech. Rep. ATLAS-CONF-2013-082, CERN, Geneva, Aug, 2013. http://cds.cern.ch/record/1570993.

[73] *Performance of missing transverse momentum reconstruction for the ATLAS detector in the first proton-proton collisions at at $\sqrt{s}$= 13 TeV*, Tech. Rep. ATL-PHYS-PUB-2015-027, CERN, Geneva, Jul, 2015. https://cds.cern.ch/record/2037904.

[74] *Expected performance of missing transverse momentum reconstruction for the ATLAS detector at $\sqrt{s} = 13$ TeV*, Tech. Rep. ATL-PHYS-PUB-2015-023, CERN, Geneva, Jul, 2015. https://cds.cern.ch/record/2037700.

[75] LHC Higgs Cross Section Working Group Collaboration, D. de Florian et al., *Handbook of LHC Higgs Cross Sections: 4. Deciphering the Nature of the Higgs Sector*, arXiv:1610.07922 [hep-ph].

[76] ATLAS, CMS Collaboration, G. Aad et al., *Measurements of the Higgs boson production and decay rates and constraints on its couplings from a combined ATLAS and CMS analysis of the LHC pp collision data at $\sqrt{s} = 7$ and 8 TeV*, JHEP **08** (2016) 045, arXiv:1606.02266 [hep-ex].

[77] T. D. Lee, *A Theory of Spontaneous T Violation*, Phys. Rev. D **8** (1973) 1226–1239, https://link.aps.org/doi/10.1103/PhysRevD.8.1226.

[78] ATLAS Collaboration, *The ATLAS simulation infrastructure*, Eur. Phys. J. **C 70** (2010) 823–874, arXiv:1005.4568 [physics.ins-det].

[79] T. Sjöstrand, S. Ask, J. R. Christiansen, R. Corke, N. Desai, P. Ilten, S. Mrenna, S. Prestel, C. O. Rasmussen, and P. Z. Skands, *An Introduction to PYTHIA 8.2*, Comput. Phys. Commun. **191** (2015) 159–177, arXiv:1410.3012 [hep-ph].

[80] P. Nason, *A new method for combining NLO QCD with shower Monte Carlo algorithms*, JHEP **11** (2004) 040, arXiv:0409146 [hep-ph].

[81] S. Frixione, P. Nason and C. Oleari, *Matching NLO QCD computations with parton shower simulations: the POWHEG method*, JHEP **11** (2007) 070, arXiv:0709.2092 [hep-ph].

[82] S. Alioli et al., *A general framework for implementing NLO calculations in shower Monte Carlo programs: the POWHEG BOX*, JHEP **06** (2010) 043, arXiv:1002.2581 [hep-ph].

[83] E. Bagnaschi, G. Degrassi, P. Slavich and A. Vicini, *Higgs production via gluon fusion in the POWHEG approach in the SM and in the MSSM*, JHEP **02** (2012) 088, arXiv:1111.2854 [hep-ph].

[84] K. Hamilton, P. Nason and G. Zanderigh, *Finite quark-mass effects in the NNLOPS POWHEG+MiNLO Higgs generator*, JHEP **05** (2015) 140, arXiv:1501.04637 [hep-ph].

[85] J. Butterworth et al., *PDF4LHC recommendations for LHC Run II*, J. Phys. G **43** (2016) 023001, arXiv:1510.03865 [hep-ph].

[86] C. Anastasiou, C. Duhr, F. Dulat, F. Herzog and B. Mistlberger, *Higgs Boson Gluon-Fusion Production in QCD at Three Loops* , Phys. Rev. Lett. **114** (2015) 212001, arXiv:1503.06056 [hep-ph].

[87] C. Anastasiou et al., *High precision determination of the gluon fusion Higgs boson cross-section at the LHC*, JHEP **05** (2016) 058, arXiv:1602.00695 [hep-ph].

[88] S. Actis, G. Passarino, C. Sturm and S. Uccirati, *NLO electroweak corrections to Higgs boson production at hadron colliders*, Phys. Lett. B **670** (2008) 12, arXiv:0809.1301 [hep-ph].

[89] C. Anastasiou, R. Boughezal and F. Petriello, *Mixed QCD-electroweak corrections to Higgs boson production in gluon fusion*, JHEP **04** (2009) 003, arXiv:0811.3458 [hep-ph].

[90] M. Ciccolini, A. Denner and S. Dittmaier, *Strong and Electroweak Corrections to the Production of a Higgs Boson + 2 Jets via Weak Interactions at the Large Hadron Collider*, Phys. Rev. Lett. **99** (2007) 161803, arXiv:0707.0381 [hep-ph].

[91] M. Ciccolini, A. Denner and S. Dittmaier, *Electroweak and QCD corrections to Higgs production via vector-boson fusion at the LHC*, Phys. Rev. D **77** (2008) 013002, arXiv:0710.4749 [hep-ph].

[92] P. Bolzoni, F. Maltoni, S.-O. Moch and M. Zaro, *Higgs Boson Production via Vector-Boson Fusion at Next-to-Next-to-Leading Order in QCD*, Phys. Rev. Lett. **105** (2010) 011801, arXiv:1003.4451 [hep-ph].

[93] O. Brein, A. Djouadi and R. Harlander, *NNLO QCD corrections to the Higgs-strahlung processes at hadron colliders*, Phys. Lett. B **579** (2004) 149, arXiv:0307206 [hep-ph].

[94] L. Altenkamp, S. Dittmaier, R. V. Harlander, H. Rzehak and T. J. E. Zirke, *Gluon-induced Higgs-strahlung at next-to-leading order QCD*, JHEP **02** (2013) 078, arXiv:1211.5015 [hep-ph].

[95] A. Denner, S. Dittmaier, S. Kallweit and A. Muck, *Electroweak corrections to Higgs-strahlung off W/Z bosons at the Tevatron and the LHC with Hawk*, JHEP **03** (2012) 075, arXiv:1112.5142 [hep-ph].

[96] J. Alwall, R. Frederix, S. Frixione, V. Hirschi, F. Maltoni, et al., *The automated computation of tree-level and next-to-leading order differential cross sections, and*

their matching to parton shower simulations, JHEP **07** (2014) 079, arXiv:1405.0301 [hep-ph].

[97] NNPDF Collaboration, R. Ball et al., *Parton distributions for the LHC Run II*, JHEP **1504** (2014) 040, arXiv:1410.8849 [hep-ph].

[98] W. Beenakker et al., *Higgs Radiation Off Top Quarks at the Tevatron and the LHC*, Phys. Rev. Lett. **87** (2001) 201805, arXiv:hep-ph/0107081 [hep-ph].

[99] W. Beenakker et al., *NLO QCD corrections to $t\bar{t}H$ production in hadron collisions*, Nucl. Phys. B **653** (2003) 151–203, arXiv:hep-ph/0211352 [hep-ph].

[100] S. Dawson, L. Orr, L. Reina, and D. Wackeroth, *Next-to-leading order QCD corrections to $pp \to t\bar{t}h$ at the CERN Large Hadron Collider*, Phys. Rev. D **67** (2003) 071503, arXiv:hep-ph/0211438 [hep-ph].

[101] S. Dawson, C. Jackson, L. Orr, L. Reina, and D. Wackeroth, *Associated Higgs boson production with top quarks at the CERN Large Hadron Collider: NLO QCD corrections*, Phys. Rev. D **68** (2003) 034022, arXiv:hep-ph/0305087 [hep-ph].

[102] Y. Zhang, W.-G. Ma, R.-Y. Zhang, C. Chen, and L. Guo, *QCD NLO and EW NLO corrections to $t\bar{t}H$ production with top quark decays at hadron collider*, Phys. Lett. B **738** (2014) 1–5, arXiv:1407.1110 [hep-ph].

[103] S. Frixione, V. Hirschi, D. Pagani, H.-S. Shao, and M. Zaro, *Electroweak and QCD corrections to top-pair hadroproduction in association with heavy bosons*, JHEP **06** (2015) 184, arXiv:1504.03446 [hep-ph].

[104] T. Gleisberg, S. Hoeche, F. Krauss, M. Schonherr, S. Schumann, et al., *Event generation with Sherpa 1.1*, JHEP **0902** (2009) 007, arXiv:0811.4622 [hep-ph].

[105] NNPDF Collaboration, R. D. Ball et al., *Parton distributions for the LHC run II*, JHEP **04** (2015) 040, arXiv:1410.8849 [hep-ph].

[106] S. Schumann and F. Krauss, *A parton shower algorithm based on Catani-Seymour dipole factorisation*, JHEP **03** (2008) 038, arXiv:0709.1027 [hep-ph].

[107] K. Melnikov and F. Petriello, *Electroweak gauge boson production at hadron colliders through $O(\alpha_S^2)$*, Phys. Rev. D **74** (2006) 114017, arXiv:0609070 [hep-ph].

[108] C. Anastasiou, L. J. Dixon, K. Melnikov and F. Petriello, *High precision QCD at hadron colliders: Electroweak gauge boson rapidity distributions at next-to-next-to leading order*, Phys. Rev. D **69** (2004) 094008, arXiv:0312266 [hep-ph].

[109] H.-L. Lai, M. Guzzi, J. Huston, Z. Li, P. M. Nadolsky, J. Pumplin, and C.-P. Yuan, *New parton distributions for collider physics*, Phys. Rev. D **82** (2010) 074024, arXiv:1007.2241 [hep-ph].

[110] T. Sjostrand, S. Mrenna, and P. Skands, *PYTHIA 6.4 physics and manual*, JHEP **05** (2006) 026, arXiv:hep-ph/0603175.

[111] M. Czakon and A. Mitov, *Top++: A program for the calculation of the top-pair cross-section at hadron colliders*, Comput. Phys. Commun. **185** (2014) 2930, arXiv:1112.5675 [hep-ph].

[112] S. Alioli, P. Nason, C. Oleari and E. Re, *NLO single-top production matched with shower in POWHEG: s- and t-channel contributions*, JHEP **09** (2009) 111, arXiv:0907.4076 [hep-ph].

[113] E. Re, *Single-top Wt-channel production matched with parton showers using the POWHEG method*, Eur. Phys. J. C **71** (2011) 1547, arXiv:1009.2450 [hep-ph].

[114] M. Aliev et al., *HATHOR - HAdronic Top and Heavy quarks crOss section calculatoR*, Comput. Phys. Commun. **182** (2011) 1034, arXiv:1007.1327 [hep-ph].

[115] P. Kant et al., *HATHOR for single top-quark production: Updated predictions and uncertainty estimates for single top-quark production in hadronic collisions*, Comput. Phys. Commun. **191** (2015) 74, arXiv:1406.4403 [hep-ph].

[116] N. Kidonakis, *Two-loop soft anomalous dimensions for single top quark associated production with a W^- or H^-*, Phys. Rev. D **82** (2010) 054018, arXiv:1005.4451 [hep-ph].

[117] ATLAS Collaboration, M. Aaboud et al., *Cross-section measurements of the Higgs boson decaying into a pair of τ-leptons in proton-proton collisions at $\sqrt{s} = 13$ TeV with the ATLAS detector*, Phys. Rev. **D99** (2019) 072001, arXiv:1811.08856 [hep-ex].

[118] ATLAS Collaboration, G. Aad et al., *Search for the Standard Model Higgs boson in the $H \to \tau^+\tau^-$ decay mode in $\sqrt{s} = 7$ TeV pp collisions with ATLAS*, JHEP **09** (2012) 070, arXiv:1206.5971 [hep-ex].

[119] ATLAS Collaboration Collaboration,, *Search for the Standard Model Higgs boson in $H \to \tau^+\tau^-$ decays in proton-proton collisions with the ATLAS detector*, Tech. Rep. ATLAS-CONF-2012-160, CERN, Geneva, Nov, 2012. https://cds.cern.ch/record/1493624.

[120] *Evidence for Higgs Boson Decays to the $\tau^+\tau^-$ Final State with the ATLAS Detector*, Tech. Rep. ATLAS-CONF-2013-108, CERN, Geneva, Nov, 2013. https://cds.cern.ch/record/1632191.

[121] *Evidence for Higgs boson Yukawa couplings in the $H \to \tau\tau$ decay mode with the ATLAS detector*, Tech. Rep. ATLAS-CONF-2014-061, CERN, Geneva, Oct, 2014. https://cds.cern.ch/record/1954724.

[122] ATLAS Collaboration, M. Aaboud et al., *Measurements of gluon-gluon fusion and vector-boson fusion Higgs boson production cross-sections in the $H \to WW^* \to e\nu\mu\nu$ decay channel in pp collisions at $\sqrt{s} = 13$ TeV with the ATLAS detector*, Phys. Lett. **B789** (2019) 508–529, arXiv:1808.09054 [hep-ex].

[123] A. Elagin, P. Murat, A. Pranko, and A. Safonov, *A New Mass Reconstruction Technique for Resonances Decaying to di-tau*, Nucl. Instrum. Meth. **A654** (2011) 481–489, arXiv:1012.4686 [hep-ex].

[124] G. Cowan, K. Cranmer, E. Gross, and O. Vitells, *Asymptotic formulae for likelihood-based tests of new physics*, Eur. Phys. J. **C71** (2011) 1554, arXiv:1007.1727 [physics.data-an], [Erratum: Eur. Phys. J.C73,2501(2013)].

[125] LHC Higgs Cross Section Working Group Collaboration, S. Dittmaier et al., *Handbook of LHC Higgs Cross Sections: 1. Inclusive Observables*, arXiv:1101.0593 [hep-ph].

[126] LHC Higgs Cross Section Working Group Collaboration, J. R. Andersen et al., *Handbook of LHC Higgs Cross Sections: 3. Higgs Properties*, arXiv:1307.1347 [hep-ph].

[127] *Jet Calibration and Systematic Uncertainties for Jets Reconstructed in the ATLAS Detector at* $\sqrt{s} = 13$ *TeV*, Tech. Rep. ATL-PHYS-PUB-2015-015, CERN, Geneva, Jul, 2015. https://cds.cern.ch/record/2037613.

[128] ATLAS Collaboration, M. Aaboud et al., *Identification and rejection of pile-up jets at high pseudorapidity with the ATLAS detector*, Eur. Phys. J. **C77** (2017) 580, arXiv:1705.02211 [hep-ex], [Erratum: Eur. Phys. J.C77,no.10,712(2017)].

[129] ATLAS Collaboration,, *Luminosity determination in* pp *collisions at* $\sqrt{s} = 13$ *TeV using the ATLAS detector at the LHC*, Tech. Rep. ATLAS-CONF-2019-021, CERN, Geneva, Jun, 2019. https://cds.cern.ch/record/2677054.

[130] ATLAS Collaboration, G. Aad et al., *Evidence for the Higgs-boson Yukawa coupling to tau leptons with the ATLAS detector*, JHEP **04** (2015) 117, arXiv:1501.04943 [hep-ex].

[131] ATLAS Collaboration, *Search for lepton-flavour-violating* $H \to \mu\tau$ *decays of the Higgs boson with the ATLAS detector*, JHEP **11** (2015) 211, arXiv:1508.03372 [hep-ex].

[132] ATLAS Collaboration, *Search for lepton-flavour-violating decays of the Higgs and* Z *bosons with the ATLAS detector*, Eur. Phys. J. C **77** (2017) 70, arXiv:1604.07730 [hep-ex].

[133] CMS Collaboration, *Search for lepton flavour violating decays of the Higgs boson to* $\mu\tau$ *and* $e\tau$ *in proton–proton collisions at* $\sqrt{s} = 13$ *TeV*, JHEP **06** (2018) 001, arXiv:1712.07173 [hep-ex].

[134] ATLAS Collaboration, G. Aad et al., *Searches for lepton-flavour-violating decays of the Higgs boson in $\sqrt{s} = 13$ TeV pp collisions with the ATLAS detector*, arXiv:1907.06131 [hep-ex].

[135] L. Breiman, J. Friedman, R. Olshen, and C. Stone, *Classification and Regression Trees*. Chapman & Hall, New York, 1984.

[136] J. Friedman, *Stochastic gradient boosting*, Comput. Stat. Data Anal. **38** (2002) 367.

[137] Y. Freund and R. E. Schapire, *A decision-theoretic generalization of on-line learning and an application to boosting*, J. Comput. Syst. Sci. **55** (1997) 119.

[138] A. Hoecker, P. Speckmayer, J. Stelzer, J. Therhaag, E. von Toerne, and H. Voss, *TMVA: Toolkit for Multivariate Data Analysis*, PoS **ACAT** (2007) 040, arXiv:physics/0703039.

[139] A. L. Read, *Presentation of search results: The CL(s) technique*, J. Phys. **G28** (2002) 2693–2704, [,11(2002)].

[140] ATLAS Collaboration,, *A search for the dimuon decay of the Standard Model Higgs boson in pp collisions at $\sqrt{s} = 13$ TeV with the ATLAS Detector*, Tech. Rep. ATLAS-CONF-2019-028, CERN, Geneva, Jul, 2019. http://cds.cern.ch/record/2682155.

[141] ATLAS Collaboration,, *A search for the rare decay of the Standard Model Higgs boson to dimuons in pp collisions at $\sqrt{s} = 13$ TeV with the ATLAS Detector*, Tech. Rep. ATLAS-CONF-2018-026, CERN, Geneva, Jul, 2018. https://cds.cern.ch/record/2628763.

[142] ATLAS Collaboration,, *Search for the Higgs boson decays $H \to ee$ and $H \to e\mu$ in pp collisions at $\sqrt{s} = 13$ TeV with the ATLAS detector*, Phys. Lett. B **801** (2019) 135148. 19 p, https://cds.cern.ch/record/2690381.

[143] CMS Collaboration, V. Khachatryan et al., *Search for a standard model-like Higgs boson in the $\mu^+\mu^-$ and e^+e^- decay channels at the LHC*, Phys. Lett. **B744** (2015) 184–207, arXiv:1410.6679 [hep-ex].